ISTANBUL TECHNICAL UNIVERSITY ★ GRADUATE SCHOOL OF SCIENCE ENGINEERING AND TECHNOLOGY

COMBUSTION SYNTHESIS AND CHARACTERIZATION OF MOLYBDENUM AND BORON CONTAINING MULTICOMPONENT COMPOSITE MATERIALS

Ph.D. THESIS

Sevinch RAHIMI MOGHADDAM

Department of Materials Science and Engineering

Materials Science and Engineering Programme

JUNE 2019

ISTANBUL TECHNICAL UNIVERSITY ★ GRADUATE SCHOOL OF SCIENCE ENGINEERING AND TECHNOLOGY

COMBUSTION SYNTHESIS AND CHARACTERIZATION OF MOLYBDENUM AND BORON CONTAINING MULTICOMPONENT COMPOSITE MATERIALS

Ph.D. THESIS

Sevinch RAHIMI MOGHADDAM
(521122010)

Department of Materials Science and Engineering

Materials Science and Engineering Programme

Thesis Advisor: Assoc. Prof. Dr. Cevat Bora DERIN

JUNE 2019

İSTANBUL TEKNİK ÜNİVERSİTESİ ★ FEN BİLİMLERİ ENSTİTÜSÜ

MOLİBDEN VE BOR İÇEREN ÇOK BİLEŞENLİ KOMPOZİT MALZEMELERİN YANMA SENTEZİ İLE ÜRETİMİ VE KARAKTERİZASYONU

DOKTORA TEZİ

Sevinch RAHIMI MOGHADDAM
(521122010)

Malzeme Bilimi ve Mühendisliği Anabilim Dalı

Malzeme Bilimi ve Mühendisliği Programı

Tez Danışmanı: Doç. Dr. Cevat Bora DERİN

HAZİRAN 2019

Sevinch RAHIMI MOGHADDAM, a Ph.D. student of İTU Graduate School of Science Engineering and Technology student ID 521122010, successfully defended the thesis/dissertation entitled "COMBUSTION SYNTHESIS AND CHARACTERIZATION OF MOLYBDENUM AND BORON CONTAINING MULTICOMPONENT COMPOSITE MATERIALS", which she prepared after fulfilling the requirements specified in the associated legislations, before the jury whose signatures are below.

Thesis Advisor :	**Prof. Dr. Name SURNAME** İstanbul Technical University	....
Jury Members :	**Prof. Dr. Name SURNAME** Istanbul Technical University	....
	Prof. Dr. Name SURNAME .... University	....
	Prof. Dr. Name SURNAME .... University	....
	Prof. Dr. Name SURNAME .... University	....

Date of Submission : 14 May 2019

Date of Defense : 26 June 2019

To my dear family,

FOREWORD

I would like to express my special gratitude to my research advisor, Assoc Prof. Dr. C. Bora DERİN, for the opportunity to work in his research project and for his valuable advices, supervision, patience and support throughout this study.

Thanks to the funding agencies which supported this dissertation: The Scientific and Technological Reasearch Council of Turkey (TUBITAK) and ITU Scientific Research Project Coordination Office.

I would like to extend my appreciation to Dr. Meltem SEZEN and Dr. Feray BAKAN for the analyses at Sabanci University.

Thank you to all the teaching assistants and lab mates who helped me during my experiments, analyses and thesis editing, especially Dr. Murat ALKAN, Dr. Mehmet BUGDAYCI, Dr. Faiz MUHAFFEL, Dr. Yakup YUREKTURK, Uzm. Inci KOL, Res. Assist. Faruk KAYA, and Sajjad ALIAKBARLU.

I would like to thank my dear uncle for his encourage and support during my study in Turkey and I also express my gratitude to my close friends for their friendship and support throughout these years.

This thesis is dedicated to my beloved parents and my dear brother who always gave me their unconditional love, support, encourage, and motivation through the whole long way of my study to puruse my goals throughout my life.

June 2019 Sevinch RAHIMI MOGHADDAM
(Materials Engineer)

TABLE OF CONTENTS

Page

ABBREVIATIONS

CS	**:** Combustion Synthesis
SHS	**:** Self-propagating High-tempearture Synthesis
MMC	**:** Metal Matrix Composites
BCT	**:** Base Centered Tetragonal
TBBC	**:** Ternary Boride Base Cermets
XRF	**:** X-ray Flourescense
AAS	**:** Atomic Absorption Spectroscopy
XRD	**:** X-ray Diffractometry
SEM	**:** Scanning Electron Microscopy
EDS	**:** Energy Dispersive Spectroscopy
BSE	**:** Back Scattered Electron
OM	**:** Optical Microscopy
PMC	**:** Polymer Matrix Composites
IMC	**:** Intermetallic Matrix Composites
CMC	**:** Ceramic Matrix Composites
WVL	**:** Wear Volume Loss
PM	**:** Powder Metallurgy

SYMBOLS

HV	: Vicker's Hardness
HRC	: Rockwell C Hardness
T_{ad}	: Adiabatic Temperature
T_m	: Melting Temperature
°C	: Celsius degrees
K	: Kelvin
t	: time
min	: minute
mm	: Milimeter
s	: Second
h	: height
η_{ingot}	: Yield of Target
g	: gram
%wt.	: Weight Percentage
at%	: Atomic Percentage
η_{loss}	: Materials Loss
U	: Burning Velocity
M_0, M_c	: Initial and Final Weights of Raw Materials
m_0, m_c	: Initial and Final Weights of Target Metal
kV	: KiloVolts
µA	: MicroAmperes
W	: Watts
N	: Newton
mbar	: Milibar
a, b, c	: Lattice Constants
γ, γ'	: Ni and Ni_3Al phases
τ	: Ternary Borides in Mo-M-B system
kJ	: Kilo Joules

LIST OF TABLES

Page

LIST OF FIGURES

COMBUSTION SYNTHESIS AND CHARACTERIZATION OF MOLYBDENUM AND BORON CONTAINING MULTICOMPONENT COMPOSITE MATERIALS

SUMMARY

New tungsten free metal matrix composites have attracted great attention in recent years due to the demand for alternative materials for high temperature, wear and corrosion resistant hard materials with less or no tungsten. Ternary boride based composites such as Mo_2NiB_2-Ni, Mo_2FeB_2-Fe, and Mo_2CoB_2-Co are the most promising candidates which have excellent properties of mechanical, abrasive resistance, corrosive resistance, and high-temperature resistance.

The conventional techniques such as reaction boronizing sintering method have been applied to produce these ternary boride composite materials at high temperatures by using pure metals or binary boride powders. The major purpose of this dissertation is to use a technique for producing these ternary borides that could overcome the limitations of conventional methods. Combustion synthesis through a thermite-type SHS reaction provides the advantages of time and energy saving, simplicity, low-cost raw materials, and high-purity products. The thermochemical modeling and the experimental procedure of SHS-under normal gravity were carried out to simultaneous production of Mo_2NiB_2, Mo_2FeB_2, and Mo_2CoB_2 reinforcements and metal matrices. The SHS process involves six reaction stages as follows: 1) reductions of metal oxides and boron trioxide with Al, 2) evolving of heat energy, 3) melting of metal matrix (Ni, Fe, and Co), 4) synthesis of the ternary borides of Mo_2NiB_2, Mo_2FeB_2, and Mo_2CoB_2, 5) dispersion of borides in metal matrix, and 6) phase separation and solidification of cast composites.

At the first stage, the synthesis of composites containing higher percentages of ternary borides was simulated by FactSage software using different initial mixtures. Secondly, the formation of different phase structures, the yield of the products and the mechanical properties of the composites were studied to determine how they change with different raw materials ratios. Thirdly, the addition of alloying elements was investigated to observe how it affects the structure and composition of obtained ternary borides. The process parameters such as pre-compaction, annealing, and arc melting after the synthesis were used to observe the changes in composition and structure of alloys. The results were discussed regarding the effect of different conditions on the residual Al, microstructure, phase composition, and mechanical properties of the bulk samples. It was observed that increasing both the B_2O_3/Al ratio (from 0.28 to 0.72) and Mo_xO_y/MoO_3 ratio (from 0.58 to 1.5) can significantly decrease the residual Al content and increase ternary boride phases in the products. The SHS-synthesized composites with the 46.5Mo-47.5Ni-5.5B and 60Ni-35Mo-5B compositions exhibited high hardness, high wear resistance, low residual Al, and high Mo_2NiB_2 content. These composites are composed of the Mo_2NiB_2 reinforcement embedded in the

$Ni_3Al/Ni_{20}Al_3B_6$ matrix. The microhardness values of composites in three Mo-Ni-B, Mo-Fe-B, and Mo-Co-B systems reach up to 1300 HV.

All those results confirmed that the ternary boride containing hard materials could be obtained from low-cost and available raw materials by using a cost-effective combustion synthesis method under normal gravity.

MOLİBDEN VE BOR İÇEREN ÇOK BİLEŞENLİ KOMPOZİT MALZEMELERİN YANMA SENTEZİ İLE ÜRETİMİ VE KARAKTERİZASYONU

ÖZET

Günümüzde, dünya tungsten madeni üretiminin %85'ini karşılayan Çin Halk Cumhuriyeti'nin, iç piyasasındaki aşırı talepler ve ihracatta uyguladığı tekelci politikası nedeniyle, az veya hiç tungsten içermeyen yüksek sıcaklık, aşınma ve korozyona dayanıklı alternatif malzemelere olan arayış hızlanmıştır.

Bu bağlamda, özellikle tungsten karbür – kobalt (WC-Co) gibi metal matrisli kompozitlere alternatif olabilecek Mo_2NiB_2-Ni, Mo_2FeB_2-Fe, MoCoB-Co gibi üçlü borür bazlı sermetler (Ternary Boride Based Cermets -TBBCs) mükemmel mekanik, aşınma, korozyon dayanımı gösteren malzemeler olup, günümüzde çok yeni çalışılan konular arasındadır. Reaksiyon borlayıcı sinterleme (reaction boronizing sintering) yöntemiyle üretilen bu yeni sermetlerin üretim aşaması sırasıyla bilyalı değirmende pahalı saf metal veya karbonil (Mo, Ni, Cr, Fe..) ve ikili borür tozların (Ni_2B,VB…) karıştırılması, kurutulması, granüle edilmesi, preslenmesi ve sinterlenmesi kademelerini içermektedir.

Bu tez çalışmasında, bu metal matrisli kompozitlerin, kendiliğinden ilerleyen yüksek sıcaklık sentezi (self-propagating high temperature synthesis - SHS) yöntemiyle daha ucuz, kolay ve saniyelerle ifade edilebilecek şekilde hızlı üretilebileceğini ön görmekteyiz.

Önerilen SHS metodunda, altı reaksiyon safhası birkaç saniye içerisinde tamamlanan tek bir süreç adımından oluşmaktadır. Bunlar; i) metal oksitler ve bor oksitin Al ile redüksiyonu, ii) yüksek miktardaki ısı enerjisinin ortaya çıkışı, iii) redüklenmiş metal matrisin erimesi (Ni, Fe veya Co), iv) ilave edilmiş üçlü borürlerin sentezi (Cr, V, Nb, Mn, Ta gibi elementler içeren Mo_2NiB_2, MoCoB veya Mo_2FeB_2), v) oluşan borürlerin metal matris içerisindeki dispersiyonu, ve vi) faz ayırımı (sermet-curuf) ve soğumadır. Açık atmosferde gerçekleştirilen SHS deneylerinde, güç kaynağından direnç teline elektrik verilip, direnç telinin şarjı tetiklemesiyle reaksiyon başlamıştır. Potanın soğumasının ardından, metal ve curuflar kırılarak ayrılmış ve analiz işlemleri uygulanmıştır.

Adyabatik şartların geliştiği bu sistemlerde oluşan ısının tümünün sıcaklığa çevrildiği varsayılmaktadır. Ekzotermik SHS reaksiyonları sırasında açığa çıkan enerji, reaksiyonların sıcaklıklarını arttırmakta ve bu sıcaklıklarda molibden, nikel, demir, kobalt ve bor sıvı fazda bulunmaktadır.

İlk aşamada, çeşitli termokimyasal veritabanlarıyla olası SHS ürün kompozisyonlarının ve adyabatik sıcaklarının tahmini sonrası, SHS deneylerinde, başlangıç karışımında farklı metal oksitlerin oranları, redükleyici ilaveler ve ısı bastırıcı etkileri incelenmiştir.

Elde edilen ürünler spektral analiz, atomik absorbsiyon spektrometresi (AAS), X-ışınları floresans (XRF), X-ışınları difraksiyonu (XRD), taramalı elektron mikroskobu (SEM), enerji dispersif spektrometresi (EDS) , mikro sertlik ve diğer mekanik test yöntemleriyle karakterize edilmiştir.

İkinci aşamada, Cr, V ve Mn gibi elementlerin ilavesiyle elde edilmiş Mo_2NiB_2-Ni, Mo_2FeB_2-Fe, MoCoB-Co sermetlerin ucuz hammaddelerden yola çıkarak kendiliğinden ilerleyen yüksek sıcaklık sentezi üzerine yoğunlaşılmıştır. Bu yaklaşım bu metal matrisli kompositlerin tek adımda üretimine (*in-situ SHS, yerinde SHS*) imkan sağlamıştır.

Üçüncü aşamada, tavlama ve vakum ortamında ergitme gibi proseslerin elde edilen malzemelerin mikroyapısı, sertliği ve fazları üzerinde etkisi incelenmiştir.

Mo-Ni-B sistemi üretimindeki ilk çalışmalarda, farklı miktarlarda redükleyici Al ilavesinin (stokiyometrik x0.85-1.15) ve toplam şarj ağırlığının %10'una kadar Al_2O_3 ilavesinin etkisi araştırılmıştır. Stokiyometrinin 1.05 katı Al ve toplam şarj ağırlığının %5'i kadar Al_2O_3 ilavesi en yüksek kazanım verimi (~%82) olarak bulunmuştur. Kullanılan oksit oranlarının mikroyapı ve faz içeriğine olan etkilerinin araştırıldığı deneylerde NiO, Fe_2O_3, CoO ve B_2O_3 oranları değiştirilmiştir. Ancak elde edilen veriler sonucunda, her ne kadar istenilen intermetalik oluşumlar elde edilebilse de, Mo-Ni-B, Mo-Fe-B ve Mo-Co-B sistemi ürünlerin çoğunda yüksek miktarda redükleyici olarak kullanılan alüminyuma (≤ ağ.% 16 Al) ve ısıtma telinden gelen bakıra (≤ ağ.% 6 Cu) rastlanmıştır. Ayrıca, bu ikili intermetaliklerin oluşum esnasında çıkardığı ilave ısı (ekzotermik) adyabatik sıcaklığı daha da yükselttiği; dolayısıyla boroksitin ve diğer oksitlerin bir kısmının redüklenmeden buharlaşmasına neden olduğu görülmüştür. Ürünlerde istenmeyen Al ve Cu birikimlerini minimize etmek amacıyla bazı değişikliklere gidilmiştir. Öncelikle Cu içeriğini azaltmak amacıyla, reaksiyonu başlatan tungsten direnç telinin bakır tel ile birleşim noktaları alümina termoçift kılıf içerisine gizlenmiştir. Bu sayede bakır tellerin yüksek sıcaklıktaki ergimiş alaşımla teması kesilmeye çalışılmıştır. Ürün içerisinde kalan Al'u gidermek için ise, her bir hammadde bileşimi için termokimyasal hesaplama yöntemiyle, ayrı ayrı çalışmalar yapılmıştır. Böylece, stokiyometrik ve katları Al ilavesi yerine, en yüksek ürün veriminin ve içerisinde en az Al'un çözüneceği şartlar hesaplanarak yüksek miktarda B_2O_3ve düşük miktarda redükleyici Al kullanılmıştır. Mo-Ni-B, Mo-Fe-B ve Mo-Co-B sistemlerinde Al içeriği yaklaşık olarak %2-3 arasına, Cu içeriği ise %0.07-0.5 arasına kadar başarıyla indirilebilmiştir. İstenilen Mo_2NiB_2, Mo_2FeB_2, Mo_2CoB_2 fazları başarıyla elde edilmiştir.

Mo-Ni-B, Mo-Fe-B ve Mo-Co-B sistemi ürünlerinde ortalama sertlik değeri 950 -1100 HV arası bulunmuştur. İki 48Mo-46.5Ni-4.5B ve %34Mo-%60-%5B kompozisiyonu, ayrıca tekrar ergitmenin ve homojenizasyonun etkilerinin incelenmesi amacıyla vakum ark ergitme cihazında ergitilmiştir. NI14M ve Ni15M olarak isimlendirilen bu ürünler, birkaç kere vakuma alma-argon verme işlemi sonrasında ergitilmiş, ardından XRF, SEM, XRD ve sertlik testlerine tabii tutulmuştur.

Bu ürünler üzerinde vakum ark ergitme ile yapılan homogenizasyon deneyleri sonucunda serlik değerlerinde yaklaşık 100 HV değerinde azalma olmuştur. Bu durum, ergitme sonrası numunelerin daha tok yapıya dönüştüklerinin göstergesi olmuştur. Cr, Mn ve V ilaveleri gerçekleştirilmiştir. Mo_2NiB_2 fazı içersine özellikle Cr ilave edildiğinde M_3B_2 olarak tarif edilen $(Mo\text{-}Ni\text{-}Cr)_3B_2$ tipi faz oluşmuştur. Bu faz ortorombik Mo_2NiB_2 fazından farklı olarak tetragonal yapıdadır. Mo-Ni-B-X (X=Cr, Mn veya V) sistemlerinde alaşım ilavesiz ürüne (908.7 HV) göre sertlik değerlerinde bir miktar azalma olduğu görülmüştür. Mo-Fe-B-X (X=Cr, Mn veya V) sistemlerinde içerisinde Mn ilavesi 996.7 HV ile en yüksek sertlik değeri göstermiştir. Mo-Co-B-X (X=Cr, Mn veya V) sisteminde tüm alaşımlar içerisinde Mn ilaveli (1249.8 HV) numune en yüksek sertlik değeri göstermiştir. Pota içerisinde konan hammadde toz karışımının reaksiyon öncesi sıkıştırma çalışmalarında 0-60 bar arası yük kullanılmıştır. Ancak metal kazanım verimine bu yükün büyük bir etkisi olmadığı anlaşılmıştır.

Sonuçlar, farklı parametrelerin kalıntı Al, mikroyapı, faz bileşimi ve kütle (bulk) numunelerin mekanik özellikleri üzerindeki etkisine ilişkin olarak tartışılmıştır. Hem B_2O_3 / Al oranının (0.28'den 0.72'ye kadar) hem de Mo_xO_y / MoO_3 oranının (0.58'den 1.5'e kadar) arttırılması, kalıntı Al miktarını önemli ölçüde azaltmış ve ürünlerdeki üçlü borür fazlarını arttırmıştır. SHS ile sentezlenen 46.5Mo-47.5Ni-5.5B ve 60Ni-35Mo-5B kompozitlerde, yüksek sertlik, yüksek aşınma direnci, en düşük kalıntı Al ve yüksek miktarda Mo_2NiB_2 fazı görülmüştür. Bu kompozitler, Mo_2NiB_2 takviyeli Ni_3Al / $Ni_{20}Al_3B_6$ matristen oluşmuştur Mo-Ni-B, Mo-Fe-B ve Mo-Co-B sistemlerinde kompozitlerin mikrosertlik değerleri 1300 HV'ye kadar ulaşılmıştır.

1. INTRODUCTION

Ternary boride based cermets (TBBCs) such as Mo_2NiB_2-Ni, Mo_2FeB_2-Fe, and WCoB-Co have excellent properties of mechanical, abrasive resistance, corrosive resistance, and high-temperature resistance. The crystal structure of Mo_2XB_2 (X=Fe, Co, and Ni) ternary compound was studied by TianWei He, et al. to discuss the stability of transition metal borides. Steinitz, et al. first proved the existence of Mo_2NiB_2 ternary boride (τ_1), and later, Y. B. Kuzma, etal. studied its crystal structure type and physical characteristics [1]. The crystal structure of Mo_2NiB_2 was confirmed by W. Rieger, et al. which determines that the structure of Mo_2NiB_2, W_2NiB_2, W_2FeB_2, and Mo_2CoB_2 ternary compounds are similar as they have the W_2CoB_2 type of crystal structure [2].

Takagi et al. first produced TBBCs by using a new reaction boronizing method and investigated them to improve their physical and mechanical properties and determine the effect of Cr and V additions on Mo_2NiB_2. It was observed that the additional alloying elements change the structure of the ternary borides from orthorhombic to tetragonal that causes considerable impovement in the mechanical properties of the cermets. The high Transverese Rupture Strength (TRS) of the Cr and V containing cermets is attributed to the tetragonal M_3B_2 boride phase that dispersed homogeneously in the nickel base matrix. The Vickers microhardness of Mo_2NiB_2 ternary compound increased from 1700 to 2200 HV with increasing Cr content. The elastic modulus increased to above 400 GPa that is comparable to that of TiC.

Superalloys which are used in a wide variety of heat resistant components are known as the backbone of the aircraft jet engine industry for more than four decades. Using them in the form of composites was studied to develop the applications of monolithic superalloys. The composites have consisted of a superalloy matrix containing discontinuous strengthening phases. The strength of superalloys is dependent on the hardening precipitates. For example, boron and carbon were added to strengthen the grain boundaries by segregating and forming carbides and borides. The segregation in the grain boundary increases the cohesive strength of the composites. Boron combines with a large number of metals and semimetals making binary and higher solid compounds, which are called borides. The borides which formed in the superalloys, have a base centered tetragonal (BCT), M_3B_2 or M_5B_3 formula, where M is a refractory element, for example Mo or Cr.

Two main groups of metal matrix composite production techniques are solid-state and liquid-state. The simultaneous formation of reinforcement and matrix occurs during the processing, falling in the category of composites which are called in-situ composites. Several researchers have studied on the synthesis of composites by in-situ method due to its advantages over conventional stir casting including fine particle size, decent interface, uniformly distributed reinforcement, and excellent wettability of reinforcement by matrix. Besides, the casting route for the production of in-situ composites is economical and suitable for large scale production compared to the powder metallurgy and spray forming methods.

The "Self-propagating High-temperature Synthesis" (SHS), frequently named as combustion synthesis is an energy and cost saving method to synthesize a wide variety of materials including intermetallics, carbides, borides, silicides, oxides, and nitrides as well as their composites or their protective coatings. In the SHS process, after initiation, highly exothermic reaction becomes self-sustaining that propagates through the SHS mixture producing the desired product. In an SHS process, adiabatic combustion temperature (T_{ad}) value is the criteria for indicating the nature of the reactions. While it is above 1800 K, the reaction can be self-sustained. The parameters such as combustion temperature, burning velocity, phase compositions, the microstructure of SHS products and also their properties are influenced by different amounts of initial mixture, composition, the particle size of reagents, and other external parameters (gas pressure, centrifugal force, magnetic and electrical fields, explosion and pressure, etc.).

Aim of the study:

China has traditionally been the world's leading tungsten producer, accounting for 85% of the world's production. China regulates its tungsten industry by limiting the number of exploration, mining, and export licenses; limiting or forbidding foreign investment; imposing constraints on mining and processing; establishing quotas on production and exports; adjusting export quotas to favour value-added downstream materials and products; and imposing export taxes on tungsten materials. China is the world's largest tungsten consumer, and since 2008 the amount of tungsten consumed domestically has exceeded the amount exported. To conserve its resources and meet increasing domestic demand, the Chinese Government was expected to continue to limit tungsten production and its exports and increase tungsten imports. Even Russia, as a second world tungsten producer, accounts for only % 4 of world's production.

As a result, due to continuing China's monopoly, nowadays, searching for alternative materials to tungsten, especially for high temperature, wear and corrosion resistant hard materials with less or no tungsten have been very important issue in the international arena.

Hard materials today are the backbone of the tool manufacturing industry with such diverse applications as machining of metallic and nonmetallic materials, chipless forming (wire drawing, can tooling, forging, stamping, mill rolls, powder compacting punches and dies, high pressure dies and anvils), mining (oil well drill bits, rock drill bits), industrial nozzles (sand blasting, water jet cutting, painting, glue dispensers) industrial wear parts (dental and medical tools), paper, plastic and textile knives, guide rolls, seal rings, road planing knives, tire studs, forestry tools, earth moving and consolidation tools and for functional applications (watch cases and bracelets). WC-Co MMCs (metal matrix composites) still have the most important place in above mentioned industrial application tools which accounts for about 60% of current tungsten consumption.

However, tungsten carbide based MMCs have excellent wear-resistant properties but insufficient in chemical resistance to corrosion, electrical and thermal conductivity etc. Therefore, like cemented carbides, borides of transition metals (Cr, Ti, Mo, Fe, Co etc.) are also strong candidates for applications as functional materials. Among the materials, these borides of transition metals have the set of many popular features and are considered as one of the most promising candidates for production new tungsten free MMCs. The materials based on binary systems (Ti-B, Cr-B, WB, etc.) are difficult to sinter, have high brittleness, which makes them inapplicable in wide use.

In this dissertation, combustion synthesis method was utilized to fabricate tungsten-free ternary boride based metal matrix composites in three different systems of Mo-Ni-B, Mo-Fe-B and Mo-Co-B. The purpose of this dissertation is the production of complex borides (Mo_2NiB_2, Mo_2FeB_2 and Mo_2CoB_2) dispersed in the metal or intermetallic matrix by a low-cost synthesis method (thermite-type SHS) using cheap and available raw materials (i.e. metal oxides of NiO, MoO_3, Fe_2O_3 and Co_3O_4) and also boron trioxide (B_2O_3) source in the presence of Al as a reducing agent. The thermodynamic description of the applied systems and prediction of the reaction mechanisms were studied by FactSage software to estimate the formation of complex borides.

At the first stage, the synthesis of composites containing higher percentages of ternary borides, was simulated by FactSage software using different initial mixtures. Secondly, the formation of different phase structures, the yield of the products and the mechanical properties of the composites were studied to observe how they change with different raw materials ratios. Thirdly, the addition of alloying elements was investigated to determine how it affects the structure and composition of obtained ternary borides. The experiments such as pre-compaction, annealing, and arc melting were carried out for reducing the porosity, toughening, and homogenization of the SHS final products, respectively. The characterization and mechanical properties of the obtained ternary boride based composites were studied by using XRF, AAS, XRD, SEM/EDS, OM, microhardness, micro-indentation, and abrasion testing methods. The results would be discussed to observe the effect of different production conditions and thermodynamical parameterson the phase composition, microstructure and mechanical properties of the produced bulk samples. The results of wear resistance testing on the SHS-synthesized as-cast alloys and WC-Co standard sample would be presented to compare the mechanical properties of these hard matrials.

2. LITERATURE

Literature review of this dissertation comprises the general information about the definition and classification of composites, the properties of superalloy (Ni, Fe and Co) based composites, the thermodynamics of ternary boride containing systems and the describing production methods of metal-matrix composites. The detailed information about SHS synthesis method which were used as an in-situ production technique will be introduced in the scope of this dissertation.

2.1 Composites

Composite materials are multicomponent systems that consist of a discrete constituent (the reinforcement) distributed in a continuous phase (the matrix). Therefore, the unique characteristics of composites come from the properties of the constituents such as their geometry and arrangement. Also, their characteristics depend on the properties of the boundaries or interfaces between the constituents [3].

Composites have a long history because the materials such as Wood and cob have been everyday composites from the ancient years. They have also been used to optimize the performance of some conventional weapons. For example, Japanese warcraft were made of the combination of the stratified steel (with the orientation of defects and impurities in the long direction) and soft iron to enhance their characteristics such as resistance for flexure and impact. In the commercial aircraft area, the specific characteristics of composite materials fulfill the manufacturers interests such as economy and performance. The lower weight of composite components reduces fuel consumption or increases payload which improves performance. The fatigue resistance of composites increases the persistence which saves the long-term cost. The good corrosion resistance of composites reduces the need for inspections which saves the maintenance cost of the product [4].

2.1.1 Reinforcements

The criteria for choosing reinforcement materials include the parameters such as elastic modulus, tensile strength, density, melting temperature, thermal stability, thermal expansion coefficient, size and shape, compatibility with matrix material, and the price [5].

Some examples of the reinforcement materials are carbides (e.g., SiC, B_4C), nitrides (e.g., Si_3N_4, AlN), oxides (e.g., Al_2O_3, SiO_2) and also the elemental mateials such as C and Si. They can be formed in different shapes including continuous fibers, chopped fibres, whiskers, platelets, or particulates. The most common examples of used particulates are alumina, boron carbide, silicon carbide, titanium carbide, and tungsten carbide. The most commonly applied whisker is silicon carbide, but whiskers of alumina and silicon nitride have also been produced. Recently, the family of discontinuously reinforced MMCs either particulate or short wiskers have attracted considerable attentions due to their relatively low cost, good formability and machinability. The density, elastic modulus, and tensile strength of the reinforcing phases influences the structural efficiency of discontinuously reinforced metal matrix composites. The chemical stability and compatibility of the reinforcements with the matrix materials are important for the end product application and also throughout the production process [5].

When the composites are used in the areas exposed to thermal cycling, the thermal mismatch strain, ε, between reinforcement and matrix is an essential consideration. Thermal mismatch strain is considered as a function of the coefficients of thermal expansion difference, Δα, between the reinforcement and matrix according to the following formulae (2.1):

$$\varepsilon=\Delta\alpha\Delta T \tag{2.1}$$

Where ΔT is the temperature change. The minimum value for Δα shows the minimization of the strain accumulation. It is noted that the formation of a dislocation network release these strains that it will change the response of the metal matrix composite to thermomechanical processing in contrast to that of the unreinforced alloys [5].

Various desirable properties in MMC applications could be obtained by using particulate reinforcements. One of these properties is isotropy, meaning that particulate reinforced composites have the same mechanical properties in all directions. The manufacturing processes affect the crystal structure of the reinforcements, for example, SiC crystals may be of β (b c c) or a mixture of β and α (h c p) phases in SiC_p reinforced aluminium alloy [5].

2.1.2 Matrix

The matrix materials are 1) Polymers including two types of thermoplastic resins (polypropylene, polyphenylene sulfone, polyamide, polyetheretherketone, etc.) and thermoset resins (polyesters, phenolics, melamines, silicones, polyurethanes, epoxies),

2) Minerals such as silicon carbide, carbon which can tolerate high temperatures, and 3) Metallic materials such as aluminum alloys, titanium alloys, oriented eutectics [4].

Composite materials whether having a continuous or discontinuous reinforcement phase(s) are usually classified regarding the type of their matrix as follows: polymer-matrix composites (PMCs), metal-matrix composites (MMCs) and ceramic-matrix composites (CMCs). Intermetallic-matrix composites (IMCs) are the subgroup of MMCs which commonly have matrices based on aluminide or silicide intermetallic systems. Polymer-matrix composites are the most widely used composite systems which are applied in aircraft and propulsion systems. MMCs have been used in advanced aircraft and engine designs, but their potentialities have yet to be determined. Intermetallic- and ceramic-matrix composites have the highest-risk among all because of their inherent brittleness, although they offer capabilities such as higher strength and lighter weight at high-temperature applications [6].

MMC and IMC composites are advantageous in special applications. Superalloy-based matrices provide excellent high-temperature mechanical properties at the cost of the density. However, titanium-based composites present lower temperature capabilities and lower density. Copper-based and refractory metal- based MMCs which have high thermal conductivity, can be used in aggressive space propulsion environments. The IMCs with commonly Ti_3AI, TiAI, NiAl, and $MoSi_2$ matrices suffer from low room-temperature ductility compared to MMCs matrices. Figure 2.1 illustrates the range of components that MMCs, intermetallics and IMCs are considered.

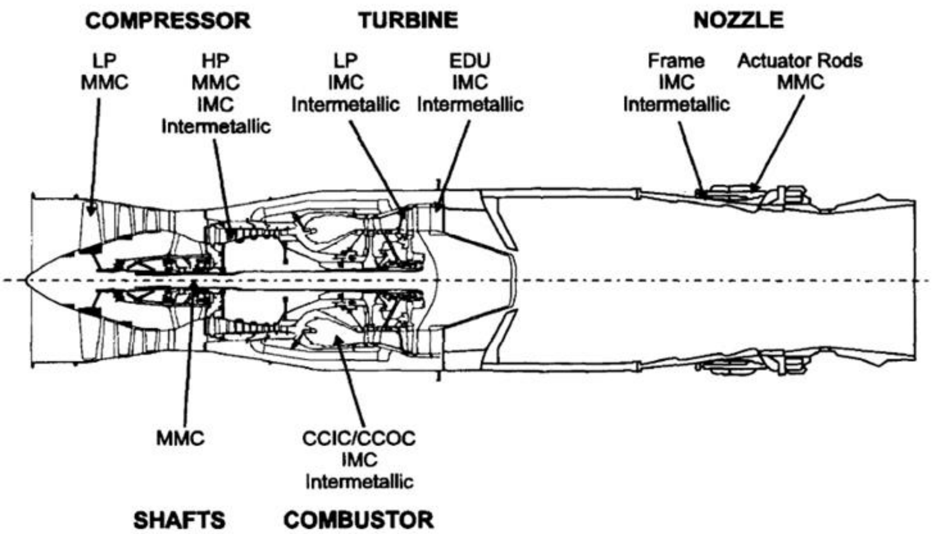

Figure 2.1 : Potential applications of MMCs, monolithic intermetallics and IMCs in military [6].

2.1.3 MMC composites

Metal composite materials have wide applications in daily life when produced in situ from the conventional processing techniques of metals. Materials like cast iron with graphite or carbide enriched steel or tungsten carbide cermets which have different carbides and metallic binders are classified in the group of metal matrix composites [7].

The types of metals used in the matrix of this kind of composites depend on the application area. Enhancing the strength and stiffness of metal matrix composites is possible by selecting an appropriate reinforcement for matrix material including volume fraction, shape and size. During the past decade, the requirements for advanced applications have changed that the conventional alloys were found not to be suitable. Therefore, a range of specific strengths versus temperatures for the reinforcement in metal or ceramic matrix composites is needed as shown in Figure 2.2. These synthethic composite materials are unstable thermodynamically and require high costs of processings, etc. Therefore, for achieving successful development and application of metal matrix composites, there are fundamental challenges like materials processing, synthesis, kinetic understanding, thermodynamic control, reinforcement stability, and strength. In order to obtain a stable metal-matrix composite, the alloy matrix design and interface reactions must be controlled [8].

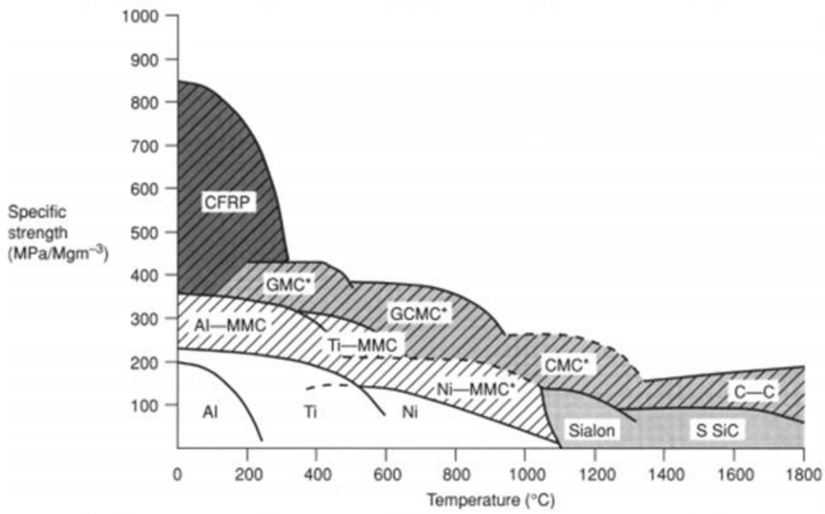

Figure 2.2 : Specific strength versus temperature for metal- and ceramic-matrix composites, carbon fibre reinforced polymers, glass-matrix composites, glass-ceramic matrix composites, ceramic-matrix and metal matrix composites [7].

The presence of thermodynamically stable dispersoids is required to use metal matrix composites for elevated temperature applications although many structural aluminum alloys such as ± 6xxx and 7xxx ± can be applied as matrices. This stability is achieved in an alloy dispersoid system with lower elemental solubility, solid-state diffusivity, and interfacial energies leading to the lower coarsening and interfacial reactions.

The production of metal matrix composites with attractive combinations of strength, ductility and toughness has been reported using low matrix alloying additions. Minor alloying elements which are commonly used in wrought alloys as grain refiners, are not necessary in discontinuous reinforced metal matrix composites. Furthermore, these additions should be avoided, because the ductility of the composites could be impaired by formation of coarse intermetallic compound during consolidation and subsequent processing [5].

2.1.3.1 Physical properties of MMCs

Both of the thermal and electrical conductivities of the reinforcement are less than those of the metallic matrix and therefore, these composites have lower values of conductivity comparing to the monolithic metal [1].

The low density alloys such as Al and Mg alloys can be selected when the low density metal matrix composites are required. Where nickel and titanium containing alloys used as matrix phase of composites, the combination of thermal stability and the optimum specific strength is achieved. The high thermal conductivity (CT) of metals is higher than most of the reinforcements used in MMCs. In order to have composites with lower thermal conductivity, the high volume fractions (>40%) of oxide or carbide reinforcements can be utilized. The properties of metal matrix composites can be formulated as (2.2) using mathematical models such as rule of mixtures (ROM) approximation:

$$\alpha_c = \alpha_m V_m + \alpha_r V_r \tag{2.2}$$

Where α is the property of interest, V is the volume fraction and the subscripts c, m, and r refer to the composite, matrix and reinforcement, respectively.

The thermal conductivity of composites by considering the effects of isostatic stress was proposed by Turner from:

$$CTE_c = \frac{(CTE_m V_m K_m + CTE_r V_r K_r)}{(V_m K_m + V_r K_r)} \tag{2.3}$$

Where K is the bulk modulus of the phase. The CTE which is calculated by this model is lower than that predicted by the ROM approximation.

The proposed model (2.4) by Hashim and Shtrikman for elastic modulus of a composite is as following:

$$E_c = E_m[E_m V_r + E_r(V_r + 1)]/[E_r V_m + E_m(V_r + 1)] \tag{2.4}$$

Where E is Young's modulus. The predictions of these equations were found to be in good agreement with the experimental results. The modulus of metal matrix composites is primarily increased by increasing the reinforcement content but it is independent of the type of reinforcements.

The strength of a crystalline solid is influenced by the stress required to either generate or move dislocations. The stress which causes the transferring of dislocations is an essential parameter in composites with matrices containing two-phase alloys. The motion of dislocations can be controlled by interaction of them with the presence of dispersoids in the matrix. The strengthening mechanisms in metal matrix composites are related to dislocations formed through the differential thermal contraction, geometrical constraints and plastic deformation.

During the processing, the substructures might be formed due to the dislocations which introduced by plastic deformation that found to control the flow stress of the metal-ceramic material. When these dislocations may be damaged by the ceramic particulates, and then retained in the matrix after annealing.

Ansell has reviewed different models that describe the strengthening mechanisms in two-phase alloys. If the moving dislocations could avoid the motion of the dispersed phases by some bypass mechanism, it may result in the plastic deformation. Therefore, the emerging flow stress would be restricted by the stress required to operate this bypass mechanism [1].

2.1.3.2 Mechanical properties of MMCs

In particulate reinforced MMCs, several interrelated factors affect the yield (YS) and tensile (TS) strength. Among them, alloy matrix is the most effective factor defining the mechanical properties of MMCs. Alloys cause the simultaneous high YS and TS strength in the MMCs but make extremely poor deformation behavior. The heat-treatment improves the elastic strain, YS, and TS values of MMCs due to its effect on elastic to plastic transition behavior. The enhanced flow stress in the composites with heat treatment implied by the dislocation interaction with both the alloy precipitates and the reinforcements. The increase in the strength of MMCs and the magnitude of this increase depend on increasing the volume fraction of reinforcements [1].

The particulate reinforced MMCs with less than 20 vol% reinforcement do not present primary and secondary creep behavior but show gradually increasing trend of creep rate throughout the creep life. Several investigators have observed the primary, secondary and tertiary stages of creep at higher volume fractions of reinforcement (greater than 20vol%). According to the creep studies of whisker and particulate-reinforced MMCs, they present a high-stress exponent and high activation energy the same as oxide dispersion strengthened alloys (ODS) and precipitation strengthened alloys (e.g.nickel-base superalloys and Al-Li alloys) with dispersoids inhibiting dislocation movements [1].

2.1.3.3 Particulate reinforced metal matrix composites

The major advantages of particulate (or particle) reinforcements include: low cost of most reinforcements, simple and low cost production processes, isotropic composite properties and formability with most conventional metalworking processes. These properties make them closer to conventional metals and alloys in terms of cost, production techniques and characteristics. Particulate reinforced composite systems can be considered in two sub-classes: ‘large particle’ and ‘dispersion’ strengthened composites, on the basis of the reinforcement or strengthening mechanisms.

Large particle composites

Particulates are the cheapest reinforcements. Many different ceramics are readily available in a wide range of sizes, but those of interest for MMCs are SiC and Al_2O_3 which are produced for grinding media. A tight particle size and control of purity are the main additional requirements for composites [2].

For composites which are reinforced by large particles, the reinforcing part is usually harder and stiffer than the matrix part that likely to inhibit the movement of the matrix. Particle-matrix interactions are indicated by the term ‘large’ that can not be used for atomic or molecular level and ‘continuum mechanics’ must be employed. In these composites, the matrix displace some of the applied stress to the particles. Therefore, the interaction at the particle-matrix interface affects strongly the efficiency of reinforcement. If it is aimed for a low cost and mass market applications, the particulates are the cheapest reinforcements [2].

An example of large particle reinforced composites is cermet in which ceramic particles are embedded in a metal matrix. The ceramic particles usually consist of tungsten carbide and the metal matrix may be nickel or cobalt that form extremely hard materials used as cutting tools [3]. Large particle composites are used widely as cutting tools for hardened steels. It is noted that both the matrix and particulate phases must be quite refractory in order to withstand the high temperatures generated by the cutting action on materials that are extremely hard [4].

Dispersion-strengthened composites

Dispersion strengthened alloys and cermets are a subgroup of the particle reinforced metal matrix composites. Often intermetallic compounds with a definite composition, crystal structure, and properties involved in the dispersion-strengthened composites. They offer hardness and brittleness to the alloys. DS alloys have matrices with additions of insoluble particle components usually ceramics in which the bonding between metal and ceramic results from their mutual or partial solubility. The fine dispersions of oxide, carbide, and boride particles act as barriers to the dislocation movement that improve the strength of the matrix [4]. In dispersion strengthened alloys, the applied stress should be sufficiently large to bend the dislocation line into a semicircular loop to expedite passing through dispersed fine. For effective dispersion hardening, the interparticle separation must be between 10 and 300 nm and, therefore, the particles should be smaller than 100 nm for volume fractions less than 15% [5]. Among dispersion-hardened alloy systems only a few have been used commercially, namely, aluminum, nickel, and tungsten; but, copper and titanium have presented significance in the laboratory and developmental stages. Considerable improvements in the elevated-temperature strength and creep resistance of the matrix alloys attributes to the development of oxide-dispersion-strengthened (ODS) composites (e.g. W-ThO_2, $NiAl_2O_3$, Cu-SiO_2, Cu-Al_2O_3, NiCrAlTi-Y_2O_3, Ni-ThO_2, Ni-HfO_2, etc.). The small (<15%) amounts of fine oxide particles in the ODS composites improve the strength without degrading the valuable matrix properties by resisting recrystallization and grain coarsening and acting as a barrier to the motion of dislocations [5].

2.1.4 IMC composites

Metal-matrix and intermetallic-matrix composites are developed for the advanced aerospace propulsion, and power development programs in which the required materials are dependent on the economics, power system requirements, and other factors. The materials required for the advanced military engines must have higher specific strength operating at higher temperatures and for the civilian engines, the selected materilas need to have long lifetimes. Metal-matrix and intermetallic matrix composites have the potential to fulfill the requirements such as high-temperature, high-thermal-conductivity, and high-strength for specific space propulsion and power applications [6].

The binary phase equilibrium diagrams which attracted the attention in the scientific community are the aluminides as follows: Ni–Al, Fe–Al, and Ti–Al. The intermetallics NiAl and Ni_3Al from the Ni–Al system, FeAl and Fe_3Al from the Fe–Al system, and Ti_3Al, TiAl, and Al_3Ti from the Ti–Al system have been studied extensively [6].

2.1.4.1 Phase equilibria and structure of intermetallic compounds

New phases in many binary phase diagrams of alloys were found to have intermediate concentrations and their range of existence does not extend to pure components. They are in two forms of stoichiometric and nonstoichiometric compounds. The stoichiometric compositions with a fixed ratio of components are known as intermetallic compounds. The nonstoichiometric or extended range of compositions are referred to intermetallic phases or alloys. The Hume-Rothery rules must be satisfied to form the intermetallic phases in the systems with substantial or complete solubility. The rules describe the conditions for a solvent and solute atoms to form a solid solution which are as follows: (i) The size factor: the difference of atomic diameters should be not more than 15%; (ii) The electrochemistry: the difference of electronegativity (chemical affinity) should not be large; (iii) the structure: the crystal structures of solute and solvent must be correlated; and (iv) the valency: the number of valence electrons must be close. For instance, the formation of the intermetallic compound in the Au-Cu system is possible because both Au and Cu have the Fcc structure, but the difference between their lattice parameters is approximately 12.8% [6].

The thermodynamic stability of intermetallics dominates the formation and microstructural properties of these phases. For instance, suitable heat treatment is required to reach the equilibrium for the metastable phases with inhomogeneous compositions which formed through solidification. The additions of alloying elements stabilize the metastable phases and improve the mechanical properties. Because the mechanical properties of the intermetallics rely strongly on their crystal structures, therefore, both the strength and ductility of intermetallics are functions of the type of structures, the ordering degree and crystallographic anisotropy [6]. The structure and planarity of the dislocation cores in these alloys affect the stability and mobility of dislocations. Also, the volume fraction of different phases appeared in multiphase intermetallic alloys manage their deformation and fracture behavior. The intrinsic mechanical properties and the environment have influence on the ductility of Ni- and Fe-aluminides at ambient temperature. Therefore, understanding the relationship between processing, structure, and properties of binary and multicomponent intermetallic alloys requires the study on phase equilibria and crystal structures [6].

2.1.5 Cermets

Cermets are constituted of two metal and ceramic parts which have several descriptions. In German, a composite material which is composed of ceramic particles embedded in the metallic matrix is called as cermet which is produced to be used for high-temperature applications. They fulfill the potential for this kind of applications which required high hardness, high wear resistance and good creep properties with high toughness. For this reason, cermets properties which are a combination of ceramic and metallic characteristics such as high corrosion, heat resistance, and high ductility, are suitable. The ceramic part may be the carbides, nitrides and carbonitrides with metallic binders such as cobalt and nickel. The binder content can be in the range of 10 to 20 wt%. The earliest studies about these materials which were similar to hard metals, but free of tungsten belong to Schwarzkopf and Hirschel in 1930s.. By using elements of Ti, Ta, Nb, V, Mo and carbon in addition to nickel and cobalt as binders, these cermets suffered from high inherent brittleness. Consequent developments in their toughness make them suitable for widespread usage [7].

2.1.5.1 Cemented carbide base cermets

Cobalt is the most commonly used binder in WC hard metals. It can be used as a binder which wets WC readily and as a sintering aid which has a temperature-dependent solubility. These properties make cobalt suitable to obtain products with excellent strength and ductility. Also, cobalt is a ferromagnetic binder which facilitates the magnetic nondestructive evaluation of the metallurgical alloy composition by the measurement of coercitivity and magnetic saturation. However, nickel is used in the place of cobalt to resist corrosion in some applications which exposed to acidic environments. Iron-based binders have been extensively applied for woodworking applications. Nickel-bonded hard metals are often nonmagnetic and can only be evaluated metallographically. The metallurgical alloying methods such as solid solution strengthening and dispersion hardening, increase the strength of nickel bonded hard metals [8].

In the commercially sintered hard metals, it is expected to have a binder phase composition in a nonequilibrium state with composition gradients.

The characteristics of hard metals are as follows [8]:

Compressive strength: Hard metals are one of the strongest materials with the compressive strength of 4-8 kNmm^{-2} which are used as anvils in diamond manufacturing and as metallic materials in hot rolls .

Tensile strength: Bending test can be used to measure the tensile strength of hard metals. The tensile strength values for hard metals are less than their compressive strength, typically 2.4 kNmm^{-2}, but are still stronger than many other materials.

Surface condition (e.g. grinding stresses) and processing route (e.g. HIPing or SINTERHIP) have a significant effect on measured values.

Hardness: Both Vickers test (HV) or the Rockwell test (HRA) can be used to measure the hardness value of hard metals. The content of cobalt and grain size of WC change the hardness values between 1000 and 2000 HV30. These values were found to correlate directly with the strength of cutting tool material.

Toughness: The Palmqvist Vickers indentation test was used to measure the fracture toughness of hard metals. The difficulties in introducing cracks with known geometry make the measurement difficult. Plane strain fracture toughness values change in the range of 7-25 $m^{-3/2}$ MPa $m^{-0.5}$ which is much higher compared to ceramics (with 2-8 $MNm^{-3/2}$).

High temperature strength: Hard metals have high strength at elevated temperatures. However, it decreases steadily with increasing temperature depending on the hard phase. Carbide additions such as (Ta, Nb)C and (Ta, Ti)C increase strength significantly.

Density: The density of the hard metals depends on the WC content. With the significant amount of WC, the density reaches up to 15- Mgm^{-3}. Higher Co contents or additions of cubic carbides and carbonitrides for the hard phase decrease the density down to 4-5 Mgm^{-3}. Although the high density is a disadvantage when specific properties are required it eases the handling of products.

Cermets have excellent wear resistance that makes them suitable for machining of ferrous and nonferrous metals in a wide range of cutting speeds. They present better surface quality after machining. Cermets have advantages such as oxidation resistance, better cutting properties, superior adhesion or diffusion wear resistance at high temperatures compared to cemented carbides. Consequently, they could work without lubricants. The production cost of cermets is lower than cemented carbides.

However, cermets have some drawbacks such as lower fracture toughness, lower resistance to plastic deformation, and higher thermal expansion compared to the cemented carbides. They cause a restriction in using coolants during turning, grooving, and threading processes due to their lower shock resistance [8].

2.2 Boride-Based Composites

The binary or higher solid compounds of boron combined with elements which include a large number of metals and semimetals, are called borides. Unlike the smaller interstitial atoms (C, H, N, O), boron's size is suitable to be exerted the B-B bonds in the lattice so that the metal-boron and metal-metal bonds are not exclusive. Besides, even for the lower borides the lattice of the basic metal can be subjected to major modifications. For these lower borides which are named M_2B, the B atoms are still apart while the M-B bonds dominate considerably. However, the essentially metallic character of the borides such as hardness, high melting point and conductivity that are some of their important features resulted from the prevailing metal-metal bonding [9].

Boron combines with transition metals to produce binary borides that exhibit high melting points, and they are metallic high temperature materials that can be mentioned in the group of the carbides, nitrides and silicides as refractory hard metals. Although a great number of metal borides were prepared by Moissan around the turn of the century, they have not established themselves in modern technology to the same extent as the refractory metal carbides. Therefore it has not been possible to develop metal boride materials that could combine the extreme hardness of refractory borides with toughness similar to cemented tungsten carbide [9].

Compositions of metal borides that are unique in the number of stoichiometries, correspond to at least 24 M:B ratios between 5:1 and 1:66 which are known. However, the most common forms of borides are the monoborides, MB; diborides, MB_2; tetraborides, MB_4; hexaborides, MB_6; dodecaborides, MB_{12}; and hectoborides MB_{66}. The binary compounds of boron, as can be observed in many metal-boron systems, contain three or more intermediate phases. Kiessling has firstly presented the classification of borides based on the boron element configuration as representative for various M:B ratios [9].

With increasing M:B ratio the tendancy to form B-B bonds increases, and pairs (M_3B_2), zigzag chains (MB), branched chains ($M_{11}B_8$), double chains (M_3B_4), plane nets (MB_2) and finally 3-dimensional arrays of boron atoms, including cross-linked nets (MB_4), interconnected B6 octahedra (MB_6), B_{12}-cubo-octahedra (MB_{12}), and interconnected B_{12}-icosahedra (MB_{66}) are found [9]. The configuration of boron atoms in borides are preseneted in Figure 2.3.

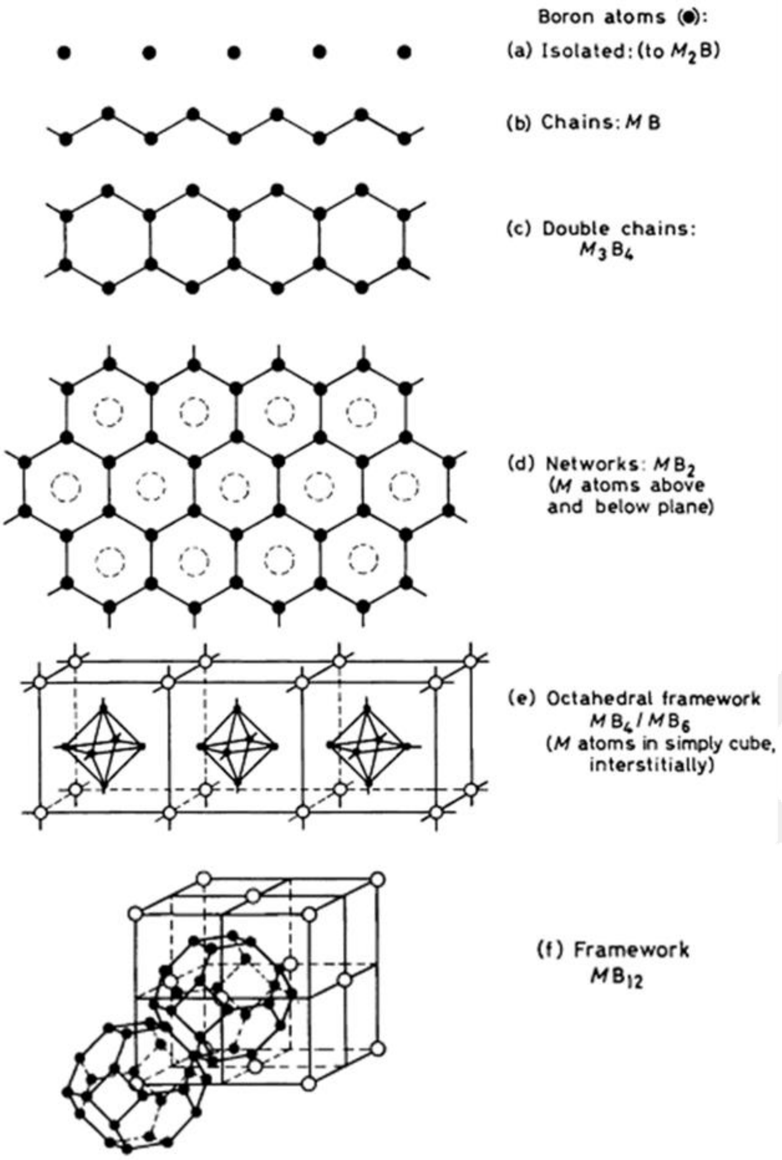

Figure 2.3 : Boron atom configuration in borides [15].

Metal borides have properties such as high melting temperature, extreme hardness, good corrosion resistance, excellent wear resistance, good thermal shock resistance, high electrical and thermal conductivities that make them superior to the oxide ceramics.

The melting temperature of boron-rich transition metal borides MB_n (n is greater than 2) are generally higher than those of the parent transition metals while the metal-rich borides often have melting temperatures as low as those of their parent metals. Many types of these borides show paramagnetic properties. Knoop hardness numbers of HK-0.1 are between 1100 and 2600 for diborides, 1650 and 2100 for hexaborides, and 2300 and 2600 for dodeca and hectoborides. Thus, most of the borides are stronger and harder than WC or α-Al_2O_3 that are known as two widely used cutting and grinding materials [9].

The oxidation resistance of the metal borides are excellent in the air at high temperatures up to 1000 ˚C when they are exposed to the molten metals, basic slags, and molten salts. Furthermore, they are resistant to nonoxidizing acids and aqueous alkalis environments excepting the alkali-metal and alkaline earth metal borides, which are salt-like and ionic. This oxidation resistance is highest for the transition metal diborides, but it is lower for more boron contents. Most of the metal borides are inert in hydrogen, nitrogen, and carbon even at high temperatures [10].

2.2.1 Mo-B binary system

The assessed Mo-B phase diagram which is studied by Spear and Liao, is shown in Figure 2.4. The invariant equilibria are reported in literature. The liquidus curves were obtained by using Gibbs energy functions through an optimization of combined thermodynamic and phase diagram data. The equilibrium solid phases of the system are as follows: (i) the terminal solid solutions of bcc (Mo) metal and rhombohedral (bB); (ii) the intermediate compounds Mo_2B, aMoB, bMoB, MoB_2, Mo_2B_5 and Mo_{1-x} B_3 (MoB_4). The solid phases in the Mo-B system have relatively small range of homogeneity [11].

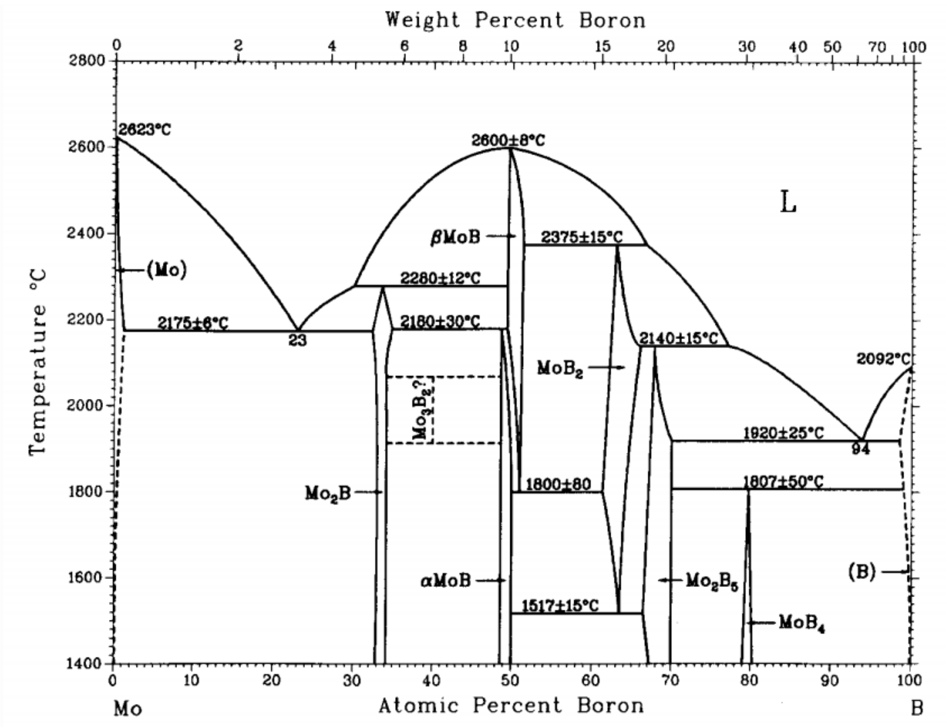

Figure 2.4 : The binary phase diagram of Mo-B system [17].

The solubility of boron in molybdenum was obtained to be 0.2% and 0.07% at 2050 °C (eutectic temperature) and 1400 °C temperatures, respectively. In the solid solution range, the increase of boron reduces the hardness of molybdenum, but beyond this range, it increases consistently with further increase in boron content. There are three intermediate phases in the system: Mo_2B, MoB, and Mo_2B_5. According to Kiessling, et.al, both MoB and Mo_2B were stoichiometric whereas Mo_2B_5 was slightly deficient in boron, existing at about 70 at% B. Bertaut and Blum, further reported a diboride MoB_2. Steinitz et al., based on X-ray diffraction results, confirmed the results of Kiessling and reported a homogeneity range for Mo_2B_5 of 68.2 to 70.0 at% B. They further proposed that (i) a high-temperature modification of MoB (ß-MoB) emerged, (ii) MoB_2 was a high temperature phase, and (iii) a further compound Mo_3B_2 existed at high temperature between 1850 and 2070 °C. The phase diagram was also studied up to 50 at% B by Gilles and Pollock who confirmed the results of Steinitz et al. α-MoB is the low temperature phase having orthorhombic crystal structure and a solubility range of about 48.5–50.5 at% B, and b-MoB have tetragonal crystal structure which is stable above 1800 °C [17].

In addition, the formation of a MoB_{12} phase by eutectoid reaction at 1807 °C was reported. Portnoi et al. constructed a phase diagram for the entire range of concentrations based on thermal, X-ray structural, and metallographical analysis, and they also basically confirmed the diagram of Rudy and Windisch except that the MoB_{12} phase melted congruently. Recently, Storms and Mueller gave phase relationships between 1527 °C and 1927 °C which were generally consistent with both Rudy and Windisch and Portnoi et al, but supported the eutectoid formation of MoB_{12} [11].

A tetragonal phase, MoB_4 was reported by Chretien and Helgorsky, but Rudy et al showed that its structure could be related to the hexagonal MoB_{12} which they reported. Later work by Galasso and Pinto showed that the diffraction pattern of the MoB_{12} phase could be reproduced by assuming that it possessed the hexagonal WB_4 structure, and then Lundstrom and Rosenberg fixed its composition at 80 at% B in agreement with the MoB_4 stoichiometry. In accordance with later work and following Spear and Liao, the most B-rich compound is taken as MoB_4 here [11].

Detailed solubility data on the terminal solid solutions are limited. Zakharov et al reviewed previous determinations of the solubility of boron in molybdenum and showed that the results from different studies varied between 0.177 and 1.75 at% B at the eutectic temperature. According to their own study, the maximum solubility was determined as 0.6 at% B at the eutectic temperature and falling to 0.019 at% B at 1200 °C.

Experimental work on the thermodynamic properties of the Mo-B system is limited to the determination of activities in the solid state. Both Gilles and Pollock and Storms and Mueller carried out vapour pressure studies across the whole composition range of Mo-B system, while Baehren and Vollath measured the activity of boron in the Mo+Mo_2B two-phase field between 1358 and 1448 K. The activity data for Mo-rich alloys from the various studies were shown by Storm and Mueller to be inter-consistent, however, at higher boron concentrations the work of Gilles and Pollock, and Storms and Mueller differ somewhat. By combining the data for Mo-rich alloys the Gibbs energy of formation of Mo_2B was estimated to be -46720+5.04T.

2.3 Superalloy-Based Composites

Superalloys have been the backbone of the aircraft jet engine industry for use in a wide variety of heat resistant components for more than four decades. The developments in the applications of monolithic superalloys by utilizing them in the form of composites have also been considered. The reinforcements in the superalloy matrix composites include discontinuous strengthening phases such as Y_2O_3 (yttria) in the oxide-dispersion-strengthened (ODS) alloys or continuous fiber reinforcements such as tungsten, molybdenum, AIP_3 (sapphire), or directionally solidified eutectic carbide phases. Superalloy-based composites have still been considered for application in turbine blades. For comparative applications, directionally solidified and single-crystal superalloys provide the best combination of performance and cost benefits. Recently, tungsten-fiber-reinforced superalloys are used in space shuttle main engine turbopump blades [13].

By the end of the 1980s, additional jet engine applications for cobalt-free oxide dispersion strengthened (ODS) superalloy were probable. These nickel- and iron-based superalloys are produced through a mechanical alloying process, first developed in 1968. Although still considered an emerging technology, rapid growth in ODS production is expected as new applications are accepted. One ODS alloy, MA-754, has been used for years in high-pressure turbine vanes of military aircraft produced by

General Electric. For the fiber-reinforced composites, the chemical compatibility in the fiber/matrix system is important to inhibit the severe reactions between them. The another important parameter is the existing bond between the fiber and matrix which allows load transfer from the weaker matrix to the stronger fiber reinforcements. Also, the coefficient of thermal expansion (CTE) mismatch between the matrix and fiber causes thermal and residual stresses which must be modified to avoid deleterious cracking. There are several studies that focused on the fiber and matrix selection and fabrication feasibility with available fibers including tungsten, molybdenum, SiC, and sapphire in the superalloy-based composites. For this reason in the past, FeCrAIY matrices were preferred because of their properties such as excellent oxidation and corrosion resistance, good fabricability, minimum reaction with tungsten and molybdenum fibers, and the thermal resistance against temperatures exceeding 1,100 °C [13].

2.3.1 Nickel-based composites

Nickel has properties such as good toughness, high tensile strength, and good corrosion resistance which make it a prevalent choice as a matrix material due to its ability to distribute both hard and soft reinforcements to develope its wear and anti-friction resistance [14].

Nickel and its alloys are often used in chemical plants, because they show good corrosion resistance at high temperatures. Because nickel has an extensive solubility with many alloying elements, the dispersed and precipitated particles are formed in solid-solution austenite (FCC, γ). Nickel has nearly complete solubility with iron and copper. The dissolution amount of some other elements are as following: Cr (35%), Mo and W (20%), Al, Ti, Mn and V (5-10%). These elements are dissolved in tough and ductile fcc matrix to provide solution hardening as well as improved corrosion resistance. Unique intermetallics can be formed between nickel and some alloying elements such as Al and Ti. For example, the formation of age hardening γ' precipitate (Ni_3(Al, Ti)) enables the formation of alloys with very high strengths for high-temperature services. Aluminum, titanium, niobium, and tantalum are strong γ' formers. The microstructural stability of Ni based alloys influence the thermal and mechanical properties of the materials. In Ni based alloys, three phases, γ, γ' and β can be formed in significant volume fractions. The γ phase with a disordered FCC structure generally acts as the matrix phase in this kind of materials while γ' phase with an ordered FCC-L12 and β phase with an ordered BCC-B_2 structures are in the form of precipitates. The effect of alloying elements on the stability of γ and β phases is shown in the schematic Ni-Al-X ternary phase diagram (Figure 2.5) calculated by thermoCalc software [15].

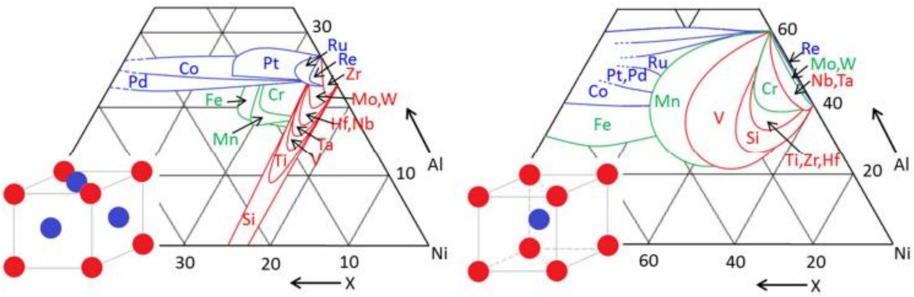

Figure 2.5 : The stability of α and β phases in schematic Ni-Al-X ternary phase diagram calculated by thermocalc software [22].

As it can be seen in Figure 2.5, the site preference of alloying elements in the lattices is dependent on the misfit of the atomic size with the base elements (i.e. Ni and Al). For example, elements such as Ti, Ta and Si prefer to occupy the Al site in the FCC-γ' and Co and Pt prefer the Ni site while Fe and Cr have no special preferences. Nickel provides a good combination of ductility and low creep rate which makes it useful as a base element for superalloys and coatings. In general, Ni-based superalloys are strengthened by precipitation while the Co-based superalloys are strengthened by solid solution. Addition of Al promotes the formation of γ' in superalloys, and hence alumina is the most effective oxide layer for protection against high temperature oxidation. A high temperature metallic coating contains a sufficient amount of Al to ensure the formation of alumina layer on the surface of the coating. Using nickel as a matrix phase of composites make them applicable by improving the poor creep resistance and high density of nickel alloys.

Because nickel is not a carbide former, carbon reacts with other elements which are alloyed with nickel to form carbides. These carbides are MC, M_6C, M_7C_3 and $M_{23}C_6$ (Where M is the metallic carbide former). MC that occurs in the form of large blocky carbides is usually not desired..But, M_6C is also blocky; when formed in the grain boundaries, it can control the grain size. The M_7C_3 (Cr_7C_3) form intergranularly that can cause embrittlement if they agglomerate due to the extended process time at high temperatures. The $M_{23}C_6$ carbides show the tendency to precipitate in grain boundaries that affect the mechanical properties. The resulted discrete grain- boundary particles in nickel-based alloys enhance rupture properties [14].

The nickel-molybdenum alloy named as Hastelloy B (N10001), was proposed in 1923. It displays excellent resistance to hydrochloric acid and other reducing environments. A minimum molybdenum content of 26% is required for very low corrosion rates in boiling hydrochloric acid even when dilute. The slightly lowering Mo content to a nominal 24% Mo and addition of 6% Fe, 5% Cr and 2.5% Co is named as hastelloy W (N10004), which is a well-known and widely used weld filler to join dissimilar high temperature alloys .

The Hastellalloy C series of alloys containing of 52 to 60%Ni- 31% Cr- 9 to 16% Mo and trace additions of the elements such as iron and tungsten were introduced in 1930s. They are used in the chemical processing, pollution control and waste treatment industries because of their properties such as heat and corrosion resistance. However these alloys are encountered some limitations. In regard to applications, the vessels containing these alloys have to be subjected to heat-treatment in order to eliminate the heat-affected zone (HAZ) precipitates.

Several studies have been carried out to determine the effects of the reduction or replacement of cobalt on the properties or microstructural characteristics of various superalloys. The NASA program for the conservation of strategic aerospace materials (COSAM) supports these studies.In nickel-base superalloys, the addition of cobalt which is applied typically in the range of 10–15%, makes a solid-solution strengthening and reduces the solubility of aluminum and titanium, through increasing the volume fraction of gamma prime, $\gamma'(Ni_3Al)$, which is a suitable phase for high-temperature strength and creep resistance. Also, cobalt in nickel-base superalloys reduces chromium depletion at the grain boundaries by reducing the propensity for grain boundary carbide precipitation. Waspaloy, a nickel-based superalloy which contains 13% Co, is used in turbine disks. A significant part of the cobalt used in gas turbine engine components is used in turbine disks because of their size and weight. Tensile strength decreased just slightly by reducing the cobalt content in the alloy. However, rupture life decreased considerably with decreasing amounts of cobalt. In addition to the slight decrease in the amount of γ', removing cobalt had a major effect on mechanical properties because of a possible higher stacking fault energy of the matrix and changes in carbide partitioning in grain boundaries. Udimet 700 (17% Co) and MAR-M 247 (10% Co) also have been studied.

The Ni-based superalloys are considered to be complex as they contain quite a good number of elements. In addition to perhaps 10 to 12 more tramp and trace elements such as Mn, Si, P, S, oxygen, and nitrogen must be controlled through appropriate melting practices. Besides this, other trace elements such as Bi, and Pb, must be controlled to very small (ppm) levels in critical parts. Ni based superalloys can be broadly classified into solid solution-strengthened and precipitation-hardenable varieties. The alloys like Inconel 600, Inconel 690, Inconel 625, Hastalloy C-276, etc. are solid solution-strengthened while Inconel X-750, Astroloy, M-252, Nimonic 115, Waspaloy, Udimet 700 etc. are precipitation-hardenable type. Mar M-246 is an equiaxed cast alloy and CMSX-10 is a single crystal superalloy, which both are used in gas turbine engine components.

The powder metallurgical techniques can be applied to the fabrication of ODS (Oxides Dispersion Strengthened) superalloys. PM2000 alloy is an example for this kind of materials that can also be manufactured with Ni-based ODS alloys,because the application ranges of iron- and nickel-based ODS alloys overlap in wide ranges. Heavy metals such as W, Re, Ta, etc. which are used as alloying elements, stabilize the intermetallic phases in the matrix (primarily the γ' in the γ matrix) of these alloys. This enhances the creep resistance, increases the alloy density, decreases the solidus temperature, and also reduces the specific properties. Oxide dispersion-strengthened composites (including yttria or thoria-dispersed Ni-20Cr, and Ni-Cr alloys containing both yttria and γ' phase that forms due to the additions of Al, Ti or Ta) were developed to improve the high temperature strength and creep resistance [16, 17].

The small percentages of fine particles of the second phase in composites resist the recrystallization, grain growth and dislocation movements. in addition to the oxides in dipersion-strenghened composites, the borides, carbides and refractory particulates have been used in these composites. The hot pressed oxide dispersion-strengthened Ni base superalloys are possible candidates to be applied in aircraft gas turbine engine parts such as vane airfoils, nozzles, blades, and combustor assemblies.

The dispersion-strengthened Ni base superalloys have better thermal stability in respect to precipitation-hardened alloys in which the second phase decomposes at high temperatures. Besides, dispersion strengthening was also used for several other families of alloys.

Nickel-based MMCs which are reinforced by WC particles with different ratios of constituents have been extensively studied. In WC containing cermets, replacing of Nickel by Cobalt reduces the costs and improves the erosion resistance.

2.3.1.1 Ni-Al intermetallics

The reported intermetallic phases in the Ni-Al binary equilibrium phase diagram are as follows: Al_3Ni, Al_3Ni_2, NiAl, Al_3Ni_5, and Ni_3Al. In this binary system, NiAl and Ni_3Al intermetallics have drawn interest because of their high melting/liquidus temperatures. The homogeneous phase field of NiAl, which has the highest congruent melting point of 1638 °C among all the Ni-Al intermetallics, is between 45 and 59 at.%. The NiAl has ordered cubic B_2 (cP2, CsCl structure) and is known to be strongly ordered even above 0.65 T_m with an intrinsic disorder parameter $\leq 5 \times 10^{-3}$. For large deviations from stoichiometry, the ordered bcc (B_2) structure of NiAl remains stable. In the Ni-rich compositions, the antisite defects which are formed by the occupation of excess Ni atoms in the Al sites cause the deviations from stoichiometry. However, in Al-rich compositions of NiAl, there are vacant Ni sites in the structure. The lattice constant of NiAl depends on Ni:Al ratio in the range of compositions, and reaches to its maximum value at the stoichiometric composition.

Ni_3Al is the first intermetallic which formed by a peritectic reaction (liquid + NiAl → Ni_3Al) at temperatures ≤1395°C with Al addition to Ni. It has a homogeneity range of ≈4.5 at.% around its stoichiometric composition. Stacking of three close-packed planes in the sequence ABC can be observed in the L12 structure of Ni_3Al. However, Gao and Bacon reported that the presence of a Ni-rich atom at the Al site is more possible than the occupation of the Ni site by Al atom regarding their energetical aspects. The formation energy of antistructure in Ni_3Al, for example, the location of the Ni atom at the Al-site is lower than that of a vacancy. Therefore, in off-stoichiometric compositions of Ni_3Al, antisite substitutions present on both Ni-rich and Al-rich sides when combined with the atoms of the other constituents. The formation of the antisite defects in Al-rich side of off-stoichiometric compositions of Ni_3Al makes it distinct from the structure of NiAl.

NiAl has a high melting point of 1649 °C comparing to titanium-based aluminides, which are not expected to be used above 925-980 °C. Only a few intermetallics have enough positive characteristics at high temperatures that can fulfill the requirements for development. Also, NiAl has reasonably low density, excellent oxidation resistance, and high thermal conductivity. Its disadvantages are loss of fracture toughness below its ductile-to-brittle-transition temperature and inadequate high-temperature mechanical properties.

Combination of NiAl with continuous-fiber reinforcements as a composite improve both the toughness and the strength. Tungsten, molybdenum, and sapphire are the fibers incorporated in the NiAl matrices. In the case of using tungsten fibers, which are usually ductile, during producing a composite by a powder metallurgy technique, toughening could not be observed but strengthening has occurred. Molybdenum fibers in a NiAl matrix improve the strength and increase the toughness. Although, incorporating sapphire fibers in NiAl by using a powder cloth process causes a weak fiber/matrix interface bond, but toughening occurs because the fibers are only weakly bonded to the matrix by frictional forces. In these composites, there is a lack of strengthening due to a weak fiber/matrix bond and not having load transfer from the matrix to the fiber. Modifications of the powder process improve the bonding between the fiber and the matrix. A rule-of-mixtures strengthening was used and it was not reported any severe damage due to the CTE mismatch between the sapphire fiber and the NiAl matrix during preliminary thermal cycling tests. However, the features of the sapphire fibers deteriorated by processing. The decreasing in Al content has been required to improve the ductility of the NiAl matrix alloys. Therefore, crack deflection by dispersions or by reinforcing fibers provide the fracture toughness of NiAl-based composites. In the case of development of NiAl-based composites, the controlling of fiber/matrix interfaces is a significant difficulty to obtain strengthening or crack deflection.

The method for development of heat resistant composites directionally solidifies two phase composites (such as Ni or Co based eutectic superalloys) for in-situ growth of reinforcements. In addition to superalloys, composites that contain Ni-Al intermetallics (NiAl and Ni_3Al) can be produced by this in-situ method. At lower temperatures (below 500 K), the ductility of polycrystalline NiAl is nearly zero but it can be improved by addition of different alloying elements as NiAl has wide range of stoichiometries. For in-situ composites the interfaces are mutually compatible beacause the interphase interface crystalizes simultaneously with the production of matrix and reinforcement. Directional solidification just like deformation processing (extrusion and forging) creates the dual-phase microstructure which has better toughness, ductility and creep resistance. Elements such as Ti, Nb, Ta, Mn, Cr, Co, Hf, W, Zr and B have been utilized in NiAl for improving the resistance to compressive creep. For increasing toughness and strength of NiAl intermetallics suitable alloying elements must be used. The second phase in directionally solidified off-eutectic pseudobinary alloys of NiAl-X (X refers to Mo, W and Cr) exhibits an improved toughness due to the deflecting of crack propagation in microstructure of NiAl. The in-situ grown composites such as in single crystal sapphire fiber reinforced off eutectic alloys of NiAl with Cr or Mo may contain ceramic fibers as reinforcement to increase their high-temperature strength and creep resistance. Besides directional solidification, deformation processes combined with heat treatment can be used for production of ductile phases of NiAl for example in the extruded Ni-30Al-20Co alloy and a Ni-36Al alloy containing of equiaxed b-NiAl grains with a necklace of γ' phase at the grain boundaries. The formation of γ' phase increases the ductility of these alloys from zero to over 0.5%.

2.3.2 M_3B_2 type ternary compounds

The M_3B_2-type boride as shown in Figure 2.6 that contains more than one metallic element has the D5a structure. The metal atoms are chosen from two groups, heavy elements with large atomic radius such as major W and minor Mo, and also relatively lighter elements with smaller atomic radius such as major Cr, trace Co, and Ni. X. B. Hu et. al have reported an atomic HAADF image projected along the four-fold [001] M_3B_2 direction of the M_3B_2 phase as shown in Figure 2.6 [12]. The existed atomic columns are divided into two groups as indicated by the red (1) and green (1') arrows. Based on the observations and the atomic configuration of D5a structure, the unit cell of M_3B_2 type boride with ordered metal atoms is given in this figure where blue balls show large metal atoms (L) such as W, Mo and green balls display small metal atoms (S) such as Cr, Co, and Ni. Therefore, M_3B_2 has to be called a ternary boride with the chemical formula of L_2SB_2 [19].

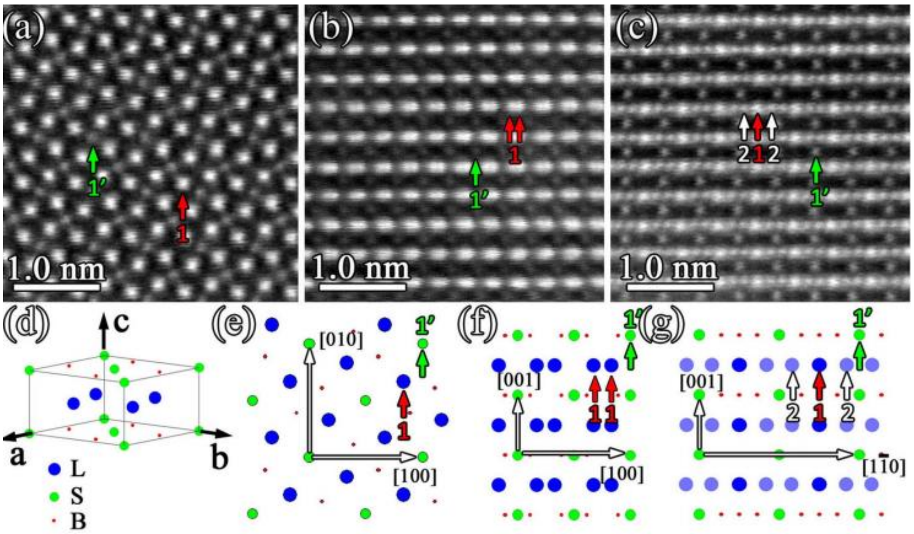

Figure 2.6 : (a-c) Atomic HAADF images projected along [001], [100] and [110] directions, respectively (d) Atomic configuration in the unit cell of M_3B_2 phase with the ordered occupation of metal atoms. The ordered M_3B_2 phase is assumed as a ternary boride with the chemical formula of L_2SB_2 [19].

In order to discuss the stability of transition metal borides, crystal structure of the investigated Mo_2XB_2(X=Fe, Co, Ni) ternary compound is shown in Figure 2.7 which is studied by TianWei He. et. al by using the first-principles calculations on the basis of the density functional theory (DFT) that performed in CASTEP code. In this study, the lattice parameters of optimized crystal structure, formation enthalpy, and cohesive energy for Mo_2XB_2 ternary system were estimated as shown in Table 2.1. The values of cohesive energy and formation enthalpy are negative which indicates that Mo_2XB_2 ternary compounds are stable and used to compare the relative stability of these compounds. It was reported that decreasing the X ionic radius in Mo_2XB_2 compounds increases the cohesive energy. Therefore, the maximum and minimum values are found to be -875.26 kJ/mol and -920.61kJ/mol for Mo_2NiB_2 and Mo_2FeB_2, respectively. Therefore, Mo_2FeB_2 has the highest structural stability and following that, high stabilities belong to Mo_2NiB_2 and Mo_2CoB_2 ternary borides.

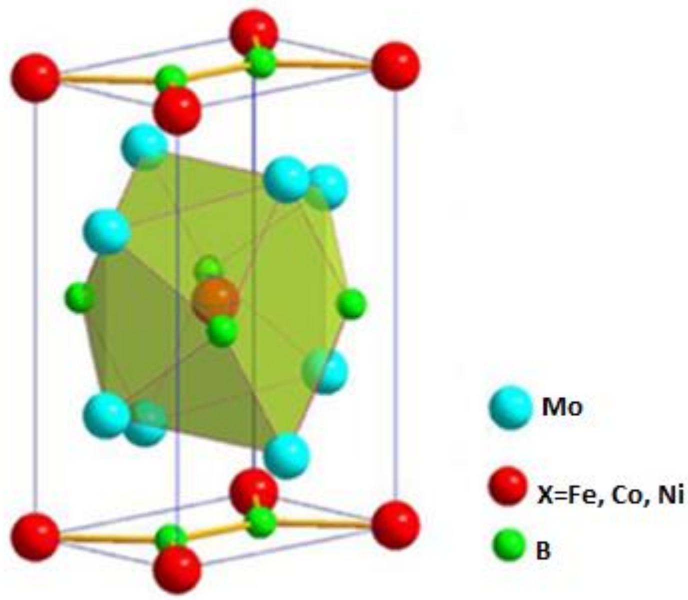

Figure 2.7 : The crystal structure of Mo_2XB_2 ternary compound [19].

Table 2.1 : Lattice parameters (a, b, and c), cohesive energy (E_{coh}), and formation enthalpy (ΔH_r) of Mo_2XB_2 [19].

Species	X ionic radius (A)	Lattice constants (A)			E_{coh} (kJ/mol)	ΔH_r (kJ/mol)
		a	b	c		
Mo_2FeB_2	0.0780	7.10	4.52	3.17	-920.61	-70.1
		7.07	4.52	3.18	-885.29	-67.85
Mo_2CoB_2	0.0745	7.12	4.57	3.16	-899.38	-66.93
		7.07	4.55	3.18		
Mo_2NiB_2	0.0690	7.01	4.54	3.18	-875.26	-55.26
		7.07	4.55	3.18	-823.24	-52.45

2.3.3 Mo-Ni-B ternary system

Up to now, a number of ternary phases with definite crystal structures have been found, namely Mo_2NiB_2, $Mo_{30}Ni_{14}B_{33}$ or Mo_3NiB_3, $Mo_3Ni_{10}B_{11}$, $MoNi_{20}B_{17}$, $Mo_4Ni_{23}B_{29}$ and possibly Mo_2NiB_4 and Mo_3Ni_3B.

Five ternary phases were found by S. Omori, et.al [18] in alloys during annealing at 950 °C for 500 to ~2500 h, two of which were known earlier (τ_1-Mo_2NiB_2 and τ_2-$Mo_{30}Ni_{14}B_{33}$) and three of them were observed for the first time (τ_3-$Mo_3Ni_{10}B_{11}$, τ_4-$MoNi_{20}B_{17}$, and τ_5-$Mo_4Ni_{23}B_{29}$).

The Mo_3NiB_3 compound with the W_3CoB_3 crystal structure was found by H. Jedlicka, et. al. and then a quite similar compound was found at somewhat different composition of $Mo_{30}Ni_{14}B_{33}$. According to their lattice parameters, it appears to be the same phase (denoted τ_2). Y. B. Kuzma, et. al found the same compound at the composition of (40-42.5) at.% Mo - (15-12.5) at.% Ni - 45 at.% B, and they reported this phase as having an unknown crystal structure [19].

The ternary compound with the formula Mo_2NiB_4 (τ_6), as reported in the first report, have a crystal structure type similar to the Cr_3B_4 type phases (the latter is of the Ta_3B_4 crystal structure). However, no confirmation (including the careful work of Omori, et.al) has been made of the formation of this compound, and it cannot be excluded that it was observed due to contamination by heating in a H_2 medium using graphite crucibles.

The compounds with composition of 15Mo-30Ni-55B (at.%) have unknown crystal structure and the second phase was found to have the formula $Mo_{0.7}Ni_{0.1}B$ with a CrB type crystal structure. The lattice parameters of $Mo_{0.7}Ni_{0.1}B$ compared to those of βMoB show only a moderate decrease in b and c, which may be the result of Ni dissolution in βMoB, stabilized at 1600 °C. However Kuzma, et. al have not observed the CrB phase as a ternary phase in alloys annealed at 800 °C (boron contents up to 60-70 at.%) and the same was occurred for the compound with composition of 15Mo-30Ni-55B (at.%) [19].

Kolomitsev and Moskaleva [20] reported the MoNiB ternary phase in alloys which contain Mo more than 10 at.%. They also confirmed the crystal structure of Mo_2NiB_2 ternary compound.

The ternary phase with crystal structure of $W_2Cr_{21}C_6$ was found in the ternary alloys with the compositions of 20-25at.%B-6.7-25at.%Mo-73.3-50at.%Ni. It has been confirmed that no phase with the $W_2Cr_{21}C_6$ crystal structure type was detected. The ternary Mo_3NiB_3 boride was not reported in the ternary Mo-Ni-B system but was observed in the approximate composition of $Mo_{3.3}Ni_{2.3}Fe_{0.4}B$ detected in an alloy with the composition of $Ni_{56.5}Mo_{23.5}Fe_{10}B_{10}$ (at.%) which was produced by consolidation of amorphous powder. During annealing of this alloy at 1100 ˚C, this boride decomposed to produce Mo_2NiB_2 and the fcc matrix phase [19].

2.3.3.1 Mo-Ni-B phase diagram

According to the isothermal sections at 800 °C and 1000 °C which were reported by Kuz'ma and kolomytsev [21; 20], the quasibinary sections of MoB with nickel borides of Ni_2B and m-Ni_4B_3 were studied. At isothermal section at 950 °C, it was observed that the MoB+Ni_2B and MoB+m-Ni_4B_3 two-phase regions are not existed due to the formation of ternary compounds. Therefore, the quasibinary eutectic was reported to be in the two-phase region of (Ni)+Mo_2NiB_2. Based on the studies, the composition of the eutectic point was reported to be $Mo_{23}Ni_{68.5}B_{8.5}$, $Mo_{25}Ni_{65}B_{10}$ and $Mo_{22}Ni_{67}B_{11}$ (at.%) at eutectic tempeartures of 1265 °C, 1270 °C and 1260 °C [19].

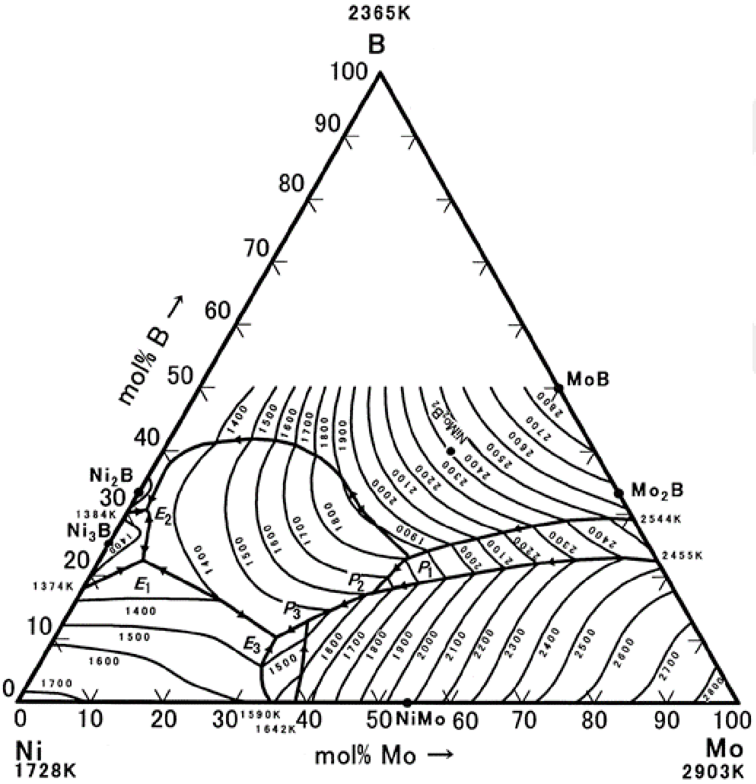

Figure 2.8 : Mo-Ni-B ternary phase diagram [27].

By using thermal analysis and XRD by M. Morishita, et. al [22], it was determined that the existence of 7 invariant four phase equilibria consisting the liquid phase, three equilibria of eutectic type (E) and four of transition type (U) as seen in the figure of ternary diagram (Figure 2.8) was constructed at different temperatures. The results illustrated in Table 2.2, show that the ternary phase Mo_2NiB_2 is formed by the reaction of L+MoB→Mo_2NiB_2. It was reported by Kolomytsev, et.al that the melting temperature of alloys consisting of 97-98% mass of Mo_2NiB_2 is 1800 °C which is close to the incongruent melting temperature of this phase while the temperature of formation (melting) of Mo_2NiB_2 is found to be 1627 °C which is noticeably lower [20].

Table 2.2 : Invariant reactions in nickel-rich alloys of the Mo-Ni-B system [25].

Equilibrium	Symbol	Coordinates of invariant point L			Temperature (℃)
		Mo	Ni	B	
L↔Ni+MoNi+Mo_2NiB_2	E_1	33 30.6 33	56.5 59.1 57	10.5 10.3 10	1160 1172 1231
L↔Ni+Ni_3B+Mo_2NiB_2	E_2	9 6 -	27 71.5 -	19 22.5 -	1080 1090 1077
L↔Ni+Mo_2NiB_2	e_{2max}	25 22	65 67	10 11	1270 1260
L↔Ni_3B+Mo_2NiB_2	e_{3max}	3	71	26	1116
L+Mo↔MoNi+Mo_2NiB_2	U_1	33.7 -	53.5 -	12.8 -	1205 1285
L+MoB↔Mo_2B+Mo_2NiB_2	U_2	42.3	34.9	22.8	1539
L+Mo↔Mo_2B+Mo_2NiB_2	U_3	40.4	42.3	17.3	1360

The thermodynamic calculation was used to interpret the liquidus surface of Mo-Ni-B ternary system by M. Morishita, et.al [22]. They optimized the interaction parameters for the binary systems related to Mo-Ni-B ternary system by using the reported experimental data which were available in the literature. They calculated the Gibbs energy of mixing of $Ni_{0.2}Mo_{0.4}B_{0.4}$ by EMF considering the pure fcc Ni, bcc Mo and orthorhombic B are adopted as standard states. The Gibbs energy of mixing of this ternary phase was expressed by the following equation (2.5):

$$\Delta_{mix}G\ (Ni_{0.2}Mo_{0.4}B_{0.4}, Ni^{liquid}, Mo^{liquid} and\ B^{liquid}) = -50000 + 3.94T + (G_{Ni}^{\circ fcc} - G_{Ni}^{\circ liquid})X_{Ni} + (G_{Mo}^{\circ bcc} - G_{Mo}^{\circ liquid})X_{Mo} + (G_{B}^{\circ Ortho.} - G_{B}^{\circ liquid})X_B (Jmol^{-1}) \tag{2.5}$$

By constructing the liquidus surface of Mo-Ni-B phase diagram, three ternary eutectic points and three peritecto-eutectic points have been evaluated that show the small discrepancies with the experimental results [22].

The liquidus surface of Mo-Ni-B system in the Ni-Ni_2B-MoB-Mo region was constructed. The incongruent Mo_2NiB_2 ternary compound was studied and also the eight fields of primary crystallization and seven 4-phase invariant equilibria were investigated on the liquidus surface. Later works in references [23, 24] were focused on the MoNi-Mo_2NiB_2-Ni_3B-Ni region. The liquidus and solidus surfaces were projected as shown in Figure 2.9 and Figure 2.10, respectively. About the observations according to the figures, the addition of B to the Mo-Ni binary systems with the phase composition of MoNi+(Ni) decreases the eutectic temperature from 1309 to 1223 °C (ternary eutectic E_1). The addition of Mo to Ni-B binary system causes a decrease in the eutectic temperature from 1093 to 1080 °C (ternary eutectic E_2). The solidus temperature for the alloys in the Mo_2NiB_2+(Ni)+Ni_3B, MoNi+Mo_2NiB_2+(Ni) and Mo_2NiB_2+(Ni) regions are 1080, 1223 and 1260 °C, respectively [23].

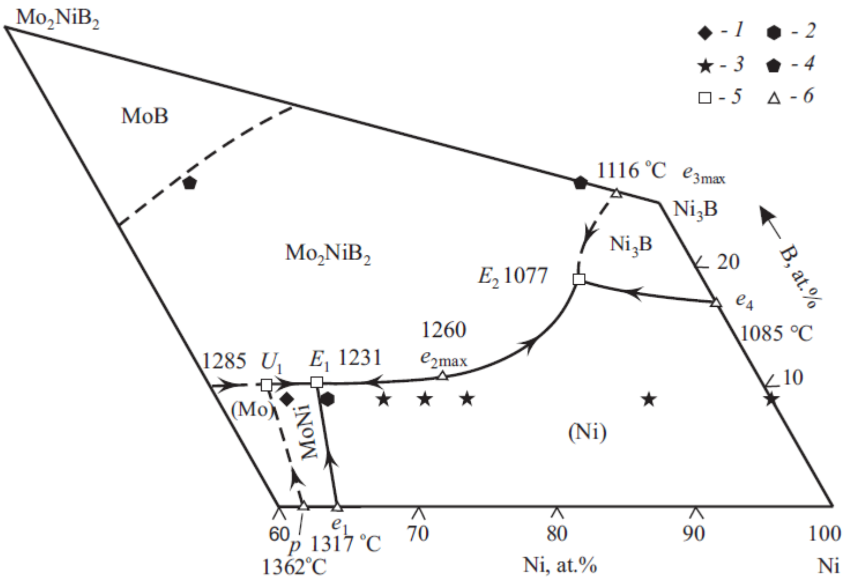

Figure 2.9 : Projection of liquidus surface in the MoNi-Mo_2NiB_2-Ni_3B-Ni region [28].

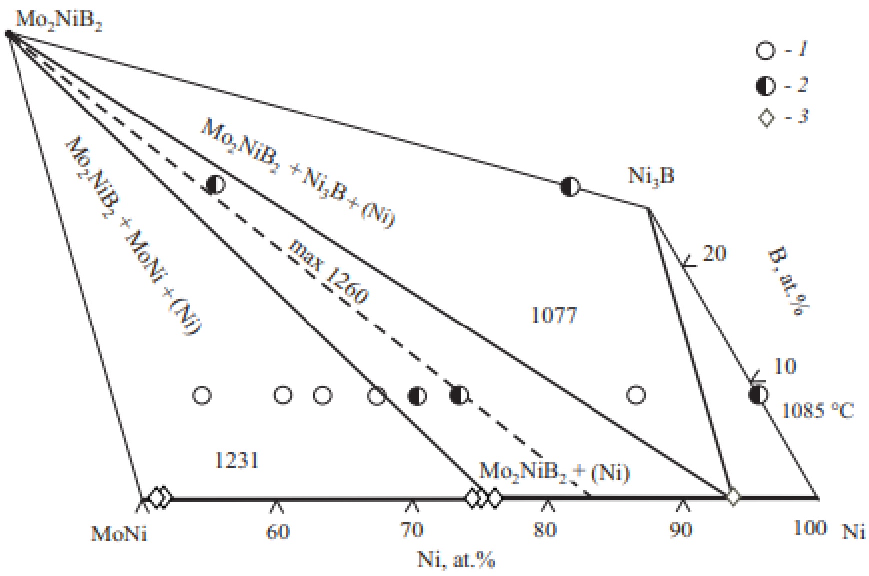

Figure 2.10 : The projected Mo-Ni-B solidus surface in MoNi-Mo_2NiB_2-Ni_3B-Ni region [28].

According to the data from the studies of V. Z. Kubliy, et.al [23], the projection of the Mo-Ni-B liquidus surface (as in Figure 2.9) shows that there are six fields of primary crystallization in the Mo_2Ni_3-Mo_2NiB_2-Ni_3B-Ni region including: (Ni), Mo_2NiB_2, MoNi, Ni_3B, (Mo), and MoB. The primarily crystallized phases in as-cast alloys are present on the co-crystallization lines for the phases. Also, according to the figure, the solidus temperatures, coordinates of the three-phase eutectic E_2, eutectics in Mo-Ni and Ni-B binary systems, and position of the MoB and Mo_2NiB_2 co-crystallization lines are identified. According to the reported microstructural analysis, the composition of the three-phase eutectic E_1 is close to the 32 Mo–59 Ni–9 B alloy that the monovariant curve L ↔ (Ni) + MoNi goes through it. The U_1 point on the liquidus surface represents another four-phase invariant equilibrium in the ternary system which is incongruent with the transition type. The L ↔ (Ni) + Mo_2NiB_2 co-crystallization curve goes through the maximum at 1260 °C, and this point corresponds to the quasi-binary eutectic e_2 [23].

As it can be observed, the solidus surface includes two wide ternary phase fields and two relatively narrow binary phase fields of equilibrium as following: MoNi + Mo_2NiB_2 + (Ni) and Mo_2NiB_2 + (Ni) + Ni_3B and Mo_2NiB_2 + (Ni) and (Ni) + Ni_3B, respectively. The solidus temperature depends on the alloys' phase compositions, for example: from 1231 ±5 °C for the MoNi + Mo_2NiB_2 + (Ni) region to 1077 °C for the

Mo_2NiB_2 + (Ni) + Ni_3B region, up to the maximum temperature at 1260 °C in the binary Mo_2NiB_2 + (Ni) region [23].

For the first time, the isothermal section of Mo-Ni-B system, considering all the compositions in the phase diagram has been constructed by Omori, et.al [18]. The alloys in the region of Ni-Mo-Mo_2B_5-NiB were studied by Kuz'ma, et.al [21] and the isothermal section of this system was established at 800 °C. This isothermal diagram was used in the later studies and development of M_3B_2 complex borides. However, the number of phases and the associated equilibria in these diagrams were unequal. The isothermal section at 1000 °C for the alloys at the range up to 50 at.% B was published by J. Doychak [20].

2.3.3.2 Mo_2NiB_2 ternary boride based composites

The ternary Mo_2NiB_2 boride (τ_1) was first reported by Steinitz, et.al. Its crystal structure was studied by Y. B. Kuzma, et.al (orthorhombic system, own crystal structure type) [19]. The crystal structure data for Mo_2NiB_2 were confirmed by W. Rieger, et.al studies which present that Mo_2NiB_2, W_2NiB_2, W_2FeB_2 and Mo_2CoB_2 ternary compounds are common in the W_2CoB_2 type of crystal structure [25].

The crystal structure of orthorhombic Mo_2NiB_2 ternary phase in Mo_2NiB_2 based cermets was investigated by Rietveld analysis. The orthorhombic Mo_2NiB_2 has a space group No.71 which agrees well with the orthorhombic W_2CoB_2 reported by Rieger.et.al [25]. The tetragonal Mo_2NiB_2 was obtained in the preparation of a cermet with the composition including 10 wt% Cr. The schematic illustration of two crystal structure types of Mo_2NiB_2 unit cells are shown in Figure 2.11. In tetragonal type Mo_2NiB_2, the Cr can substitute for Ni that makes a more isotropic M_3B_2 structure in comparison to orthorhombic crystal structure.

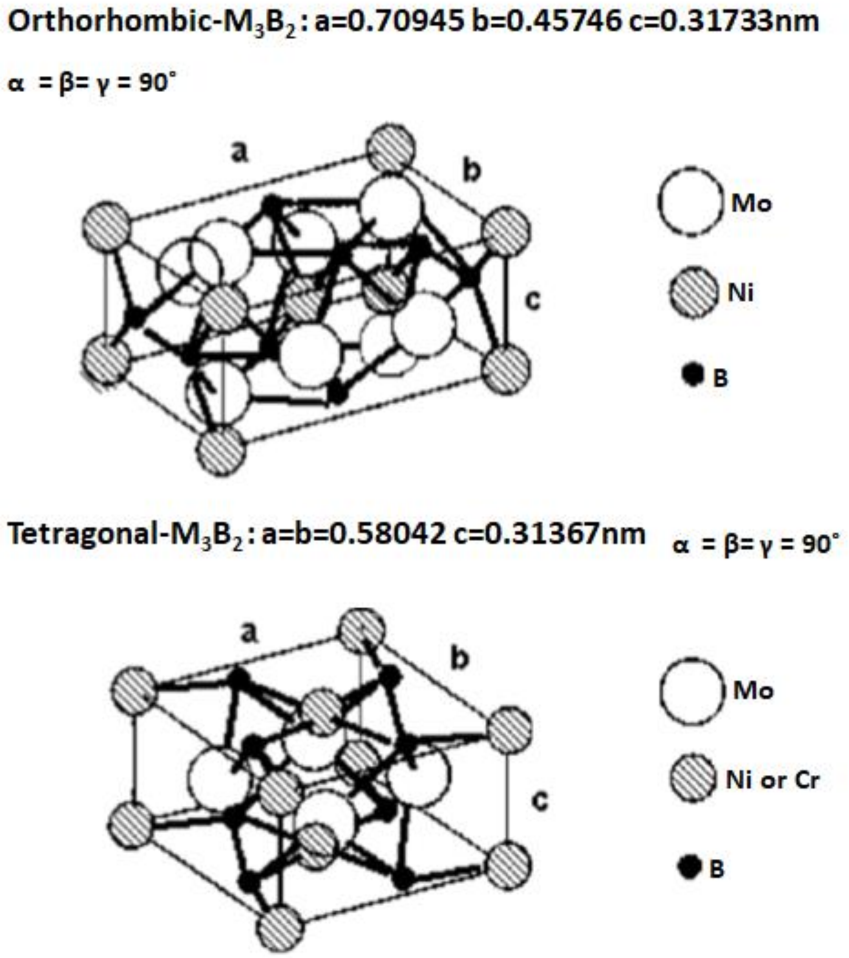

Figure 2.11 : Orthorhombic and tetragonal crystal structure of Mo_2NiB_2 ternary boride [29].

According to the work of American Electro Metal Corporation [26], the production of new hard refractory metal boride compositions which can be used in the place of metal carbides such as tungsten carbide was presented. This invention was related to compositions containing a ternary boride compound of the formula Mo_2MeB_2 wherein Me is either nickel or cobalt, two elements which were used as matrix for cementing the hard metal carbide or boride particles. The desired compounds in this study were Mo_2NiB_2 or Mo_2CoB_2 compounds. Combinations containing ternary boride compounds with a binary boride are obtained with compositions of 70% to 30% molybdenum, 1% to 40% nickel or cobalt, and 15% to 60% boron (in atomic percents).

The existence and composition of Mo_2NiB_2 was reported by Kolomytesev, et.al and in their later work, the crystal structure of this phase was found to be tetragonal with the lattice parameters of a=10.036 and c=11.952A [20]. The other study conducted by Kuz'ma, et.al have proved the crystal structure of Mo_2NiB_2 to be orthorhombic with the specific type structure and the calculated lattice parameters are a=4.55, b=7.07 and c=3.18A. Since the ternary Mo_2NiB_2 phase has a very narrow region of homogeneity, the production of pure form was difficult. Based on the studies of Kolomytsev, et.al [20], the physicochemical and mechanical properties of a 95-98% Mo_2NiB_2 phase-containing alloyare reported.

2.3.3.3 Physical and mechanical properties of Mo_2NiB_2 containing alloys

According to the literature, the electrical resistivity and hardness of two-phase alloys containing ternary compound of Mo_2NiB_2 and binary phases in Mo-Ni-B system were investigated. It was observed that the electrical conductivity increases by increasing the amount of ternary boride but decreases by increasing the amount of Mo_2B. The lowest hardness is referred to the alloys consisted of the Ni solid solution and the boride Ni_3B, and the highest hardness belongs to the alloys with the Mo solid solution and the boride Mo_2B. By increasing the amount of the boride phase, the hardness values of the alloys containing the mixture of ternary and binary borides increase at RT and higher temperatures [20].

Also the creep rate (i.e. a characteristic of heat resistance) of alloys in Mo-Ni-B system was studied by Kolomytsev, et.al [20] by using indentation testing. It was observed that the most effective phases that result in increasing the resistance of these alloys are Mo_2B and ternary Mo_2NiB_2 phase, and the least effective phase is the boride Ni_3B. Because the interatomic bond strength in the molybdenum borides is higher than in the nickel borides they exert a strengthening influence in the alloys.

The mechanical tests and Auger spectra analysis observations by Y. Yamasaki, et al. [27] show that hardness increases with increasing Mo/B ratio in the Mo_2NiB_2 base alloys which was resulted not only from the refinement of boride grains but also from the solution strengthening of the Ni base binder. They suggested that the Ni base binder phase changes from a Ni base solid solution to Ni-Mo intermetallic compound and then to a Mo base solid solution by increasing Mo/B ratio. The Vickers microhardness of the Mo_2NiB_2 ternary boride, quasibinary (Ni)+Mo_2NiB_2, ternary eutectic of Ni_3B+(Ni)+Mo_2NiB_2 and quasibinary of Ni_3B+Mo_2NiB_2 are 15-20, 5.1-5.4, 6.3 and 10-11(GPa), respectively. Based on the works by B. Yuan, et.al [28], applying an optimum sintering temperature for the production of Mo_2NiB_2-Ni hard alloys causes the bending strength and the HRA values reach to 1.85+004GPa and 85.7+0.1HRA, respectively.

The cohesive energy (E_{coh}=-875.26), formation enthalpy (ΔH_r=-55.26) and bulk modulus (330.2GPa) of Mo_2NiB_2 structure were calculated by first-principles methods [29]. They reported the ratio between bulk and shear modulus (i.e. B/G) value indicating the ductility or brittleness for Mo_2NiB_2 and $MoNi_2B_4$ compounds which are 1.78 and 2.37, respectively. Therefore, it was observed that $MoNi_2B_4$ among the Mo-Ni-B solid phases could be used as a precipitate to improve the toughness of superalloys. The elastic modulus of pure Mo_2NiB_2 ternary compound was found to be more than 400 GPa for the 1673 K sintering temperature which was investigated by Takagi, et al. [30].

2.3.3.4 Effect of alloying elements addition on properties of Mo_2NiB_2 based alloys

The effect of addition of V, Mn, Fe, Co, Ti, Zr, Nb and W (10% mass) on transverse rupture strength and hardness properties of ternary Ni-6B-58.6Mo (mass%) based hard alloys was studied by Takagi, et.al [31]. Addition of 0-10% mass Cr by Cr powder and CrB powder as addition source showed that using CrB provides superior mechanical properties to the Cr added alloys due to the crystal structure change from orthorhombic to tetragonal with the increasing temperature [32]. As Molybednum is the main component to form Mo_2NiB_2 ternary boride in the cermets, the effect of Mo percentage was studied in several papers. In the composition based on Ni-35.6Mo-5B-3.5Cr-11.5V hard alloys, by fixing B content and changing the Mo percentage between 35.6-66.4 (wt%), it was observed that higher stoichiometric Mo, for example, the Mo/B ratios between 1.1 and 1.2 produce a very fine two-phase microstructure. The distribution of a tetragonal M_3B_2-type complex boride was found to be homogeneous in a solution-strengthened Ni base binder that results in an excellent TRS with the value of 2.7 GPa and the rockwell hardness was found to reach 88RA [33].

TRS and hardness of three model cermets with the compositions of Ni-6B-58.6Mo-(0Cr, 10Cr and 10V) are shown in Figure 2.12 which exhibit that Cr and V additions improve the TRS. Both the Cr and V alloying elements increase the hardness from 84.5 Ra to 86.5 and 90. TRS and hardness values of these composites are comparable to that of cemented carbides.

As it was reported in the works of Takagi, et.al, Cr and V additions result in the structural change of the ternary boride from orthorhombic to tetragonal and make a considerable improvement of mechanical properties and structural refinement of cermets. The high TRS for the cermets with Cr and V additions are due to the homogeneous distribution of the tetragonal M_3B_2 boride phase.

Effect of Mn addition on Mo_2NiB_2 based cermets with the composition of Ni-5B-53.3Mo-(0-10) Mn (mass%) and also on high strength V added cermets with the composition of Ni-4.5B-46.9Mo-12.5V-(0-10)Mn (mass%) showed that Mn addition improves mechanical properties and unlike Cr and V, it did not change structure, so that the boride phase in these cermets has its original orthorhombic structure. Higher TRS values are attributed to the refinement in the grains' size and the uniformity in the distribution of the boride particles in the Ni base matrix [24].

The effect of (0-15 mass%) Cr addition to the Mo_2NiB_2 ternary boride compound on the hardness and elastic modulus was studied [30]. The Vickers microhardness of this ternary compound was found to increase from 1700 to 2200 with increasing Cr content. The elastic modulus was increased to above 400 GPa that is comparable to that of TiC. Furthermore, the 5B-51Mo-Ni composition with double addition of V (5 mass%) and Cr (12.5 mass%) demonstrated the excellent corrosion resistance for a molten fluorocarbon resin [34].

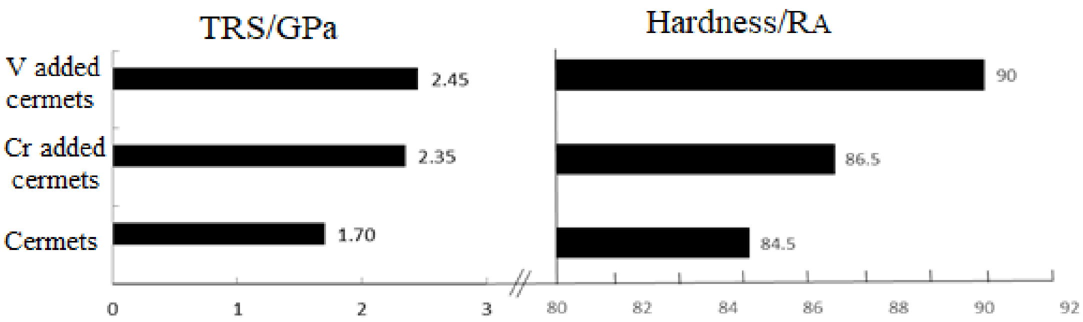

Figure 2.12 : Hardness and TRS values of Mo_2NiB_2 based cermets with V and Cr additions [29].

2.3.3.5 Amorphous Mo-Ni-B alloys

The wettability of Mo_2B_5 disks by molten nickel was studied by Yasinskaya, et.al. The Mo-Ni-B alloys with the composition of 72 at.% Ni, 14 at.% Mo and 5-14 at.% B were found to have amorphization ability. The crystallization temperatures are maximum 456 °C (433-543) and maximum 676 °C (650-769) which were revealed by DSC analysis technique. At the first stage, only the Ni phase was crystallized after annealing at 440 °C and the crystallization of Ni, Mo_2NiB_2 and Ni_3B phases occurs during the second stage after annealing at 650-770 °C, as indicated by phase diagrams. [19].

The crystallization mechanism and the phase transformations of $Ni_{70}Mo_{10}B_{20}$ alloy which is produced by spinning and the consequent annealing above the glass-transition temperature of 473 °C were observed. This alloy contains three crystalline phases of nanocrystalline (with the dimensions of 2-5 nm) pure nickel with fcc structure and lattice parameter a=354.1pm, nickel solid solution of $Mo_{15}Ni_{85}$ with nanocrystals of 20-50 nm and also Ni_3B phase with the lattice parameters of a=521.1, b=661.9 and c=438.9pm [19].

2.3.4 Fe-based composites

Iron is used as the basis for the steel materials which exhibit relatively high Young's modulus and high range of adjustable tensile and yield strengths in technical applications, and excellent wear behavior of steels makes them suitable for tools.

Because of the demands, stainless steels were developed in the second and third decades of the 20th century in order to make it stronger, more corrosion-resistant forhigh-temperature applications, and it became a starting point for the satisfaction of high-temperature engineering requirements. However, it was found that these materials also have limitations in their strength capabilities. The metallurgists have responded to increasing needs by making what might be termed ‘‘super-alloys’’ of stainless diversities. The invention and adaption of alloys has been derived for the gas turbine [35].

Iron, nickel, and cobalt are generally face centered cubic (fcc-austenitic) in crystal structure when they are the basis for superalloys. However, the normal room-temperature structures of iron and cobalt elemental metals are not fcc. Both iron and cobalt undergo transformations and become fcc at high temperatures or in the presence of other elements alloyed with iron and cobalt. Nickel, on the other hand, is fcc at all temperatures. In superalloys based on iron and cobalt, the fcc forms of these elements are generally stabilized by alloy element additions, particularly nickel, to provide the best properties.

The Cr-Mo steels are widely used in chemical industries and electrical power generating stations due to the improved creep strength derived from Mo addition and the enhanced corrosion resistance from Cr. Creep strength generally increases with higher amounts of Mo and Cr generated from the solid-solution strengthening of the ferrite matrix by carbon, molybdenum and chromium; and precipitation hardening by carbides. The Cr-Mo-V steels are manufactured with higher carbon ranges and suitable for bolts, compressor wheels in gas turbines and other parts operating at high temperatures (1000 F) due to the relatively high yield strength and creep strength.

The modified 9Cr-1Mo steel is an attractive alloy because its strengths exceed the allowable stresses of stainless steel. The improved strength of the modified steels derived from fine $M_{23}C_6$ precipitate nucleated on Nb(C,N) during the heat treatment and retardation of further grain growth of $M_{23}C_6$ by diffused vanadium at service temperature.

The Fe-based 16-25-6 (Cr-Ni-Mo) alloy have been extensively used in turbine wheels and remained dominant for many years. A number of precipitation hardenable alloys were developed, which include Discaloy, A286 and V-57. These alloys, which offered higher strength, are still in use. The alloys in this system contain around 25 wt% Ni to stabilize the austenitic structure and 15 wt% Cr to improve the corrosion resistance [36]. More recent alloys contain a total of 2-3 wt.% Al +Ti for achieving precipitation hardening. Conventional wrought alloys for higher temperature are likely to be unacceptable by the industries due to a tendency toward phase instability as the alloy content is increased. This problem can be solved by replacing part of the iron with nickel, thus making highly alloyed and stronger material without the formation of detrimental phases. This has been achieved in nickel-iron alloys such as Incoloy 901, Inconel 718 and D-979. Incoloy MA 956 possesses excellent strength and fabricability with outstanding resistance to prolonged exposure up to 1573 K. Its exceptional properties result from the mechanical alloying by which it is made. It is a process that allows a fine distribution of yttrium oxide particles into a highly corrosion resistant Fe-Cr-Al alloy.

The maraging steels were strengthened by precipitation of intermetallics at temperatures about 900 F. The maraging steels with very high nickel, cobalt and molybdenum contents and very low carbon contents have yield strengths as high as 3450 MPa. Carbon is an impurity which should be kept as low as commercially feasible in order to minimize the formation of titanium carbide that can affect the ductility and toughness of steels [37].

At different temperatures, dissimilar second phases are found, moreover the composition of precipitate phases depends on the alloy composition. Nickel is the main alloying element because it is a basic constituent for strengthening intermetallic compounds that it forms with Ti, Mo and Al. The addition of Co reduces the solubility of Mo that increasesthe fraction of nickel intermetallics and promotes the precipitation of Fe-Mo phase. For aging at low temperatures (400-450 °C), the probable ordered and coherent phases are ω (A_2B), s (A_8B), X (A_3B) and μ (Fe_7Mo_6) which are appeared in the martensitic matrix.

During aging at temperatures higher than 450 °C, rapid hardening occurs. Mo-rich phases are appeared in nanometric dimentions that make the uncertainty in the characterizations. However, it was found that hardening is attributed to precipitation of Ni_3(Ti,Mo) and Fe-Mo phases in dislocations in the martensitic matrix and at lath boundaries. The first precipitate is Ni_3Ti with contribution of higher strength in steels in which the elements Fe and Co can substitute for Ni in a small amount while Ti atoms can be substituted by Mo and Al. These phases can be rod shape or ellipsoidal while the Ni_3Mo precipitates appear in form of needle-like clusters.

When the matrix is enriched with Mo, the spherical Mo-rich phase is produced. The phase composition has not been clearly identified; in some works it is recognized as a Laves phase (Fe_2Mo), in other works as a μ phase (Fe_7Mo_6). The austenite reversion in maraging steels depends on the temperature. At temperatures higher than 500 °C, the formation of austenite occurs while the Fe_2Mo forms as the consequence of the dissolution of Ni_3Mo precipitates. This decomposition enriches the matrix with Mo and Ni, where the Ni acts as an austenite stabilizer.

At all temperatures, boron is essentially insoluble in austenite that shows that borides can basically form during melting. In the steel making operations, boron is in the form of precipitate that first reacts with nitrogen to form BN and then with carbon to form carbides and borides.The dissolution of boron in carbides, formation of mixed borides-carbides (e.g. $M_{23}(B, C)_6$ and $M_2(B,C)$) and precipitation of M_2B phase occur at low, intermediate and high B/C ratios, respectively. The maximum solubility of boron in these three stainless steels were found to be 58 ppm, 95 pm and 158 ppm according to Goldschmidt. Also in all the cases, the precipitating phase was (Fe, Cr)$_2$B which formed at low melting point eutectic between 1150 and 1225 °C. In the case of excess boron contents, a boride either a $Cr_{23}C_6$ type or (Fe, Ni, Cr)$_x$B (where x=2) are precipitated. Borides appear at grain boundaries as very small and discontinuous particles. At higher boron levels, a nearly continuous network of austenite-boride eutectic forms that encloses the austenite grains. At 4.63 at.% of B, austenite+ massive boride+ globular eutectic regions appear. In 1980, Loria and Isaac observed that type 304 stainless steel with 1-2 wt% boron has been applied for control rods and fuel racks.

Although the parts which are exposed to abrasion-corrosion wear are generally made of high alloyed Cr-Mo white iron and martensitic steels, but abrasive elements in mining, process industry and civil engineering are silica, corundum and other mineral particles. These materials suffer from their relatively low toughness that can cause dangerous damages in the related constructions. The best choice for the machine parts is the combination of high hardness, high impact toughness and high dynamic strength. Therefore, the composites made of ceramic reinforcement such as SiC particles in the steel based matrix can provide the desired properties. In order to achieve these composites with optimized distribution of reinforcement and with appropriate content, the production route must be considered. The normalized Steel-SiC MMC castings (sandvik) as an excavators tooth made by cast-in-carbide technique have shown larger resistance to the abrasive wear than eutectic carbon steel [38].

There are limitations in achieving the optimal distribution and particle size of hard materials in iron matrix because of using fusion metallurgical processes. However, this problem could be overcomed by using powder metallurgy route. The examples of materials produced by this process are Ferrotitanit (From the company Edelstahl Witten Krefeld Gmbh) and Fe-based PM2000 (from the company Plansee) which are used in tool steels [17]. Besides the common powder metallurgy, in-situ Fe-based composite materials can also be produced by mixing the basic materials followed by consolidation [17]. The in-situ MMCs are comparable with other tool steels and exhibit better wear properties that can lower the production cost. The superaustenitic 654 SMO and duplex stainless steels with TiN and Al_2O_3 particles as reinforcement have good wear and corrosion properties that make it suitable for the environments that are exposed to corroding liquids and gases in chemical and petrochemical industry (for example, pumps, valves, scoring dies, and mixers, or pulp and paper industry) and also heat exchanger tubes. Hot work tool steel with Cr_3C_2 particles as reinforcemnet can be used as cutting blades, metal forming tools (such as extrusion dies, tube forming rolls, rolling mill rolls), and also they are suitable for wear resistant parts in mining and earth-moving operations. According to the studies of Pagounis, et.al [39], both stainless steel and tool steel were used as the matrix and the effect of using different carbide, oxide and nitride particulate reinforcements of Al_2O_3, TiC, Cr_3C_2 or TiN on the mechanical properties of steel matrix composites has been studied extensively.

2.3.4.1 Fe-Al intermetallics

The reported intermetallic phases in the Fe-Al binary equilibrium phase diagram are as follows: Fe_3Al, FeAl, $FeAl_2$, Fe_2Al_3, Fe_2Al_5, and $FeAl_3$. In this system, only FeAl and Fe_3Al have significance for structural applications, while the rest of the phases are recognized to be very brittle. The unit cell of FeAl has ordered bcc (B2, cP2) structure. The Al content in FeAl changes between 35 and 50 at.% Al. By addition of Al concentration, the melting temperature decreases until it reaches 1250 °C at 52 at.% Al. At higher Al contents, the B2 structure of FeAl maintains up to the melting point. The ordered cubic crystal structure (D03, cF16) of Fe_3Al transforms into an imperfect ordered bcc structure (B2, cP2) at temperatures higher than 541 °C, which is the critical temperature for ordering. Three bcc phases observed in Fe-rich part of the Fe–Al phase diagram are as follows: a disordered solution (α-bcc), an ordered bcc phase (B2-structured FeAl), an ordered cubic phase (D03Fe_3Al), and also two binary phase regions of α + D03 and α + B2 were present in the compositions with Al content between 18 and 25 at.% at temperatures above 550 °C. The defected structure of B2 FeAl is complex which includes the substitutional atoms, vacancies, or both. In the Fe-rich alloys because of the deviations from stoichiometry in the B2 alloys, antisite imperfections generally are appeared. Therefore, the Fe atoms move into the vacant Al sites. However, in the Al-rich combinations, excess Al atoms do not move into all the vacant Fe sites. Accordingly, Fe-aluminides consist of vacancies up to 10 at.%. At 800 °C (homologous temperature = 0.71), the vacancy concentration is approximately 40 times more than that in normal metals when they are in their melting temperatures.

2.3.5 Thermodynamics of Mo-Fe-B system

During the thermochemical heat treatment of steels with a transition metal borides (ZrB_2, TiB_2, CrB_2), a ternary compound of $(Fe,Mo)_2B$ was appeared with the hardnesss of 20-23GPa [40]. It was found to be equal with another complex boride (Mo_2FeB_2 with ferrous binder) in the case of corrosion and wear resistance [40].

The boron additions to the alloyed sintered steels results in Mo-Fe-B phases with excellent properties that are suitable for automotive industry and wear resistant structural components. Also, the alloys that were produced by molybdenum additions to the iron borides can be used as cutting tools. Two ternary phases of τ_2-Mo_2FeB_2 and τ_4-$Mo_{1+x}Fe_{2-x}B_4$ have different crystal structures from the other unary and binary solid phases. The τ_1-$Mo_2Fe_{13}B_5$ phase was reported to be produced from the melt at ~1100 °C and decomposes below 1000 °C [41].

Table 2.3 : The crystallography and properties of solid phases in Mo-Fe-B system [45].

Phase/Temperature range	**Pearson Symbol/ Space group/Prototype**	
Fe_2B **<1399**	tI12 I4/mcm $CuAl_2$	33.3 at.% B
FeB **<1603**	oP8 Pnma FeB	50 at.% B
Fe_3B	tI Fe_3P	Metastable produced by quenching of liquid $Fe_{76}B_{24}$, exists in the approximate temperature interval 1150 to 1250˚C
σ, MoFe **1611-1235**	tP30 $P4_2$/mnm σCrFe	43.3 to 57.1 at.% Fe
μ, Mo_6Fe_7 **<1370**	hR39 R3-m W_6Fe_7	56 to 61 at.% Fe
R, Mo_2Fe_3 **1488-1200**	hR159 R3- $Co_5Cr_2Mo_3$	61.5 to 66.1 at.% Fe
λ, $MoFe_2$ **<927**	hP12 P63/mmc $MgZn_2$	66.7 at.% Fe
τ, $Mo_2Fe_{13}B_5$ **<1000**	tP32 P42/n Ti_3P	Annealed at 1050˚C
τ, Mo_2FeB_2	tP10 P4/mbm U_3Si_2	Annealed at 1000˚C
τ, $Mo_{1-x}Fe_xB$	oC8 Cmcm CrB	6.5 to 9 at.% Mo at 50 at.% B, T=1050˚C Annealed at 1050˚C
τ, $Mo_{1+x}Fe_{2-x}B_4$	oI14 Immm Ta_3B_4	13 to 25 at.% Mo at 57 at.% B, T=1050˚C x=0, annealed at 1000 x=1, x=0.06, x=0.43 annealed at 1050

A. Leite, et.al reported that the $MoFe_{14}B_5$ phase was produced by the additions of molybdenum for stabilizing the metastable Fe_3B phase (with the same Ti_3P type structure) that has a narrow stability range of 1110-1080 °C. The crystal structure of τ_3-$Mo_{1-x}Fe_xB$ is similar to the βMoB structure and can be considered as an iron stabillized βMoB phase [41].

According to the established isothermal section of Mo-Fe-B system at 1000 °C in the concentration range of 0-50 at% B, five compound phases which are originated in the binaries (i.e. Fe-Mo) were presented by E.I. Gladshevyskii, et al. (Figure 2.13): MoB, FeB, Mo_2B, Fe_2B and the p-phase. The ternary compound $(Mo,Fe)_3B_2$ (U_3Si_2-type structure) was determined with a homogeneity region of 40 at% B, 20-28 at% Fe, 40-32 at% Mo that includes the composition of Mo_2FeB_2 which was reported to have a limited solubility in the binary compounds [41].

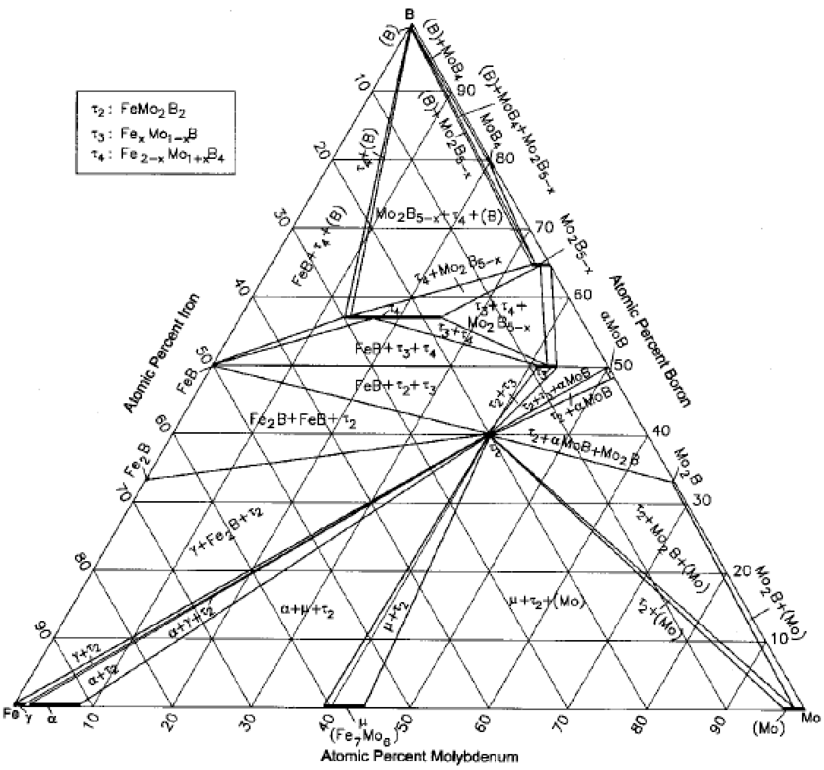

Figure 2.13 : Ternary phase diagram of Mo-Fe-B system [45].

The detected (Mo,Fe)B phase is the high-temperature form of the MoB phase which is stabilized by addition of iron at lower temperatures. The additional ternary compound $Fe_{13}Mo_2B_5$ (i.e. M_3B) was also reported by H. Hashke, et.al constructing an isothermal section of the Fe-Mo-B system at 1050 °C. This metastable phase was produced by rapidly quenching of Fe-B alloys. This phase was reported to be stable just above 1000 °C but decomposes by eutectoid reaction at about 1000 °C. However, it was determined that in Mo-rich alloys there is an equilibrium between Mo_2FeB_2 phase and Mo(bcc) slid solution, whereas the equilibrium between Mo_2B and p-phase was observed. The calculated isothermal sections of the Fe-Mo-B system at 1000 °C and 1050 °C were established by H. Hashke, et.al. considering the experimental results.

In the isothermal sections at the temperature range of 1200-1280 °C for the B concentration range up to 34 at.%, four phases of L, Fe solid solutions (γ and α), hypothetical continuous series of solid solutions between Mo_2B and Fe_2B as well as the μ, Mo_6Fe_7 phases are considered to be stable [41].

The formation of the liquid phase during the liquid phase sintering mechanism by boron additions to the Fe and Fe-Mo prealloyed powder compacts with (0.5-3.5 mass%)Mo-Fe-XB compositions have been investigated. It was observed that the alloys containing Fe-1.5Mo-0.4B sintered at 1200 °C have the tensile strength of 487-550 MPa, elongation of 2.5-4.8%, Vickers hardness above 2 GPa and density of 7150 $kg.m^{-3}$ [42]. The alloys in Mo-Fe-B system which consist of 6 mass% Mo and annealed at 1073 to 1327 °C temperatures range have a composite structure based on two phase (Mo_2FeB_2 hard phase + Ferrite binder). Different Mo ranges in Mo-Fe-B system affect the properties of alloys as 2% was observed to be hardenable by a bainitic transformation from austenite to ferrite, those with 4 mass% Mo were hardened by the solid solution mechanism, the alloys containing 9-19 mass% Mo were strengthened by precipitation of the R and Mo_2Fe_3 phases. The compositions having up to 1.1% B and 5 mass% Mo which were compacted and sintered at 1200 °C, have negative effects on the ductility by forming Mo_2FeB_2 phase [43].

A eutectic liquid phase of $Fe+Fe_2B$ was formed which activates the sintering of Fe-1.5mass%Mo+B powder system [43].

The isothermal section at 1050 °C in Mo-Fe-B system was constructed by V. Raghavan considering the experimental results and by using sintered and arc-melted samples. It was observed that τ_1 is not stable and other ternary compounds of τ_2, τ_3 and τ_4 are present in the phase diagrams whereas the phases of τ_1, τ_2, τ_3 and τ_4 are $Fe_{13}Mo_2B_5$, Mo_2FeB_2, $FeMo_8B_{11}$ and $FeMo_2B_4$, respectively. The solubility of Fe in Mo_2B_{5-x} and αMoB are 2.3 and 0.5 at%, respectively [43].

2.3.5.1 Crystal structure of Mo_2FeB_2 ternary boride

Calculations based on the density functional theory (DFT), explain the interaction between ionic core and valence electrons to estimate the crystal structure. Therefore the structure stability, magnetism, electronic structure and elastic properties of Mo_2FeB_2 in nonmagnetic, ferromagnetic and antiferromagnetic cases are resulted from the nature of the bonding. As the result of magnetism analysis, Fe atoms play significant role. Ferromagnetic and antiferromagnetic cases of the Mo_2FeB_2 have a lower bulk modulus, but higher shear modulus and youngs modulus than nonmagnetic case, so that these properties affect the brittleness of the intermetallic. Mo_2FeB_2 phase is U_3Si_2-type or it can be assumed as an intergrowing of CsCl-type MoFe and AlB_2-type MoB_2 phases. Besides Mo_2FeB_2, a variety of intermetallics possess the U_3Si_2 structure which is shown in Figure 2.14. Mo_2FeB_2 has tetragonal symmetry and belongs to the space group of P4/mbm with lattice parameter a=b=5.807A, c=3.142A. The unit cell contains four molybdenum atoms, two iron atoms and four boron atoms [44].

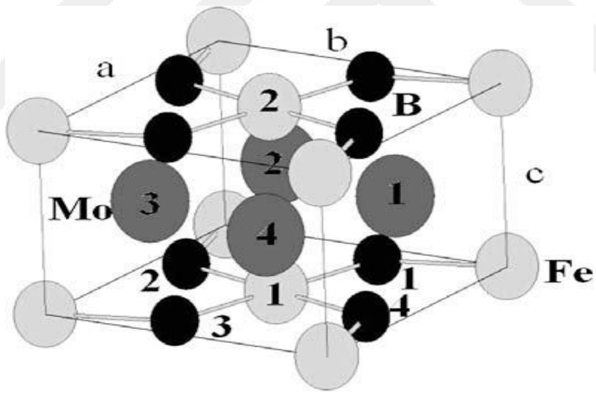

Figure 2.14 : Crystal structure of Mo_2FeB_2 [48].

2.3.5.2 Properties of Mo_2FeB_2 base cermets

K.i. Takagi, et.al produced the ternary Fe-6%B-(38-53%) Mo by liquid phase sintering and they studied the production mechanism by dilatometry and differential thermal analysis. The sintering of prealloyed Fe-1.5Mo (wt%) powders with boron additions of 0-0.6pct was investigated by A. Molinari, et.al [45]. In this study, it was found that the presence of liquid phases obtained from the released heat during solid-state reactions causes the formation of borides and also the ternary boride compound (Mo_2FeB_2) in the eutectic structure. The Mo_2FeB_2-Fe cermets were produced through sintering method by using two different raw materials of elemental powder or MoB powder for studying on their densification, mechanical and magnetic properties [46]. According to the study of J. Karwan [47], the iron-molybdenum alloys were sintered by addition of various percentages of boron in order to investigate their structural applications. The formation of Mo_2FeB_2 in these alloys during sintering is found to strengthen the Fe-Mo matrix but inhibits the sintering process [47]. The production of Mo_2FeB_2 based cermets was studied by H. Tashiro, et.al [48] through sintering and MIM process to obtain complex shaped parts that were observed to present the same good mechanical properties as those of the press-sintered. H. Yu, et.al [49] studied on the effects of sintering temperature and soaking time on the microstructure evolution of products such as grain size, and also transformation and liquid phase sintering mechanisms were discussed. They observed the formation of phases by increasing temperature from 600 °C up to 1080 °C. At 800 °C, Mo_2FeB_2 was produced from Fe_2B and FeB phases by consuming Mo that causes densification to be completed at 1080 °C. The mechanical properties of these cermets such as hardness and TRS are the the same as the cemented carbides. Also, density of ternary boride cermets is found to be about three-fifth of cemented carbides, but similar to those of steels. The fracture toughness of cermets is rather high in respect to the cemented carbides but the thermal expansion coefficient is similar to those of steels [49].

Most recently, the cohesive energy (E_{coh}=-920.61 Kj/mol), formation enthalpy (ΔH_r=-70.10 Kj/mol) and bulk modulus (309.2 GPa) of Mo_2FeB_2 structure were calculated by using first-principles methods by T. He, et.al [29]. The calculated formation enthalpy of Mo_2FeB_2 shows that it has the highest structural stability among Mo_2XB_2 (Fe, Co, Ni) compounds. According to the analysis of electronic structures, the covalent bonding dominates the bonding behaviors of ternary borides, but the ionic and metallic may also be formed. Mo_2FeB_2 has the largest shear and Yong's modulus as 204.3 GPa and 500.3 GPa, respectively, which shows the strong chemical bonding [29].

2.3.5.3 The effect of alloying elements addition on the properties of Mo_2FeB_2 base cermets

The Mo_2FeB_2-based cermet as the name of TBB (ternary-boride-based) hard cladding material with the composition of hard phase (Mo_2FeB_2+(Mo, Fe, Cr)$_3B_2$) and the binder phase (a-Fe, γ-Fe and (Fe,Ni)) was developed by W. Yongguo, et.al using reaction sintering at 1563 K with the reported hardness of 84.5HRA [50].

Mo_2FeB_2-based ceramic has relatively good comprehensive mechanical properties, excellent corrosion resistance and good wear resistance, but worse transverse rupture strength. The previous studies have focused on improving the overall mechanical properties of Mo_2FeB_2-based ceramic by adding alloying elements such as C, Cr, Ni, Mn, V, etc. The addition of alloying elements causes the fine-grain strengthening and solid-solution strengthening. Mo_2FeB_2-based ceramic which contains Cr or Ni has better corrosion resistance. However, some elements, such as carbon, can form the third phase during sintering, which gives the negative effect on the mechanical properties. When the hardened phases such as TiB_2 and SiC are added, the performance of Mo_2FeB_2-based ceramic is improved.

The Mo_2FeB_2-based cermets which were used in K.i. Takagi, et.al works are called V30 and V50 with the compositions of Fe-6B-47.5Mo-2.9Ni-2.4Cr and Fe-4.3B-35.2Mo-2.9Ni-8.1Cr-3.8W, respectively [24]. It was found that the matrix of these cermets changes between ferrite, martensite or austenite that is dependent on the Ni and Cr content. They found that in these cermets, the physical properties such as density was calculated to be close (three fifth of) to those of cemented carbides and the same as those of steels. And their fracture toughness values are higher than those of cemented carbides but the thermal coefficients are close to those of steels. The wear resistance of these cermets in comparison to the cemented carbide specimen under the same conditions was proved to be better due to the formation of oxides during sliding that prevents adhesion [24].

The valence-electron structures (VES) of the hard phases in Mo_2FeB_2-based cermets and the relationship between their plasticity and the covalent bondings were calculated by the empirical electron theory (EET) of solids and molecules by Xum., et.al. It was observed that the bonds between Fe-Fe atoms cause the brittleness and the plasticity was improved by dissolution of Mn in the form of $(Mo,Fe,Mn)_3B_2$ in the hard phase of these cermets. In addition, the experimental results about the effect of Mn (0-10 wt%) addition to Mo_2FeB_2 based cermets (with the nominal composition of Fe-48Mo-6B-2.9Ni-2.5Cr-0.5C(wt%)) were reported by H. Yu, et.al [51]. They proved that Mn addition improves the wettability between the Fe binder phase and hard phase of

Mo_2FeB_2, and accordingly decreases the porosities and also grain size of Mo_2FeB_2 particles and improves the TRS of the cermet [51].

The influence of V content (0-7.5 wt% in 2.5 wt% increments) on the nominal composition of Mo_2FeB_2-based cermet was studied by H. Yu, et.al study [52]. They observed that V addition decreases the wettability between the binder and hard phase, and accordingly increases the porosities and contiguity. The optimum amount of V addition was found to be 2.5 wt% which exhibited the smallest grain size and the highest TRS, hardness and fracture toughness of 2350 MPa, 90.6 HRA and 15.1 $MPam^{1/2}$, respectively [52].

The effect of C content (0-1.5 wt% in 0.5 wt% increments) on the cermets with the above-mentioned compositions was studied by H. Yu, et.al [53]. It was investigated that C addition increases the dissolution of Mo in the binder, changes the binder phase from the ferrite to martensite and decreases the grain size. The highest hardness for these cermets was in the composition with 0.5 wt% C addition. However, carbon in these cermets with Fe binder forms a third phase of Fe_3C that can have negative effects on the mechanical properties and accordingly lowers the fracture toughness and TRS [53].

The preparation of Mo_2FeB_2 cermet coating on steel substrate was performed by M.A. Zhuang, et.al [54] by using reactive thermal spray method at 1000 °C heat treatment. It was observed that the obtained cermets exhibit the thermal shock resistance and wear resistance 65 and 8.35 times higher than the substrate Q235 steel, respectively [54]. The effect of using different raw materials (FeB powder) and (2wt%)Ni+(0-12.5wt%) Cr additions in reactive sintering production of Mo_2FeB_2-based cermets was studied by Q. Fang, et.al [55]. It was concluded that both Ni and Cr improve the hardness and TRS, however the influence of Cr was significant due to changing the microstructure of the obtained cermets [55].

The effect of Nb/V (0-6wt%) addition on the Mo_2FeB_2-Fe cermets produced by liquid phase reaction sintering method was studied by D.Ke, et.al [56]. The results revealed that by addition of Nb/V, the hardness and TRS both increase initially and then descend, and the grain size decreases with Nb content. The optimum amount of 4 wt% Nb exhibited the highest hardness and TRS of 90.6 HRA and 1970 MPa and the best dry sliding wear resistance [56].

Using first-principles calculation of Mo_2FeB_2 base cermets, the bulk modulus, Youngs modulus, poisons ratio and B/G of Mo_2FeB_2 and $Mo_2(Fe,Mn)B_2$ phase were calculated, theoretically by C. SUN, et.al [57]. And also the experimental results of the effect of 10 wt% Mn addition on microstructure and mechanical properties of sintered cermet were investigated. It was concluded that the Mn addition causes the grain refinement and better ductility but a decrease in the hardness [57].

The calculated elastic modulus shows that Mo_2FeB_2 has better mechanical properties when alloying elements are at Fe site instead of Mo site. Moreover, Cr addition can improve the volume deformation resistance of Mo_2FeB_2, and Mn addition can improve the shear deformation resistance for Mo_2FeB_2. The calculated B/G ratio shows that Ni addition can improve the brittleness of borides. Furthermore, the hardness of Mo_2FeB_2 can be enhanced by adding Cr and Mn elements. The calculated electronic structure indicates that the increasing of elastic modulus is attributed to the formation of Cr–B and Mn–B covalent bonds.

2.3.5.4 Amorphous Mo-Fe-B alloys

According to the studies, the crystallization in $(Mo_5Fe_{95})_{83}B_{17}$ metallic glass occurs within a two-step process. By using three various applied types of calorimetric techniques including peak shift, temperature change and isothermal, the activation energy after first cycle of crystallization has been determined. The investigations have reported the thermal behavior of amorphous $Mo_{13.3}Fe_{63.4}B_{23.3}$, $Mo_{11.3}Fe_{58.7}B_{30}$, $Mo_{16.3}Fe_{73.6}B_{10.1}$ and $Mo_{1.9}Fe_{74.7}B_{6.4}$ alloys. The crystallization temperatures were found to be in the range of 745-771 K (472 to 498 ˚C) for B contents of 6.4-30 at.% in alloys produced by electrolytic plating at a heating rate of 10 $Kmin^{-1}$ [43].

Magnetic properties of the Mo-Fe-B amorphous alloys were observed in several studies. The electrical resistivity of $(Mo_xFe_{1-x})_{80}B_{20}$ (x=0.05 to 0.18) amorphous alloys as a function of temperature between 4.2 and 300 K was studied [43].

2.3.6 Co-based composites

The cobalt-based alloys can be categorized according to their applications: High-carbon alloys which are used for wear service, low-carbon alloys for high-temperature service and low-carbon alloys in order to prevent corrosion and wear. Many of the properties of these alloys are derived from crystallographic nature and solid solution strengthening effects of Cr, W, Mo and carbides. For high temperature applications such as gas turbine vanes and buckets, the softer and tougher compositions were applied while for resistance to wear, the harder ones are suitable [21].

Many conventional alloys are derived from the ternary systems of Co-Cr-Mo and Co-Cr-W studied by Elwood Haynes at the turn of the 19th century. He studied the high strength and corrosion resistance of Co-Cr binary alloys that found to be strengthened by Mo and W which later was called stellite alloys. After that, these alloys were used as cutting tools and hardfacing alloys. The hardfacing alloys were applied in plowshares, oil well drilling bits, dredging cutters, hot trimming dies, and internal combustion engine valves and valve seats. Among the corrosion resistant Co-Cr-Mo alloys, the ones with low carbon content were developed to be suitable as investment-cast dental material. This biocompatible material which is called vitallium is used for surgical implants nowadays. The developments in these alloys were performed by modifying their carbon and tungsten contents. The carbon content and volume fraction of carbides are factors that determine the alloys types. For example, stellite3 consists of 2.4 wt% carbon that causes the formation of 30% carbides with the types of M_7C_3 (Cr-rich primary) and M_6C (W-rich eutectic) where M represents the metal component. The size and shape of carbide particles in the stellite alloys are affected by cooling rate and chemistry changes [21].

Cobalt base alloys are widely used for the devices that are surgically implanted in the body. These applications include hip replacements, knee replacements and implants that fix bone fractures. The properties of interest for orthopedic implants include biocompatibility, corrosion resistance, wear resistance and mechanical properties including strength, ductility and high-cycle fatigue behavior [21].

Chromium in the cobalt-based stellite alloys has a dual effect that are both carbide former and the alloying element in the matrix which provide more strength and resistance to corrosion and oxidation. Tungsten and molybdenum in the stellite alloys provide additional strength to the matrix because of their large atomic size when present as a solute atoms. High contents (in stellite1) cause the precipitation of M_6C carbides during alloy solidification [21].

The Laves phase alloys include the tribaloy family of wear resistant materials which are known as T-400 and T-800 alloys. In these alloys, molybdenum and silicon are added with levels higher than their solubility limit in order to precipitate the Laves phases (CoMoSi and Co_3Mo_2Si). The carbon is kept low to prevent the carbide formation. The Laves intermetallic phases have high fraction in these materials that govern the properties of materials. Therefore, the effect of matrix phase which is lower in concentration is less pronounced in contrast to stellite alloys. The Laves phase is responsible for abrasion resistance but retards the ductility and impact strength [21].

In order to provide alloys with outstanding resistance to aqueous corrosion and resistant to wide range of temperatures, several low-carbon wrought Co-Ni-Cr-Mo alloys were produced. Molybdenum addition in these alloys imparts a greater resistance to a variety of wet corrosive media. The carbide formation and solubility of carbon must be controlled in these alloys to improve resistance to heat-affected-zone sensitization during weldings. In the multiphase alloys (MP) of MP35N and MP159 produced by vacuum induction melting followed by vacuum arc remelting (VIM/VAR), the combination of ultrahigh strength, high ductility and corrosion resistance including the resistance to stress-corrosion cracking make them high performance aerospace fastener alloys. The main strengthening mechanism in these alloys is solid-state phase transformation of the matrix from fcc to hcp during cold working due to the higher content of Co. Therefore, this phenomenon is termed as "multiphase reaction" in which the presence of two structures makes a barrier to the motion of dislocations that results in strengthening [21].

The cobalt in these alloys imparts an unstable fcc crystal structure with a very low stacking fault energy. When it is cooled extremely slowly, it transforms from fcc to a hexagonal close-packed crystal structure at 417 °C. The properties such as high yield strengths, high work-hardening rates, limited fatigue damage and the ability to absorb stresses are derived from the sluggish nature of the fcc to hcp transformation and unstable fcc structure of Co [21].

Cast Vitallium (Co-27Cr-5.5Mo-2.5Ni-0.25C) turbo supercharger blades were engine tested with success. Modification of mentioned alloy was done later to reduce the tendency for carbide precipitation and subsequent loss of ductility in service. Both cast and wrought cobalt-based superalloys are generally FCC (austenite) and they are solid solutions containing one or more carbides. Their strength is achieved by solid-solution hardening with a combination of Ta, Nb, Mo, W and Cr, and also through dispersion hardening by carbides of these elements or Zr. The FCC structure of these alloys is stabilized by nickel. Nickel also counterbalances the tendency of the refractory metals to cause transformation to the hexagonal-close-packed structure. The microstructure of cast cobalt-based alloys such as Mar-M 509, contains blocky, script and eutectic carbides in a solid-solution matrix without any intermetallic compounds. Intermetallic compounds are occasionally for strengthening cobalt based alloys due to their tendency toward instability at elevated temperatures. In past, popular wrought cobalt-based alloys included S-816 that was used in many turbine buckets and L-605 sheet that found application in burners and ducts [21].

Because the cobalt-base alloys are wear resistant, corrosion resistant, and heat resistant (i.e. strong even at high temperatures) materials, they have wide applications in these areas. For example the main application of cobalt-base alloys is in the area of wear resistant components and/or applications. But in heat resistant area, cobalt is more widely used as an alloying element in nickel-base alloys which have cobalt tonnages in excess of those used in cobalt-base heat resistant alloys.

Cobalt-based superalloys have better capibilities in corrosion resistance compared to stainless steels and therefore, cobalt-chromium-molybdenum alloy (MP-35N) is used as a casting alloy. The cobalt based cast alloys are superior to noncast in wear resistance, pitting resistance and crevice corrosion resistance. The ease of processing and properties of cobalt alloys make them suitable for a wide range of orthopedic applications including all metallic components of all joint replacements as well as fracture fixation devices. In age-hardenable nickel based alloys, the γ(prime) intermetallic (Ni_3Al) is formed which plays a significant role in strengthening. Cobalt based superalloys may contain some precipitation strengthening phases from carbides (Cr_7C_3, $M_{23}C_6$) but no intermetallic phase strengthening like gamma prime presented in nickel based alloys.

The microstructure effect on the fatigue behavior of cobalt-base eutectic composites which contain the fibrous reinforcements such as Tantalum carbide fibers (called Cotac) with the percentages of Cr in the composition is studied. In the case of the cobalt based composites, for example Ni or Co additions have been adjusted in such a way that the allotropic transformations of HCP to FCC were suppressed and accordingly the abrupt dimensional variations during temperature changes were avoided. These composites were developed for possible high temperature applications in advanced aircraft gas turbines.

Cobalt has been the traditional choice for a binder metal since Schroter patent (in 1923 Germany) proposed using cobalt as a binder in WC hardmetals production. The advantages of using Co in these cermets are high solubility of WC in cobalt at sintering temperatures, the best comminution characteristics in milling and superior wettability for WC.

2.3.6.1 Al-Co intermetallics

The phases appeared in the equilibrium binary phase diagram of Co-Al are as follows: two fcc solid solutions γ (Co) and γ (Al), hcp-Co (ε), β with CsCl structure, and the intermetallic phases Co_2Al_5, $CoAl_3$, Co_4Al_{13}, and Co_2Al_9. The equilibrium phase diagrams are indirectly bound with various changes in the physical properties of alloys. For example, abnormal behavior at the phase boundaries in some alloy systems confirms a magnetic transition. The phase boundaries in the Co-Al binary system may be classified as such a category. The Co-Al system consists of one eutectic reaction concerning the liquid phase and six invariant reactions between the solid phases. The peritectic reactions of Co_2Al_5, $CoAl_3$, Co_4Al_{13}, and Co_2Al_9 were determined by McAlister, Dupin, and Ansara through thermal analysis and metallographic studies. It was found that there is a large homogeneity range from 22% Al to almost 50% Al at higher temperatures but with a remarkable decrease in the lower temperature region for the B2 (β) phase which formed congruently from the melt at an almost equiatomic composition. There is a wide composition range two-phase region for the Al (γ)/B2 (β) phases which spread with decreasing temperature. But the experimental values were not approved with the assessment of the binary phase diagrams due to the sudden drop in the homogeneous region. The unusual shape of the phase boundary was studied by Hiroshi Ohtani. et.al. According to their preliminary analysis, it was found that the anomaly at the phase boundary appeared due to a phase separation occurred by an order-disorder transition of the B2 phase.

The metastable (A2 + B2) two-phase region which is formed in the Co-rich side of the phase diagram and their two-phase separation with the bcc structure, describes the peculiarity in the phase boundaries in the Co-Al binary system. This situation and the Gibbs free energies of the B2 (β) and the A1 (γ Co) phases are illustrated in Figure 2.15. At higher temperature, T1, it was observed that the two-phase separation does not occur mainly due to the effect of the entropy of random mixing on the atomic arrangement. On the other hand, at lower temperatures, T2, the tendency towards ordering becomes stronger. The resulted two-phase separation occurs due to the attractive interaction between unlike atoms at the maximum degree of ordering in the B2 structure which is the acute point of the free energy curve at 50%Al composition or the equiatomic composition with a decreased enthalpy term. They have concluded that this situation results in a significant transfer of the the (γ Co + β)/β region's phase boundary to the equiatomic composition.

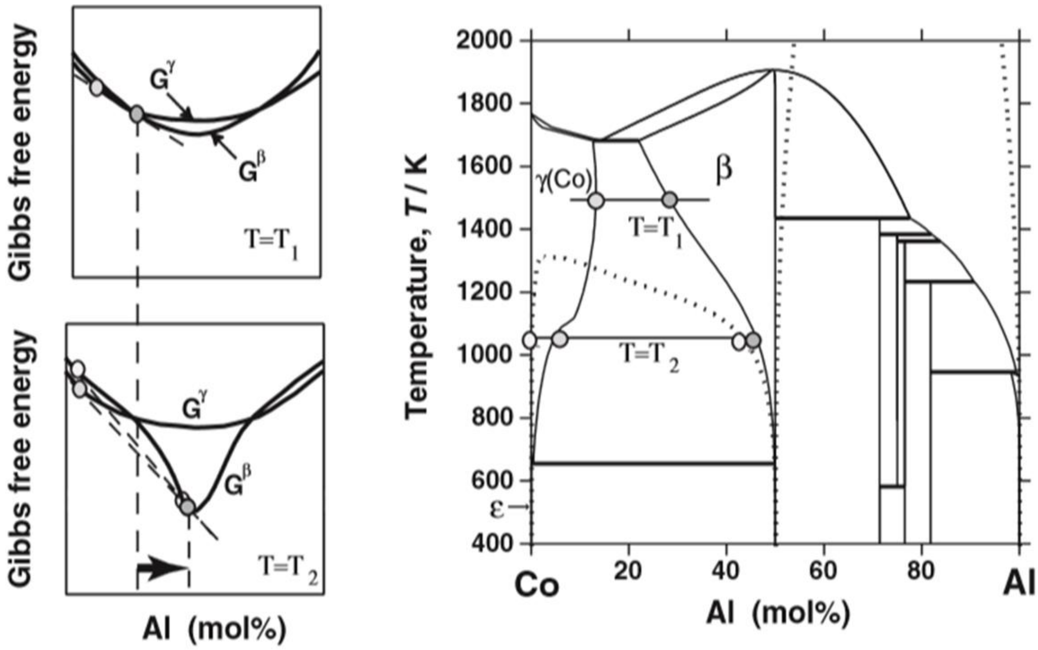

Figure 2.15 : The schematic Gibbs free energy of the B2 (β) and A2 (γCo) phases in the Co-Al system [58].

2.3.7 Thermodynamics of Mo-Co-B system

WC-Co is a common material and widely used in the metal-working. It was observed that the superhard ternary boride (WCoB) coating is formed due to the addition of boron in WC-Co composites that exhibit a sharp rise in wear resistance and microhardness of these composite materials. Therefore these enhancements in mechanical properties have increased service life of the WC-Co instruments [40]. Also, MoCoB and WFeB ternary compounds are similar to WCoB with the same orthorhombic unit cells [58].

2.3.7.1 Thermodynamics of Co-Mo and B-Co systems

The Co-Mo phase diagram is shown in Figure 2.16. This system contains total of eight phases: four solution phases: liquid, cph (Co), fcc (Co), and a bcc (Mo) terminal solid solutions, plus four intermetallics: θ (“Co_9Mo_2”), ε (“Co_3Mo”), μ (“Co_7Mo_6”), and σ (“Co_2Mo_3”) [59]. The Co-base solid solutions include low-temperature ferromagnetic and high-temperature paramagnetic phase fields, denoted in Figure 2.16 as α, α′ and β, β′ for the cph (Co) and the fcc (Co) phases, respectively. For the whole compositional range, the liquidus curve was determined. As for the solid phases, a controversy still exists over the stability limits of the para-cph (Co) solid solution and its relation to the high-temperature θ phase; both phases have identical crystal structures and very similar lattice parameters as shown in Table 2.4.

Table 2.4 : Crystal structure and lattice parameter data of the cph (Co) and Ө phases [62].

Phase	Structure	Type	Space group	Parameters	
				a	b
Cph (Co)	cph	Mg	$P6_3/mmc$	2.567	4.11
Ө	cph	Mg	$P6_3/mmc$	2.597	4.21

In the earlier studies, it was assumed that the cph (Co) phase field extended into the Co-Mo system up to 1273 K, dissolving almost 20 at.% Mo. In later interpretations, the stability of the cph phase was limited to 970 ± 150 K with a maximum solubility of only several at.% Mo. In these latter representations, the Co-rich cph phase containing 16 to 18 at.% Mo existed as an isolated θ phase, stable between 1290 and 1473 K. The cph (Co) and θ phases are structurally identical and have close compositions. Because further clarification of the existence of the θ phase as a separate compound is insufficient, the authors have accepted a description similar to the case of the Co-Cr system, in which the high-temperature Co-rich phase with the cph structure was treated as a paramagnetic cph (Co) phase. Following this interpretation, the cph (Co) and θ phases are described as Co-base cph solid solutions with two separate stability fields: the ferro-cph (Co) region, located in the Co-rich corner of the diagram below about 800 K, and the para-cph (Co), stable in the limited temperature-composition range of 1291 to 1473 K at 16 to 19 at.% Mo [62].

The homogeneity ranges of all the intermetallic compounds in the system were systematically investigated as shown in Figure 2.16. According to the study of A. Kattner, et.al, the θ phase (or the para-cph (Co) solid solution) is homogeneous in the range of 17 to 19 at.% Mo, the ε phase from 23.5 to 25 at.% Mo, and the μ phase from 41.5 to 48.5 at.% Mo. The range of the σ phase was not well established, but was located within the limits of 60 to 65 at.% Mo. For the above intermetallics, this work confirmed the temperature-stability limits, except for the lower limit of the σ phase that was extended from 1523 to 1273 K, as reported. The peritectoid decomposition of the ε phase was corrected from 1298 K (as estimated) to the more accurate value of 1319 K.

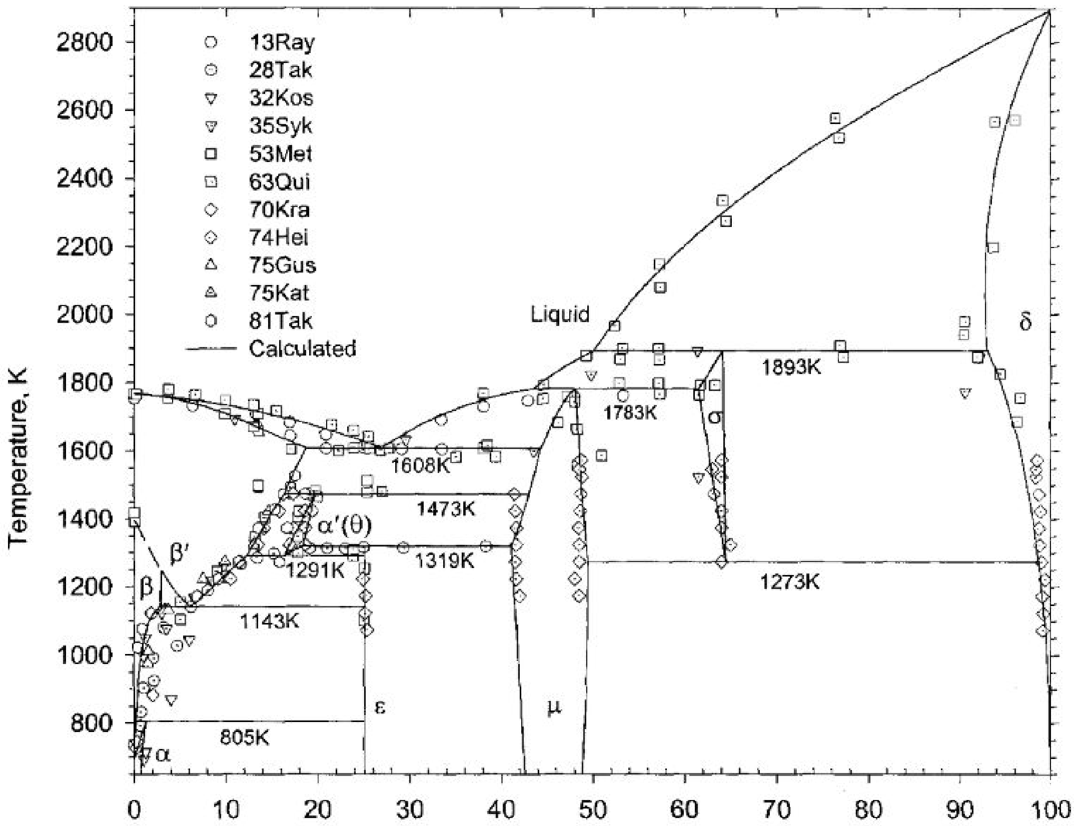

Figure 2.16 : Experimental and calculated phase diagram for Co-Mo system: α, ferro-cph (Co); α', para-cph (Co); β, ferro-fcc (Co); δ, bcc (Mo); ε, μ and σ, intermetallic compounds [62].

Three intermediate phases of Co_3B, Co_2B and CoB are occurred in B–Co system. The Co terminal solid solution phase is formed due to the slight solubility of boron in AlCo, whereas no Co solubility has been detected in the rhombohedral B (ß) phase. The eutectoid decomposition of Co_3B was occurred at 845 ˚C [60]. Figure 2.17 shows the B-Co binary phase diagram.

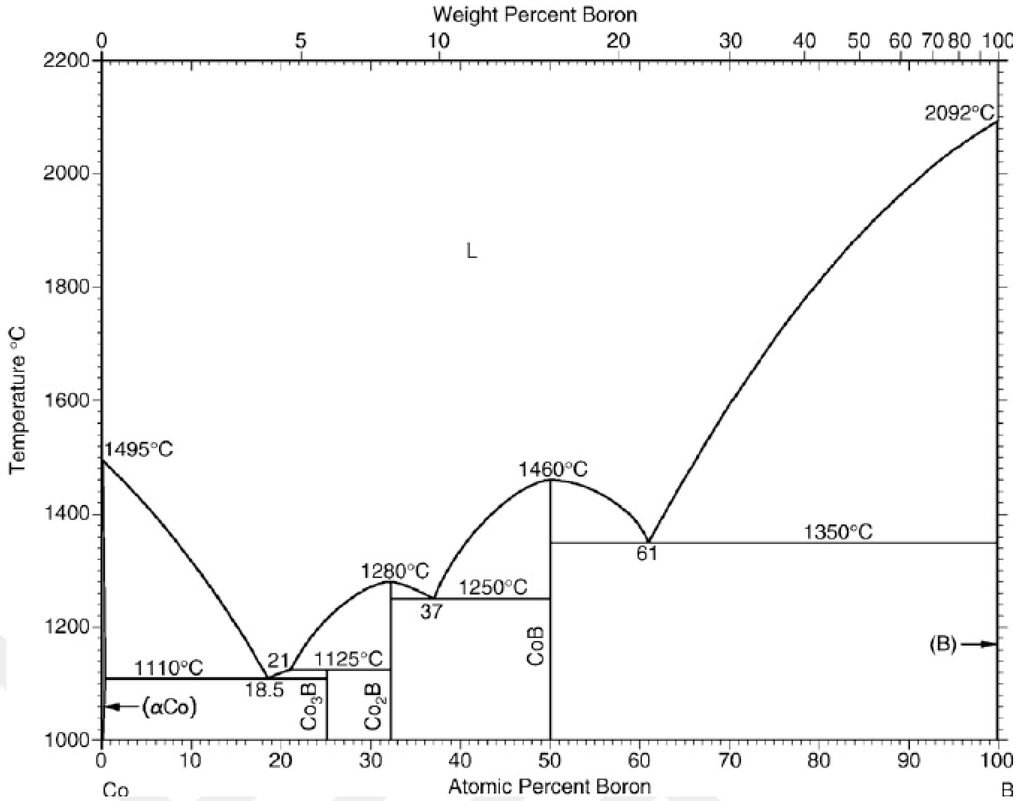

Figure 2.17 : Calculated B-Co phase diagram [63].

Kuzma et al. defined the structure of MoCoB and determined all the lattice parameters of WCoB and gave it a structure type PbCl2 with a pearson symbol oP12, spatial group Pnma. No.62 and obtained the XRD file [61].

There are some published papers based on studies about the Molybdenum-cobalt-boron system in which the occurrence of MoCoB phase is investigated since 1965. The more probable phase in this ternary diagram is $MoCoB_4$. The phase MoCoB was found to be formed peritectically by reaction of Mo_2CoB_2 with the liquid. It was investigated that a sample Mo/Co/B=9/70/21 at.% showed primary crystallization of MoCoB. Wolfgang Jeitschko has studied about the crystal structure of MoCoB that has an orthorhombic unit cell, space group Pnma. They found that the crystal structure is of the ordered $PbCl_2$ type. They reported that the compounds WCoB and WFeB are isotypic with MoCoB. Because the unit-cell dimensions and the atomic radii for MoCoB and WCoB are similar, the atomic parameters of both the phases should be the same [61].

Also the equilibria in the ternary system cobalt-molybdenum-boron were investigated in the region around τ ($Cr_{23}C_6$ structure) and MoCoB (unknown structure) by H.H. Stadelmaier, et.al. As observed in Figure 2.18, in the alloys quenched from 800 ˚C the composition of τ is found at $Co_{21.7}Mo_{1.3}B_6$. Reaction between Co solid solution and μ-phase Co_7Mo_6 is occurred [61].

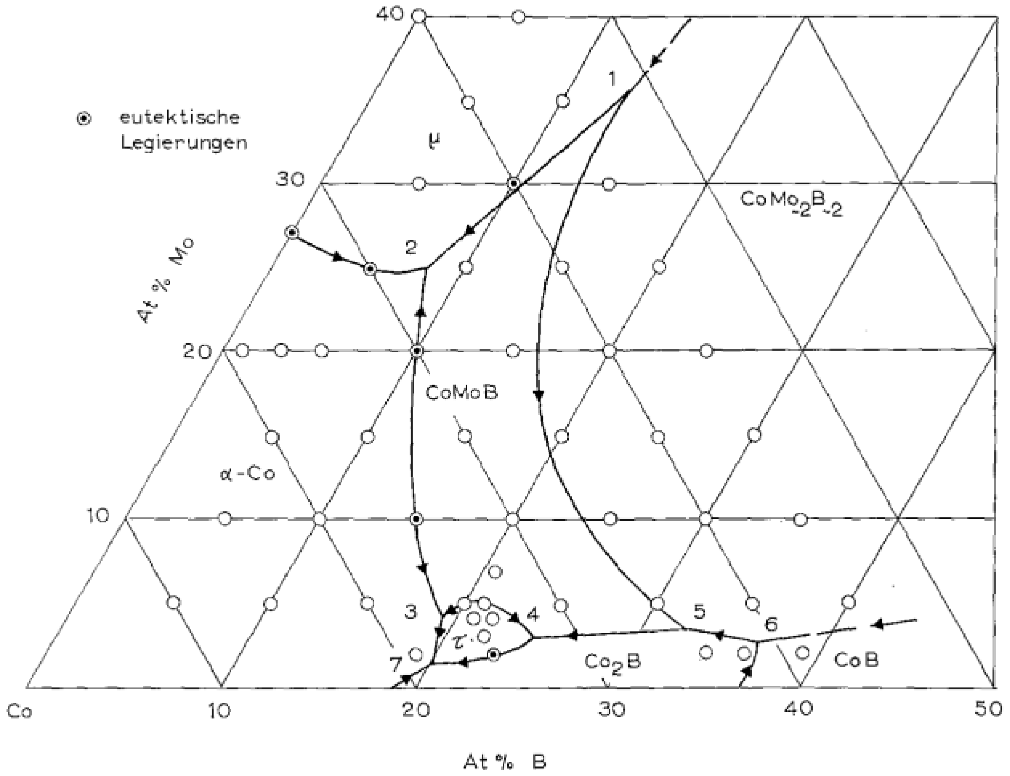

Figure 2.18 : Cobalt-rich region of Mo-Co-B ternary phase diagram [61].

2.3.7.2 Properties of Mo_2CoB_2 ternary boride based composites

The WC/Co coatings which were prepared by HVOF spray coating method have exhibited high durability agaisnst molten pure Zn or Zn-Al due to the effective inclusion of double carbides of miu-phase (Co_3W_3C and Co_6W_6C) in the WC/Co coatings where miu phase reduces free metal Co with high reactivity. However, the miu phase in these coatings has only limited resistance for the molten alloys at relatively lower temperatures less than 750 K. Therefore, the thermal spray coating of MoB/CoCr was reported to show higher durability against molten Al and Al/Zn alloys at higher temperatures [61]. The structure of MoB/CoCr powder which has been produced from ball milling of the commercial Co base alloys and MoB containing powders was proven by XRD to be composed of ternary double borides of Mo_2CoB_2/MoCoB. The cermet coating was performed on steel substrate by high velocity oxy-fuel spraying method (HVOF) and its durability was tested by the molten 55%Al-Zn-1.5%Si bath at 923 K [61]. The microstructure and microhardness of these coatings were studied by H.P. Lv, et.al [62]. According to the studies of X. Chen, et.al

[63], the thermal sprayed coatings with layer structure composed of ternary borides of Mo_2CoB_2 and MoCoB have excellent performance of bond strength and thermal shock resistance with the excellent durability in the Al-12.07%Si molten alloy.

The MoCoB-CoCr cermet coating produced by HVOF spraying technique has been applied in a glass forming process due to the outstanding characteristics of these cermets at 773-1073 K temperatures. These properties are extremely low friction coeffiecient to glass, higher oxidation resistance compared to other cermets such as WC-Co and Cr_3C_2-Ni/Cr, and very low mechanical abrasion.

It was observed that the friction stress produced by boride cermet coating was lower than the stainless steel friction against SiO_2-CaO type glass. The experimental results based on the applying of MoCoB-Co/Cr cermet to the lower mold during the glass forming process in an industrial scale were satisfactory [64].

2.4 Processing of Metal Matrix Composites

The selection of base metal depends on many factors like the degree of microstructural integrity, desired type and level of reinforcement loading. It is possible to manufacture MMCs with specific formulation (With same matrix and reinforcement combination) by more than one route. Processing of metal matrix composites (MMCs) can be classified into two main categories: Solid-State and Liquid-State Processing [65].

2.4.1 Solid-state processing

The two main fabrication methods for processing of metal matrix composites in solid-state, are powder blending and consolidation, and physical vapor deposition. 1) Powder blending and consolidation (PM processing): blending of base metal alloy powder with reinforcement fibre/whisker particle is well known technique for the production of MMCs. During this process, the blending is performed in liquid or dry liquid suspension and subsequently, the cold compaction, canning, degassing and high temperature consolidation stage such as hot iso-static pressing (HIP) or extrusion are usually carried out. The processing conditions and powder history in the production of PM-MMCs have great role on the oxide particles formation with a few tens of nm thick and on the volume fractions ranging from 0·05 to 0. The fine particles act as a strengthening-dispersion agent that often influence the matrix properties especially during heat treatment [65].

2) Diffusion Bonding: Diffusion bonding (foil-fibre-foil) route is generally used to produce Mono filament-reinforced MMCs. By using foil-fibre foil diffusion technique aluminum-boron fibre composites have been produced. However, for Ti based fibre reinforced composites, the diffusion process was used. In this process the fibre volume and homogeneous fibre distribution are difficult to be achieved and hence, it is not recommended for producing complex shapes and components.

3) Physical Vapour Deposition: Between the partial high pressured metal regions a continuous fibre is passing through the metal to be deposited. Meantime, condensation takes place so as to produce a relatively thick coating on the fibre. The vapour is produced by directing a high power electron beam onto the end of a solid bar feed stock. In this process 5–10 μm per minute deposition rate can be achieved very easily. The composite fabrication occurs through assembling these coated fibres together and hot pressing method,. 80% uniform distribution of fibre and volume fraction can be produced in this process.

2.4.2 Liquid-state processing

a) Stir Casting: In this process the base metal is in molten state in which the reinforcement particulates are introduced, mixed and then allowed to be solidified. Here, creating very good wetting between the reinforcement and the molten state base alloy is important. Stir casting technique or vortex technique is the simplest and most commercially used technique that uses the rotating impeller for creating the vortex of molten alloy in which the pre-treated reinforcement particles were introduced. Presently several aluminium companies improved the process to fabricate variety of MMCs on commercial scale. But in this process, accumulation of particle in the bottom of the melt and subsequently during solidification causes the microstructural inhomogeneities. Inhomogeneity in the distribution of reinforcement in composites could also be a problem causing the interaction between suspended reinforcement particles during solidification. Usually 30% of reinforcement material can be added to molten alloys. The alloy–reinforcement particle slurry can be transferred directly to a shaped mould or it may be allowed to solidify in billet or rod shape. Another type of stir casting process is compo-casting in which the ceramic particles are incorporated into the alloy in the semi-solid state.

b) Squeeze Casting: In this method, MMCs are produced by injecting the liquid base alloy into the porous pre-forms of continuous fiber/short fiber or particle or whisker. Based on the nature of reinforcement volume fraction pre-form can be infiltrated, with or without the application of pressure or vacuum. In this technique, depending on using different types of infiltration techniques, the MMCs can be achieved with volume fraction from 10% to 70% reinforcement. Silica alumina based binder or mixture is used to retain its integrity and shape. The MMCs produced by this technique exhibit some level of porosities and local variations ofthe volume fractions of the reinforcement.

c) Spray deposition: Depending on whether the stream droplet is produced from molten bath or by feeding continuous cold metal into a zone of rapid heat injection it is classified into two distinct Osprey process or thermal spray process. Injecting the reinforcement in the form of particle/whisker/short fibre has been extensively explored for the production of MMCs by spray process. The composites produced by this process often show inhomogeneous distribution of reinforcement particles. Porosity in the as-sprayed state is typically about 5– 10%. By subsequent process the depositions are typically consolidated to full density. This process allows to produce the continuous fibre reinforced MMCs and the cost of production of MMCs by this process will be comparatively less.

d) In-Situ Processing: There are several various processes will fall under this category including liquid-liquid, liquid-gas, liquid-solid, and mixed salt reactions. In these processes refractory reinforcements are created in the alloy matrix. Directional oxidations of aluminium (DIMOX process) and Martin–Marietta's exothermic dispersion process (XDTm process) are in-situ techniques for composite processing. Two major limitations of in-situ technique (Figure 2.19) are kinetic restrictions on volume fraction, size and shape of the reinforcements which are achieved through chemical reactions, and thermodynamic restrictions on the nature of the reinforcement phase and composition that can form in a given system [65].

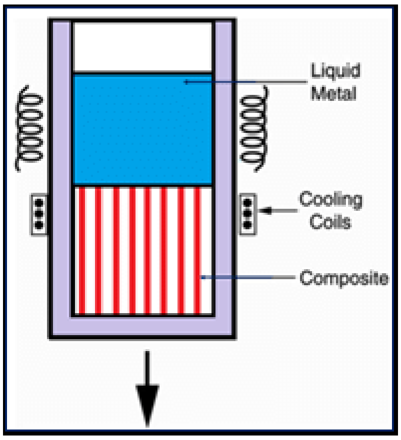

Figure 2.19 : Schematic of directional solidification process to obtain in situ composites [68].

2.4.3 Production methods of ternary boride composites

According to the ternary phase diagram, it was found that during sintering, the enhancement of the reaction between a binary boride and metallic elements results in a novel liquid-phase sintering technique of boride base cermets along with the in-situ reacting formation of ternary borides in a metal matrix.

In this method, at higher temperatures prior to liquid formation, a ternary boride is formed at the contacting points of the initial powders by solid-state reactions. At this stage which is crucial during the sintering process, a quasi-eutectic reaction between the ternary boride and the metal matrix leads to the formation of a eutectic liquid. Consequently, considerable densification was appeared due to the particle rearrangement and solution/reprecipitation of the ternary boride. Finally, the produced sintered compact had the two-phase structure of the ternary boride and the metal matrix.

Liquid phase sintering is another type of sintering which involves the formation of a liquid phase to enhance sintering kinetics. This type of sintering was applied on a compact with a low melting constituent and heated above the melting point of this constituent. Other types such as spark sintering, microwave sintering, and laser sintering are also used for specific applications. The Metal Injection Molding (MIM), which is a processing way for the production of complex shapes and high-performance components, has increased the P/M products remarkably.

2.5 Combustion Synthesis (CS, Self-propagating High-temperature Synthesis SHS) Method

Conventional synthesis methods of ceramics suffer from their limitations in large-scale production because of their requirement for high temperature furnaces and long processing times. In 1970s, the Soviets tried to overcome these shortcomings of conventional methods to achieve high productivity using alternative cost effective techniques. These methods include gas phase plating, low cost plasma, shock wave compression and also a novel method named self-propagating high-temperature synthesis. The spontaneous propagation of combustion wave through reactants resulted in exothermic reaction and production of ceramics and refractory compounds by SHS method. This method provides advantages such as lower energy consumption, lower process time, large-scale products and simplicity in operation [66].

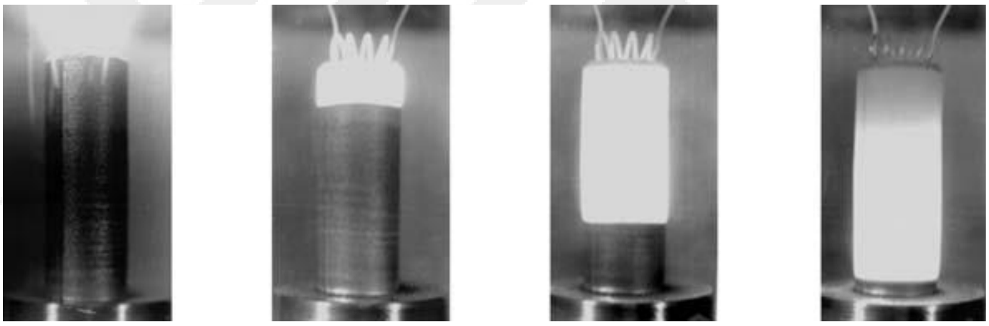

Figure 2.20 : Combustion synthesis process [66].

2.5.1 History of SHS

As the electrical current provided by batteries was used by Humphry Davy to isolate alkali metals from their compounds, the metallothermic reaction was developed for the first time in early 19th century in order to liberate metals from their compounds by using alkali metals in succession. In 1824, the Swedish chemist Jons Jakob Berzelius found that the combustion reaction of zirconium can be ignited even below room temperature to form zirconium oxide. It was probably the first production of a ceramic refractory material by combustion method. When the Aluminium ingot was produced by French chemist Henri Saint-Claire Deville through the heating of $AlCl_3$-NaCl with metallic sodium in the 1850s; German metallurgist Hans Goldschmidt used aluminium powder for fabrication of chromium and manganese in 1892 following the developments in industrial scale production of Aluminium as reducing agent. Also metallothermic method was used to prepare uranium by magnesium reduction of UF4 during World War II in order to produce atomic bomb by the US. The Luxemburg metallurgist Wilhelm Kroll (1889-1973) used the magnesiothermic reduction of $TiCl_4$ compound to fabricate pilot-scale metallic titanium [10].

American scientists such as Alexander and Walton have used combustion synthesis for producing nitrides of alkali metals, refractory coatings and ceramic-metal composites in the 1940s and 1950s. It was also found that aluminium phosphide can be produced by inserting of magnesium ribbon in the mixture of aluminium and phosphorus during a self-propagating process. In 1964, Krap reported that a self-sustained exothermic reaction can be ignited by passing electrical current through a powder mixture in a press die. Combining exothermic reactions with pressing is a suitable methode to produce intermetallic-based compounds because of providing sufficient required heat for the initial charge and obtaining produced compounds in desired shapes.

A real history of SHS is accompanied by the discovery of the so-called solid flame. The mechanism of combustion was described in the gasifying condensed systems such as explosives, gun powders, and solid propellants in the 1960s. The authors have discussed the role of the gasification in combustion to verify the hypotheses through gasless iron-aluminum thermite which is diluted with alumina. It was found that the gasless combustion was consistent with the predictions of the simplest combustion theory compared to the gasifying system. A search for new gasless systems has led to a remarkable discovery which was later termed as solid flame (SF) phenomenon. In the solid-state combustion or SF, the reactants and products remain in a solid state even at high combustion temperatures. Chemically inert powder of refractory metals (Nb, Ta, Mo, W, etc.) and nonmetals (B, C) are used as reactants to produce the refractory compounds (borides, carbides). This method which is known as Self-propagating High-temperature Synthesis (SHS) became an efficient way of producing refractory materials. The studies on the mechanism and theory of combustion in gasifying condensed systems, along with the experiments in the combustion of thermites in the low gasifying systems, have been significant in the development of SHS [67].

Nowadays, the self-propagating high-temperature synthesis (SHS) method is being used all over the world in synthesizing many advanced materials and also in various industrial applications. The process is also known with some other words such as combustion synthesis or gasless combustion, etc. Although, Goldschmidt (1898) is the originator of the aluminothermic process, a sub-group of SHS reactions, but the current interest in the topic is first related to the work of Merzhanov and his group in Russia, starting in the early seventies (Merzhanov and Borovinskaya 1975). The discovery of solid flame phenomenon resulted in SHS method. This discovery was made by A.G. Merzhanov, et al. in 1967 at the Research Center of the USSR Academy of Sciences which is located at Township of Chernogolovka, 30 miles north-east of Moscow.

One of their initial observations was the production of hard and relatively dense TiB_2-based alloy which was found to retain its original shape. Since this discovery revealed the potential of this simple process, the synthesis of a large number of ceramics, composites and intermetallics based on carbides, borides, nitrides and rare earth metal compounds has started to be expanded. An early pilot-scale production of refractory compound powders began with an output of 10-20 tons per year. For example, the production of titanium carbide could substitute for high-cost W based ceramics and diamond products. More than 30 different institutes and universities from all over the former U.S.S.R have been involved in the research and development about SHS since 1976. The publications and achievements in SHS field by Russia have attracted the international attention resulting in extensive research being conducted in Russia, the USA and Japan by the middle of the 1980s [68].

In the USA, the combustion synthesis research was performed in the DARPA (Defence Advanced Research Projects Agency) as a twoyear program (1984-1986). At the U.S. Army Material Laboratories, the production of the materials in Ti-C and Ti-B systems was studied while Rice et al. investigated the simultaneous reaction and densification of ceramic materials and composites. Kaedia and Moore have studied the different effective reaction parameters such as particle size, heating rate and atmosphere on final products during the SHS synthesis of Ni-Ti shape memory alloys.

In Japan, Koizumi and Miyamoto reported the synthesis of refractory ceramics such as TiB_2, TiC and SiC by the high pressure combustion sintering method at the Institute of Scientific and Industrial Research of Osaka University in 1984. This method was found to be useful in joining metals and ceramics. Odawara and his colleagues at the

Tokyo Institute of Technology have successfully used the combination of SHS and centrifugal methods in order to deposit corrosion-resistant coatings on the inner walls of pipes.

2.5.2 CS (SHS) principles

Considering the chemical nature of "Combustion Synthesis" process, there are three main types of reactions distinguished. The first one is "gasless combustion synthesis from elements" which can be described by the following equation:

$$\sum_{i=1}^{n} X_i^{(s)} = \sum_{j=1}^{m} P_j^{(s,l)} + Q \tag{2.6}$$

Where $x_i^{(s)}$ are elemental reactant powders , $P_j^{(s,l)}$ are products, Q is the heat of reaction, and the superscripts (s) and (l) indicate solid and liquid states, respectively. The most common reaction of this type is carburization of titanium:

$$Ti + C = TiC + 230\, kJ/mol \tag{2.7}$$

The second type is gas-solid combustion synthesis which includes at least one gaseous reactant in the combustion reaction:

$$\sum_{i=1}^{n-p} X_i^{(s)} + \sum_{i=1}^{p} Y_i^{(g)} = \sum_{j=1}^{m} P_j^{(s,l)} + Q \tag{2.8}$$

Where $Y_i^{(g)}$ represents the gaseous reactants (e.g. $N_2, O_2, H_2 and\ CO$), which, in some cases, penetrate the sample by infiltration through its pores. This type of combustion synthesis is called "infiltration (or filtration) combustion synthesis". The nitridation of titanium is a common example:

$$Ti^{(s)} + 0.5N_2^{(g)} = TiN^{(s)} + 335\, kJ/mol \tag{2.9}$$

The third type of combustion synthesis is "reduction combustion synthesis" which can be described by the following formula:

$$\sum_{i=1}^{n-q-r} (MO_x)_i^{(s)} + \sum_{i=1}^{r} Z_i^{(s)} + \sum_{i=1}^{q} X_i^{(s)} = \sum_{j=1}^{m-k} P_j^{(s,l)} + \sum_{j=1}^{k} (ZO_y)_j^{(s,l)} + Q \tag{2.10}$$

Where $(MO_x)_i^{(s)}$ is an oxide that reacts with areducing metal $Z_i^{(s)}$(e.g. Al, Mg, Zr and Ti), resulting in the appearance of another more stable oxide $(ZO_y)_j^{(s,l)}$, and reduced metal $M_i^{(s,l)}$. This reaction may be followed by the interaction of $M_i^{(s,l)}$with other elemental reactants $X_i^{(s)}$ to produce desired products $P_j^{(s,l)}$.

Therefore, the reduction combustion synthesis is a process that consists of two steps. The first step is a “thermite reaction”:

$$\sum_{i=1}^{n-q-r}(MO_x)_i^{(s)} + \sum_{i=1}^{r} Z_i^{(s)} = \sum_{j=1}^{k}(ZO_y)_j^{(s,l)} + \sum_{j=1}^{l} M_j^{(s,l)} + Q_1 \quad (2.11)$$

And the second step is the synthesis reaction from elements as follows:

$$\sum_{j=1}^{l} M_i^{(s,l)} + \sum_{i=1}^{q} X_i^{(s)} = \sum_{j=1}^{m-1} P_j^{(s,l)} + Q_2 \quad (2.12)$$

$$\sum_{j=1}^{l} M_i^{(s,l)} + \sum_{i=1}^{q} X_i^{(s)} = \sum_{j=1}^{m-1} P_j^{(s,l)} + Q_2 \quad (2.13)$$

With the total heat release of $Q = Q_1 + Q_2$. A common example for this kind of combustion reactions is as following equation (2.14) :

$$\begin{aligned} B_2O_3^{(s)} + 2Al^{(s)} + Ti^{(s)} \\ = Al_2O_3^{(l)} + TiB_2^{(s,l)} + 700\, kJ/mol \end{aligned} \quad (2.14)$$

2.5.3 Thermodynamical aspects of CS (SHS)

The reactions involved in SHS process have highly exothermic nature that ignition makes them to propagate and reach high temperatures in a short period of time. The required formation enthalpy during the propagation of adiabatic reaction wave and rising the temperature from 298 K to the adiabatic temperature, T_{ad}, is called $\Delta H_{reaction}$. The value of the enthalpy is equal to the standard enthalpy of formation of the product (ΔH_f, 298). The types of reactions in SHS processes are classified according to difference between the values of reaction’s adiabatic temperature (T_{ad}) and product’s melting temperature (T_m). There are three cases as follows:

$$\Delta H_{f,298} = \int_{298}^{T_{ad}} C_{p(product)} dT \qquad \text{if} \quad T_{ad} < T_m \quad (2.15)$$

$$\Delta H_{f,298} = \int_{298}^{T_{ad}} C_{p(product)}\, dT + \upsilon \Delta H_m \qquad \text{if} \quad T_{ad} = T_m \quad (2.16)$$

$$\Delta H_{f,298} = \int_{298}^{T_{mp}} C_{p(product)}\, dT + \Delta H_m + \int_{T_{mp}}^{T_{ad}} C_{p(liquid)}\, dT \qquad \text{if } T_{ad} > T_m \tag{2.17}$$

Although the T_{ad} for different compounds is available in literature but the calculated values are found to be different from the actual ones because the calculations predict the upper limit of T_{ad}. The linear correlation between ΔH_f, 298/C_p, 298 and T_{ad} shows the self-sustaining of the reactions. If the ΔH_f, 298/C_p, 298 ratio be lower than 2000 °C, the reaction would not propagate spontaneously [69].

2.5.4 Kinetics of SHS

Combustion wave theory is based on the characteristic parameters such as propagation rate, mechanism and attendant activation energy. The combustion wave can be considered as a plane of reaction propagating through the reactant mixture when it is initiated by an energy to increase the temperature of reactants above the ignition temperature. The characteristics of the combustion phenomenon such as heat evolution (ϕ) and also the temperature distribution were illustrated in Figure 2-21.

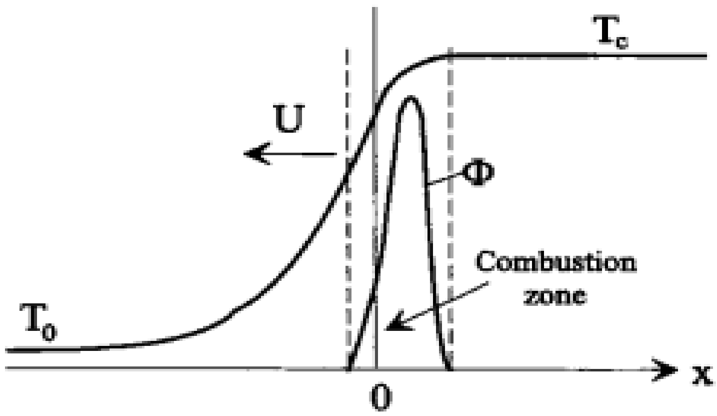

Figure 2-21 : Heat evolution and temperature distribution during combustion process [69].

Azatyan et.al have described an expression based on an elementary model for the rate of propagation of a planar combustion front travelling through a cylindrical compact placed in a reaction chamber. In this model, the calculations are performed assuming a uniform radial distribution or a planar front. It was assumed that the heat loss from the body occurs through radiation and conduction. Then the rate of propagation of a flat combustion zone is calculated from the utilization of Fourier's one-dimensional heat equation [69].

$$C_p\rho\frac{\partial T}{\partial t} = k\frac{\partial^2 T}{\partial x^2} + Q\rho\emptyset(T,\eta) - 2\frac{\alpha}{r}(T - T_0) - 2\epsilon\frac{\sigma}{r}(T^4 - {T_0}^4) \tag{2.18}$$

$$\emptyset(T,\eta) = \frac{\partial\eta}{\partial t} \tag{2.19}$$

where C_p is the heat capacity, ρ, the density, T, the temperature, T_o, the ambient temperature, η, the fraction reacted, t, the time, k, the thermal conductivity, x, the axial distance, Q, the heat of reaction, α, the heat transfer coefficient, r, the sample radius, ε, the emissivity coefficient, σ, the Stefan-Boltzman constant, and Ø, the kinetic function.

If the heat losses and the transient effects be neglected, the above equation can be rewritten as follows:

$$C_p\rho\frac{\partial T}{\partial t} = k\frac{\partial^2 T}{\partial x^2} + Q\rho\emptyset(T,\eta) \tag{2.20}$$

The solution of the above equation is as follows:

$$u^2 = \sigma_n\frac{k}{Q_p}\frac{RT_{ad}^2}{E}K_0\pi r^2 \tag{2.21}$$

Where σ_n is a constant depending upon the order of the reaction, u is the velocity, E is the activation energy and K_0 is a constant. The activation energy can be found from the graph of $\ln(u/T_{ad})$ versus $1/_{T_{ad}}$.

The classical combustion theory emphasizes on the prediction of macroscopic characteristics such as combustion front velocity and stability nature. However, the principle issues of microstructural aspects of the combustion process are also needed for further development in this field.

2.5.5 CS (SHS) technologies

The wide spectrum of powders, compacts and coatings is possible to be obtained by known SHS processing techniques which are divided into six types: SHS process of manufacturing the blanks and powders, SHS sintering, SHS powder compacting, SHS metallurgy, SHS welding and the production process of the SHS coatings.

2.5.5.1 SHS process of manufacturing blanks and powders

The SHS technique for manufacturing powders and blanks is the most simple and common method among all kinds of techniques. Since 1972, the mass production of SHS synthesis method has been performed in a steel cylinder with two locks equipped with the reactor gas inlet/outlet systems, water cooling and ignition, check and remote control of the SHS process. This reactor design makes it possible to synthesize in vacuum or in the medium of inert and reacting gases under the pressure of up to $2.5*10^7$ Pa.

At the present time, the SHS process is used to produce more than 500 materials: carbides, silicides, nitrides, hydrides, carbonitrides, chalcogenides, oxides, etc.

2.5.5.2 SHS-sintering

The high temperatures achieved in self-propagating high-temperature synthesis method is high enough to heat the products to be sintered but decrease their strength. Therefore, the maximum compression strength of 10^7 Pa for the products can be achieved in the reactors at pressures of $P=10^5$ to 10^7. For performing this kind of synthesis which is called gas-static version, some special apparatuses contributing a high-strength reactor and a device for making gas pressure inside the reactor were manufactured in the USSR between 1975 and 1979.

Combustion synthesis, the Self-propagating High temperature Synthesis (SHS)-type, must be carried out by highly exothermic reactions to be self-sustaining. In a typical combustion synthesis reaction, the mixed reactant powders are pressed into a pellet with a certain green density, then the ignition is performed either locally at one point (propagating mode) or by heating the whole pellet (simultaneous combustion mode). The different ignition sources include laser irradiation, radiant flux, resistance heating coil, spark, chemical oven, etc. The ignition temperature, T_{ig}, is the point where the exothermic reaction initiated and generated heat, and combustion temperature, T_{c}, is the maximum temperature during the combustion process.

The combustion synthesis has some advantages compared with conventional processing methods. The production of high-purity products is possible due to the volatilization of low-boiling-point impurities at generated high temperatures, therefore there is not any requirement for expensive processing facilities and equipments due to the exothermic nature of the process. The processing time duration which is short results in low operating and processing costs, the high thermal gradients result in the formation of non-equilibrium phases, and rapid cooling rates result in the formation of inorganic materials which all are synthesized and consolidated into a final product in a single step by using the chemical energy of the reactants. Because of these advantages of the process, it has been possible to produce novel and improved materials with enhanced mechanical, electrical, optical, and chemical properties.

2.5.5.3 SHS compaction

The SHS process can be modified by combining it with mechanical compacting such as: SHS compaction, SHS with explosion treatment, SHS rolling, and SHS extrusion. In SHS compaction which is used most frequently in USSR, the initial mixture is placed under the press punch. The samples such as powder mixtures of Ti, Cr, Ni, Mo, Cu with C and B are ignited, kept under pressure and compacted by a hydraulic pressing. The porosity of the synthetic solid tool materials does not exceed 0.5% and the maximum hardness value is in the range of 86-93 HRA and the bending strengths are not more than$20*10^7$ Pa. This method was used to obtain the rollers for rolling metals, dies, press-tool equipment and cutting plates in industrial scales. During SHS extrusion, the long items of molybdenum disilicide hard alloys in the form of the shaped bars are manufactured. The products can be applied for electric spark alloying and production of high-temperature heaters. In SHS explosion treatment, the compact samples were obtained in the shape of bars, pipes, and disks which are made of TiC, TiB_2, other compounds of transition metals and hard alloys of TNM-20 and TNM-50.

2.5.5.4 SHS metallurgy

The SHS metallurgy is used to obtain pore-free castable refractory materials, items and coatings. In this method, initial mixtures of metal and nonmetal oxides with reducing agents of Al and Mg are used to provide combustion temperatures higher than melting point of final products. In this case, conducting the reactions at atmospheric pressure, causes a significant amount of material loss. In order to suppress the spread of these kinds of combustion syntheses, high pressure reactors or centrifugal machines must be used.

2.5.6 Classification of SHS products

The production of several types of compounds such as carbides, borides, intermetallics, silicides, aluminides, composites, nitrides, hydrides, and oxides by using SHS and VCS methods is reported in the literature.

Merzhanov and Borovinskaya, 1972; Hardt and Holsinger, 1973 are the first scientists who worked on the production of relatively pure ZrB_2, TiB_2, HfB_2, and MoB. Following that, Holt et al., 1985; Rice et al., 1987; Mei et al., 1992; Fu et al., 1993a; Li, 1995 have observed that most of the metal borides can be produced by using combustion synthesis in SHS mode. The other combustion synthesized borides include TiB, TaB_2, LaB_6, and NbB_2. This method primarily was examined using pure elements as raw materials for the production of transition metal borides and carbides such as TiB_2 and TiC.

2.5.6.1 Products of thermite-type SHS

There are various products that can be obtained by thermite-type self-propagating reactions. The magnesiothermic processes are suitable due to the formation of MgO that can be leached easily in the final product. Because of the high heats of formation for this kind of processes, the products are completely molten at combustion temperatures. It is reported that the centrifugal casting is used to produce oxide-carbide ceramics by the following reaction: $MO_x + Al + C \rightarrow MC_y + Al_2O_3$. In general, the carbides of titanium, chromium, molybdenum and tungsten are synthesized with an alumina melt in the combustion wave in the systems of Cr_3C_2-Al_2O_3, WC-Al_2O_3, (Ti, Cr)C-Al_2O_3 and MoC-Al_2O_3. Also by using Fe-group metal oxides such as NiO, CoO and Fe_2O_3, ceramic composites containing (Ti,Cr))C-Ni as a metal binder and the carbide phase can be produced. The lighter oxide phase can be separated from the cermet by centrifugal acceleration. For example, the acceleration of 150 g is sufficient to separate MoC from Al_2O_3 while 300 and 1000 g are needed to separate WC-Co cermet and WC from Al_2O_3, respectively. An interesting application of a thermite-type SHS reaction with centrifugal overload is the fabrication of multilayered composite pipes. A simple composition of Fe_2O_3+2Al was used to produce an Al_2O_3/Fe lining inside the steel pipe. More complex structures can be formed by using multicomponent mixtures like Ti-C-Ni-Al-O reaction system which results in multiphase gradient layers. It is reported that the production of steel pipes with a lining of alumina-zirconia ceramic layer by using reaction system of Fe_2O_3+Al+Zr+additives is possible.

2.5.7 Phenomenology of combustion synthesis

The characteristic features of combustion synthesis are process variables such as combustion wave velocity and temperature-time history. The combustion front velocity changes with the changes of the combustion temperature. The process parameters, for example, green mixture composition, dilution, initial density, gas pressure and reactant particle size affect the combustion velocity, the temperature-time profile and the synthesis process.

2.5.7.1 Thermodynamic considerations

Thermodynamic calculations were used to determine the adiabatic combustion temperature as well as the estimation of equilibrium phases and compounds. The agreement between the experimental and theoretical values is obtained when the full conversion has been realized. These calculations help to determine the equilibrium products in order to illustrate the possibilities for controlling the synthesis process. The correlation of these calculations with the equilibrium phase diagram for each system establishes a basis for predicting possible chemical interactions and limits of combustion. As an example, the thermodynamical calculations for the equilibrium combustion temperature and product composition of a three-component (Ni-Al-NiO) reduction-type system, show that the maximum adiabatic temperatures are 3140 K and 3000 K for the 2Al+3NiO and 5Al+ 3NiO green mixtures with reaction heats of $Q = 810\ kCal/g$ and $Q = 860\ kCal/g$, respectively. The lower adiabatic temperature can be attributed to the dissociation of formed nickel aluminides and the consequent reduction. The thermodynamic calculations reveal the presence of a product in gas phase for initial mole fractions of Al from 0.3 to 0.7. The increasing nickel amount in the green mixture reduces adiabatic temperature and promotes the formation of nickel aluminides. Therefore, the experimental studies have shown that changes in the initial composition of the green mixture result in a wide variation of synthesis conditions and products that provide useful information for controlling the process [70].

2.5.7.2 Dilution

The most effective way which is commonly used to modify the synthesis conditions is to dilute the initial mixture with a chemically inert compound. There is a correlation between the amount of dilutions and combustion temperature in which the increasing this amount results in the decrease in combustion temperature and velocity. Besides the amount of diluent, the particle size of this inert compound also influence the combustion characteristics. For example, in the Ti-C system, the combustion velocity is a function of dilution for different TiC particle sizes. For the smaller particles (d_{TiC} < 100 um), the combustion velocity decreases. However, for the larger TiC particles (d_{TiC}> 1000 um), velocity remains constant due to the incomplete heating in the combustion wave. Moreover, dilution is an effective way of increasing the final extent of conversion for some gas-solid systems especially when the melting of the reactants and products occurs.

From the experimental studies about the effect of dilution on the combustion conditions, it can be concluded that for a wide range of systems, the combustion front velocity and temperature decrease with increasing dilution.

The dilution depends on the T and U parameters which are usually accompanied by the phase transition processes occurring in the combustion wave (for example melting, dissociation and evaporation).

When the combustion temperatures are higher than the melting points of the reactants and products in gas-solid systems, dilution is an effective way for increasing final conversion, by avoiding the effects of melting, particle coalescence and the subsequent reduction of sample.

2.5.7.3 Density of green mixture and initial gas pressure in gas-solid systems

In gas-solid system, the effect of green density and initial reactant gas pressure on the combustion synthesis process is important. Different regimes may occur depending on the initial sample porosity and reactant gas pressure. There are two identified types of reaction propagation, including with and without reactant gas infiltration to the combustion front. The type of propagating wave with infiltration of reactant gas includes three types of surface combustion and layer-by-layer combustion with either incomplete or complete conversion.

2.5.7.4 Particle size

The dependencies of combustion velocity, temperature and conversion as functions of particle size are described experimentally. The particle diameter as an important parameter influences the process, since the combustion velocity decreases with increasing particle size. In the solid-flame systems, the propagation velocity and temperature are independent of particle size of the initial reactants. In the systems with reactions reaching to the high adiabatic combustion temperatures that results in melting of one reactant, the large particle size influences the velocity of propagating wave. However, rather smaller particle size has no effect on the combustion phenomenon.

The other combustion conditions that can influence the combustion synthesis process include the ignition conditions, initial temperature of the green mixture and sample dimensions.

2.5.8 SHS production of hard alloys

Some modifications which were applied on the SHS synthesis method such as SHS-pressing, in which the combustion and densification of product occurs in one stage, were found to be the most efficient ways to prepare large scale hard alloys.

For example, a hard alloy of TN-20 grade (79 wt.% TiC, 16 wt.% Ni, 5 wt.% Mo) which is very popular in Russia was manufactured by pilot-scale batches of SHS TiC. The SHS TiC was synthesized in two ways: The first one was through the reagents of Ti and C (synthesis from elements), while the second one was through the following reaction: $TiO_2+2Mg+C=TiC+2MgO$.

The first product was conglomerates of TiC single crystals that exhibited higher wear resistance and purity due to self-purification at the combustion temperatures about 2800-3000 ˚C but it presented larger particle size compared to that of conventionally produced materials. In the SHS synthesis of TiC powders, it was found that using titanium particles (as reagent) with dendrite structure and minimum size would yield the finest TiC powders. But, the best TiC powders were produced by using SHS with a reduction stage. These powders were reported to become finer than conventionally produced ones and were rather uniform that didn’t require additional grinding. The pilot batches of cutting plates are made of TN-20 hard alloys. The cutting plates made of TiC which are manufactured by SHS method including a reduction stage exhibit the longest service life. During tests on milling gray cast iron in different modes, SHS produced TiC-based cutting plates have presented stability similar to the commercially produced TN-20 alloy plates. Therefore, SHS can be successfully used for manufacturing TiC powders for producing a number of hard alloys by conventional methods [71].

3. EXPERIMENTAL PROCEDURE

The experimental procedure for this dissertation covers studies on three sections for ternary Mo-Ni-B, Mo-Fe-B, and Mo-Co-B systems. Each one includes the preliminary experiments; FactSage thermodynamic calculations, the effect of using different diluents, choosing an optimum amount of raw materials, the combustion synthesis (SHS) of the alloys, metallographic preparation of the obtained alloys, and the characterization studies. The characterization sub-section discusses the crystal structure, microstructure and elemental compositions of the products using X-ray diffraction, SEM/EDS microscopy, and atomic absorption analysis methods. Different testing methods such as microhardness, wear resistance test and micro-indentation of the obtained alloys provide the mechanical properties of the SHS alloys. The comparison of wear resistance between the Mo_2NiB_2 containing SHS alloys and WC-Co cermets reveals their properties for the specific applications. Finally, the influence of heat treatment and arc melting on the microstructure, phase composition and hardness of the selected SHS synthesized alloys were studied.

3.1 Raw Materials

In all the experiments, the metal oxides, boron trioxide, and Al were used as raw materials to produce ternary boride containing composites through thermite-type SHS process. Since three Mo-Ni-B, Mo-Fe-B, and Mo-Co-B ternary systems present high adiabatic temperatures and high materials loss during the combustion reactions, the functional additives such as Al_2O_3 in the raw materials mixture was examined to suppress the released high heat energies. In the present work, the high purity metal oxides and the boric acid were supplied from Alfa Aeser Company and also Eti Maden, respectively. The applied metal oxides were MoO_3, NiO, Fe_2O_3, Co_3O_4, Cr_2O_3, V_2O_5, MnO_2, Ta_2O_5, and Nb_2O_5. In all the thermite-type SHS reactions, Al was applied as a reducing agent. Table 3.1 presents the purity and particle size of raw materials.

Table 3.1 : The purity and particle size of raw material powders.

Raw materials	Purity, %	Particle size
MoO_3	99,5	< 60 µm
NiO	99,0	< 40 µm
Al	99,7	< 60 µm
Fe_2O_3	99,6	< 50 µm
Al_2O_3	99,0	< 50 µm
Co_3O_4	99,7	-400 mesh
Al_2O_3	99,0	< 50 µm
Cr_2O_3	98	-325 mesh
V_2O_5	99,2	< 45 µm
MnO_2	99	< 45 µm
Ta_2O_5	99	-100 mesh
Nb_2O_5	99.5	-100 mesh

Boron trioxide powder was prepared by the calcination of boric acid in the Ni plate at 1000 ˚C. The produced glassy B_2O_3 crystals were milled and dried to obtain whitish pure B_2O_3 powders. Figure 3.1 presents the crystal structure of the obtained B_2O_3.

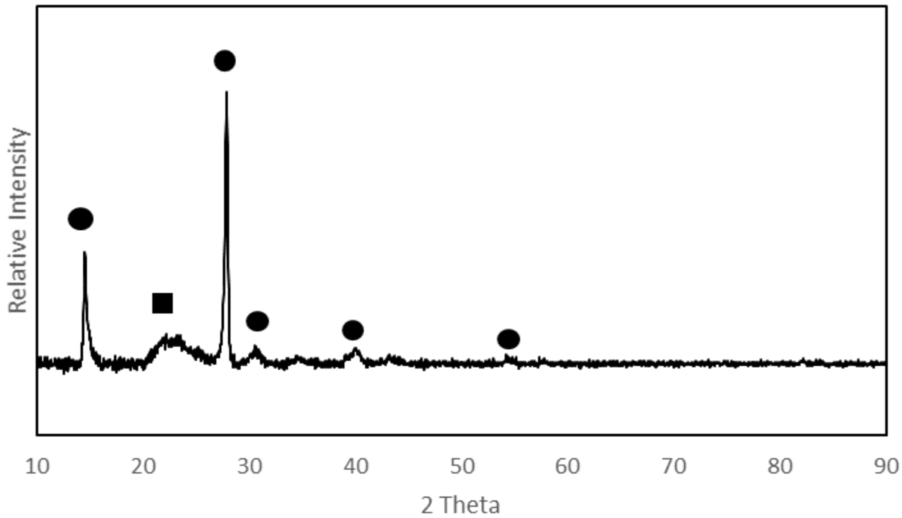

Figure 3.1 : X-ray diffraction analysis of the synthesized B_2O_3 powder (●B_2O_3 (06-0297), ■ B).

3.2 Thermodynamic Calculations

Usingthermodynamical simulations reduces the number of experiments. The advanced "Equilib" module of FactSage 7 was used to predict the produced phases and T_{ad} values. The prediction of products' composition and concentrations was evaluated by using the Gibbs energy minimization method in "Equilib" module. Adiabatic temperature (T_{ad}) is the temperature that occurs during a complete combustion process without any heat transfer or changes in kinetic or potential energy.

In the first series of experiments, the effect of different diluents such as Al_2O_3, excess Al, and B_2O_3 on reducing the adiabatic temperature was studied. In the second series, the estimation of the possible produced species enables the choosing an optimum amount of raw materials. In the calculations, the reactions were assumed as adiabatic ($\Delta H=0$) and the initial reaction temperature was selected as 25 °C. SGTE and FT oxide databases were chosen to calculate solid/liquid alloys and slags in the products, respectively. All gas and other stoichiometric solid phases were selected from the Fact PS database.

In the Mo-Ni-B ternary system, the metal oxides were equilibrated with Al using Equation (3.1) In the thermodynamical calculations by FactSage software, different ratios of MoO_3, NiO, B_2O_3, Al and Al_2O_3 were used to study the effect of different SHS reaction conditions on the resultant products.

$$\begin{gathered}\upsilon_1(\mathrm{MoO_3} + 2\mathrm{Al}) + \upsilon_2(\mathrm{NiO} + \mathrm{Al}) + \\ \upsilon_3(\mathrm{B_2O_3} + 2\mathrm{Al}) + \alpha\mathrm{Al_2O_3} \rightarrow \mathrm{Mo_xNi_yB_z} + \beta\mathrm{Al_2} + \mathrm{Q}\end{gathered} \tag{3.1}$$

Whereas, the υ_1, υ_2, υ_3, and α characters identify the weight percentage of raw materials. Also, the x, y and z letters refer to produced Mo, Ni, and B elements, respectively.

In the Mo-Fe-B ternary system, the metal oxides were equilibrated with Al using Equation (3.2). In the thermodynamical calculations by FactSage software, different ratios of MoO_3, Fe_2O_3, B_2O_3, Al and Al_2O_3 were used to study the effect of different SHS reaction conditions on the resultant products.

$$\begin{aligned}&\upsilon_1(\mathrm{MoO_3} + 2\mathrm{Al}) + \upsilon_2(\mathrm{Fe_2O_3} + 2\mathrm{Al}) + \\ &\upsilon_3(\mathrm{B_2O_3} + 2\mathrm{Al}) + \alpha\mathrm{Al_2O_3} \\ &\quad \rightarrow \mathrm{Mo_xFe_yB_z} + \beta\mathrm{Al_2O_3} + \mathrm{Q}\end{aligned} \tag{3.2}$$

Whereas, the υ_1, υ_2, υ_3, and α characters identify the weight percentage of raw materials. Also, the x, y and z letters refer to produced Mo, Fe, and B elements, respectively.

In the Mo-Co-B ternary system, the metal oxides were equilibrated with Al using Equation (3.3). In the thermodynamical calculations by FactSage software, different ratios of MoO_3, Co_3O_4, B_2O_3, Al and Al_2O_3 were used to study the effect of different SHS reaction conditions on the resultant products.

$$v_1(MoO_3 + 2Al) + v_2(Co_3O_4 + Al) + v_3(B_2O_3 + 2Al) + \alpha Al_2O_3 \rightarrow Mo_xCo_yB_z + \beta Al_2O_3 + Q \quad (3.3)$$

Whereas, the υ_1, υ_2, υ_3, and α characters identify the weight percentage of raw materials. Also, the x, y and z letters refer to produced Mo, Co, and B elements, respectively.

Table 3.2 presents the calculated enthalpy and adiabatic temperature of aluminothermic reactions of different metal oxides. In the case of Cr, V, Mn, Ta, and Nb alloying elements addition into the ternary systems, the following table presents the reactions of Cr_2O_3, MnO_2, V_2O_5, Ta_2O_5 and Nb_2O_3 oxides with Al.

Table 3.2 : The enthalpy and adiabatic temperature for the experimental reactions.

Reaction	ΔH, kj	Adiabatic Temperature, °C
$0.5Fe_2O_3 + Al = Fe + 0.5Al_2O_3$	-424.96	2851.3
$0.38Co_3O_4 + Al = 1.14Co + 0.5Al_2O_3$	-503.213	2923.5
$1.5NiO + Al = 1.5Ni + 0.5Al_2O_3$	-477.47	2908.9
$0.5MoO_3 + Al = 0.5Mo + 0.5Al_2O_3$	- 465.27	3397.7
$0.5B_2O_3 + Al = B + 0.5 Al_2O_3$	- 201.9	1972.0
$3/10V_2O_5 + Al = 6/10V + 1/2Al_2O_3$	- 661	2864.48
$1/2Cr_2O_3 + Al = Cr + 1/2Al_2O_3$	-545.378	2027.26
$3/4MnO_2 + Al = 3/4Mn + 1/2Al_2O_3$	-725.563	2186.83
$3/10Ta_2O_5 + Al = 6/10Ta + 1/2Al_2O_3$	-500.303	2497.78

3.3 Combustion Synthesis of Ternary Alloys

The SHS experiments under normal gravity were performed at process metallurgy pilot based laboratories. Figure 3.2 illustrates the schematic of the SHS experimental set-up equipment.

The raw materials mixtures with the calculated amounts were weighed by using a high sensitivity scale. Afterwards, raw materials mixture was placed in the metallic container of the WAB turbula mixer to mix the powders homogeneously for 15 min. The mixed powder was placed in etuve to be dried for 30 min. Then, the prepared raw materials were placed in a copper crucible and were compacted. The height, inner and outer diameters of the copper crucible used in the experiments were 140 mm, 40 mm and 50 mm, respectively.

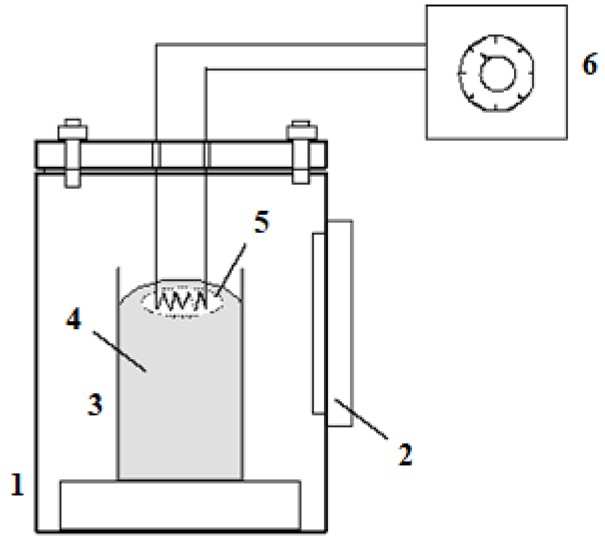

Figure 3.2 : Schematic of SHS set-up, 1.steel reactor, 2. Window, 3. Copper crucible, 4. SHS raw material mixture, 5. Resistance wire, 6. Power supply.

The electric current passes through the copper wire into the tungsten filament which placed at the top of the mixture. The electricity triggers the SHS reaction by heating the mixture under an ambient environment. The combustion flow travels spontaneously from top to the end of the mixture resulting in a melted product. The obtained alloy and slag were separated while the combustion extinguishes and the mixture was let to cool down to the room temperature. Due to the earth gravity, the metallic alloy which is heavier than the slag gathered at the bottom of the copper crucible.

The parameters such as different shapes, dimensions, and materials of crucibles were observed to determine how they influence the combustion process and final products. Table 3.3 presents the typical features of the applied crucibles.

Table 3.3 : Characteristics of crucibles applied in combustion process.

Crucible	Inner diameter	Outer diameter	Height
Copper 1	4 cm	6 cm	14 cm
Copper 2	6 cm	8 cm	7 cm
Magnesia	4.5 cm	5.5 cm	9 cm
Schamot (conical)	Upper side: 6 cm Bottom side: 4 cm	8 cm	7 cm

The images of the obtained SHS-synthesized alloys are presented in Figure 3.3 which reveals the effect of reducing agent, crucible type, composition, and compaction on the appearance of the as-cast alloys. The obtained alloys were prepared metallographically to conduct further microstructural analysis and mechanical testing.

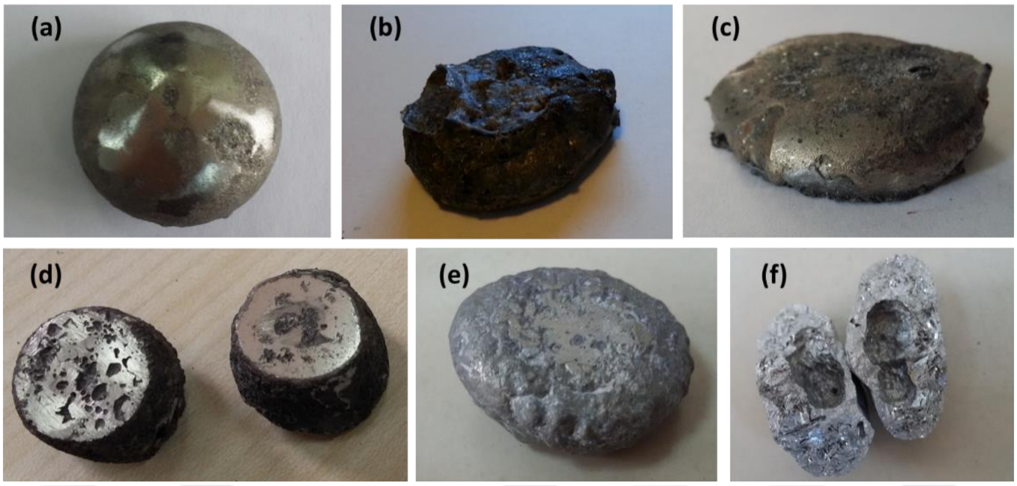

Figure 3.3 : The obtained SHS-synthesized Mo-Ni-B alloys, a) using B in initial mixture, b) using copper crucible, c) using pre-compaction, d) using schamot crucible, e) Mo-Co-B alloy, and f) cross-section of the Mo-Co-B alloy.

During the SHS experiments, the controlling of combustion reaction parameters is necessary. These parameters include the burning velocity (mm/s) thatidentifies the duration time of propagating wave through the height of crucible which means from the top of the reaction mixture to the bottom of the crucible.

The SHS experimental parameters include the yield of target (η_{ingot}), materials loss (η_{loss}), and combustion velocity (mm/s). The reaction velocity was measured by dividing the height of the powder mixture in the crucible to the reaction duration time. The material loss shows the sputtering and gasification occurred during the combustion process. This value is calculated from subtracting the product weight (means both alloy and slag) from the initial raw materials weight. The yield of target shows the deviation of the actual product weight from the estimated weight of alloys. The overall equations for calculating the SHS parameters are as follows (3.4), (3.5), (3.6):

$$Burning\ velocity, U = {}^{h}/_{t}\ (cm/s)\ 3 \tag{3.4}$$

$$Material\ Loss, \eta_{loss} = \left[{}^{(M_0 - M)}/_{M_0}\right] \times 100\ (\%) \tag{3.5}$$

$$Yield\ of\ target, \eta_{ingot} = \left({}^{m}/_{m_c}\right) \times 100\ (\%) \tag{3.6}$$

Where h is the height of initial powder mixture; t, the duration time of combustion wave; M_0, the weight of initial material; M, total obtained product weight; m, the produced alloy weight; m_c, the estimated metal weight.

The distribution of elements $[D_{Me}]$ in wt% is calculated using the following equation (3.7):

$$[D_{Me}] = \frac{[\%Me] \times Aloy\ wt.}{\%Me\ Raw\ materials \times Raw\ materials\ wt.} \times 100 \tag{3.7}$$

Where $[D_{Me}]$ is the distribution of Me element in product, [Me%] is the weight percentage of Me element in the alloy.

3.4 Characterization Investigations of the CS (SHS) Products

The metallic part was separated from the slag when the reactions completed. The polished surface of all the alloys was analysed by the XRF method to detect the impurities and concentration of elements. Thermo Scientific XRF analyzing instrument with copper anode X-ray tube was used working under 50 kV, 100 uA, and 2 W conditions. Five points on the surface area of each sample were analyzed to ensure accuracy. Before analyses, the slag samples were ground using a vibratory disc mill to obtain powder samples with high homogeneity. Helium gas was used to detect the low atomic number elements. The duration times of 60 seconds and 90 seconds were used to analyze the alloys and slags, respectively.

The samples were ground or cut into small parts for chemical analysis. In our studies, Perkin Elmer Analyst 800 atomic absorption spectrometry (AAS) was used to detect Al, Cu, and B elements in the products. The technique uses the principle that free gaseous atoms generated in an atomizer vessel absorb radiation at a specific frequency. Atomic absorption spectroscopy quantifies the absorption of the ground state atoms in the gaseous state. The atoms absorb ultraviolet or visible light and make transitions to higher electronic energy levels. The amount of absorption shows the analyte concentration.

X-ray diffraction (XRD) investigations of the as-cast alloys were performed using a PANalytical PW3040/60 with a Cu-Kα radiation in the 2Theta range of 20-90°. The international Center for Diffraction Data (ICDD) powder diffraction files were utilized for the indentification of crystalline phases. The phase percentages of selected samples were identified by the semi-quantitative Rietveld method.

Each sample was cut and then mounted for grinding with the SiC papers (180-400-600-800-1000-1200 grits). Then, they were polished by diamond suspensions with particle sizes of 3 and 1um. The elemental analysis and mapping of bulk as-cast alloys were carried out using Jeol JSM-840 Scanning Electron Microscope (SEM) coupled with an energy-dispersive spectrometer (EDS-Oxford Instruments Xmax N). Image analyzing method (ImageJ software) was used to measure the reinforcement and matrix ratios in the higher magnification SEM images (x500).

3.5 Mechanical Testing of the SHS Products

Shimadzu HMV Microhardness Tester was used under a load of 5 N to conduct Vickers microhardness testing of the SHS samples. Microhardness test result for each sample includes the arithmetic mean of ten successive indentations and standard deviations. The samples were also subjected to reciprocating sliding wear tests at room temperature in a laboratory atmosphere by a Tribotech Oscillating Tribotester using a 6 mm alumina ball under an applied force of 4 N, with a sliding speed of 6 mm/s and a stroke length of 2 mm for a total sliding distance of 20 m. Wear tracks of the worn samples were analyzed using the Hitachi TM-1000 SEM.

Wear volume loss (WVL=$(\pi/4)$*width*depth*length) values are the arithmetic mean of three different measurements for each sample. Relative wear resistance values are the ratio of highest wear volume loss to the wear volume of each sample.

The depth-sensing indentation study was conducted using CSM International MHT SN 06-0212 with a Vickers indenter at a peak load of 100 N. The applied load-penetration depth curves were prepared at the loading and unloading rate of 500 mN/min for the holding time of 2 s at the peak load. Also, the elastic modulus of the samples was measured using the Oliver-Pharr method (Oliver and Pharr, 1992).

3.6 Annealing of the SHS Alloys

The samples were placed in a tube furnace under argon flow to perform annealing. Figure 3.4 presents the schematic of the annealing set-up. Two different as-cast alloys were annealed to discuss the heat treatment effect on the composition. Also, the crystal structure, microstructure, and hardness of the annealed alloys were studied using XRD, SEM, and Vickers indentation.

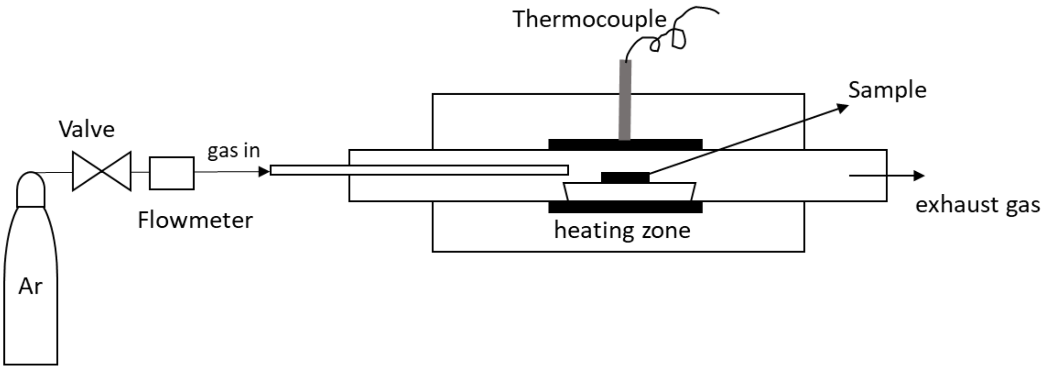

Figure 3.4 : Schematic of annealing set-up.

3.7 Arc Melting of the SHS Alloys

The remelting process was carried out in a high purity argon atmosphere with high vacuum values up to 10^{-6} mbar by arc melting while the contact of W electrode with a water-cooled copper plate generates the arc. The as-cast samples were placed in an Edmund Buhler MAM-1 arc furnace to perform refining process as shown in the figure. In this dissertation, two different compositions were remelted in an arc furnace to study the compositional and microstructural changes.

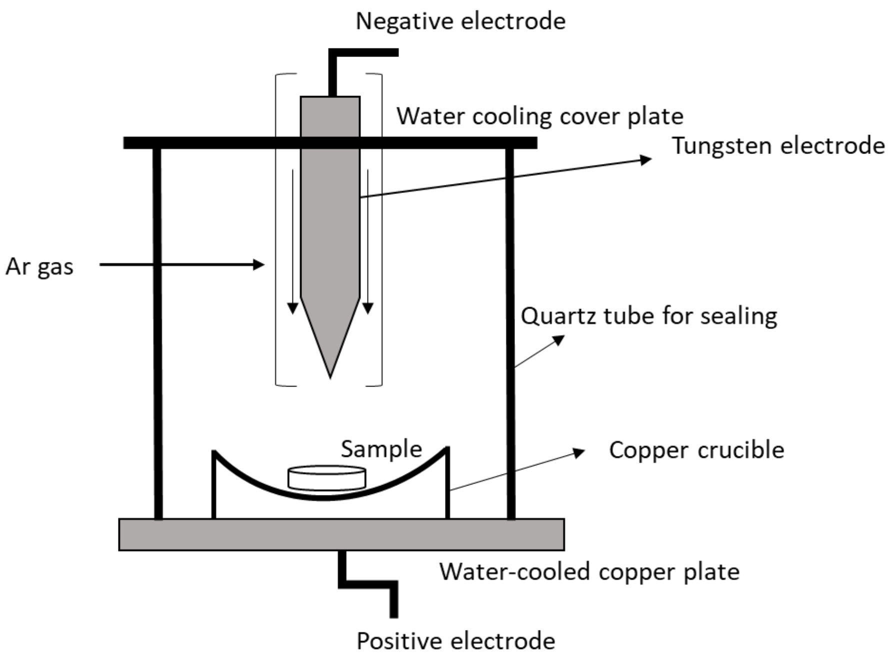

Figure 3.5 : Chematic of vacuum mini arc melter.

4. RESULTS AND DISCUSSIONS

This chapter of the dissertation includes three main sections which explain and discuss the experimental results of the combustion synthesis of three different ternary boride (i.e. Mo_2NiB_2, Mo_2FeB_2 and Mo_2CoB_2) based alloys. The first part discusses the synthesis parameters such as diluent and the ratio of raw materials while the second part investigates the analysis results. The crystal structure, composition, microstructural and mechanical characterizations of the products were studied to observe the effect of different process conditions.

4.1 Production of Mo_2NiB_2 Ternary Boride Based Alloys

In this section, the combustion synthesis in Mo-Ni-B ternary system was performed to produce Mo_2NiB_2-based composites. The effect of the addition of Al_2O_3, excess Al and B_2O_3 on adiabatic temperature was discussed using FactSage simulations and experimental trials. Also, different NiO, B_2O_3, and NiO/MoO_3 ratios were examined to study the effect of raw materials on the product compositions. The composition, microstructural and mechanical properties of the obtained composites were analyzed by using AAS, XRD, SEM/EDS analyses and Vickers indentation. Finally, the Cr, Mn and V alloying elements were added to three ternary systems to observe their effect on the produced Mo_2NiB_2 ternary boride and the matrix phase.

4.1.1 Effect of diluent additions on the SHS products

In the first series of experiments, the excess Al and Al_2O_3 (as diluent) with different ratios of NiO and B_2O_3 raw materials were used to study the effect of functional additive on the formation and microstructure of the final products. Before experiments, the simulation calculations were conducted to determine the effect of excess Al and Al_2O_3 diluents on the adiabatic temperature and produced species. The composition and microstructure of the obtained alloys change by the formation of Ni-Al intermetallics in the matrix of alloys. In the second series of the experiments, the excess B_2O_3 and the different raw materials mixtures (i.e. NiO/MoO_3 ratios) were used to observe the effect of B_2O_3 as diluent on the final products. The phase composition, microstructure, and hardness of obtained composites were investigated to observe how they were affected by the formation of Mo_2NiB_2 in the reinforcement and $Ni_{20}Al_3B_6$ in the matrix. In the third series of the experiments, the microstructure of ternary boride composites was investigated to determine how it was improved by the addition of alloying elements.

4.1.1.1 Thermodynamic investigations

Before the first series of SHS experiments, 2 moles of MoO_3, 0.5 moles of NiO, and 1 mole of B_2O_3 were equilibrated with different amounts of Al to simulate the reaction. Figure 4.1 presents the simulation of the possible product contents formed by increasing Al ratios in the initial mixture. The heat released was assumed to increase the adiabatic temperature by initiation of the exothermic reaction resulting in the formation of liquid Mo, Ni, B, and Al in the products.

Among the oxides in the initial materials mixture, B_2O_3 starts to dissolve in the slag phase due to its lower melting temperature. MoO_3 transforms into MoO_2 sub-oxide and then, it is reduced to release Mo when Al reaches to 4.8 moles. The primary molten nickel in the system reacts with obtained Mo to produce alloys by increasing Al ratio. Then, the reduction of B_2O_3 in the slag phase starts when Al reaches to 5 moles. The adiabatic temperature was raised by increasing Al ratio in the initial mixture and when Al content reaches to 5 moles, the undesired Al in the system dissolves in the liquid alloys. The boron reduction continues even after the complete reduction of MoO_3 and NiO oxides. By increasing the Al ratio, at the stoichiometric content of 7 moles Al, the maximum contents of Mo, Ni, B, and Al are formed along with increase of the gasification. In this figure, the GAS curve refers to the total produced gaseous species.

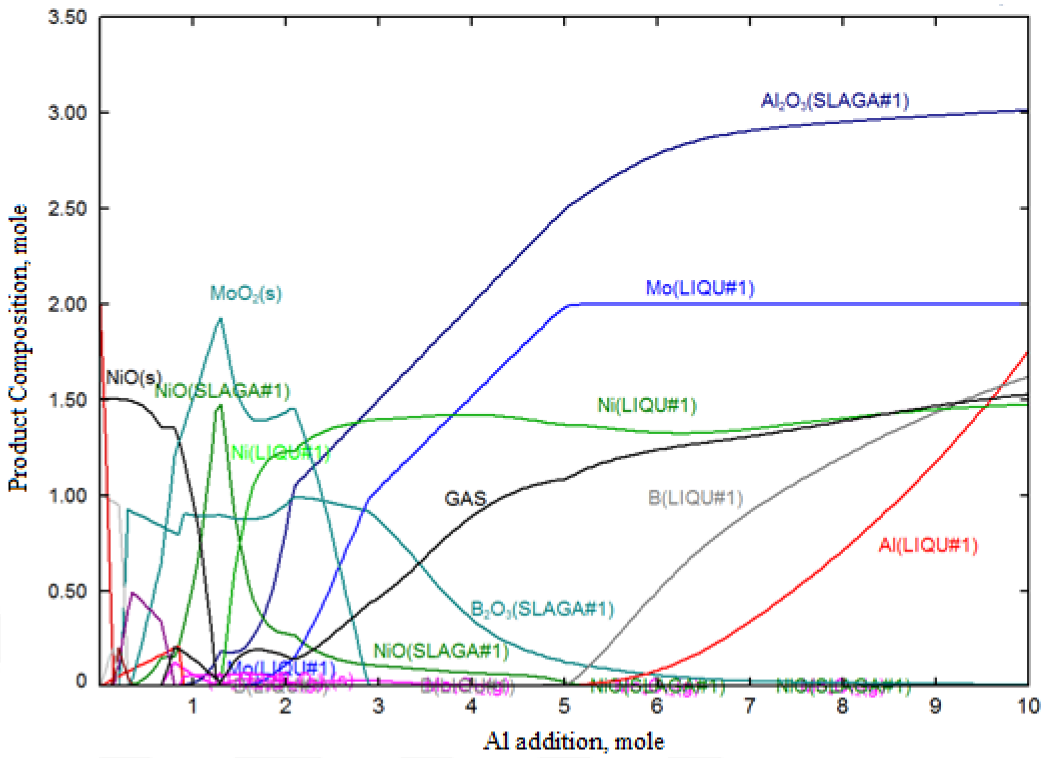

Figure 4.1 : Simulation of reaction products (molar ratio) using 2 mole MoO_3, 0.5 mole NiO and 1 mole B_2O_3 raw materials mixture at 1 atm and room temperature (25 °C) with different amounts of Al additions.

Figure 4.2 presents the amounts of produced alloys and slags in the different Al reducing agent amounts. The SHS-produced alloy weight is 289.88 gram that consists of 66.2% Mo, 27.24% Ni, 3.407% B, and 3.15% Al (in wt%) at the stoichiometric ratio of Al (7 moles) in the system. Thermodynamically, the complete reduction of metal oxides and boron trioxide occurs but the residual Al diffuses into the final product composition due to the high percentage of gas formation during combustion.

When the excess Al with the 5% additional amount was used, the weight of obtained alloy increases to 295.49 gram that consists of 64.95% Mo, 27.12% Ni, 3.741% B and 4.198% Al. The gaseous species weight equals to 1.3069 moles that comprise 10 weight percent of the total final products. The produced gases are 45.68% $AlBO_2$, 11.9% BO, 3.424% Al_2O, 3.039% Ni, 1.446% B_2O_3, 1.277% $(BO)_2$ and other species. On the other hand, the calculated total slag weight is 289 gram that consists of 99.41% Al_2O_3, 0.58% B_2O_3 and 0.0249% NiO (in wt%).

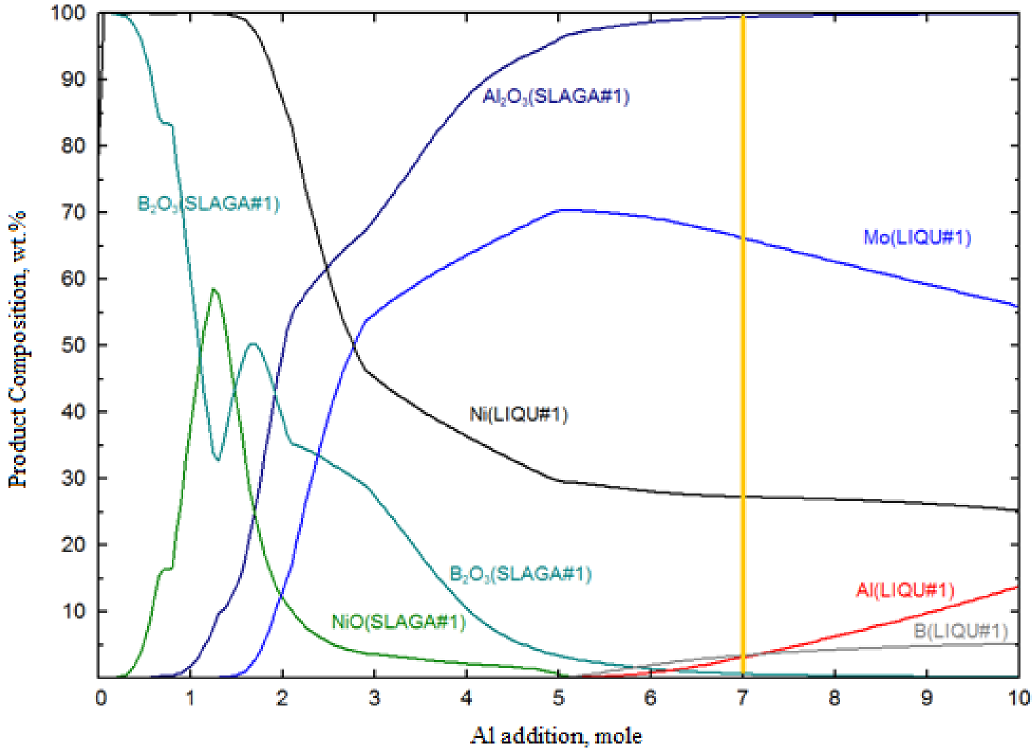

Figure 4.2 : Simulation of reacton products (wt%) using 2 mole MoO_3, 0.5 mole NiO and 1 mole B_2O_3 raw materials mixture at 1 atm and rom temperature (25 °C) with different amounts of Al addition.

The Al_2O_3 additions to the initial mixture decreases the adiabatic temperature as shown in Figure 4.3. This functional additive reduces the loss of the material and inhibits the gasification. The amounts of Al_2O_3 addition are 0, 0.05, 0.1 and 0.15 percentages of the total initial mixture which reduce the adiabatic temperatures to 2703.37, 2674.3, 2646.2 and 2604.89 °C, respectively.

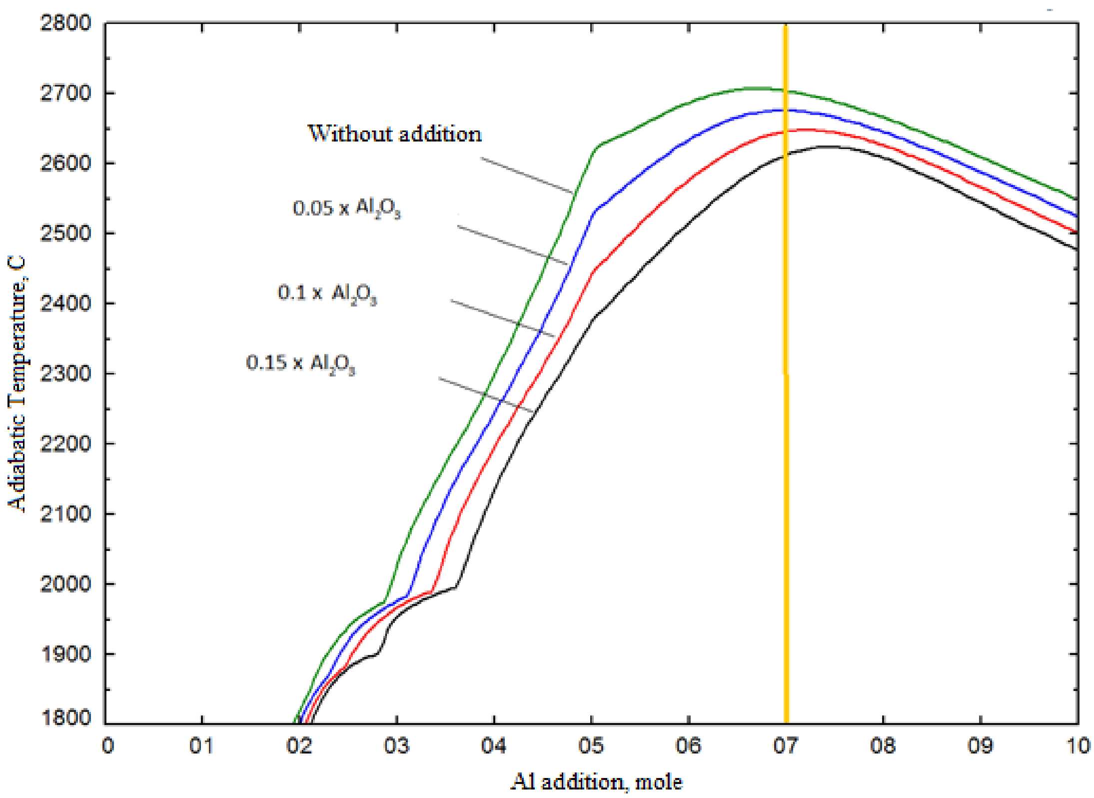

Figure 4.3 : Simulation of adiabatic temperature variation versus different amounts of Al and Al_2O_3 additions using 2 mol MoO_3, 0.5 mol NiO and 1 mol B_2O_3 raw materials mixture at 1 atm and room temperature (25 °C).

4.1.1.2 Effect of excess Al and Al_2O_3 addition on SHS products

In the experiments, the amounts of MoO_3, NiO, and B_2O_3, and their ratios were fixed to observe the effect of Al and Al_2O_3 addition on the target yield and materials loss. The amounts of Al and Al_2O_3 addition change in the ranges of 0 to 15 (weight% of stoichiometric Al) and 0 to 15 (weight% of total raw materials weight), respectively. Table 4.1 presents the amounts of raw materials mixture and adiabatic temperatures of 7 samples.

Table 4.1 : Raw materials amount and adiabatic temperature (˚C) for experimental study about the effect of Al and Al_2O_3 additions.

Exp. No	NiO, g	MoO_3, g	B_2O_3, g	Al, g	Stoich. Al, %	Al_2O_3, g	Al_2O_3, %	Adiabatic Temperature, °C
1	29,63	76,15	18,40	49,60	0	0	0	2704,41
2	29,63	76,15	18,40	52,10	5	0	0	2695,59
3	26,93	76,15	18,40	54,60	10	0	0	2682,22
4	26,93	76,15	18,40	57,10	15	0	0	2665,9
5	29,63	76,15	18,40	49,60	0	8,68	5%	2674,37
6	29,63	76,15	18,40	49,60	0	17,36	10%	2642,06
7	29,63	76,15	18,40	49,60	0	26	15%	2604,89

Also, the target yield, materials loss, and burning velocity values were found to change with excess Al and Al_2O_3 diluents. Figure 4.4 shows that the target yield values range between 62% and 72% while the loss of materials values varies between 3% and 18% using different Al amounts. The addition of 5% Al results in the highest target yield value. However, the higher amounts of Al additions didn't show any significant effect on the target yield value.

The yield of target target and materials loss values change between 43-81% and 10-12% with different Al_2O_3 amounts, respectively. These results show that Al_2O_3 acts better than excess Al on increasing the yield and reducing materials loss. This fact refers to the positive effect of Al_2O_3 on decreasing the adiabatic temperature. However, the higher amount of Al_2O_3 addition results in a decrease in yield of target values due to the difficulty in the metal/slag separation. The burning velocity changes between 4.6 mm/s and 11.7 mm/s.

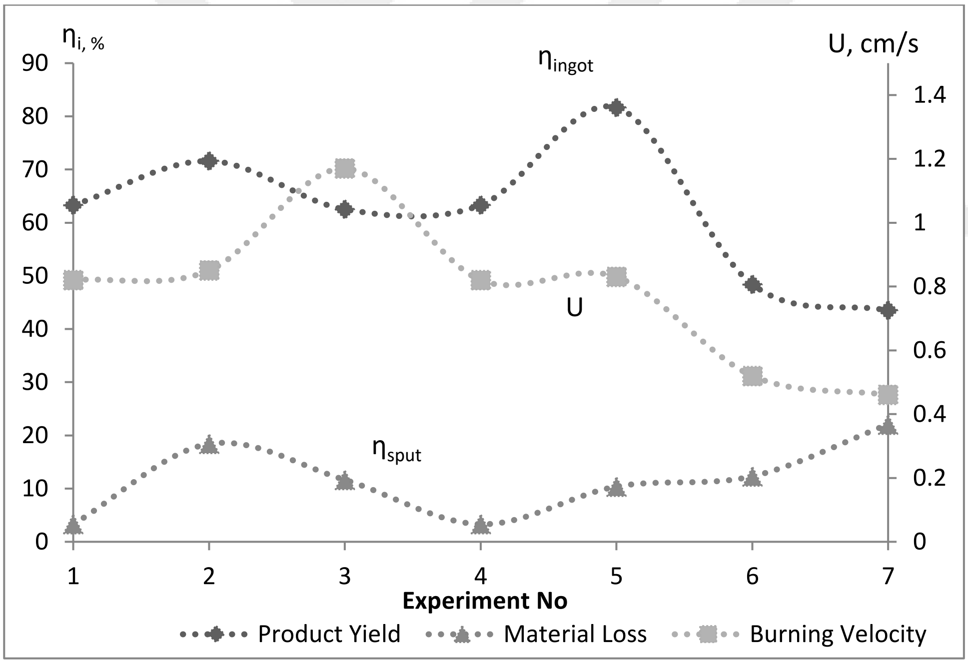

Figure 4.4 : The effect of Al and Al_2O_3 additions on SHS parameters such as Yield of target, Material loss and Burning velocity.

Table 4.2 presents the effect of Al and Al_2O_3 addition on the elemental compositions of obtained SHS alloys. The elemental analysis results assume that impurities such as Al, Cu and Fe contents in the compositions reach to 5 wt%, 2.75 wt% and 11 wt%, respectively. The boron contents changing between 3.5 and 4.6%wt were lower than estimated percentages.

Table 4.2 : Atomic absorption spectroscopy analysis results of the selected SHS alloys obtained from the experimental study about the effect of Al and Al_2O_3 additions.

Exp. No	Mo	Ni	B	Al	Fe	Cu
1	56.56	33.15	3.55	11.28	-	-
2	62.7	33.7	4.62	10.65	-	-

Optimum amounts of excess 5% Al and 5% Al_2O_3 addition to the initial mixture were chosen to increase the target yield value. The compaction before every SHS experiment helps to obtain lower porosity and cracks in the obtained alloys.

The influence of compaction of raw materials on the yield of the obtained alloys was studied using 0, 10, 20, 40 and 60 bar pressures. The microstructure of the obtained alloys are less porous than the SHS-synthesized alloys without compaction. However, the SHS synthesis parameters such as yield of target, materials loss, and burning velocity remain unchanged.

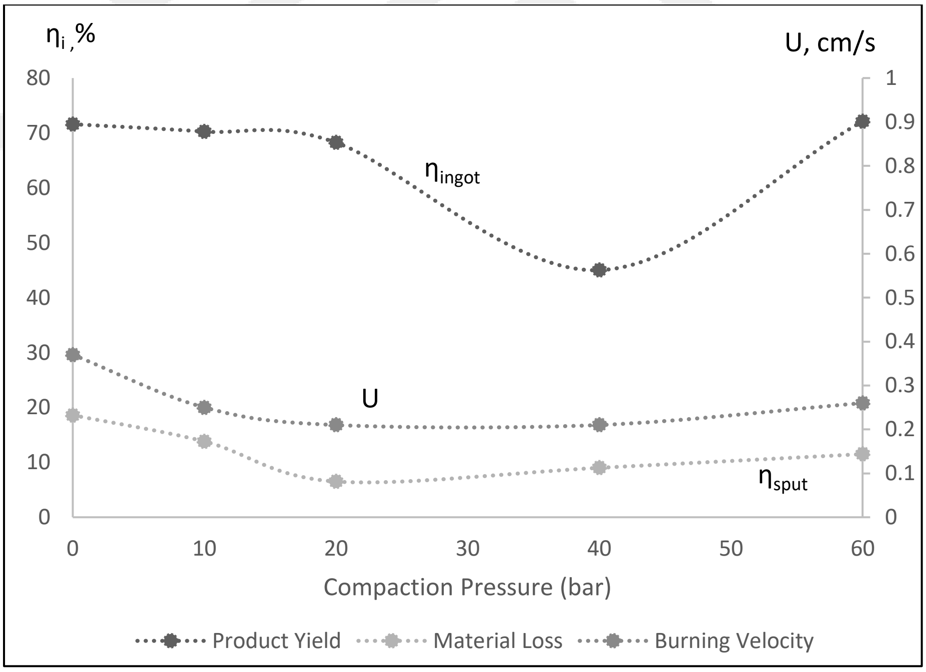

Figure 4.5 : Yield of target, materials loss and burning velocity of obtained samples from experimental study about the effect of compaction.

Effect of the initial NiO additions on SHS products

In the first series of experiments, the combination of Al and Al_2O_3 was used to reduce the combustion temperature. However, Al dissolution in the final product was more than expected.

Besides the 5% excess Al and 5% Al_2O_3, 22.3 to 30 grams NiO were used to observe the effect of oxide ratios on composition. Table 4.3 shows the raw materials amounts with increasing NiO.

Table 4.3 : Raw materials amounts (gram) for combustion synthesis of target alloys with increasing NiO.

No	MoO_3	NiO	B_2O_3	Al	Al_2O_3
NI1	76,1	29,6	18,4	52,1	8,6
NI2	76,1	31,2	18,4	52,8	8,8
NI3	76,1	32,6	18,4	53,2	9,0
NI4	76,1	35,5	18,4	54,0	9,2
NI5	76,1	38,5	18,4	54,7	9,4
NI6	76,1	41,9	18,4	55,5	9,6
NI7	76,1	44,9	18,4	56,3	9,8
NI8	76,1	46,9	18,4	58,3	10,6
NI9	78,4	46,2	18,9	55,3	9,9

The target yield, materials loss, and burning velocity values were found to change with increasing NiO amounts. Figure 4.6 presents the target yield values range between 50% and 75% while the loss of materials values varies between 20% and 30% using different Al amounts. The maximum yield of the target value of 74.89% and the lowest Al weight percentage refers to NI7 sample. The yield of target for different compositions is the subtracting of the excess Al weight from the alloy weight.

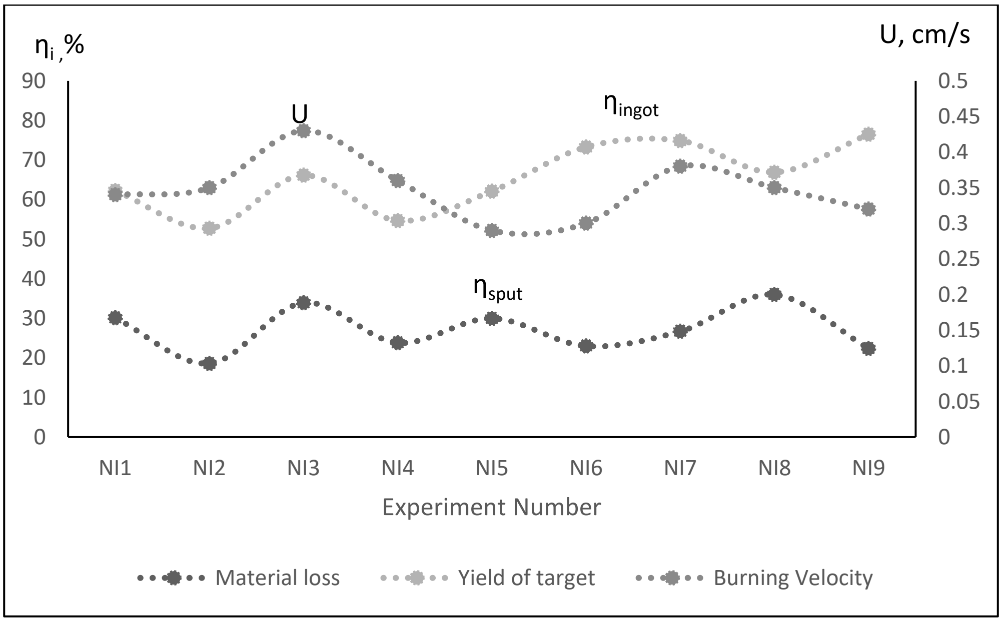

Figure 4.6 : The effect of NiO addition on SHS parameters such as Yield of target, material loss and burning velocity.

Table 4.4 presents the atomic absorption spectroscopy results of the selected alloys with estimated Ni weight percentages of 29.41, 31.2, 34.9, 38.89 and 39.75wt%. The Al weight percentage in these alloys changes between 8.36 and 13.4wt% while B weight percentage varies between 3.9 and 4.4wt%. The Cu weight percentage in alloys varies between 1.10 and 2.77wt% which is contamination resulted from the copper electric wire.

Table 4.7 : The atomic absorption analysis results of the SHS alloys obtained from the experimental study about the effect of NiO addition.

Exp. No	Estimated target composition, % wt.	Analysis results, % wt.				
		Mo	B	Al	Cu	Ni
NI1	63,4Mo-29,4Ni-7,2 B	58,10	4,40	11,70	1,10	24,7
NI3	61,83Mo-31,2Ni-6,97B	58,70	4,15	12,40	2,27	22,48
NI5	58,5Mo-34,9Ni-6,6B	55,00	4,06	13,40	1,99	25,55
NI7	54,87Mo-38,89Ni-6,23B	52,90	3,93	8,36	2,77	32,04
NI8	54.1Mo-39.75Ni-6.13B	51.05	-	11	0.49	41.9
NI9	54.9Mo-38.8Ni-6.2B	39.7	3.07	15.9	-	41.01

Figure 4.7 determines the distribution of elements in the final products. The percentage of elements increase by nickel oxide addition in the initial mixture.

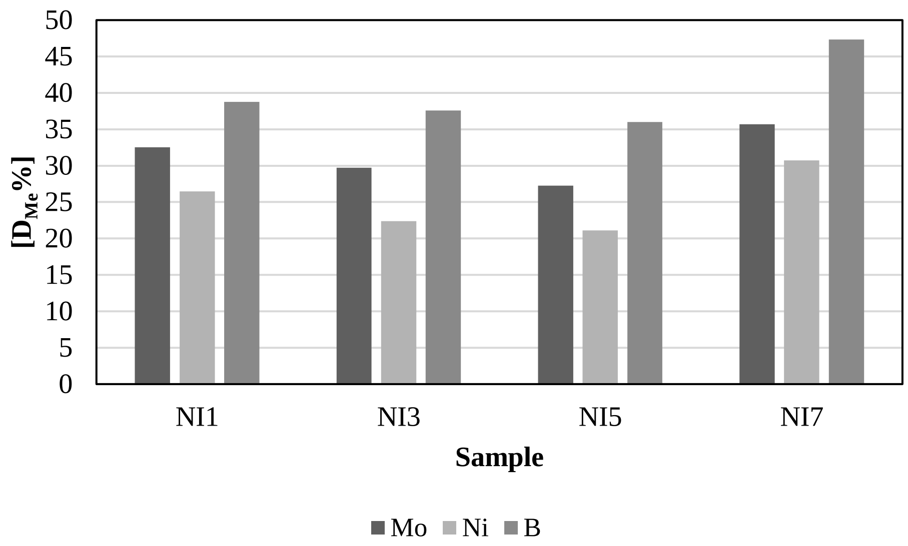

Figure 4.7 : Elemental distribution in obtained SHS alloys.

After the elemental analysis, the x-ray diffraction method was used to interpret the effect of NiO on the phase composition. Figure 4.8 presents the XRD patterns of NI1, NI3, NI5, NI7, and NI9 alloys. Ternary boride Mo_2NiB_2 didn't appear until the NiO amount reached to 30 gram in the initial materials mixture. The Mo-rich phases of Mo2B and MoB were detected in all the alloys regardless of the amount of NiO. The intermetallic phase AlB_{10} forms in all the samples due to the high Al concentration in the alloy. Besides, Ni-Al intermetallics formed in the matrix of alloys with higher Al content. The intensities of phases change by increasing the Ni/Mo ratio in compositions. The Mo_2B, MoB, NiAl and AlB_{10} phases formed in NI1, NI3, and NI5 alloys while the ternary boride didn't appear. The Mo_2NiB_2 complex boride, NiAl/Ni_3Al mixture, Mo_2B, MoB, and AlB_{10} formed in NI7 and NI8 samples.

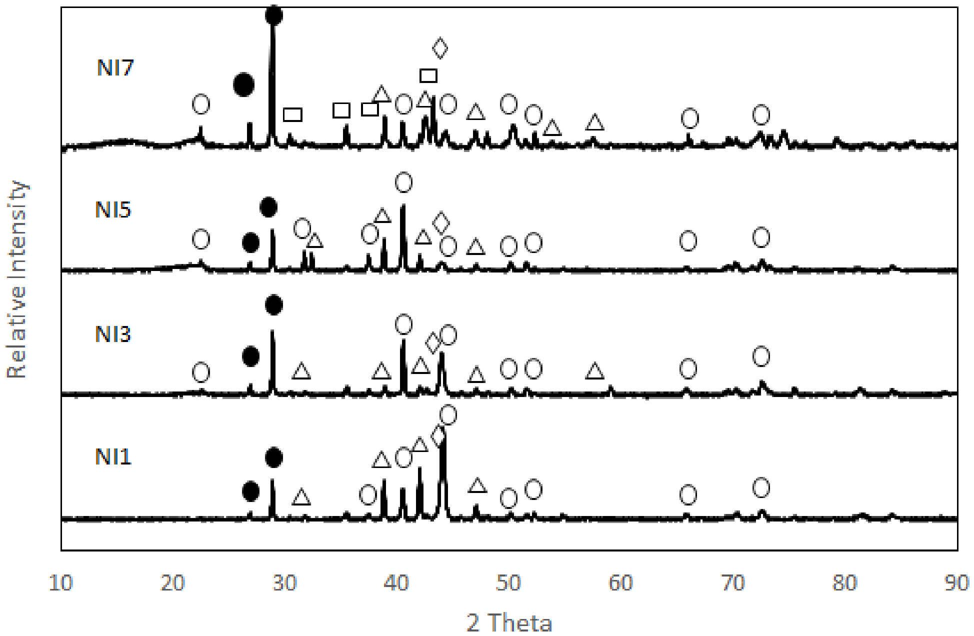

Figure 4.8 : XRD analysis results of NI1, NI3, NI5 and NI7 as-cast alloys obtained from combustion synthesis method (○ Mo_2B (00-006-0593),◊ NiAl (03-065-5171), Δ MoB (01-073-1768), □ Mo_2NiB_2 (01-089-2542), ● AlB_{10} (00-022-0002)).

Furthermore, Figure 4.9 presents the XRD pattern of slag produced from the NI7 sample raw materials mixture. The dominant phases in the slag sample were Al_2O_3 with two different allotropes. The lower intensities belong to the MoO_2 sub-oxide that show the incomplete aluminothermic reduction of MoO_3 during the combustion process.

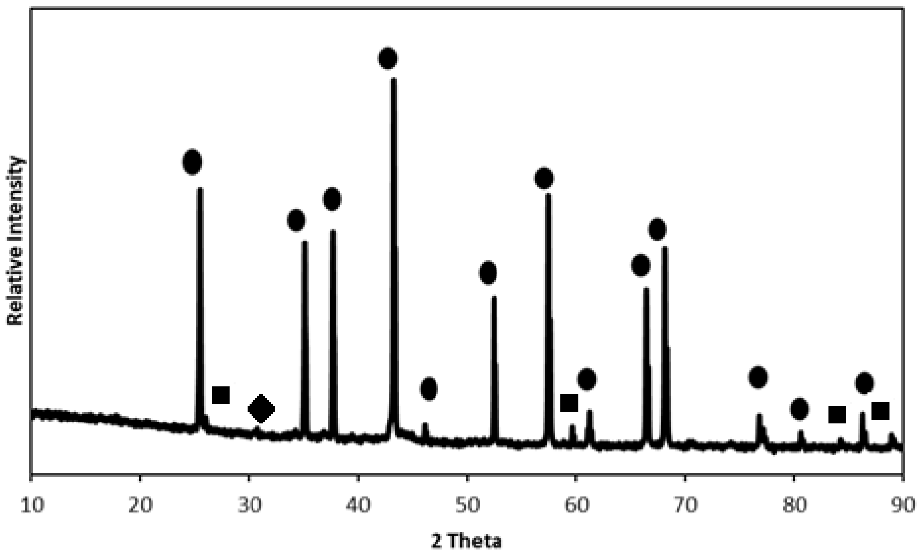

Figure 4.9 : X-ray pattern of obtained slag from the combustion synthesized NI7 sample (● Al_2O_3 (corundum, 01-083-2080), ■ MoO_2 (01-076-1807), ♦ Mo_2NiB_2 (01-089-2542)).

SEM/EDS analysis method was used to detect the microstructure of NI1, NI3, NI5, NI7, and NI8 samples. Figure 4.10 presents the SEM micrographs of the NI1 sample at X500 magnification. The elemental distributions of the phases in as-cast alloy which are revealed by EDS scans, are listed in Table 4.4. The NiAl intermetallic (point.1) forms due to the high Al concentration (11.7wt%) in the matrix phase of the NI1 sample. The light gray grains consist of MoB phases and the darker gray regions inside the grains are Mo_2B phases (points 2 and 3). The excess Cu has been dissolved in the Ni-rich matrix phase but has not been dissolved in the reinforcement phase. The elemental mapping of the NI1 sample confirms that B dispersed all over the sample while Al dispersed in the matrix phase only. Regarding the XRD results, Ni appears in the matrix but does not appear in the reinforcement phase. The analysis shows that the formation of Ni-Al intermetallic and Mo-B binary borides occurs in the alloy and this is in a good agreement with XRD result.

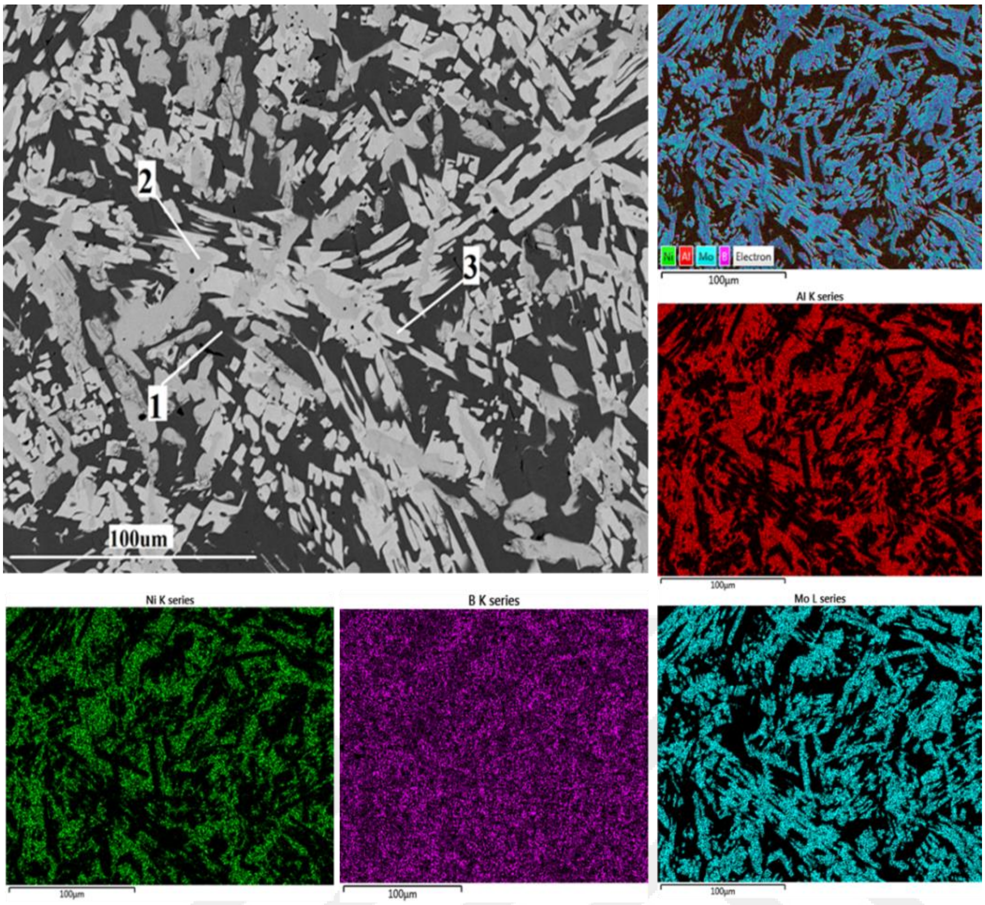

Figure 4.10: SEM/BSE image and EDS elemental mappings of SHS synthesized NI1 sample at x500 magnification.

Table 4.4: Elemental analysis of SHS synthesized NI1 sample, %wt.

Point	**B**	**O**	**Al**	**Ni**	**Cu**	**Mo**
1	-	-	27,76	68,86	2,22	1,16
2	11,51	2,15	-	3,09	-	83,26
3	11,65	2,29	-	1,45	-	84,61

Figure 4.11 presents the SEM micrographs of the NI3 sample at X500 magnification. The elemental distributions of the phases in as-cast alloy which are revealed by EDS scans, are listed in Table 4.5. The NiAl intermetallic (point.1) forms due to the high Al concentration (12.4wt%) in the matrix phase of the NI3 sample. The light gray grains consist of MoB phases and the darker gray regions inside the grains are Mo_2B phases (points 2 and 3). The excess Cu has been dissolved in the Ni-rich matrix phase but has not been dissolved in the reinforcement phase. The elemental mapping of the NI3 sample confirms that B dispersed all over the sample while Al dispersed in the matrix phase only. Regarding the XRD results, Ni appears in the matrix but does not appear in the reinforcement phase. The analysis shows that the formation of Ni-Al

intermetallic and Mo-B binary borides occurs in the alloy and this is in a good agreement with XRD result.

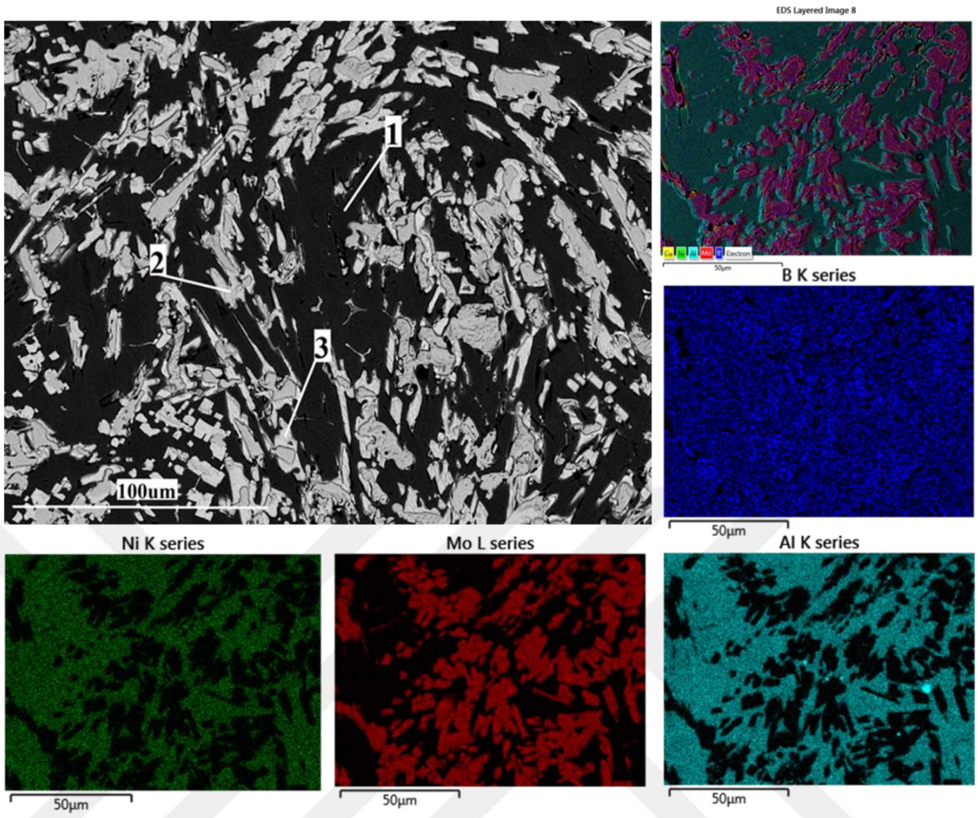

Figure 4.11 : SEM/BSE image and EDS elemental mappings of SHS synthesized NI3 sample at x500 magnification.

Table 4.5 : Elemental analysis of SHS synthesized NI3 sample, %wt.

Point	B	O	Al	Ni	Cu	Mo
1	-	-	30,82	64,76	4,42	-
2	19,38	2,39	-	1,21	-	77,03
3	11,59	1,77	-	1,65	-	84,99

Figure 4.12 presents the SEM micrographs of the NI5 sample at X500 magnification. The elemental distributions of the phases in as-cast alloy which are revealed by EDS scans, are listed in Table 4.6. The NiAl intermetallic (point.1) forms due to the high Al concentration (13.4wt%) in the matrix phase of the NI5 sample. The dark gray grains consist of MoB phases and the light gray regions around the grains are Mo-Ni-B phases which may form from interfering of NiAl and MoB phases (points 2 and 3). The darker gray areas inside the distributed hard phase particles are MoB_2 binary boride phase. The excess Cu has been dissolved in the Ni-rich matrix phase but has not been dissolved in the reinforcement phase. The elemental mapping of the NI5 sample confirms that Mo and Al were dispersed in reinforcement and matrix phases,

respectively. The EDS mapping results show that B concentration in the matrix phase decreases but Ni distribution in the reinforcement phase increases in sample NI5. The analysis shows that the formation of Ni-Al intermetallic and Mo-B binary borides occurs in the alloy which is in a good agreement with XRD result.

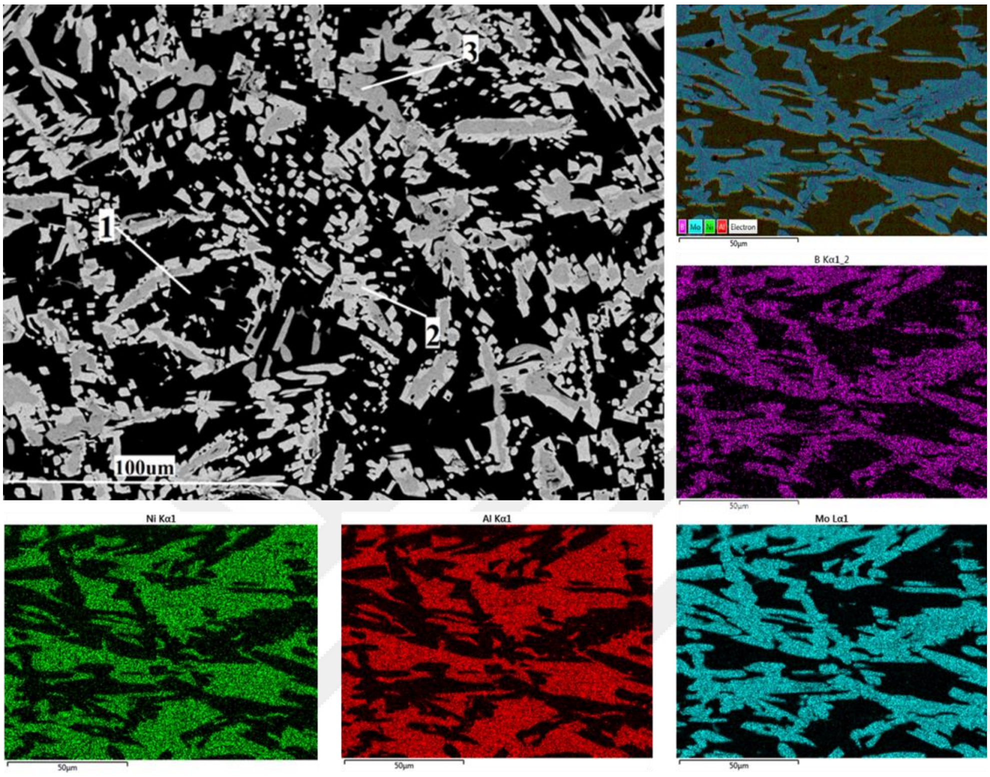

Figure 4.12 : SEM/BSE image and EDS elemental mappings of SHS synthesized NI5 sample at x500 magnification.

Table 4.6 : Elemental analysis of SHS synthesized NI5 sample, %wt.

Point	**B**	**O**	**Al**	**Ni**	**Cu**	**Mo**
1	-	-	27,71	67,37	4,95	-
2	14,02	2,0	-	3,0	-	80,97
3	19,04	-	5,85	20,09	1,42	53,60

Figure 4.13 presents the SEM micrographs of the NI7 sample at X500 magnification. The elemental distributions of the phases in as-cast alloy which are revealed by EDS scans, are listed in Table 4.7. The Ni_3Al intermetallic (point.1) forms due to the high Al concentration (8.36wt%) in the matrix phase of the NI7 sample. The ternary boride appears in dark gray areas inside the grains (point 2). The whitish-gray grains consist of MoB phases (point.3). The excess Cu has been dissolved in the Ni-rich matrix phase but has not been dissolved in the reinforcement phase. The elemental mapping results

of NI7 sample confirm that B dispersed all over the sample. Ni also appears in both the matrix phase and the grain boundaries of the reinforcement phase.

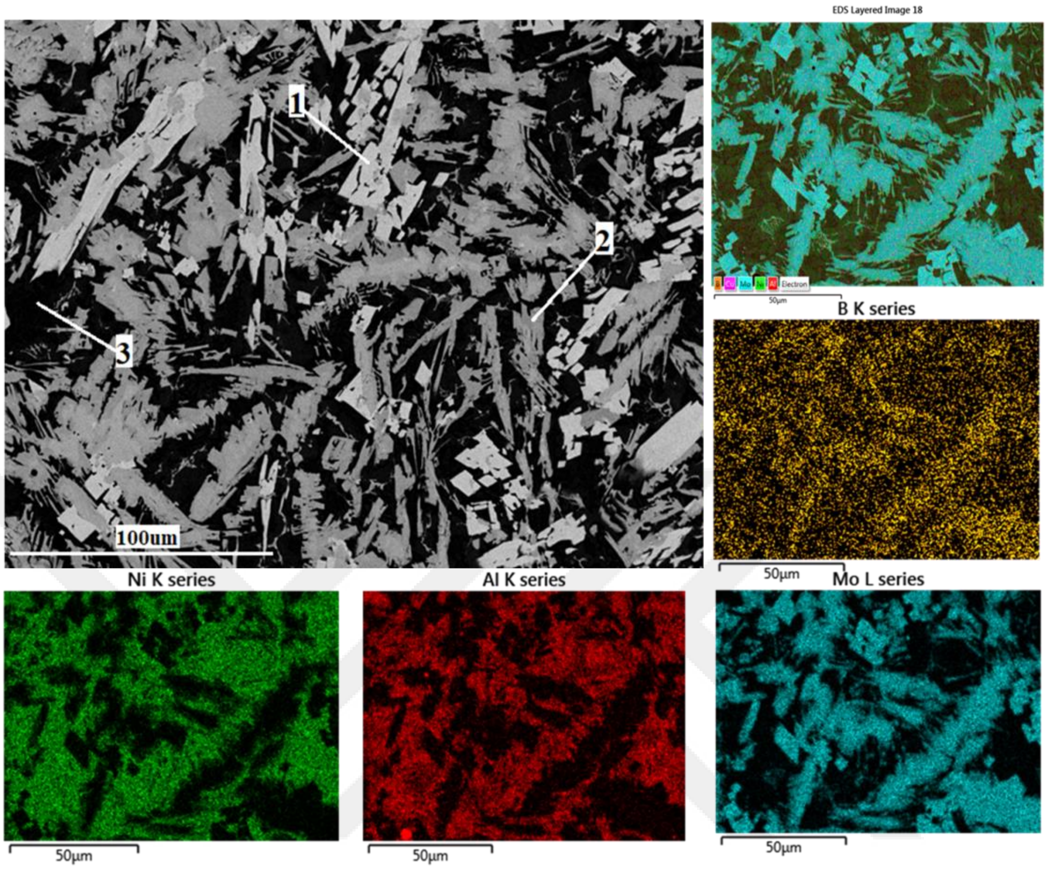

Figure 4.13 : SEM/BSE image and EDS elemental mappings of SHS synthesized NI7 sample at x500 magnification.

Table 4.7 : Elemental analysis results of SHS synthesized NI7 sample, %wt.

Point	B	O	Al	Ni	Cu	Mo
1	-	-	16,57	74,36	6,71	2,35
2	13,76	-	-	16,14	-	70,10
3	-	-	19,60	72,57	5,31	2,52

Figure 4.14 presents the SEM micrographs of the NI8 sample at X500 magnification. The dual phase of Ni_3Al/NiAl intermetallic (point.2) forms due to the high Al concentration (11.89wt%) in the matrix phase of the NI8 sample. The ternary boride in this sample appears in the grain boundaries (point.3). The Mo_2B and MoB binary phases are detected in the light gray regions inside the elongated particles (points 1 and 4). The elemental mapping results of NI8 sample confirm that B dispersed all over the sample. Ni also appears in both the matrix phase and the grain boundaries of the reinforcement phase.

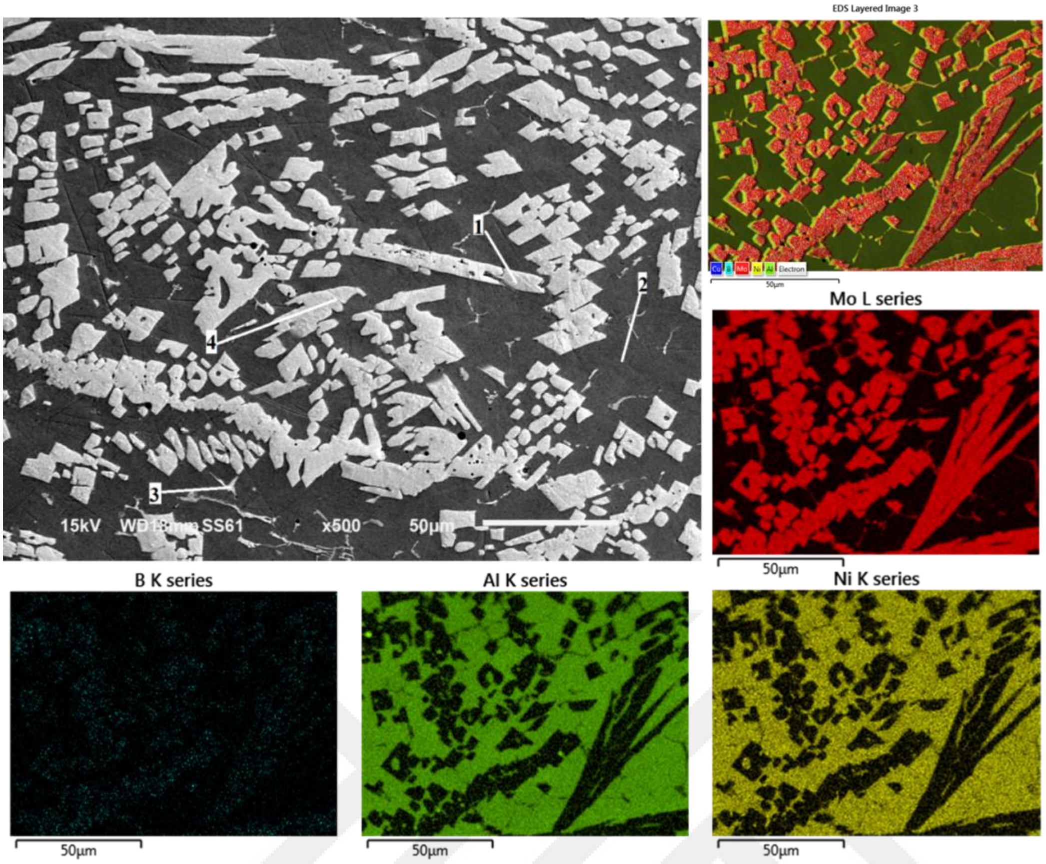

Figure 4.14 : SEM/EDS analysis (at x500 magnification) and elemental mapping of SHS synthesized NI8 sample.

The reinforcement area fractions of NI1, NI3, NI5, and NI7 samples were calculated by image analysis of SEM micrographs (at x500 magnification) that the values are 50.1%, 45%, 48% and 51% respectively. The all produced alloys are Mo based and the phase structures are close together. It was assumed that the microstructure of NI1, NI3, NI5 and NI7 alloys must be influenced by nickel content. The increasing of Ni wt% in composition reduces the reinforcement fraction in microstructure. However, the presence of Al in final composition causes an increase in matrix fraction. The higher concentration of Al in NI3 and NI5 samples reduces the reinforcement percentage by increasing the amount of solid solutions in matrix and consequently inhibits the formation of molybdenum based solid solutions in reinforcement. Among the samples, NI7 alloy has the lowest Al weight percentage in the composition that gives rise to production of ternary borides and increasing reinforcement/matrix ratio to the highest value.

Effect of initial B_2O_3 additions on SHS products

In addition to the NiO increase in raw materials mixture with excess Al and Al_2O_3 as diluents, the B_2O_3 addition was examined to improve the SHS parameters and phase composition of alloys. Table 4.8 presents the raw materials with different amounts of B_2O_3 change between 19.35 and 23.97 gram. The stoichiometric reactions were used to calculate the raw materials amounts. The numbers of alloys with different contents of B_2O_3 are MNB1, MNB2, MNB3, MNB4, and MNB5.

Table 4.8 : Raw materials amounts of alloys with increasing B_2O_3.

No	MoO_3	NiO	B_2O_3	Al	Al_2O_3
MNB2	76,15	29,60	19,35	52,86	8,92
MNB3	76,15	29,60	20,40	53,24	9,02
MNB4	76,15	29,60	22,12	54,00	9,17
MNB5	76,15	29,60	23,97	54,75	9,30

Figure 4.15 presents the effect of B_2O_3 stoichiometric addition on the yield of the target, material loss, and burning velocity. The target yield changed between 65.67 and 82.68% while the loss of material value changed between 18.16 and 33.95%. The average burning velocity value equals to 3.6 mm/s.

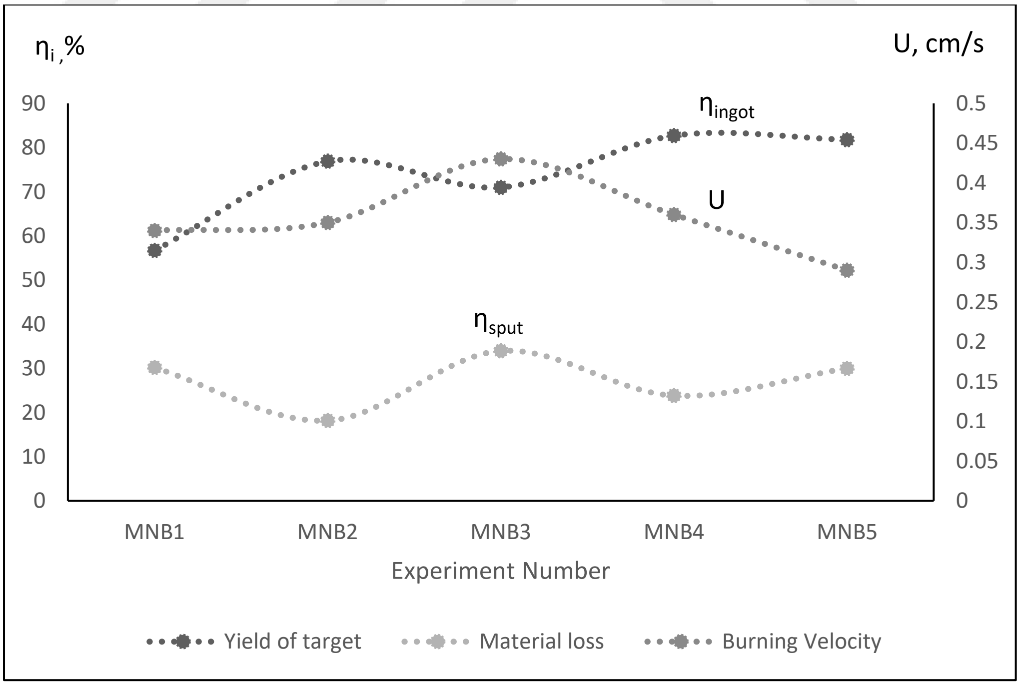

Figure 4.15 : The effect of B_2O_3 addition on SHS parameters such as Yield of target, material loss and burning velocity of the obtained alloys.

The elemental analysis results of different compositions show that the maximum weight percentage reaches to 5.22 wt%, 25.35 wt%, and 58.7 wt% for B, Ni, and Mo, respectively. According to Table 4.9, the maximum weight percentages of impurities such as Al and Cu were 12.7 and 2.95 wt%, respectively. The decrease in the concentration of the element is due to the high amounts of gasification during the combustion process.

Table 4.9 : The atomic absorption spectroscopy analysis results of the SHS alloys obtained from the experimental study about the effect of B_2O_3 addition.

Exp. No	Estimated composition, wt.%	Analysis results, wt.%				
		Mo	B	Al	Cu	Ni
MNB3	62,95Mo-29,2Ni-7,84B	54,60	4,40	12,70	2,95	25,35
MNB5	62,1Mo-28,8Ni-9,11B	58,70	5,22	12,48	0,59	23,01

Figure 4.16 presents the SEM micrographs of the MNB3 sample at X500 magnification. The elemental distributions of the phases in as-cast alloy which are revealed by EDS scans, are listed in Table 4.10. The NiAl intermetallic (point.1) forms due to the high Al concentration (13.4 wt%) in the dark gray matrix area of the MNB3 sample. The light gray area (point.2) in the reinforcement phase consists of Mo_2NiB_2 ternary boride phase. Since the Mo weight percentage in this sample decreases, the formation of MoB_2 phase in dark gray regions (point 3) inside the reinforcement grains becomes more probable. The elemental mapping results of MNB3 sample confirm that Mo presents in the reinforcement while Ni and Al dispersed in the matrix area.

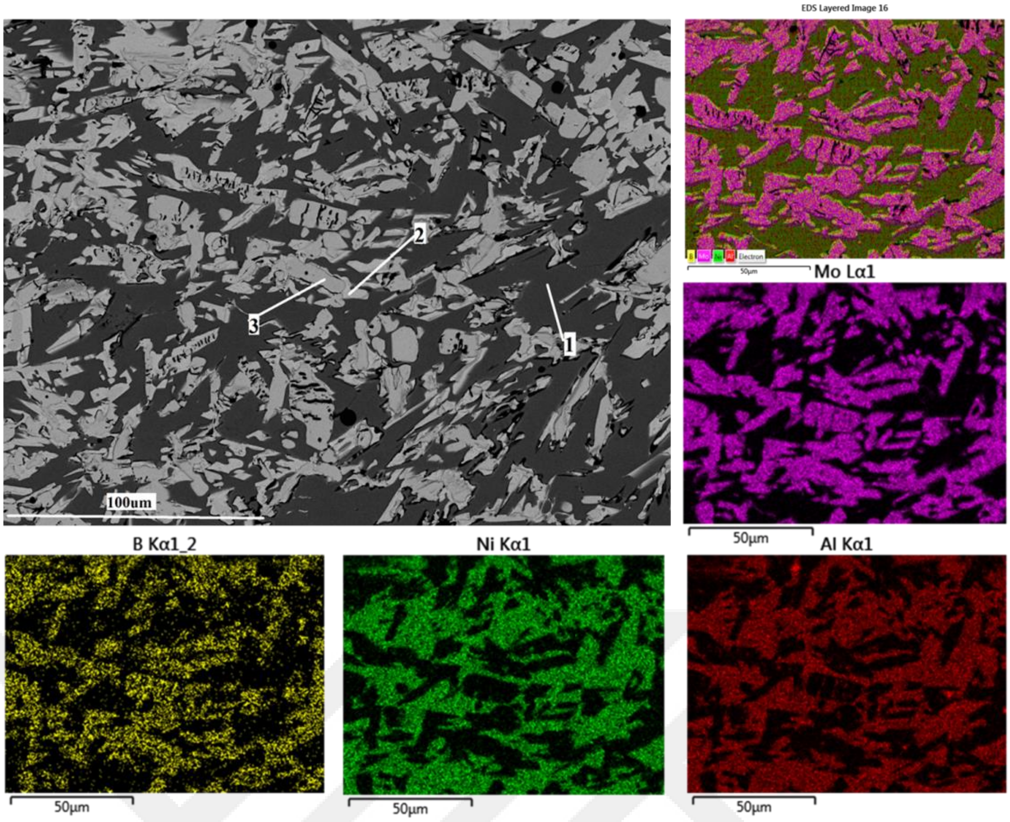

Figure 4.16 : SEM/BSE image and EDS elemental mappings of SHS synthesized MNB3 sample at x500 magnification.

Table 4.10 : Elemental analysis of SHS synthesized MNB3 sample, %wt.

Point	B	O	Al	Ni	Cu	Mo
1	-	-	30.63	62.95	6.41	-
2	16,73	2,78	2,42	16,93	1,98	59,16
3	18,58	-	-	1,11	-	80,31

Figure 4.17 presents the SEM micrographs of the MNB5 sample at X500 magnification. The elemental distributions of the phases in as-cast alloy which are revealed by EDS scans, are listed in Table 4.11. The NiAl intermetallic (point.3) forms due to the high Al concentration (12.48wt%) in the dark gray matrix area of the MNB5 sample. The excess Cu has been dissolved in the Ni-rich matrix phase but has not been dissolved in the reinforcement phase. The MoB (point.2) and MoB_2 phase form in darker gray regions inside the grains (point 1). The elemental mapping results of MNB5 sample confirm that Mo presents in the reinforcement while Ni and Al dispersed in the matrix area. Boron disseminates within the entire sample.

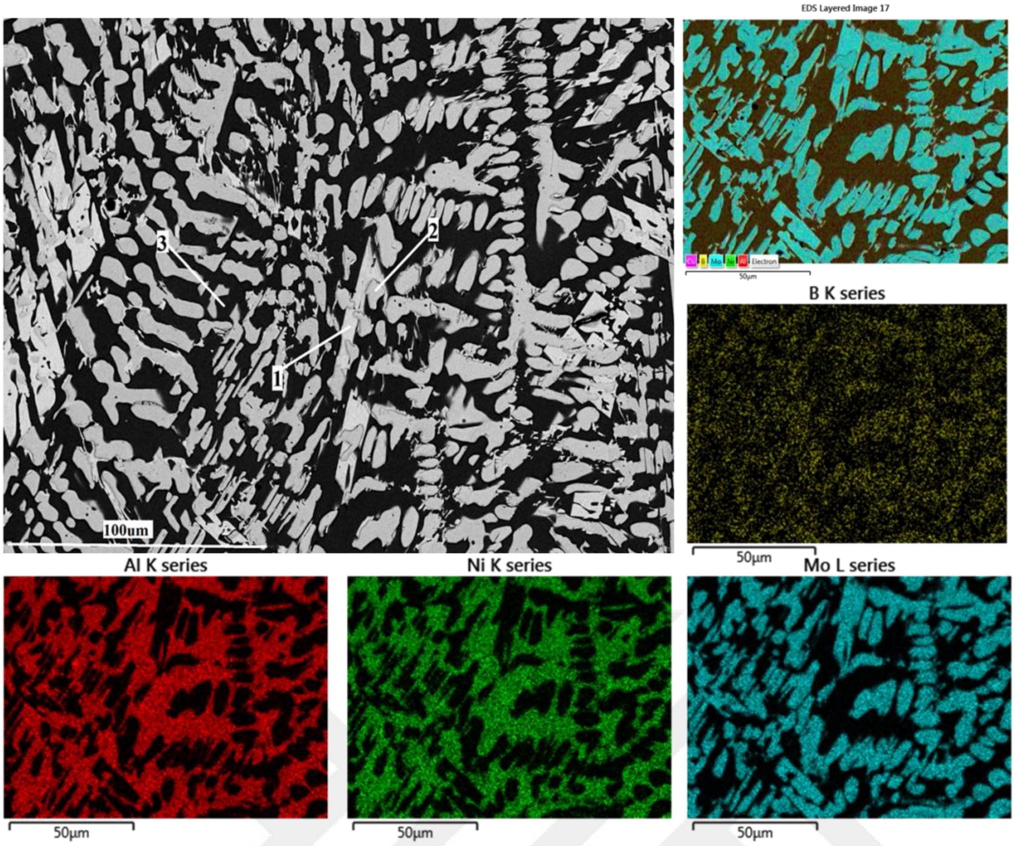

Figure 4.17 : SEM/BSE image and EDS elemental mappings of SHS synthesized MNB5 sample at x500 magnification.

Table 4.11 : Elemental analysis results of SHS synthesized MNB5 sample, %wt.

Point	B	O	Al	Ni	Cu	Mo
1	19,84	-	-	1,61	-	78,55
2	10,05	-	-	1,38	-	88,57
3	-	-	30,79	67,91	-	1,30

The higher boron concentration in the final composition does not affect the reinforcement/matrix ratio significantly. Image analysis calculations on MNB3 and MNB5 samples reveal that the increase in the Al dissolution makes a lower reinforcement/matrix ratio.

4.1.1.3 Effect of excess B_2O_3 on the SHS products

The excess B_2O_3 diluent was used to study its effect on the adiabatic temperature and the final composition. Figure 4.18 shows the reaction of 1 mole MoO_3, 3 moles NiO and 2 moles B_2O_3 with different amounts of Al calculated by using the "Equilibrium" module. The reduction of NiO and MoO_3 starts at 2 at.% of Al and then, the formation of B starts at 4 at.% of Al. The gaseous species which consist of B_2O_3, $(BO)_2$, BO_2, and $AlBO_2$, increase by proceeding of boron trioxide reduction.

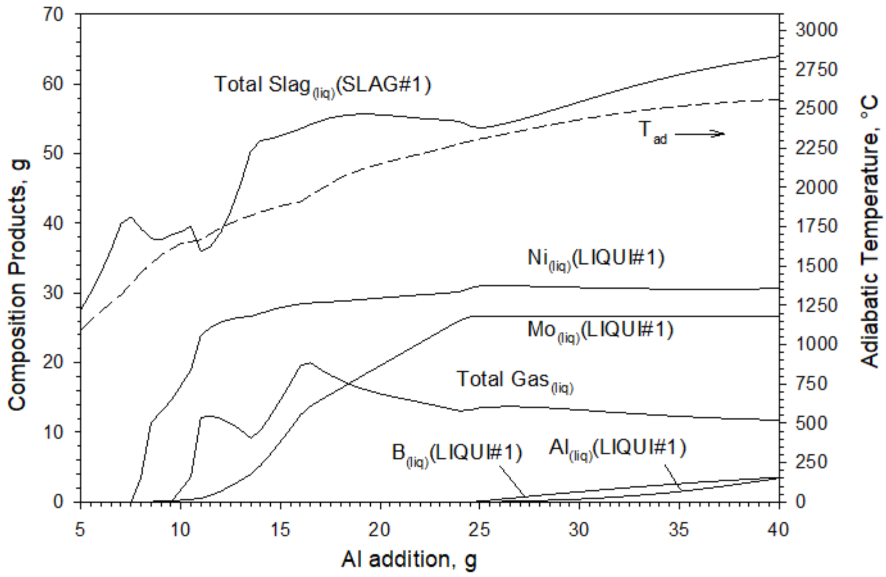

Figure 4.18 : Product composition in Mo-Ni-B system using extra B_2O_3.

Also, the calculations were performed to predict the SHS produced alloy melting and the possible microstructures. For this purpose, the alloy consisting of 50 wt% Ni, 44 wt% Mo, 4 wt% B, and 2 wt% Al by mass, used to model the equilibrium solidification starting from 1600 °C down to 100 °C. Figure 4.19 shows that Mo_2NiB_2 is the first solid product formed in the liquid alloy. The solid solution α-Ni and Mo_2NiB_2 phase coexist below solidus temperature (1360 °C). Following the Mo_2NiB_2 solidification, the Mo_2B and Ni_3Al phases nucleate at 680 °C and 601 °C, respectively. The nickel and molybdenum are supplied from α-Ni and Mo_2NiB_2 phases to form Ni_3Al and Mo_2B phases. The subsequent calculations also revealed that if boron content is higher than the stoichiometric need of Mo_2NiB_2 existed in the alloy, the formation of additional phases, MoB or Ni_3B, is possible depending on Mo/Ni ratio in the matrix.

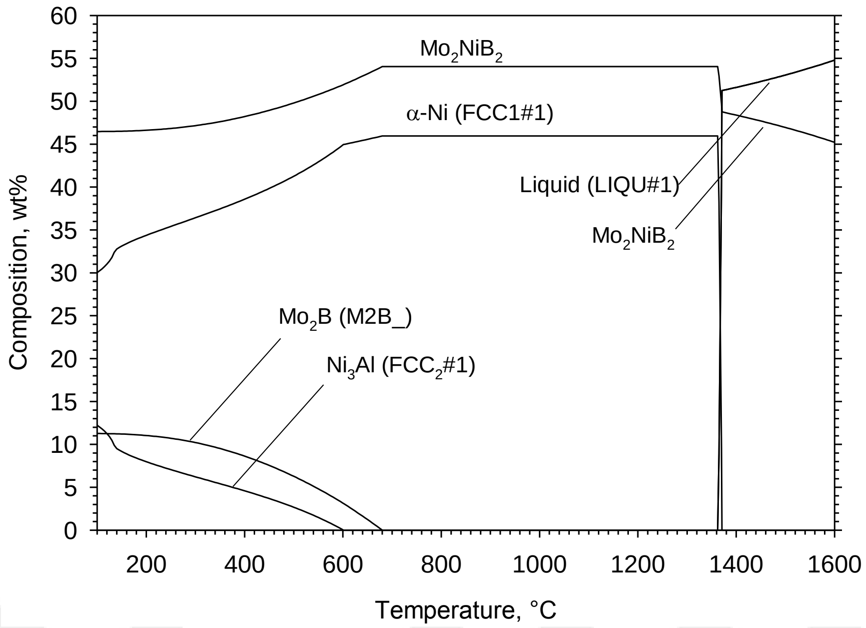

Figure 4.19 : FactSage calculation of a selected SHS alloy for equilibrium solidification (50% Ni, 44 % Mo, 4% B, and 2 wt% Al, by mass).

Effect of different NiO/MoO_3 ratios on SHS products

Table 4.12 presents the raw materials for NI10 sample in which the metal oxide ratios were fixed but B_2O_3 and Al used greater than and less than stoichiometric amounts, respectively. The SHS parameters and AAS analysis results of the obtained alloy NI10 which are presented in Table 4.13, were found to change by the excess B_2O_3 amount.

Al weight percentage decreases from 8.39 to 2 wt.% and B remains the same in NI10 sample when comparing with the NI7 sample. The addition of B_2O_3 in the same B_2O_3+Al containing systems, was reported to reduce the adiabatic temperature [6].

Although the excess B_2O_3 was found to reduce the undesired Al content, the Mo_2NiB_2 percentage is low yet. Different MoO_3/NiO ratios were used to observe the effect of metal oxides on the compositions. Therefore, Al and B_2O_3 amounts kept constant but the MoO_3/NiO ratio decreased as follow: 1.5, 0,85, 0.6, 0.28, and 0.26 in the raw materials. Table 4.12 presents the target compositions and the raw materials amounts calculated using FactSage. Also, it presents the crucible types used for each SHS experiment.

Table 4.12 : The estimated target composition and raw materials amount of experimental study about different NiO/MoO_3 ratios.

No	Composition (wt%)	MoO_3	NiO	B_2O_3	Al	Crucible
NI10	55.5Mo-38.5Ni-5B-1Al	75	45	40	55	Copper2
NI11	55.5Mo-38.5Ni-5B-1Al	56.25	33.75	30	41.25	Magnesia
NI12	55.5Mo-38.5Ni-5B-1Al	56.25	33.75	30	41.25	Copper1
NI13	48Mo-46.5Ni-4.5B-0.9Al	50	42	30	40	Copper2
NI14	48Mo-46.5Ni-4.5B-0.9Al	50	42	30	40	Copper1
NI15	34Mo-60Ni-5B-0.9Al	40	60	40	42	Copper1
NI16	34Mo-60Ni-5B-0.9Al	40	60	40	42	Copper2
NI30	72Mo-21Ni-7B	42.42	11.11	20.04	26.44	Graphite
NI32	60.92Mo-31.5Ni-7.26B	37.43	10.69	26.74	25.13	Graphite

Table 4.13 presents the SHS parameters and elemental compositions of the obtained alloys. The Al concentration was lower than 6 wt% except for the alloy NI30. The boron weight percentage changed slightly and reached a maximum of 9 wt% in alloy NI32. By increasing the MoO_3 amount in raw materials mixture, the exothermic nature of MoO_3+Al reaction causes higher Al content in the product.

Table 4.13 : The atomic absorption spectroscopy analysis results of SHS alloys obtained from the experimental study about the effect of different NiO/MoO_3 ratios.

No	Mo	Ni	Al	W	Cu	Si	B	Yield, %
NI10	42	50.2	2	0.5	0.1	-	-	65.8
NI11	44.1	46.5	3.24*	0.75	0.07*	2.8	2.83*	67.6
NI12	50.2	42.6	-	0.56	0.08	-	-	54.65
NI13	47.8	43	-	0.6	0.1	-	-	71.5
NI14	33.1	57	2.3*	1.04	0.21*	2.6	3.3*	58.65
NI15	26.3	61.0	2.2*	0	0.6	0.56	4.1	45
NI30	40.48	33.99	21.39	-	-	-	3.65	31.3
NI32	51.75	38.28	6.57	-	-	-	13.03	58.69

* AAS analysis

Figure 4.20 presents the XRD pattern of slag produced from the NI14 sample with B_2O_3 addition to the raw materials mixture. The dominant phase in this slag sample was Al_2O_3. The other peaks with the lower intensities belong to the MoO_2 sub-oxide and $Al_{18}B_4O_{33}$ that show the interaction of excess B_2O_3 and the MoO_2 sub-oxide during the combustion process as it was also estimated by FactSage software.

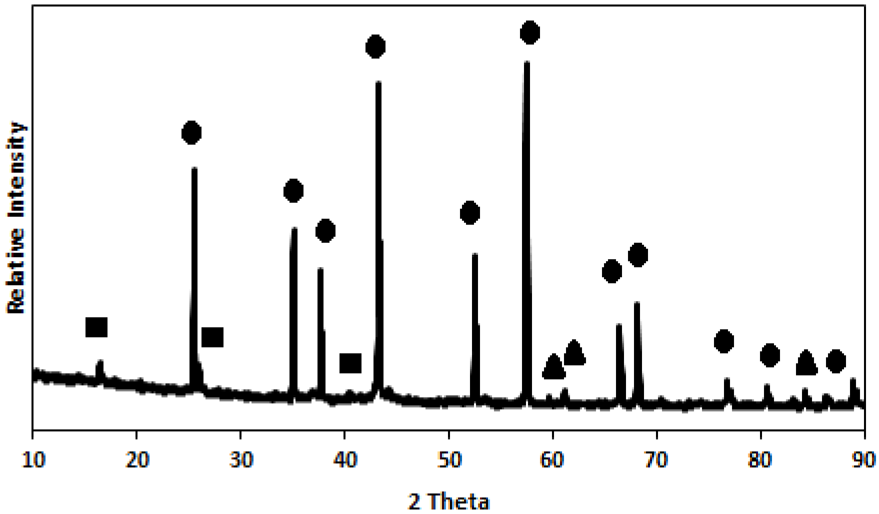

Figure 4.20 : X-ray pattern of obtained slag from the combustion synthesized NI14 sample (● Al_2O_3 (01-075-1862), ■ $Al_{18}B_4O_{33}$ (00-053-1233), ▲ MoO_2 (01-078-1070)).

Figure 4.21 presents the XRD analyses of the SHS-synthesized as-cast alloys using the initial mixture of MoO_3: NiO: B_2O_3: Al. This figure shows the produced phases through SHS by excess B_2O_3 in the raw materials (NI11). The AlB_{10} phase was disappeared by increasing B_2O_3 and reducing the adiabatic temperature in NI10 sample compared to NI7. According to the figure, the dominant phase in this alloy is MoB due to the decrease in Al content. Also, the lower Al reduces the NiAl intensity replacing by $Ni_{20}Al_3B_6$. There exists the ternary boride Mo_2NiB_2 phase in the obtained alloy.

The main phases in the NI30 are ternary boride MoAlB and binary borides of MoB, MoB_2. Nickel aluminides of Ni_2Al_3 and NiAl compose the matrix phase due to the higher concentration of Al. By increasing Ni weight percentage in the sample NI32, the binary borides of MoB_2, orthorhombic MoB, and tetragonal MoB phases formed. Also, in this sample nickel aluminide of AlNi composes the matrix phase. In NI11 sample, hexagonal MoB_2, orthorhombic MoB, tetragonal MoB and ternary boride of Mo_2NiB_2, NiAl, γ'-Ni_3Al, and τ-$Ni_{20}Al_3B_6$ formed by further increasing Ni. The produced phases are proved to show stability at higher temperatures of the combustion synthesis process.

The phases of Mo_2NiB_2, γ'-Ni_3Al, and τ -$Ni_{20}Al_3B_6$ appeared by increasing Ni/Mo ratio in NI14 sample. Consequently, the Mo-rich phase such as MoB binary boride has lower intensity. Finally, the main phases of Mo_2NiB_2, τ -$Ni_{20}Al_3B_6$, and γ'-Ni_3Al formed in the NI15 sample with the highest Ni content. The MoB phase in this alloy disappeared completely. The Rietveld analysis results confirm the obtained phases contents in the NI14 and NI15 samples.

NI14 sample comprises 46.7% Mo_2NiB_2, 26.9% $Ni_{20}Al_3B_6$, 22.8% Ni_3Al and 3.6% MoB with the Goodness of fit value of 1.21. The phases 50.7% $Ni_{20}Al_3B_6$, 25.7% Ni_3Al, and 23.7% Mo_2NiB_2 presented in the NI15 sample with 1.26 GOF value.

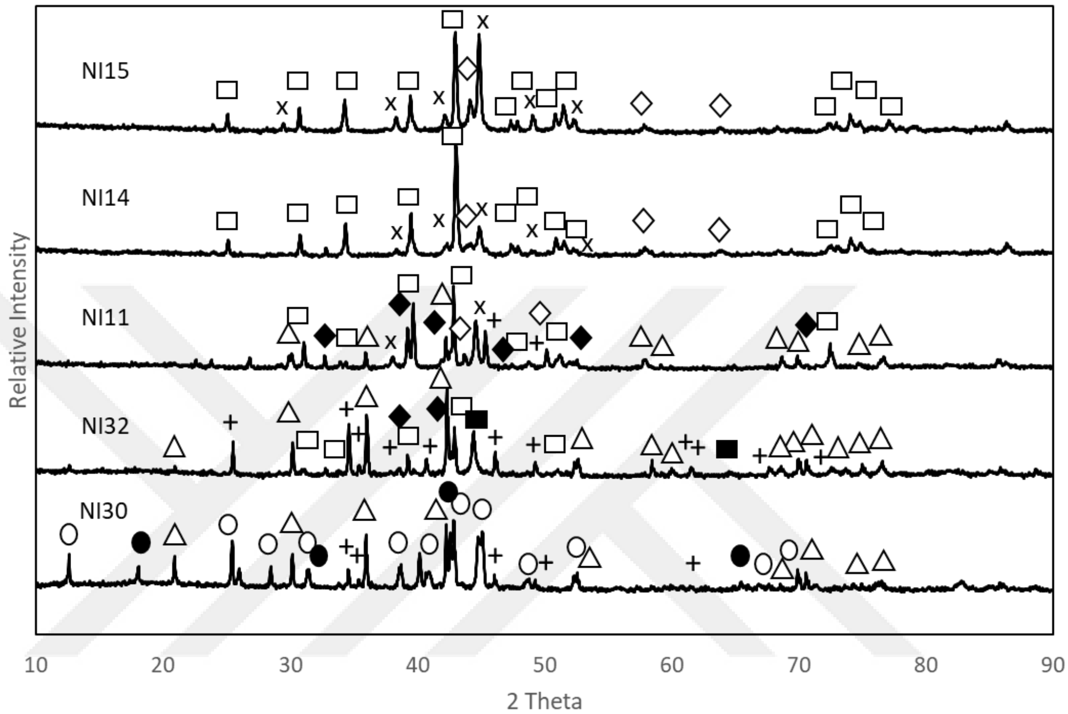

Figure 4.21 : XRD analysis results of NI30, NI32, NI11, NI14 and NI15 as cast alloys obtained from combustion synthesis method (○ MoAlB, Δ MoB (01-073-1768), + MoB_2, ● Ni_2Al_3 (00-014-0648), t MoB (tet, 00-006-0636), □ Mo_2NiB_2, ▪ NiAl, X $Ni_{20}Al_3B_6$ (01-088-1558), ◊ Ni_3Al (00-050-1265)).

Therefore, according to the XRD results, the alloys with higher Mo_2NiB_2 intensities were analyzed by SEM/EDS analysis method. Figure 4.22 presents the SEM micrographs of NI11 sample at two different magnifications. The two-phase structure with coarse particles consists of different intermetallic phases dispersed in a uniform matrix phase. This alloys structure and morphology is typical of all other alloys.

Figure 4.22(a) shows the elongated particles (light gray) distributed throughout the matrix region (dark gray). The higher magnification SEM image in Figure 4.22 (b) and the corresponding EDS analysis presented in Table 4.14 reveals the following phases: a) MoB (1, Whitish gray) formed in the middle of the grains b) elongated Mo_2NiB_2 particles near the boundaries (2, light gray), and c) the matrix consisting of $Ni_{20}Al_3B_6$ (3, dark gray) with mixture of Ni_3Al and NiAl (4, black dot) phases.

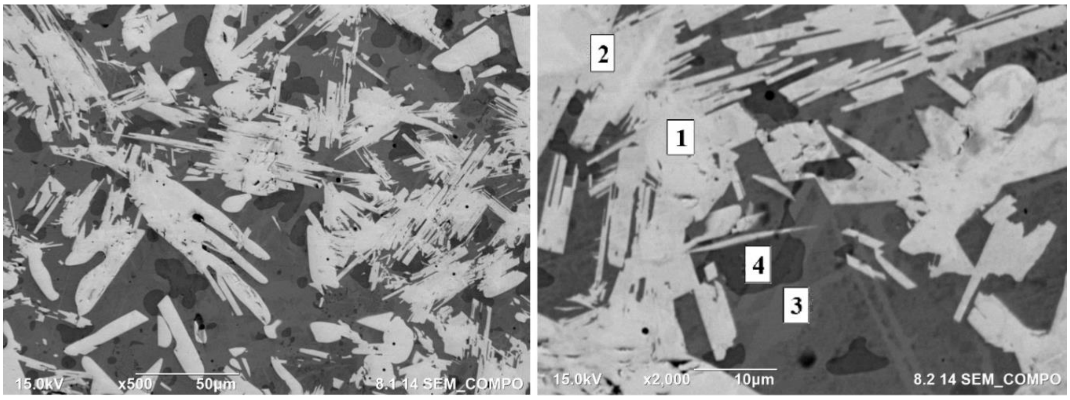

Figure 4.22 : SEM/BSE images of the as-cast NI11 alloy sample with the magnifications of a) x 500 and, b) x 2000.

Table 4.14 : Elemental analysis of SHS synthesized NI11 sample.

No	Mo	Ni	B	Al
1	89.48	2.06	8.47	-
2	75.46	17.96	6.58	-
3	-	84.34	7.18	8.47
4	-	74.06	-	25.94

Figure 4.23 shows the SEM micrograph of NI14 sample with the composition of 47.6Mo-46.6Ni-4.8B. Also, the elemental distributions of the phases in as-cast NI14 alloy which are revealed by EDS scans are listed in Table 4.15. It shows the plate-like particles (light gray) which almost uniformly distributed throughout the region. The figure reveals the existence of a) plate-like Mo_2NiB_2 (3, light gray) particles , b) α-MoB (2, whitish gray) formed in the coarse Mo_2NiB_2 grains, and c) τ-$Ni_{20.5}Al_{2.5}B_6$ (4, gray) and Ni_3Al (1, dark gray) phases as the matrix.

According to Figure 4.23, the sample's microstructure consists of two parts including intermetallic based reinforcement and matrix. The grains with elongated rectangular shape are distributed homogeneously in dark matrix. The elemental distributions of particles composition resulted by Energy Dispersive Spectroscopy (EDS) scans, agrees well with XRD patterns whereas the largest region belongs to Mo_2NiB_2 ternary phase. The higher magnification of matrix phase in sample reveals the existence of max 12 wt% Al in nickel corresponding to Ni_3Al phase. There are some regions close to the grain boundaries that contain 3-4 wt% B representing $Ni_{20}Al_3B_6$ ternary phase with $M_{23}B_6$-type structure.

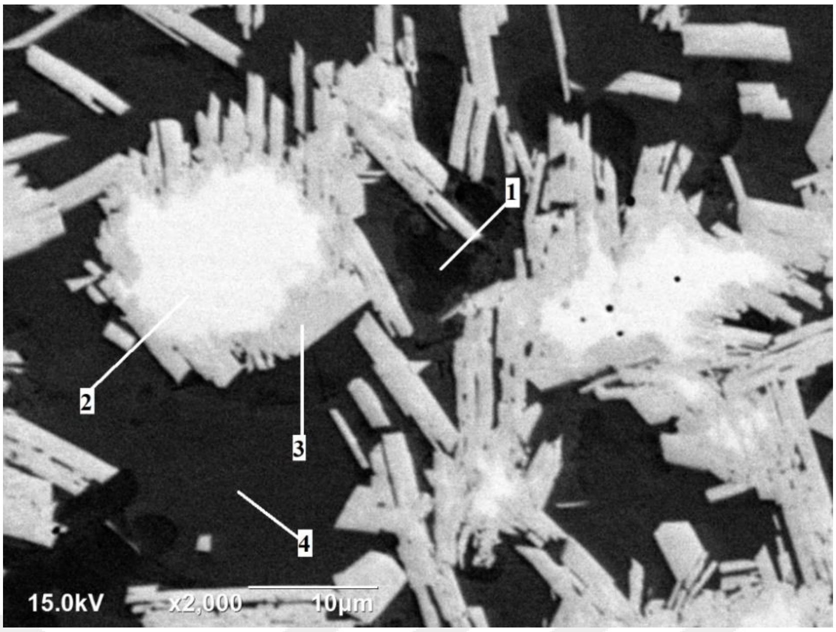

Figure 4.23 : SEM micrograph of SHS synthesized NI14 sample (×2000 magnification).

Table 4.15 : Energy dispersive spectroscopy analysis of NI14 alloy synthesized by SHS method.

Point	**Mo**	**Ni**	**Al**	**B**	**W**
1	-	86,29	12,09	-	-
2	85.93	-	-	10,36	2,05
3	70,59	22,41	-	7,00	-
4	-	94,87	5,31	-	-

Figure 4.24 shows the SEM micrograph of NI15 sample with the composition of 33.9Mo-59.8Ni-5.4B-0.9Al and Table 4.16 presents the elemental composition of this alloy. According to this figure, the sample's microstructure consists of two parts including intermetallic based reinforcement and matrix. The elemental distributions of particles composition resulted by Energy Dispersive Spectroscopy (EDS) scans, agrees well with XRD patterns whereas the largest region belongs to Mo_2NiB_2 ternary phase.

The figure reveals the existence of a) Ni_3Al (1, dark area), b) $Ni_{20}Al_3B_6$ (2, dark gray) phases formed in the matrix with the distribution of c) MoB (3, whitish-gray) small regions in the coarse particles of d) Mo_2NiB_2 (4, light gray).

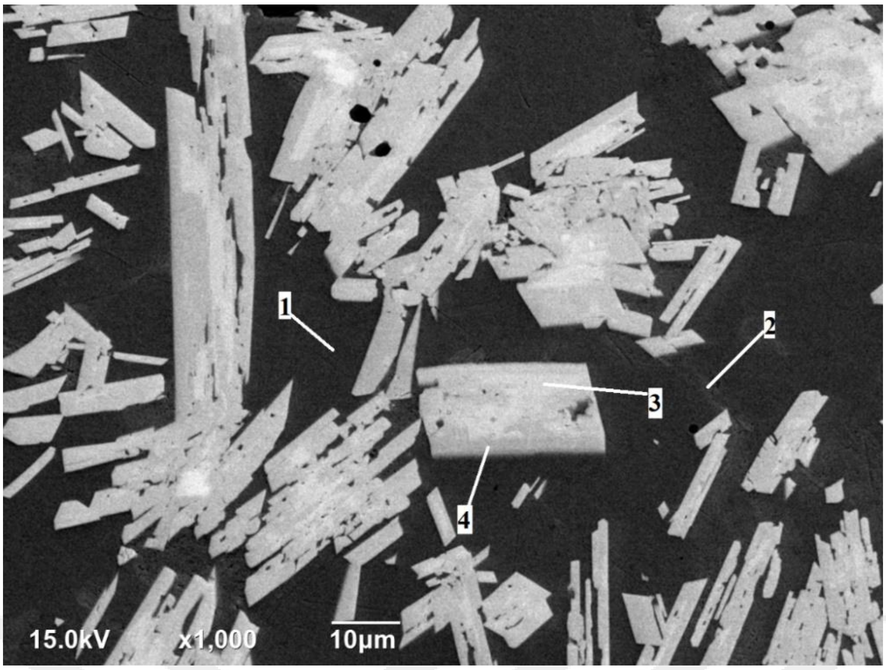

Figure 4.24 : SEM micrograph of SHS synthesized NI15 alloy (x1000 magnification).

Table 4.16 : Energy dispersive spectroscopy analysis of NI15 alloy synthesized by SHS method.

Point	Mo	Ni	Al	B
1	-	92.42	3.8	3.75
2	-	94.39	4.53	-
3	86	-	-	14.4
4	75.97	18.92	-	5.3

Image analysis results for calculating area fraction of reinforcement phase in NI11, NI14, and NI15 samples are 55, 56 and 42%, respectively. Image analysis software (ImageJ) was used to measure the fraction area of the region which exists in the matrix phase. The average area fraction of distributed particles in the presented SEM image of NI15 sample is approximately 42% with the standard deviation of 4.7 resulted from analyzing the micrographs of the alloy’s microstructures in different magnifications. The average width size of calculated 80 grains is about 7.48 um. The reinforcement/matrix ratio should decrease by the increasing of Ni in the compositions. However, the presence of excess Al in the NI11 sample results in the higher matrix area.

4.1.2 Effect of the addition of alloying elements on SHS products

Because nickel has an extensive solid solubility for many alloying elements, the microstructure of nickel alloys consists of the fcc solid-solution austenite (γ) in which dispersoid and precipitate particles can form. According to phase diagrams, nickel completely dissolves copper and has a nearly complete solution with iron. It can dissolve ~35% Cr, 20% each of molybdenum and tungsten, and 5 to 10% each of aluminum, titanium, manganese, and vanadium. Cobalt, iron, chromium, molybdenum, tungsten, vanadium, titanium, and aluminum are all solid-solution strengtheners in nickel. These elements have about 1-13% differences in atomic diameters in comparison with nickel. The addition amount of alloying elements are 5% in the composition of the produced alloy. Figure 4.25 shows the results of the combustion process such as yield of the target, material loss, and burning velocity. The target yield of the experiments, which have included additional oxides in initial mixtures, was almost equal to the values of NI7 and NI9. Burning velocity for alloys changes slightly between 1.8 and 5 mm/s, but this factor for Mn containing alloy which was equal to 5 mm/s, is a little higher than the other elements. In Mo-Ni-B-Al-X multicomponent alloys, X refers to alloying elements such as Mn, Cr, V and Ta with addition amount of 5 wt%.

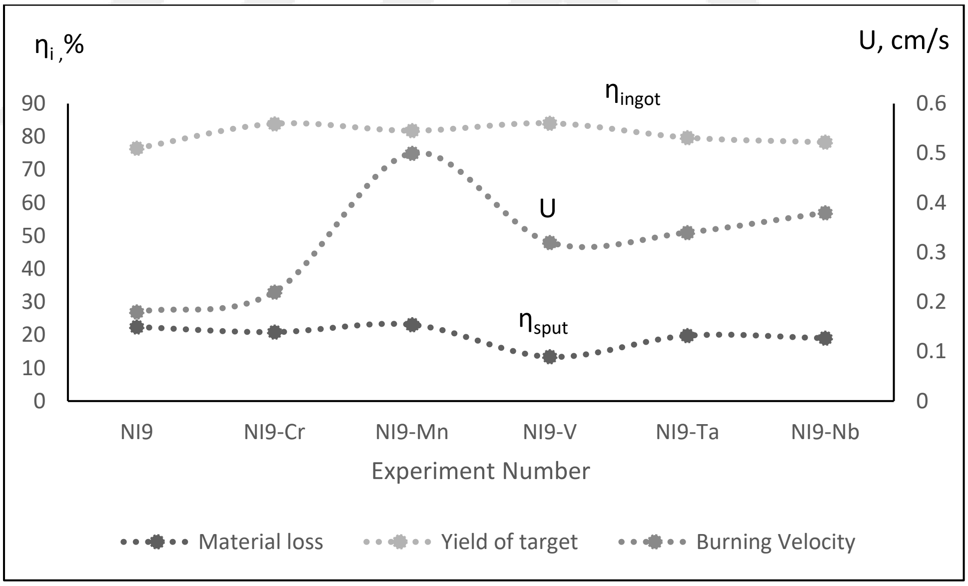

Figure 4.25 : The effect of additional alloying elements (Cr, Mn, V, Ta and Nb) on SHS parameters such as yield of target, material loss and burning velocity.

Figure 4.26 shows the XRD analyses of the SHS-synthesized as-cast products using the initial mixture of MoO_3: NiO: B_2O_3: Al and addition of other metallic oxides (such as MnO_2, Cr_2O_3, Ta_2O_3, and V_2O_5). Cr as the additional alloying element resulted in the presence of free Mo and Ni_2B in addition to the typical Mo_2NiB_2, NiAl, and Mo_2B

phases. In the case of vanadium addition, the free Mo, AlNi, Mo_2B, Ni_3V, Al_2V_3, and Mo_2NiB_2 phases formed.

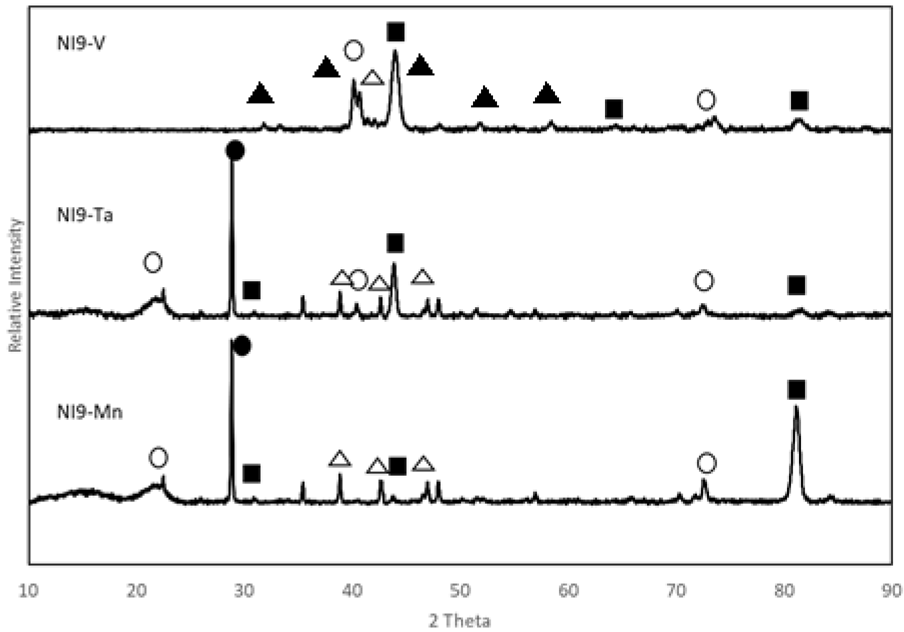

Figure 4.26 : XRD analysis of NI9-V, NI9-Ta, NI9-Mn as-cast alloys obtained from combustion synthesis method (○ Mo_2B, Δ MoB, ● AlB_{10}, ▪ NiAl, ▲Mo_2NiB_2).

Table 4.17 : The atomic absorption spectroscopy analysis results of the SHS alloys obtained from the experimental study about the effect of additional alloying elements (Cr, V, Mn, Ta and Nb)

No	Ni	B	Mo	Al	Mn	V	Cr	Nb	Ta
NI9	41.01	3.07	39.70	15.90	-	-	-	-	-
NI9-Mn	41.89	2.66	33.35	17.89	2.97	-	-	-	-
NI9-Cr	39.68	2.74	37.35	16.08	-	-	3.76	-	-
NI9-V	40.06	2.84	37.50	16.02	-	3.90	-	-	-
NI9-Ta	42.12	2.69	36.02	15.33	-	-	-	-	-
NI9-Nb	41.87	2.87	36.10	16.04	-	-	-	2.93	-

Table 4.18 shows the raw materials amounts used for the production of alloys with additional alloying elements. The raw materials mixture was the same as NI15 with the addition of Cr_2O_3, MnO_2, and V_2O_5 metal oxides.

Table 4.18 : The estimated composition and raw materials amount for experimental study about the effect of additional alloying elements (Cr, Mn and V).

No	Estimated target composition, % wt.	MoO_3 (g)	NiO (g)	B_2O_3 (g)	Al (g)	MnO_2 (g)	Cr_2O_3 (g)	V_2O_5 (g)
NI22	36.2Mo-47.1Ni-5.4B-10.9V	45	50	45	50	-	-	16
NI23	38.7Mo-51.1Ni-4.4B-5.2Mn	40	45	35	40	15	-	-
NI24	35.6Mo-46.9Ni-5.0B-11.6Cr	40	45	30	42	-	15	-
NI28	35.0Mo-50.0Ni-5.0B-10Mn	18.40	23.6	19.47	23.68	14.73	-	-

After the production of alloys, the weight of alloys and slags were used to calculate the target yield as presented in Table 4.19.

Table 4.19 : The effect of additional alloying elements (Cr, Mn and V) on yield of target.

No	Actual metal weight	Expected metal weight	Yield of target	Slag weight
NI22	64.3	82.9	77.56	-
NI23	50.9	68.8	73.98	51
NI24	60.7	74.8	81.15	71.7

All the Ni-based alloys were examined in copper 2 crucible to obtain the desired results except the NI15, NI22, NI23, and NI24 samples which produced in the schamot crucible. Schamot crucible has lower thermal conductivity with a conical shape comparing to the copper crucible. Table 4.20 shows the XRF and chemical analyses of Mo-Ni-B containing alloys with different alloying elements. The Al and Cu contents in these alloys are lower than 4 wt% and 1.9 wt%, respectively. The inclusion of W refers to tungsten filament on top of the raw material.

Table 4.20 : The atomic absorption spectroscopy analysis results of the SHS alloys obtained from the experimental study about the effect of additional alloying elements (Cr, V, Mn, Ta and Nb).

No	Mo	Ni	B	Al	W	Cu	V	Cr	Mn
NI15	26.3	57.59*	4.10*	2.20*	0	0.63*	-	-	-
NI22	27.7	43.4		8.3	0.2	1.2	9.0	-	-
NI23	27.9	46.4		3.2	0.2	1.9	-	-	9
NI24	29.0	41.48*	3.57*	2.21*	0	0.9*	-	9.44*	-
NI28	34.12	47.6	4.21	2.53	-	-	-	-	11.49

* AAS analysis results

The XRD analyses of the as-cast products obtained from the experiments by using the initial mixture of MoO_3: NiO: B_2O_3: Al and addition of other metallic oxides (such as

MnO_2, Cr_2O_3 and V_2O_5), are presented in Figure 4.27 and Figure 4.28. The basic alloy composition of this series of experiments is 34Mo-60Ni-5B. The XRD patterns of the NI23 and NI22 samples with Mn and V additions confirm the formation of Mo_2NiB_2 ternary boride. The other observed phases are Ni_3V, Ni, $MoNi_4$ (in NI22), Ni_3Al (in both Ni22 and Ni23 samples), $Al_{0.96}Ni_{1.04}$ and $Ni_{20}Al_3B_6$ (in NI23 sample) and . The addition of higher percentage of Mn (in Ni28) results in the MoB binary boride as the main constituent.

According to the literature, The $(MoNiCr)_3B_2$ type tetragonal M_3B_2 complex borides formed in the hard phase of Cr containing Mo_2NiB_2 based composites. Additional Cr changes the crystal structure from the orthorhombic Mo_2NiB_2 to tetragonal. Figure 4.27 shows M_3B_2 tetragonal crystal structure, orthorhombic Mo_2NiB_2 (as hard phase) and Metallic Ni (as the matrix). The tetragonal Mo_2NiB_2 have a crystal structure similar to that of Mo_2FeB_2.

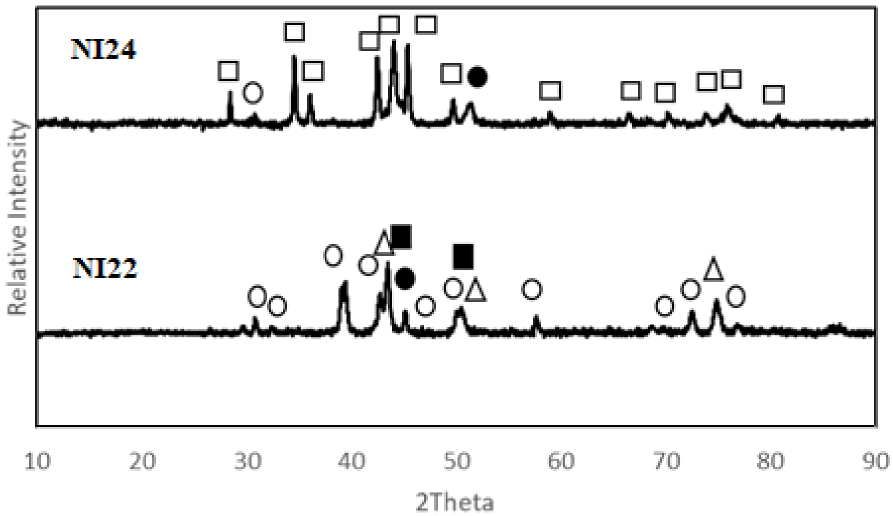

Figure 4.27 : X-ray diffraction patterns of combustion synthesized NI22 and NI24 as-cast alloys (Δ Ni_3Al, ● Ni, ▪Ni_3V, □Mo_2NiB_2 (tetragonal), ○Mo_2NiB_2 (orthorhombic)).

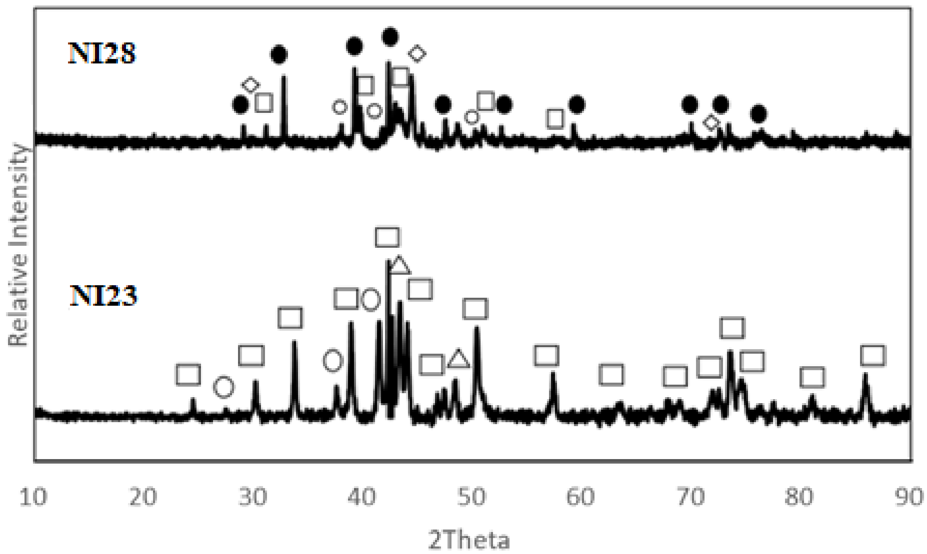

Figure 4.28 : X-ray diffraction patterns of combustion synthesized NI23 and NI28 as-cast alloys (□Mo_2NiB_2, ○$Ni_{1.04}Al_{0.96}$, Δ Ni_3Al, ◊ $Ni_{20}Al_3B_6$, ●MoB, t NiAl).

Figure 4.29 shows the SEM micrograph of the NI22 sample with 36,2Mo-47,1Ni-5,4B-10,9V composition at x2000 magnification. Table 4.21 shows the elemental composition of the hard phase and the matrix. The figure reveals that; a) $(MoNiV)_3B_2$ grains (1, Light gray area) having a rectangular shape with the inner part consist of b) MoVB (2, dark gray area) distributed in the c)Ni_3V (3, black area) matrix. According to the analysis, the V substitutes Al sites in the γ' structure formed in the matrix of nickel base SHS alloys.

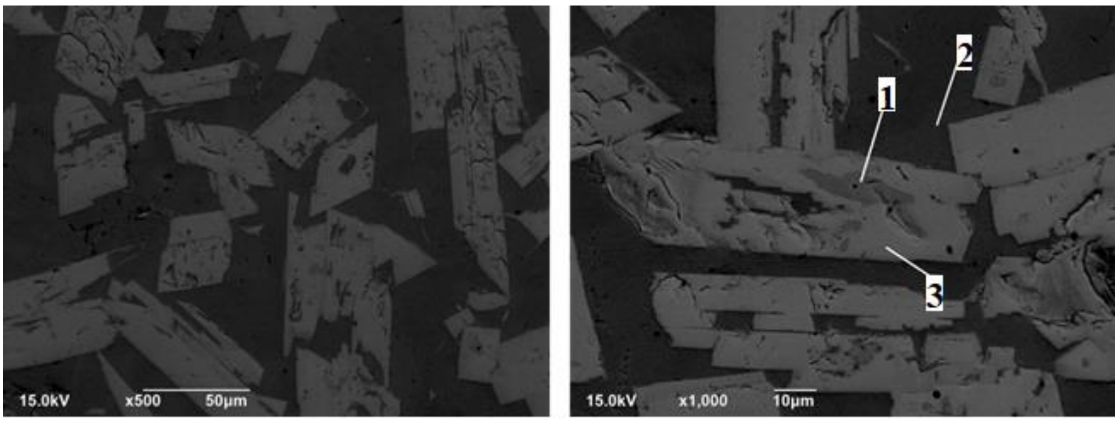

Figure 4.29 : SEM micrograph of SHS synthesized NI22 alloy (x500 and x1000 magnifications).

Table 4.21 : Energy dispersive spectroscopy analysis of NI22 alloy synthesized by SHS method.

Point	Mo	Ni	B	Al	V
1	70.5	1.29	10.8	-	17.4
2	1.6	88.8	-	1.7	7.8
3	66.5	17.1	7.4	-	9.01

The analysis of NI22 sample at lower magnifications shows that it has larger grains than the other produced Ni-based alloys. The vanadium-containing Mo_2NiB_2 grains are more isotropic having a tetragonal crystal structure.

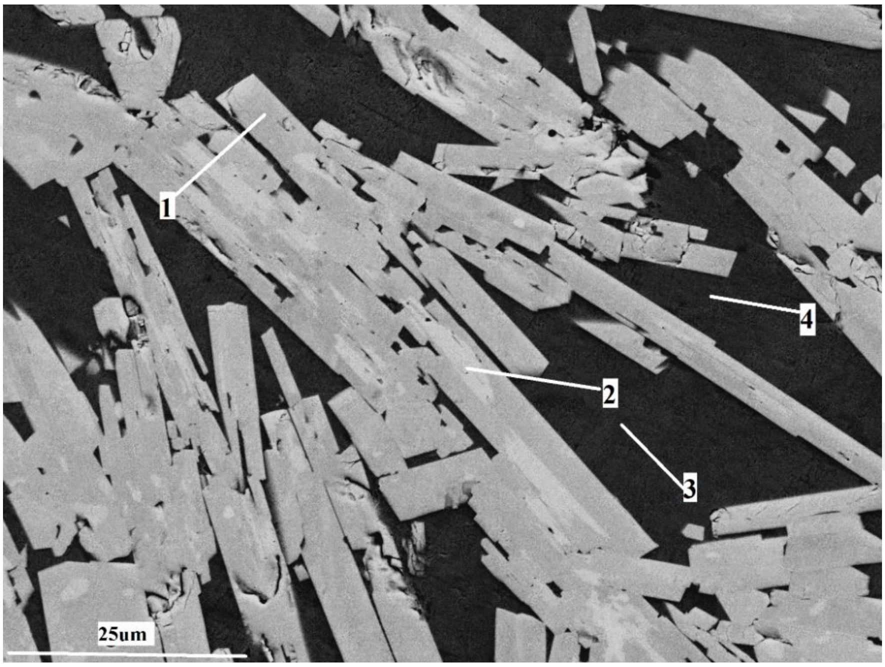

Figure 4.30 : SEM micrograph of SHS synthesized NI23 alloy (x1000 magnification).

Figure 4.30 shows the SEM micrograph of NI23 with the composition of 38,7Mo-51,1Ni-4,4B-5,2Mn having a two-phase structure. Table 4.22 presents the phase compositions of the hard phase and matrix. The figure reveals that; a) Mo_2NiB_2 (2, light gray area) are elongated grains with the inner part of b) Mo_2NiB_2 with lower nickel content (1, white area) distributed in the uniform c) Ni(Mn) matrix (3, dark gray area). The dissolution of Al, Mo, and Mn in the matrix phase are lower than 2.2 wt%, 2.9 wt%, and 11.5 wt% respectively. The distribution of elongated angular grains in the matrix is more uniform than NI15 and NI22 samples. The microstructure of Mn-containing alloys is the same as NI15 sample without additional elements. The reported studies show that the additions of silicon, tungsten, and molybdenum present effects similar to those of manganese and chromium additions in Ni-base alloys.

Table 4.22 : Energy dispersive spectroscopy analysis of NI23 alloy synthesized by SHS method.

Point	Mo	Ni	B	Al	Mn
1	76.2	15.8	7.9	-	-
2	72.1	21.8	6.1	-	-
3	2.3	84.3	-	1.8	11.5

Among the alloying elements, it is proposed to study the effect of Cr addition on the microstructure and composition of SHS-synthesized alloys. Figure 4.31 shows the SEM micrograph of NI24 sample with the composition of 35.6Mo-46.9Ni-5B-11.6Cr containing two-phase microstructure. Table 4.23 presents the elemental distributions in the matrix and hard phase composition. The figure reveals that; a) M_3B_2 (2, light gray areas) with tetragonal crystal structure distributed in b) Ni(Cr) matrix (1, black area) having a trace amount of c) (Mo, Cr)Ni with a composition of sigma phase (3, light spots).

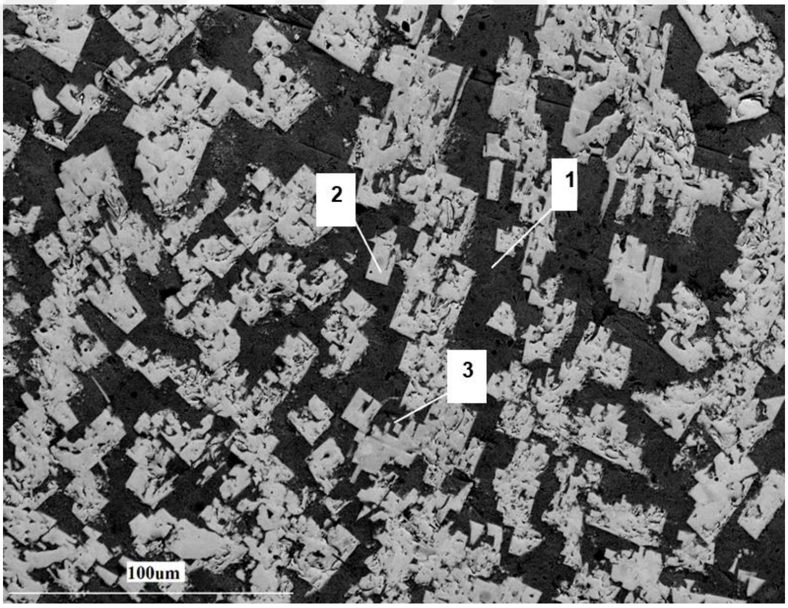

Figure 4.31 : SEM micrograph of SHS synthesized NI24 alloy (x500 manification).

Table 4.23 : Energy spectroscopy dispersive analysis of NI24 alloy synthesized by SHS method.

Point	Mo	Ni	Cr	B	Al
1	1.0	88.9	6.2	-	3.8
2	61.6	12.3	16.3	9.7	-
3	73.5	10.3	15.7	-	-

SEM analysis reveals the (MoCr)Ni phases that did not appear in XRD analysis patterns and emerged due to the interaction of electrons with the Ni-rich matrix phase. The existence of Cr in the alloy shows the refinement of grains in the microstructure. The addition of alloying elements reduces the matrix phase area fraction due to the dissolution of elements in reinforcement phase. The area fractions of reinforcement phase in NI22, NI23 and NI24 samples are 48, 52 and 49%, respectively. However, the vanadium addition in alloy NI22 causes a significant increase in the grain size. The morphology and grain size of NI23 alloy is the same as NI15 base alloy. The addition of Cr to NI15 alloy composition affects the shape and morphology of reinforcement phases and results in the reduction of the grain size.

4.1.3 Vickers microhardness testing results of the Mo_2NiB_2 containing compsoites

Table 4.24 and Table **4.25** present the Vickers microhardness (HV) and Rockwell C (HRC) values of NI1-3-5-7 and MNB3-5 samples, respectively. The hardness values change between 716 and 943 HV that NI1 and NI7 samples have the highest hardness values among all the samples. The higher B weight percentage in the MNB5 sample does not have any significant effect on the hardness. As a result, the Mo and Al contents control the phase composition of alloys and therefore, the hardness of the alloys. The samples Ni1, Ni3, Ni5, MNB1 and MNB3 comparing to the second series of experiments have relatively low hardness values due to the presence of NiAl in the matrix and also higher matrix/reinforcement ratio. The matrix/reinforcement ratio is high in these samples because Ni content is low and it has not dissolved in the reinforcement phase. By increasing NiO amount in raw materials mixture, the decrease in Al weight percentage enhances the formation of Mo_2NiB_2 ternary boride (as in sample Ni7). The Ni1 and Ni7 samples both have the same hardness values because they have the highest reinforcement area fractions of about 51% in the first series of experiments. The Ni3 and Ni5 which contain smaller particles of MoB/MoB_2 phases distributed in the larger fraction of matrix have lower hardness values of 704 and 840HV.

Table 4.24 : The effect of different NiO amounts on vickers hardness values of obtained SHS alloys.

Hardness testing No	NI1 (HV)	NI1 (HRC)	NI3 (HV)	NI3 (HRC)	NI5 (HV)	NI5 (HRC)	NI7 (HV)	NI7 (HRC)
1	965,07	69	791,95	64	1061,86	70	943,84	69
2	1022,95	69	673,79	59	945,2	69	1192,39	-
3	869,18	67	855,12	66	737,26	62	744,12	62
4	913,02	68	564,81	54	827,83	65	941,43	69
5	923,01	68	696,85	60	815,33	65	892,83	67
Average	938.65	68.2	716.5	62	877.5	66.2	942.92	66.75

Table 4.25 : The effect of different B_2O_3 amounts on vickers hardness values of obtained SHS alloys.

Hardness testing No	MNB1 (HV)	MNB1 (HRC)	MNB3 (HV)	MNB3 (HRC)	MNB5 (HV)	MNB5 (HRC)
1	965,07	69	698,7	61	806,46	65
2	1022,95	69	747,98	63	935	68
3	869,18	67	767,39	63	823,24	65
4	913,02	68	745,34	62	772,65	64
5	923,01	68	874,38	67	873,36	67
Average	938.646	68.2	819.57	63.2	842.145	65.8

The MNB5 sample with the highest B content have round grains of MoB and MoB_2 with the reinforcement fraction of 48% and hardness of 800HV. The Mo_2NiB_2 ternary boride was observed in Ni7 and MNB3 samples but with different matrix compositions. In Ni7 with lower Al content, the MoB/Mo_2NiB_2 particles were distributed in nickel rich Ni_3Al containing matrix. Therefore, the main effective parameters on the hardness of the first series of samples are the residul Al content in the final composition and the matrix/reinforcement ratio.

Table 4.26 presents the Vickers microhardness (HV) and Rockwell C (HRC) values of the NI11-14-15-30-32 samples. These values change between 805 and 1195.56 HV. The NI30 and NI11 samples have the lowest and the highest hardness values, respectively. As a result, increasing the Mo content increases the hardness of alloys due to the formation of binary borides of MoB and Mo_2B. Therefore, as it was observed in the studies about the similar alloy compositions, the increase in Mo/B ratio change the Ni base solid solutions to the Mo-rich compounds or intermetallics. However, NI30 has the lowest hardness value due to the presence of higher percentages of Al that results in the formation of MoAlB ternary phase instead of Mo_2NiB_2.

In these second series of the experiments which have excess B_2O_3 in the raw materials mixture, the hardness values of the samples are higher than first experiments due to the significant decrease of Al content in the matrix that causes the formation of Mo_2NiB_2 in the reinforcement phase. At the other hand, the presence of 3%wt. Al and the formation of dual phase Ni_3Al/ NiAl results in higher hardness value for the sample Ni10 by a precipitation strengthening in the Ni matrix. Sample Ni10 which has the highest hardness value (1196 HV), contains four reinforcement phases (α and β-MoB, MoB_2 and Mo_2NiB_2) and three matrix phases (τ-$Ni_{20.5}Al_{2.5}B_6$, NiAl, and ϒ′-Ni_3Al). When the Mo content in the composition decreased, the hardness of the alloys exhibits a small decrease because of the decrease in Mo-rich compounds like MoB binary boride in Ni14. As expected, after a certain value of Ni, the hardness values reduces due to the increasing matrix/reinforcement ratio in the as-cast alloy Ni15. Therefore, the matrix/reinforcement ratio, as well as the produced solid solutions and intermetallics have effects on the hardness of the final alloys in second series of experiments.

Table 4.26 presents the Vickers microhardness (HV) values of the NI22-23-24 samples. These values change between 832.08 and 900.3 HV with NI23 presenting the highest value. The Cr addition changes the microstructure of the sample NI24 and results in the formation of the tetragonal Mo_2NiB_2 with Mo(Ni)-Cr intermetallic phases in the grain boundaries. In this sample, the reinforcement particles with lower width to length ratio distribute in a Ni-rich matrix. There isn't any evidence of Ni-Al phases or other intermetallics in the matrix that causes a decrease in the hardness comparing to the Ni15 sample.

By addition of V in the Ni22 sample, the Ni-free Mo_2VB_2 and Mo_2NiB_2 ternary phases formed as large particles with higher width to length ratio. Accordig to the XRD and SEM/EDS analysis results, the matrix in this sample contains Ni_3V/ Ni_3Al pseudo-binary phase which imparts high hardness. By V and Cr addition to the base alloy composition (i.e. Ni15), the hardness values of 847 and 832 HV were obtained. These values are found to be close to the reported results for the compositions of Ni-4.5B-46.9Mo-12.5V and Ni-5B-51Mo-17.5Cr with hardness values of 86.4 HRA (~997 HV) and 84.4 HRA (840 HV), respectively [29]. In our study, the hardness value for V containing alloy is much lower than the obtained result in the literature due to the lower Mo content which was chosen for Ni22 composition.

Since the microstructure of Mn-containing alloy remains constant, the hardness of NI23 is similar to that of NI15 sample. The presence of Ni-Mn intermetallic in the matrix of this sample and also the related hardness value (900.3HV) are close to the reported results for the Ni-5B-53.3Mo-5Mn alloy composition with the hardness of 85.6 HRA (~ 930 HV) in the literature [29].

The hardness of ternary boride containing as-cast SHS alloys are found to range between 7 and 12 GPa. The obtained hardness values are supposed to be comparable to the coatings that made up of hard materials such as MoS_2, WC, Al_2O_3 and MoB with the high hardness values between 8.1 and 16.4 GPa [75].

Table 4.26 : Effect of additional alloying elements (Cr, Mn and V) on vickers hardness values of obtained SHS alloys.

Exp. No	HV (mean value)
NI30	805.32±152.44
NI32	976.3±75.73
NI11	1195.56±71.19
NI14	1084.2±55.56
NI15	908.7±74.38
NI22	832.08±80
NI23	900.3±75.6
NI24	847.5±83.86

4.2 Production of Mo_2FeB_2 Ternary Boride Based Alloys

In this section, the combustion synthesis in Mo-Fe-B ternary system was performed to observe the formation of Mo_2FeB_2-based composites. The effect of the addition of Al_2O_3, excess Al and B_2O_3 on adiabatic temperature was discussed using FactSage simulations and experimental trials. Also, different Fe_2O_3, B_2O_3, and Fe_2O_3/MoO_3 ratios were examined to study the effect of raw materials on the product compositions. The composition, microstructural and mechanical properties of the obtained composites were analyzed by using AAS, XRD, SEM/EDS analyses and Vickers indentation. Finally, the Cr, Mn and V alloying elements were added to three ternary systems to observe their effect on the produced Mo_2FeB_2 ternary boride and the matrix phase.

4.2.1 Effect of diluent additions on the SHS products

In the first series of experiments, the excess Al and Al_2O_3 (as diluent) and different ratios of Fe_2O_3 and B_2O_3 raw materials were used to study the effect of functional additives on the formation and microstructure of the final products. Before experiments, the simulation calculations were conducted to determine the effect of excess Al and Al_2O_3 diluents on the adiabatic temperature and produced species. The composition and microstructure of the obtained alloys change by the formation of Fe-Al intermetallics in the matrix of alloys. In the second series of the experiments, the excess B_2O_3 and the different raw materials mixtures (i.e. Fe_2O_3/MoO_3 ratios) were used to observe the effect of B_2O_3 as diluent on the final products. The phase composition, microstructure, and hardness of obtained composites were investigated to observe how they were affected by the formation of Mo_2FeB_2 in the reinforcement and Fe in the matrix. In the third series of the experiments, the microstructure of ternary boride composites was investigated to determine how it was improved by the addition of alloying elements.

4.2.1.1 Thermodynamic investigations

Before the first series of SHS experiments, 2 moles of MoO_3, 0.75 mole of Fe_2O_3, and 1 mole of B_2O_3 were equilibrated with different amounts of Al to simulate the reaction. Figure 4.32 presents the simulation of the possible product contents formed with increasing Al ratios in the initial mixture. The released heat was assumed to increase the adiabatic temperature by initiation of the exothermic reaction resulting in the formation of liquid Mo, Ni, B, and Al in the products.

Among the oxides in the initial materials mixture, B_2O_3 starts to dissolve in the slag phase due to its lower melting temperature. MoO_3 transforms into MoO_2 sub-oxide and then, it is reduced to release Mo. The primary molten nickel in the system reacts with obtained Mo to produce alloys by increasing Al ratio. Then, the reduction of B_2O_3 in the slag phase starts when Al reaches to 5 moles. The adiabatic temperature was raised by increasing Al ratio in the initial mixture and when Al content reaches to 5 moles, the undesired Al in the system dissolves in the liquid alloys. The boron reduction continues even after the complete reduction of MoO_3 and NiO oxides. By increasing the Al ratio, at the stoichiometric content of 7.5 moles Al , the maximum contents of Mo, Ni, B, and Al are formed along with the increase of the gasification. In this figure, the GAS curve refers to the total produced gaseous species.

Figure 4.33 presents the amounts of produced alloys and slags in the different reducing agent Al amounts. The SHS produced alloy weight is 281.52 gram that consists of 68.17% Mo, 26.1% Fe, 3.74% B, and 2% Al (in wt%) at the stoichiometric ratio of Al (7.5 moles) in the system. Thermodynamically, the complete reduction of metal oxides and boron trioxide occurs but the residual Al diffuses into the final product composition due to the high percentage of gas formation during combustion.

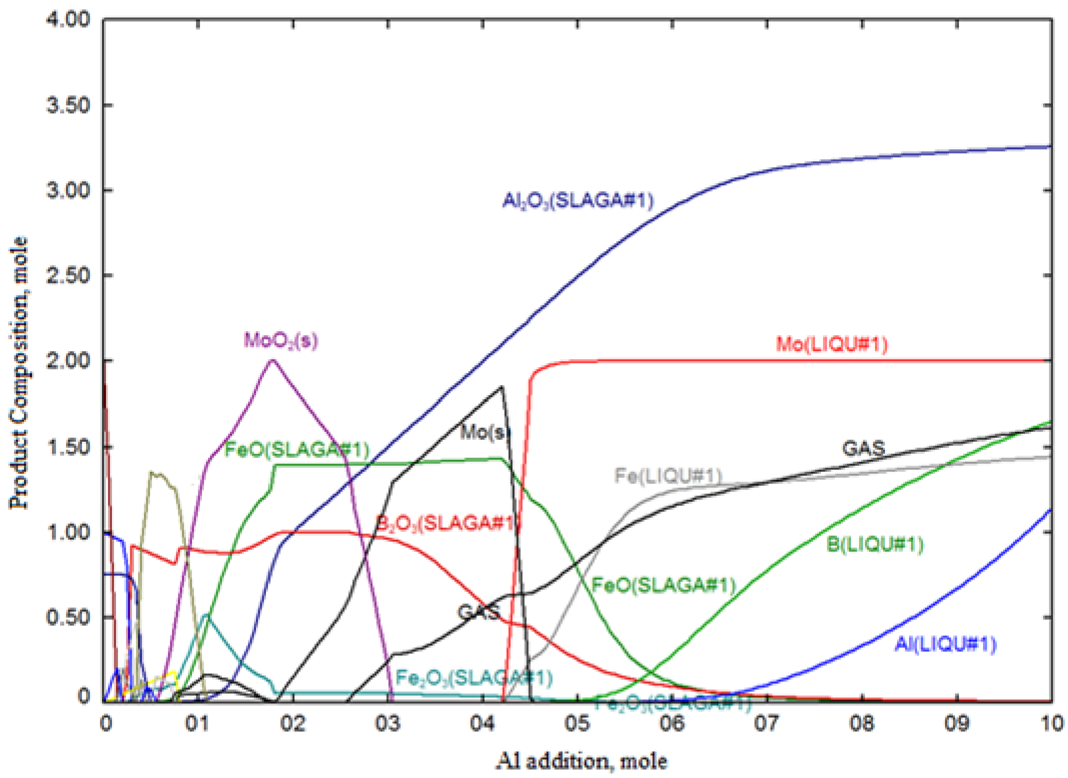

Figure 4.32 : Simulation of reaction products (molar ratio) using 2 mole MoO_3, 0.75 mole Fe_2O_3 and 1 mole B_2O_3 raw materials mixture at 1 atm and room temperature (25 °C) with different amounts of Al additions.

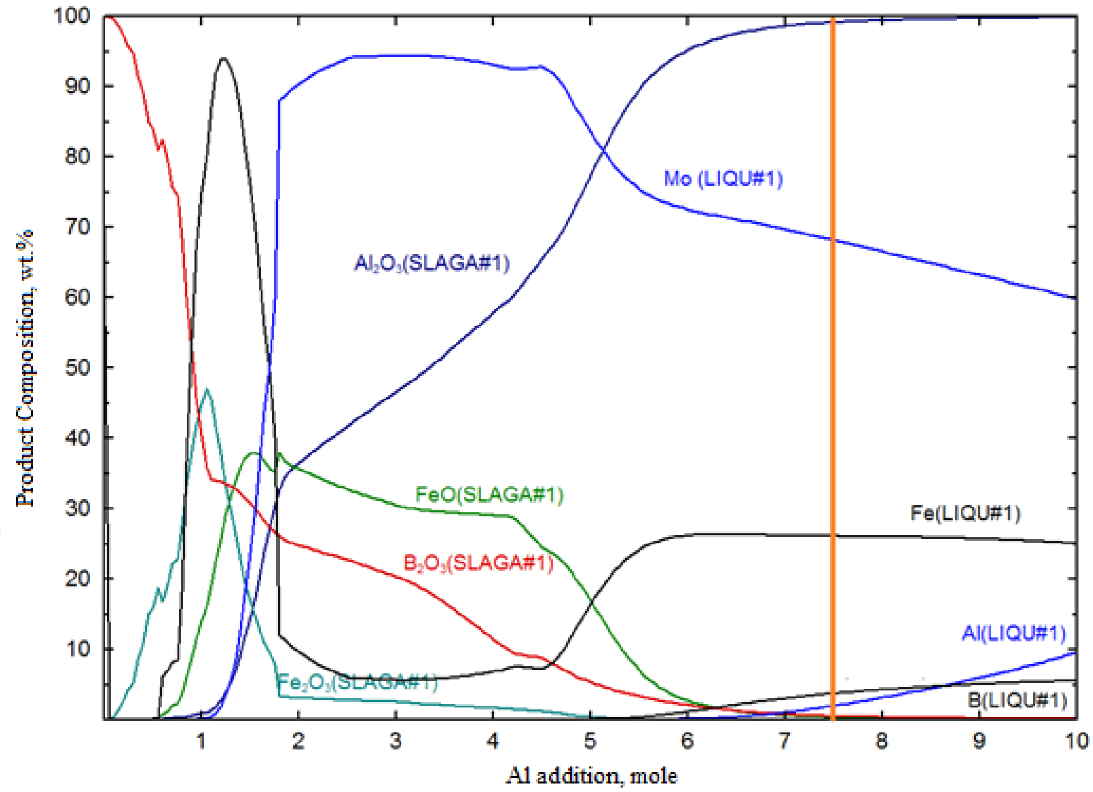

Figure 4.33 : Simulation of reacton products (%wt.) using 2 mole MoO_3, 0.75 mole Fe_2O_3 and 1 mole B_2O_3 raw materials mixture at 1 atm and room temperature (25 °C) with different amounts of Al addition.

When the excess Al with the 5% additional amount was used, the weight of obtained alloy increases to 287 gram that consists of 66.87% Mo, 26.04% Fe, 4.18% B, and 2.91% Al. The gaseous species weight equals to 1.3989 moles that comprise 11.15 weight percentage of total final products. The produced gases are 44.74% $AlBO_2$(g), 34.714% Al_2O(g), 3.34% Fe(g), 2.73% BO(g), 1.22% $(BO)_2$(g), 1.162% Al(g) and 1.113% B_2O_3(g) and other species. On the other hand, the calculated total slag weight is 326.42 gram that consists of 99.12% Al_2O_3, 0.52% B_2O_3, 0.366% FeO and 0.01% Fe_2O_3 (in wt%).

The Al_2O_3 additions to the initial mixture decrease the adiabatic temperature as shown in Figure 4.34. This functional additive reduces the loss of the material and inhibits the gasification. The amounts of Al_2O_3 addition are 0, 0.05, 0.1 and 0.15 percentages of the total initial mixture which reduce the adiabatic temperatures to 2679.7, 2651.5, 2612.8, and 2565.4 °C, respectively.

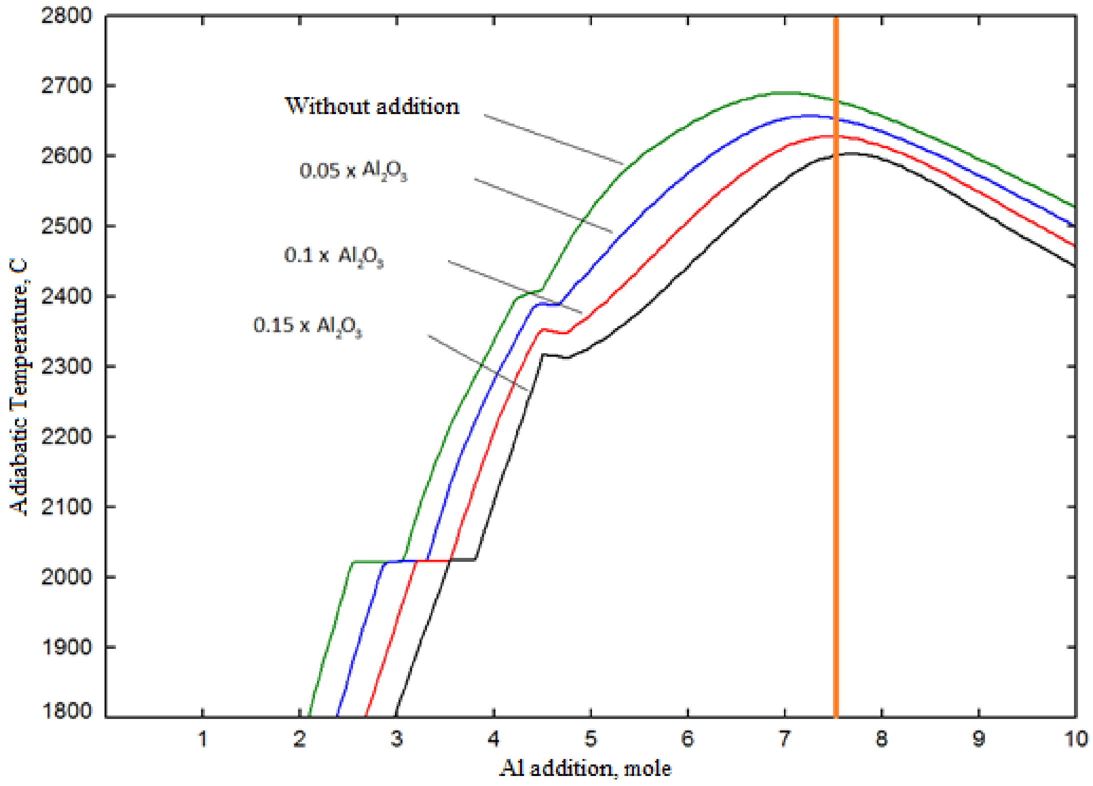

Figure 4.34 : Simulation of adiabatic temperature variation versus different amounts of Al and Al_2O_3 additions using 2 mol MoO_3, 0.75 mol Fe_2O_3 and 1 mol B_2O_3 raw materials mixture at 1 atm and room temperature (25 °C).

4.2.1.2 Effect of excess Al and Al_2O_3 addition on SHS products

In the experiments, the amounts of MoO_3, Fe_2O_3, and B_2O_3, and their ratios were fixed to observe the effect of Al and Al_2O_3 addition on the yield of target and materials loss. The amounts of Al and Al_2O_3 addition change between 0 and 10 (% of total initial mixture weight).

Also, the target yield, materials loss, and burning velocity values were found to change with excess Al and Al_2O_3 diluents. Figure 4.35 presents that the target yield values range between 70% and 80% while the loss of materials values change between 20% and 30% using different Al_2O_3 additions.

Table 4.27 shows the effect of Al_2O_3 addition on the elemental compositions of obtained SHS alloys. The elemental analysis results confirmthat impurities such as Al, Cu, and W contents in the compositions reach to the maximum of 11, 4, and 3.6 wt%, respectively. The optimum Al and Al_2O_3 additions were 5% and 10 wt% of total initial mixture.

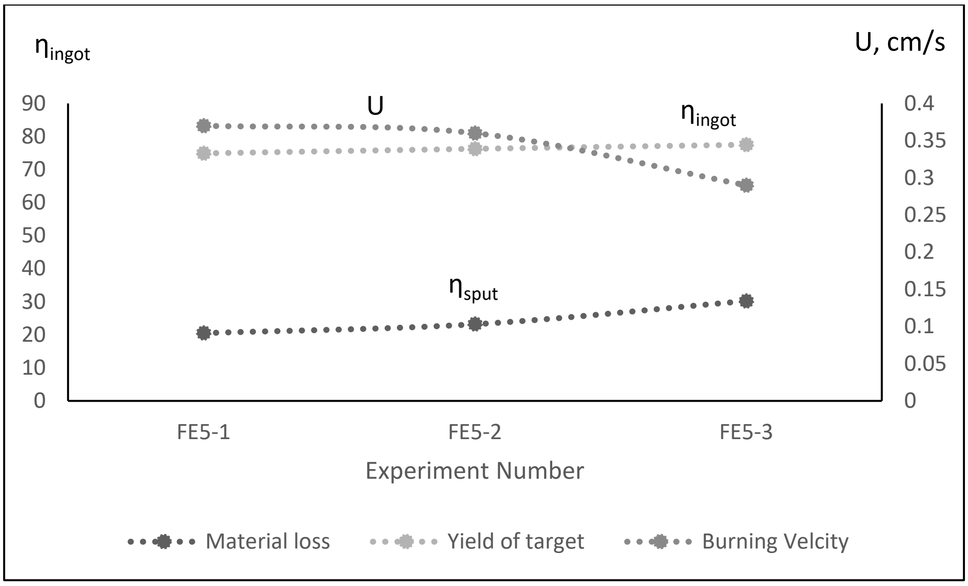

Figure 4.35 : The effect of Al_2O_3 addition on SHS parameters such as Yield of target, Material loss and Burning velocity.

Table 4.27 : The XRF analysis results of the SHS alloys obtained from experimental study about the effect of Al_2O_3.

Exp. No	Mo	Fe	Al	Cu	W	Si
FE5-1	42.45	37.69	11.27	4.18	3.6	0
FE5-2	45.53	39.97	8.86	2.6	0.97	1.65
FE5-3	48.49	39.07	5.96	4.19	0	1.12

Effect of initial Fe_2O_3 additions on SHS products

In the following experiments, the combination of 5% Al and 10% Al_2O_3 was used to reduce the combustion temperature. Besides the 5% excess Al and 10% Al_2O_3, 18 to 30 (wt%) of Fe_2O_3 were used to observe the effect of oxide ratios on composition. Table 4.28 shows the initial mixture amounts with increasing Fe_2O_3.

Table 4.28 : Raw materials amounts for combustion synthesis of FE1 to FE12 samples.

No	**Estimated composition, % wt.**	**MoO_3**	**Fe_2O_3**	**B_2O_3**	**Al**	**Al_2O_3**
FE1	64,13Mo-28,66Fe-7,22B	76,97	32,78	18,62	56,92	9,30
FE2	63,64Mo-29,87Fe-7,16B	76,97	34,42	18,62	57,5	9,40
FE3	62,75Mo-30,62Fe-7,06B	76,97	36,08	18,62	58,12	9,50
FE4	61,04Mo-32,74Fe-6,87B	76,97	39,36	18,62	59,28	9,70
FE5	59,43Mo-34,52Fe-6,69B	76,97	42,62	18,62	60,44	9,90
FE6	57,57Mo-35,98Fe-6,47B	76,97	45,92	18,62	61,53	10.15

Table 4.28 (continued) : Raw materials amounts for combustion synthesis of FE1 to FE12 samples.

No	Estimated composition, % wt.	MoO_3	Fe_2O_3	B_2O_3	Al	Al_2O_3
FE7	56,18Mo-37,53Fe-6,31B	76,97	49,05	18,62	62,73	10.36
FE8	64.13Mo-28.66Fe-7.22B	57.73	24.58	13.96	40.67	6.90
FE9	61.04Mo-32.74F-6.87B	57.73	29.52	13.96	42.30	7.20
FE10	57.57Mo-37.98Fe-6.47B	57.73	35.70	13.96	44.15	7.30
FE11	52.88Mo-41.25Fe-5.87B	57.73	42.99	13.96	46.80	7.40
FE12	48.77Mo-45.72Fe-5.51B	57.73	51.58	13.96	49.70	7.50

The effect of Fe_2O_3 amount on yield of target and material loss of obtained products and burning velocity are presented in Figure 4.36. The maximum target yield (with 76.16% value) belongs to the FE3 sample. The target yield for different compositions is the subtraction of the excess Al weight from the alloy weight.

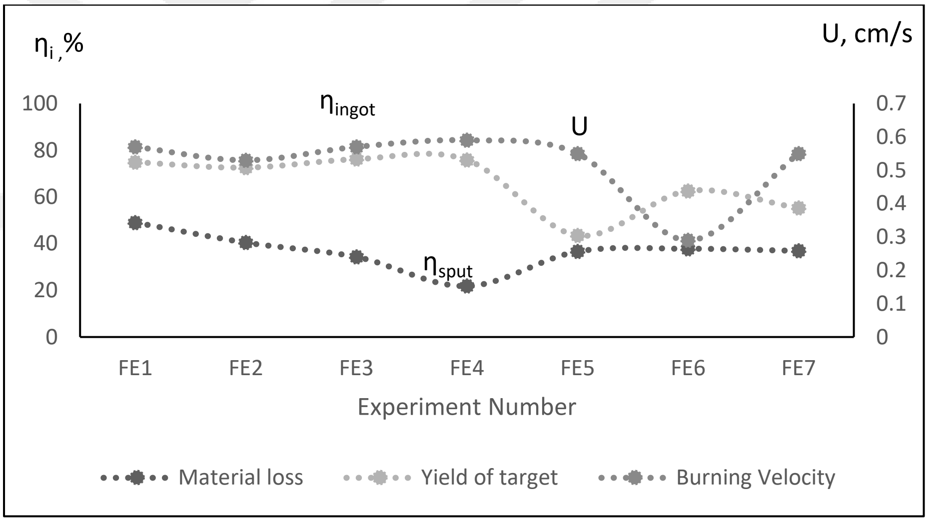

Figure 4.36 : The effect of Fe_2O_3 addition on SHS parameters such as Yield of target, Material loss and Burning velocity.

SEM/EDS analysis method was used to detect the microstructure; In this case, Figure 4.37 presents the SEM micrograph of the FE3 sample at X500 magnification. The FeAl intermetallic (point1) forms due to the high Al concentration (12.4 wt%) in the matrix phase of the FE3 sample. The light gray regions consist of MoB and MoFe phases (points 2 and 3). The excess Cu and Mo dissolve in the Ni-rich matrix phase. The large plate-like regions are Mo-rich oxide phases which formed due to the oxidation.

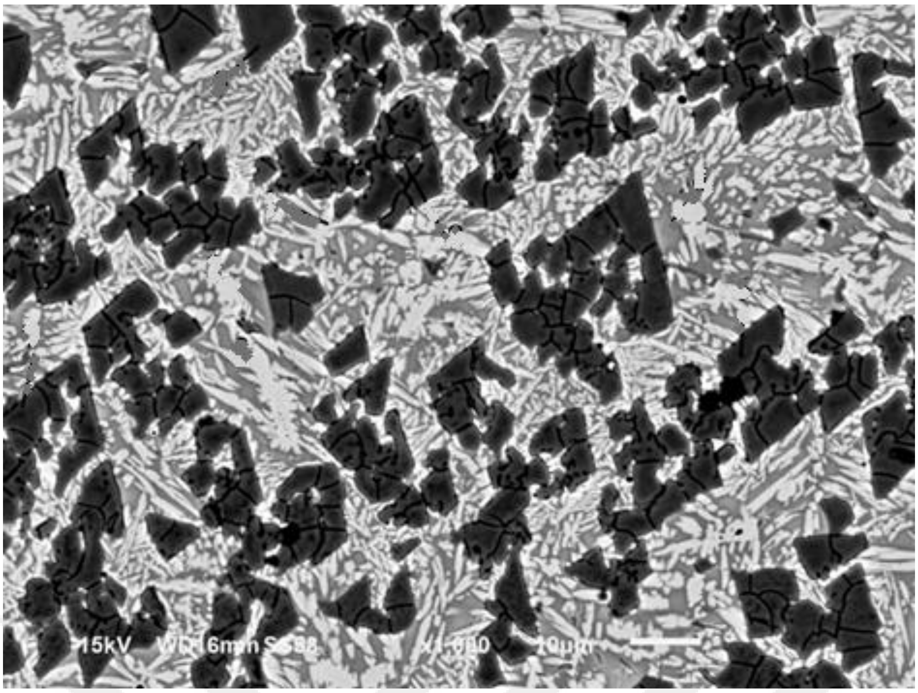

Figure 4.37 : SEM-BSE micrograp of SHS synthesized as-cast FE3 sample at x1000 magnification.

The target yield and material loss change between 45 and 80% by increasing the Fe_2O_3 amount as shown in Figure 4.38. The burning velocity of this system was slower than the velocity of nickel-containing system.

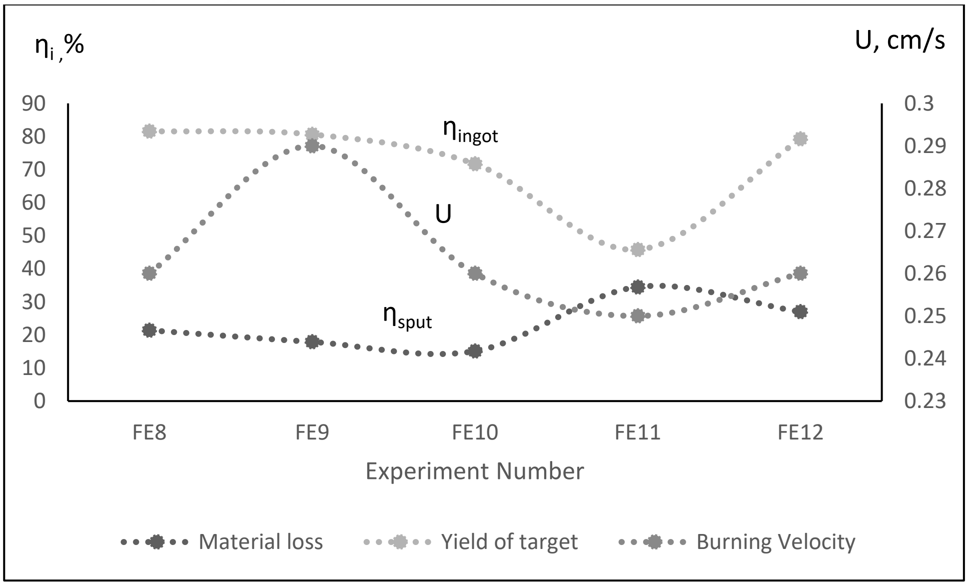

Figure 4.38 : The effect of Fe_2O_3 addition on SHS parameters such as Yield of target, Material loss and Burning velocity.

Table 4.29 presents the compositions of alloys obtained by changing the initial mixture. The impurity elements such as Cu and W appear in the final compositions originating from the Cu wire and tungsten filament.

Table 4.29: XRF analysis results of SHS alloys obtained from the experimental study about effect of Fe_2O_3 and B_2O_3 additions.

Exp. No	Mo	Fe	Al	Cu	W
FE8	54.39	35.16	4.13	3.10	1.00
FE10	49.47	40.98	2.43	3.38	3.13
FE12	40.17	47.98	4.12	4.00	2.63
MFB8	52.17	33.74	4.34	5.59	3.48

After the elemental analysis, the x-ray diffraction method was used to interpret the effect of Fe_2O_3 on the phase composition. Figure 4.39 presents the XRD patterns of FE8, FE10, and FE12 alloys. Ternary boride Mo_2FeB_2 appears at 17 wt.% of Fe_2O_3 in the initial mixture. But, the dominant phases in the FE8 sample are MoB and MoFe. In this sample, FeAl forms in the matrix. By increasing Fe_2O_3 content to 23.5 wt.% in the FE10 sample, Mo-rich phases disapear while Mo_2FeB_2 becomes the dominant phase. Further increasing Fe_2O_3 in the sample FE12, increases the Fe-rich phases. All the samples contain FeAl phase in the matrix due to the high Al concentrations.

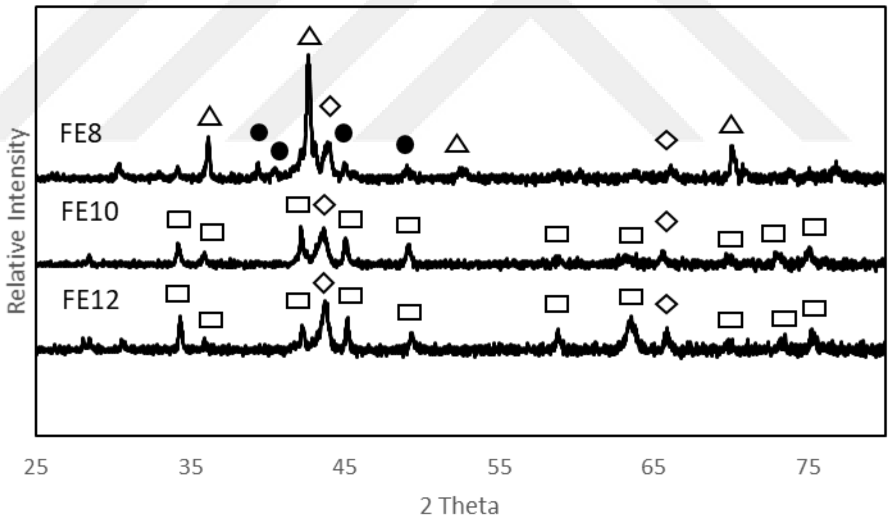

Figure 4.39 : XRD analysis results of FE8, FE10, and FE12 as-cast alloys obtained from combustion synthesis (□ Mo_2FeB_2 (01-089-3630), ◊ FeAl (03-065-6132), ● MoFe, Δ MoB (00-006-0644)).

Figure 4.40 presents the SEM micrograph of FE8 sample at X500 magnification. The elemental distributions of phases which are revealed by EDS analysis for the FE8 as-cast alloyare listed in Table 4.30. The FeAl forms in the matrix (point1) due to the high weight percentage of Al (15.33wt%) in the sample. The Fe and Mo dissolve in both matrix and reinforcement phases; however, the excess Cu dissolves only in the matrix. The compounds μ and Fe_2Mo in the Fe-Mo system treated as (Al, $Fe)_7Fe_2$(Fe, Mo)$_4$ and (Fe, Mo)$_2$(Al, Mo) in the Al-Fe-Mo system, respectively as reported [3]. Therefore, the EDS analysis reveals that the dark gray areas composition is close to the latter one i.e. (Fe, Mo)$_2$(Al, Mo). The capillary needle-like grains (point 2) which composed of MoB phase without any impurities disperse in the matrix phase.

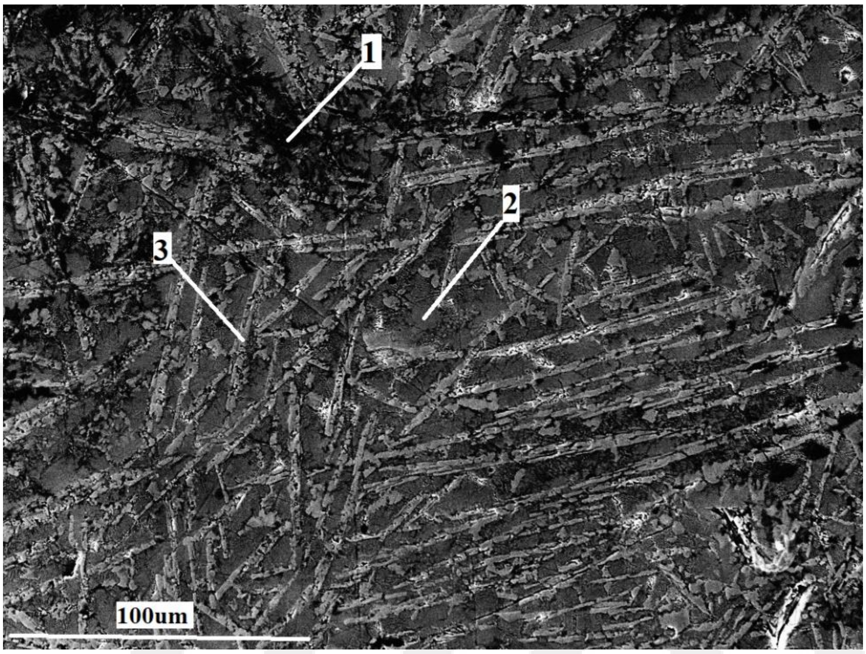

Figure 4.40 : SEM micrograph of SHS synthesized as-cast FE8 sample at x500 magnification.

Table 4.30 : Elemental analysis results of SHS synthesized FE8 sample, %wt.

No	Mo	Fe	Al	B	O
1	39.72	41.56	18.72	-	-
2	89.27	1.63	-	7.52	1.58
3	43.19	38.76	18.04	-	-

Figure 4.41 presents the SEM micrographs of FE10 sample at X500 magnification. The elemental distributions of the phases in the FE10 as-cast alloy which are revealed by EDS analysis are listed in Table 4.31. The FeAl forms in the matrix due to the high content of Al (9.09wt%). The Mo and Fe in the matrix form (Fe, Mo)$_2$(Al, Mo) which corresponds to point1. The excess Cu has been dissolved in the matrix phase but has not been dissolved in the reinforcement phase. The elongated grains, unlike sample FE8, dissolved more Fe and composed of (Fe, Mo)$_2$B and Mo_2FeB_2 phases (point 2). By increasing Fe_2O_3, these phases are more likely to be formed due to having lower negative energy of formation than Fe_2B and Mo_2B.

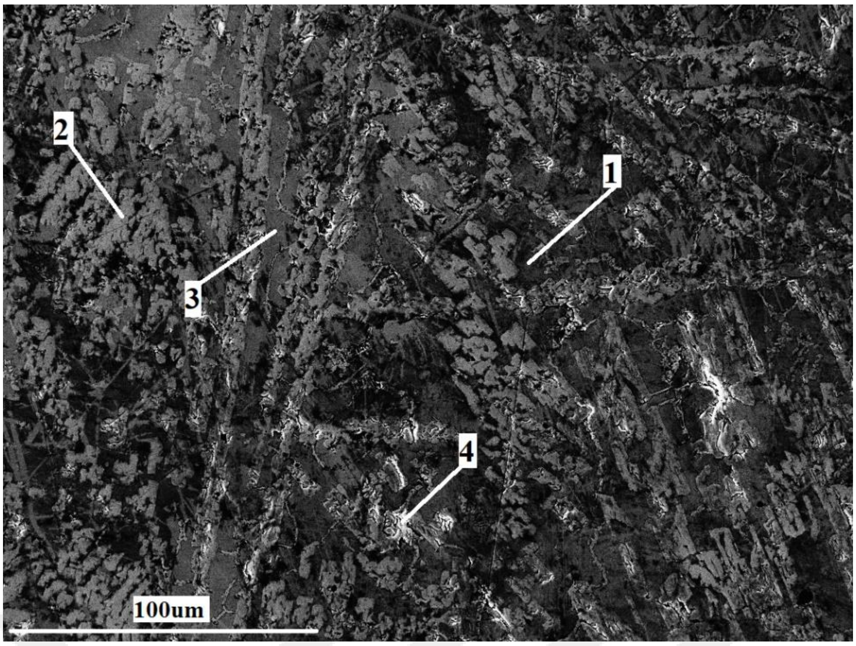

Figure 4.41 : SEM micrograph of SHS synthesized as-cast FE10 sample at x500 magnification.

Table 4.31 : Elemental analysis results of SHS synthesized FE10 sample, %wt.

No	Mo	Fe	Al	B	Cu
1	82.02	11.94	0.39	3.59	-
2	35.07	46.78	12.97	-	5.19
3	37.62	44.80	12.70	-	4.87

Figure 4.42 presents the SEM micrograph of FE12 sample at X500 magnification. The elemental distributions of phases which are revealed by EDS analysis for the FE12 as-cast alloy, are listed in Table 4.32. The FeAl forms in the matrix due to the high weight percentage of Al (9.09wt%). The Mo and Fe form (Mo, Al)(Fe, Mo)$_2$ in matrix phase corresponding to the point2. The excess Cu has been dissolved in the matrix phase but has not been dissolved in the reinforcement phase. There are dendritic eutectic phases (point 1) and grains with rectangular shapes (point 2) that include MoFe (close to sigma phase) and Mo_2FeB_2 intermetallic phases, respectively. The sigma phase in Fe-Mo systems is an intermetallic that can precipitate at grain boundaries as a secondary phase and it causes brittleness [4]. The binary Mo-B phases disappeared in this sample due to having the highest iron weight percentage (44.6wt%). Figure 4.42 shows that the composition is in agreement with the x-ray diffraction pattern of this sample that Mo_2FeB_2 phase has the highest peak intensity.

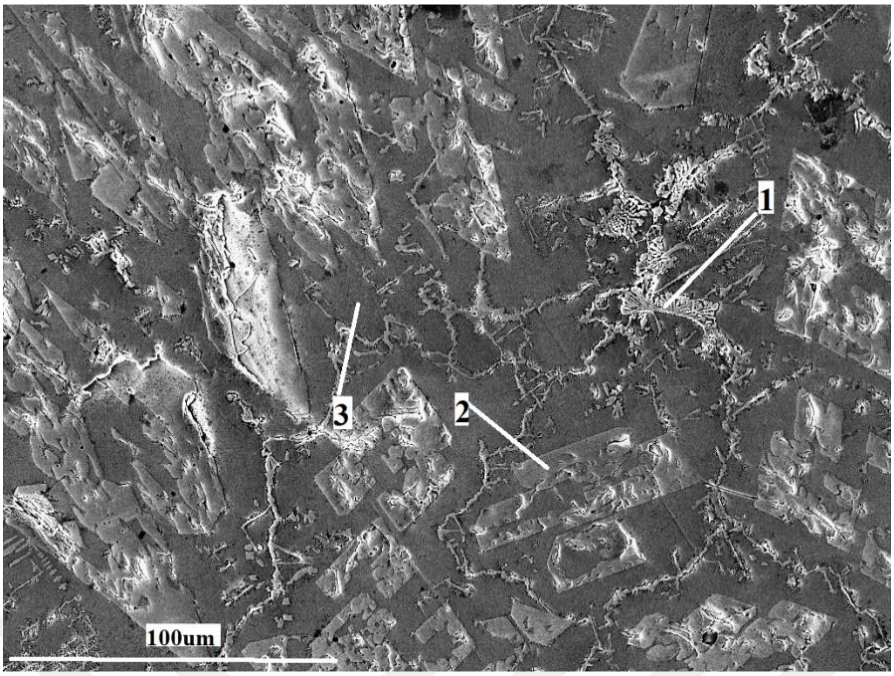

Figure 4.42 : SEM micrograph of SHS synthesized as-cast FE12 sample at x500 magnification.

Table 4.32 : Elemental analysis results of SHS synthesized FE12 sample, wt%.

No	Mo	Fe	Al	B	Cu
1	74.45	22.15	2.19	-	1.21
2	80.84	16.10	-	3.06	-
3	30.12	51.52	12.76	-	5.59

Effect of initial B_2O_3 additions on SHS products

Besides the Fe_2O_3 addition to the initial mixture, the SHS parameters and phase composition changes were studied by using B_2O_3 additions. Table 4.33 shows the amounts of raw materials with increasing B_2O_3 between 19,53 and 24.18 gram. The alloys numbers are MFB1, MFB2, MFB3, MFB4, and MFB5.

Table 4.33 : Raw materials amounts for production of samples with increasing B_2O_3 amount.

No	Estimated target composition, % wt.	MoO_3	Fe_2O_3	B_2O_3	Al	Al_2O_3
MFB2	63,89Mo-28,55Fe-7,55B	76,97	32,78	19,53	57,65	9,35
MFB3	63,66Mo-28,45Fe-7,88B	76,97	32,78	20,47	58,4	9,43
MFB4	63,21Mo-28,25Fe-8,54B	76,97	32,78	22,32	59,90	9,59
MFB5	62,76Mo-28,05Ni-9,18B	76,97	32,78	24,18	61,41	9,77
MFB7	63.66Mo-28.45Fe-7.88B	57.73	24.58	15.35	43.80	7.6
MFB8	63.21Mo-28.25Fe-8.54B	57.73	24.58	16.70	44.90	7.7

The increase in the stoichiometric B_2O_3 was examined to study its effect on the yield of the target, material loss, and burning velocity as presented in Figure 4.43. The yield of target changes with the composition in the range of 65.67-82.68% and the materials loss values between 14.5 and 18.05%. The burning velocity is almost constant with the average value of 4.6 mm/s. The total boron weight percentage increases up to 8.54wt%.

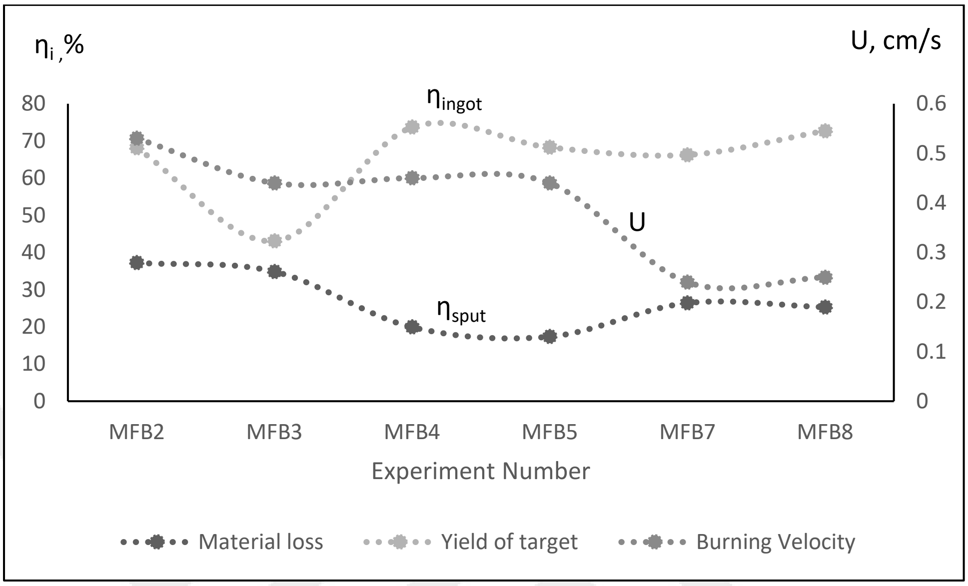

Figure 4.43 : The effect of B_2O_3 addition on SHS parameters such as Yield of target, Material loss and Burning velocity.

Figure 4.44 presents the SEM micrograph of MFB5 sample at X500 magnification. The elemental distributions of the phases in the as-cast alloy were revealed that the FeAl forms due to the high weight percentage of Al (14wt%) in matrix phase as observed in the dark gray region (point1). The Cu and Mo elements dissolved in the matrix phase. The clusters of (light gray) eutectic grains (points 2 and 4) have the highest boron weight percentage with the composition close to MoB_2 binary phase.

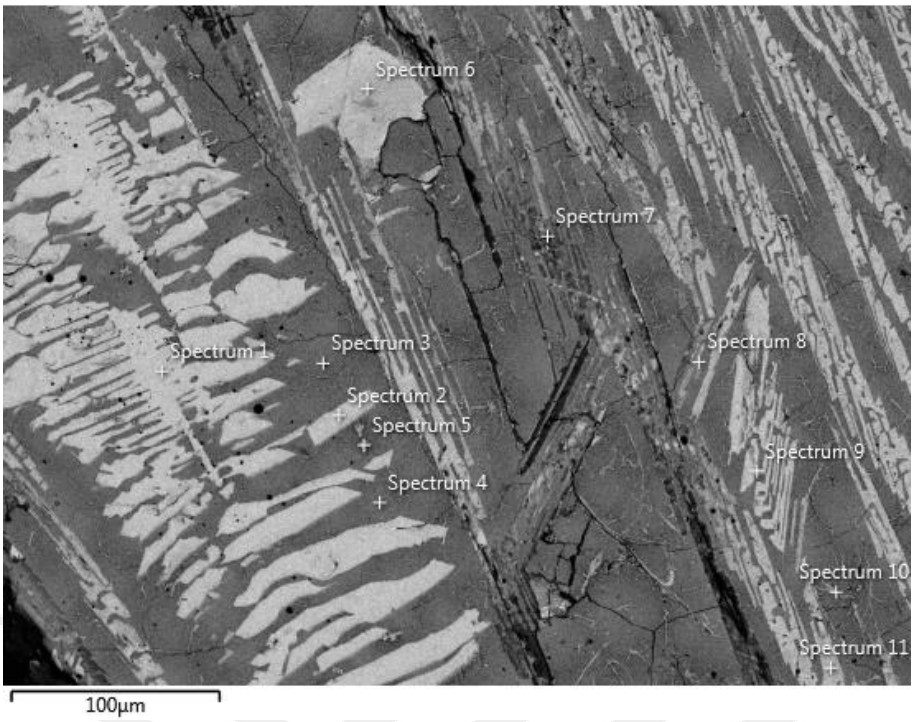

Figure 4.44 : SEM-BSE micrograph of SHS synthesized as-cast MFB5 sample at x500 magnification.

According to the XRD result of MFB8 sample using B_2O_3 addition to the initial mixture, this sample composes of free Mo, MoB, $Mo_{0.125}$Fe0..875 and $Fe_{14}Al_{86}$. The formation of Mo_2FeB_2 was retarded due to the production of Mo-rich phases in this sample. The high Al dissolution in the alloy resulted in the presence of free Mo and the formation of iron aluminide in the product.

Figure 4.45 presents the SEM micrographs of MFB8 sample at X500 magnification. Also, the elemental distributions of the phases which are revealed by EDS analysis for the MFB8 as-cast alloy are listed in Table 4.34. FeAl forms in the matrix (dark gray, point1) due to the high weight percentage of Al (18.64wt%). The elements such as Cu and Mo dissolve in the matrix. The needle-like particles (gray, point 2) and large rectangular grains (point 3) compose of MoB and MoAl, respectively. The particles dispersed on the upper surface of the sample (light gray) are Al-rich phases.

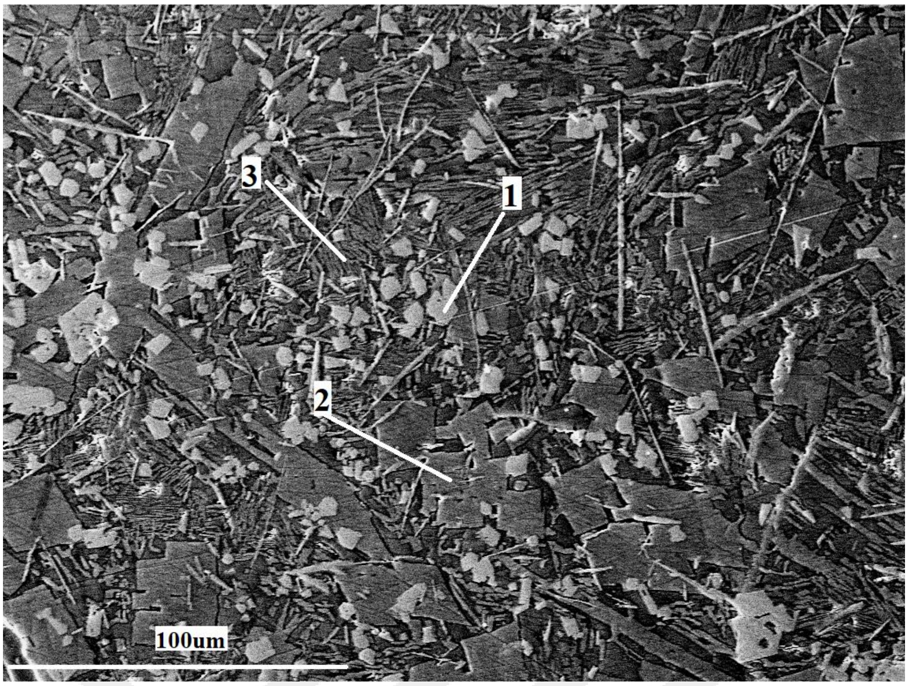

Figure 4.45 : SEM/BSE analysis micrograph of SHS synthesized as cast MFB8 sample.

Table 4.34 : Elemental analysis results of SHS synthesized MFB8 sample, wt%.

No	Mo	Fe	Al	B	Cu
1	73.63	13.93	11.17	-	1.26
2	49.63	4.78	35.84	-	9.75
3	9.12	50.66	27.08	-	13.15
4	90.21	1.87	-	6.48	-

The reinforcement area fractions of MFB5, FE8, FE10, FE12, and MFB8 samples were calculated by image analysis of SEM micrographs (at lower magnifications x500) that the obtained values are 57.85, 34.34, 36.9 and 25.49%, respectively. The FE8, FE10, and FE12 alloy's reinforcement/matrix ratio decreases by increasing iron weight percentage in composition.

4.2.1.3 Effect of excess B_2O_3 on the SHS products

The B_2O_3 addition to the initial mixture was examined to observe its effect on the adiabatic temperature and microstructure of obtained alloys. The excess B_2O_3 was used in the initial mixture with an Al content lower than the stoichiometric amount.

Effect of different Fe_2O_3/MoO_3 ratio on SHS products

The amounts of raw materials mixture for production of FE14, FE19 and FE21 samples with decreasing Fe weight percentage from 56.2 wt.% to 38.1 wt.% are presented in Table 4.35.

Table 4.35: Raw materials amounts for production of alloys with different Fe_2O_3/MoO_3 ratio.

No	Target compositions	MoO_3	Fe_2O_3	B_2O_3	Al
FE14	36.4Mo-56.2Fe-6.9B	40	60	40	50
FE19	47.58Mo-46.5Fe-5.88B	27	25.92	30	24.69
FE21	55.6Mo-38.1Fe-5.89B	31	20.93	18.6	25.58

Figure 4.46 presents the XRD analyses of the SHS-synthesized as-cast alloys using the initial mixture of MoO_3: Fe_2O_3: B_2O_3: Al. This figure shows the produced phases through SHS by excess B_2O_3 in the raw materials. The Mo_2FeB_2 ternary boride appears as the main phase in all these samples. The matrix phase consists of the mixed Fe/FeAl phases only in the sample FE21. This figure shows that existing phases from the highest to the lowest intensities are Mo_2FeB_2, MoB, and Fe. Decreasing the Mo/Fe weight percentage from 1.2% to 0.65% does not change the Mo_2FeB_2 ternary phase, but the intensity of MoB in the samples decreases. As it was reported for the same compositions [60], a small amount of Fe_3B phase also appears in FE19 and FE14 samples due to the excess Fe and B content.

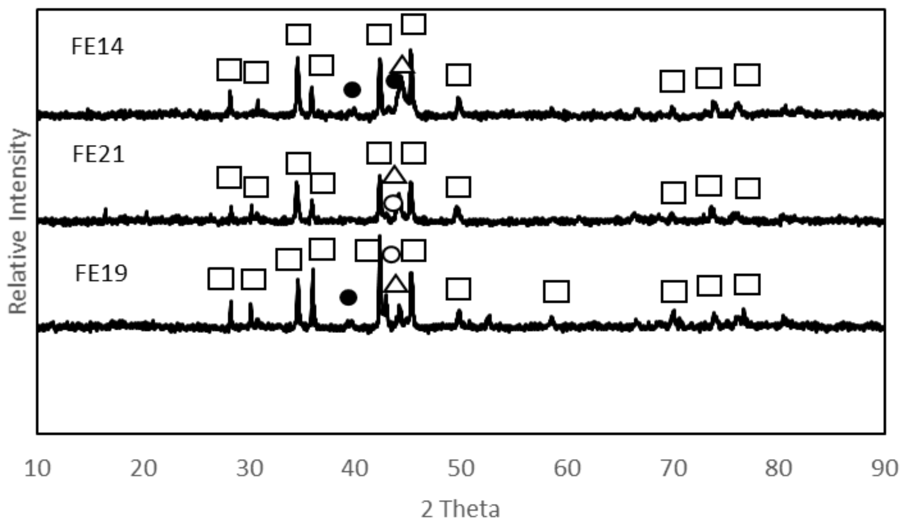

Figure 4.46 : XRD analysis of FE21, FE19 and FE14 samples (□ Mo_2FeB_2 (01-089-3630), ○ MoB (00-006-0644), Δ Fe (00-006-0696), ● Fe_3B (00-039-1315)).

Figure 4.47 presents the SEM micrographs of FE19 sample at X500 magnification. Also, the elemental distributions of the phases in as-cast alloys revealed that Fe_3Al forms in the matrix (dark gray, point 1) due to the low weight percentage of Al (3wt%). The coarse angular grains (point 2, 4) consist of Mo_2FeB_2 ternary boride. The fine rounded grains distributed uniformly in the matrix consist of Mo_2FeB_2 ternary boride without any impurities in composition. The eutectic grains (point 3) which dispersed in the matrix of the sample have the composition similar to MoFe binary phase. According to the Image analysis results, the reinforcement/matrix ratio is 60% area fraction which is the highest among all other alloys.

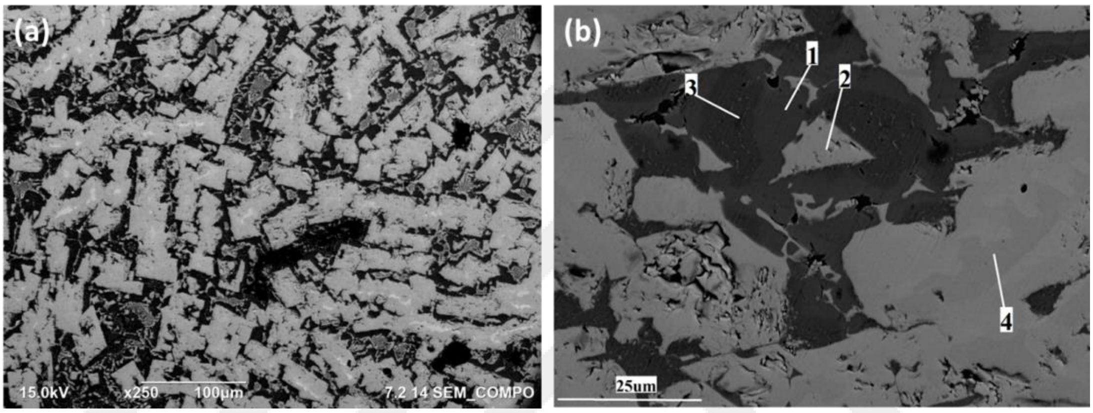

Figure 4.47 : SEM/EDS analysis results of FE19 sample (a) x250, (b) x2000 magnifications.

Figure 4.48 shows the SEM/BSE image of as-cast alloy (FE14) with 36,4 Mo-56,2Fe-6,9B composition. The matrix/reinforcement structure of this sample and its ratio was calculated by using the ImageJ. There are two types of grains including the angular coarse grains and fine particles dispersed in the matrix phase. Iron-rich phase formed in the matrix through dissolving the 3wt% Al and 4wt% Mo. The reinforcement phase with an average area fraction of 40% and a standard deviation of 5.9 has a homogeneous composition of Mo_2FeB_2 ternary boride which is confirmed by EDS spectroscopy. As it was observed in Fe alloys with the 1.1 mass% B and 5 mass% Mo additions is possible [27], the formation of Mo_2FeB_2 is more probable than other ternary borides. The EDS results show that the matrix phase contains a homogeneous Fe (Al) solid solution. The grains have rectangular shapes with an average width size of 12.45 um. The size of these grains is smaller than the grains of the FE19 sample with higher Mo content.

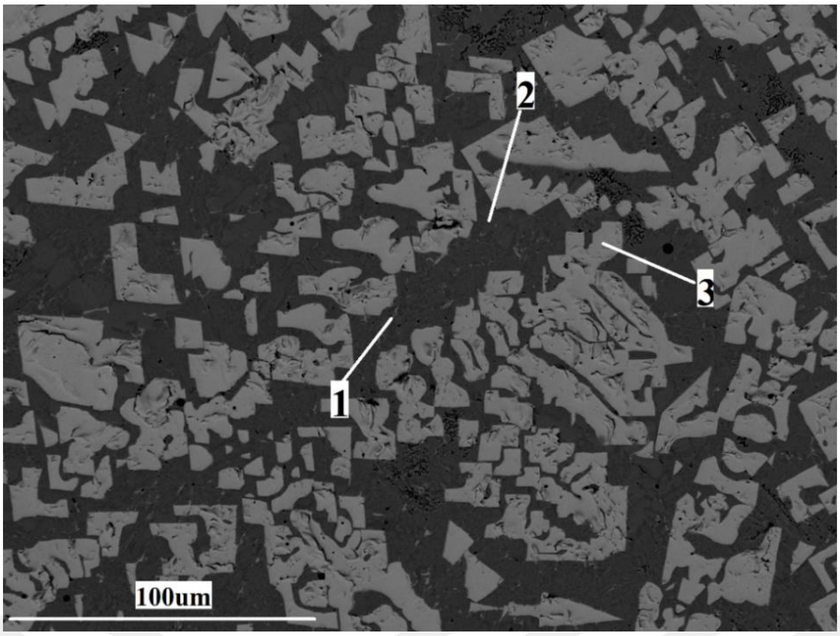

Figure 4.48 : SEM micrograph of SHS sythesized FE14 alloy.

Table 4.36 : The energy dispersive spectroscopy analysis results of FE14 alloy synthesized by SHS method.

Point	Mo	Fe	B	Al
1	-	94.2	-	3.3
2	75.9	24.1	-	-
3	70.1	21.6	8.3	-

4.2.2 Effect of the addition of alloying elements on Mo_2FeB_2 contaning composites

In Mo-Fe-B-Al-X multicomponent alloys, X refers to alloying elements such as Mn, Cr, and V with the addition of between 5% and 12 wt%. The addition of Cr, Mn, and V to the 36.5%Mo-56.3%Fe-6.9%B composition was examined to observe the effect of alloying elements on the microstructure of ternary alloys. Table 4.37 shows the estimated target alloys and the initial amount of mixture.

Table 4.37: The estimated target compositions and raw materials amount in the experimental study about effect of excess B_2O_3.

Exp. No	Composition (%wt)	MoO_3 (gr)	Fe_2O_3 (gr)	B_2O_3 (gr)	Al (gr)	MnO_2 (gr)	Cr_2O_3 (gr)	V_2O_5 (gr)
FE14	36,4Mo-56,2Fe-6,9B	40	60	40	50	-	-	-
FE15	37,0Mo-42,9Fe-7,5B-12,1Cr	40	45	40	50	-	15	-
FE16	40,6Mo-47,1Fe-6,0B-4,2Mn	40	45	40	50	15	-	-
FE17	38,0Mo-43,6Fe-6,1B-11,9V	40	45	40	50	-	-	15

Increasing the B_2O_3 and Fe_2O_3 ratios in the initial mixture decreases the undesired Al in the final product. The obtained samples of FE15, FE16 and FE17 were analyzed using XRF method which proved the dissolution of some Al and Cu in the final compositions. The FE15, FE16, and FE17 samples are the alloys with the Cr, Mn, and V additions. The sample FE14 is a Fe-rich alloy with the composition close to the NI15 sample.

Table 4.38 presents the XRF and AAS analysis results of Mo_2FeB_2 containing alloys. The amounts of components according to the elemental analysis clearly show the decreasing of aluminum dissolution in the iron matrix. The content of impurities, for instance, Cu in products decreases.

Table 4.38 : The XRF and AAS analysis results about the study on the effect of different additional alloying elements (Cr, V and Mn).

Exp. No	Mo	Fe	B	Al	Cr	Mn	V	Cu
FE14	33.5	51.46*	4.85*	0.98*	-	-	-	0.6*
FE15	41.6	43.9	-	-	12.2	-	-	0.8
FE16	37.2	54.8	4.9*	1.2*	-	5.6	-	0.51*
FE17	39.3	44.26*	4.3*	2.05*	-	-	6.89*	0.6*

* AAS analysis results

Figure 4.49 presents the XRD analysis results of the as-cast products obtained from the experiments using the initial mixture of MoO_3: Fe_2O_3: B_2O_3: Al and addition of other metal oxides (such as MnO_2, Cr_2O_3, and V_2O_5). The addition of Cr to the iron-based alloy produces the 37.0Mo-42.9Fe-7.5B-12.1Cr composition resulted in the formation of the Mo_2FeB_2 and Fe phases. The observed structure in the FE16 and FE17 samples with the Mn and V additions are mainly composed of Mo_2FeB_2. The other phases that found in the FE16 and FE17 samples are AlFe and $AlVFe_2$, respectively.

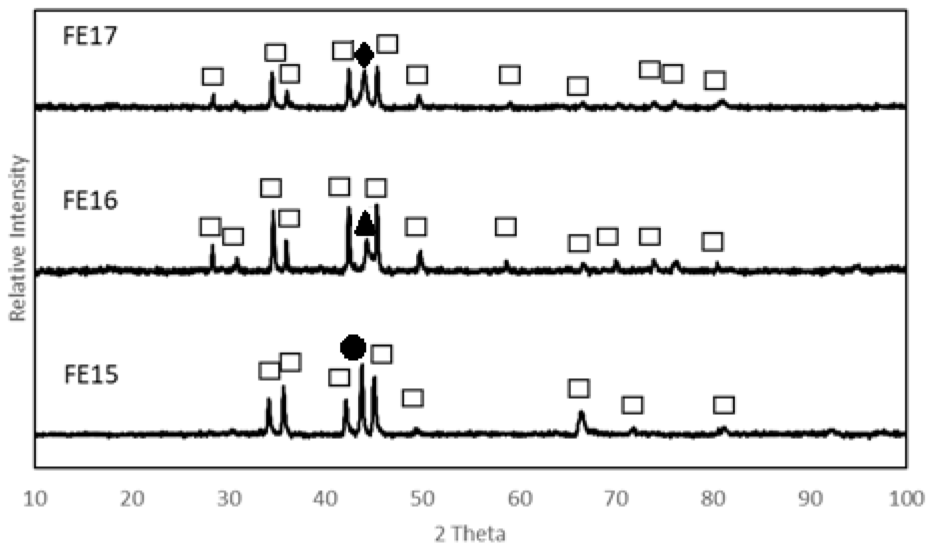

Figure 4.49 : XRD analysis results of FE15, FE16 and FE17 samples (□ Mo_2FeB_2 (01-089-3630), ▲AlFe (03-065-6132), ● Fe (01-085-1410), ♦ $AlFe_2V$ (03-065-6846)).

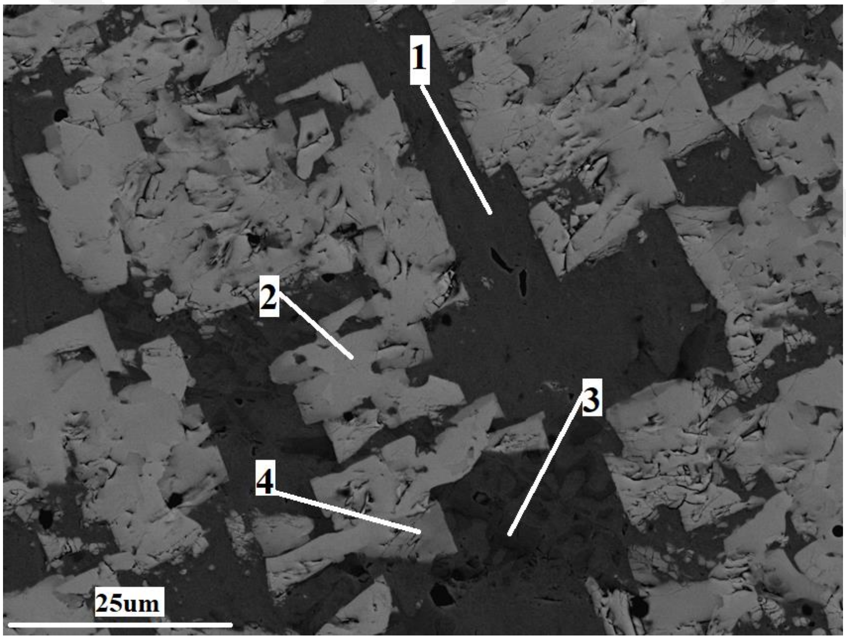

Figure 4.50 : SEM image of SHS synthesized FE15 alloy.

Figure 4.50 shows the SEM micrograph of FE15 alloy with the composition of 37,0Mo-42,9Fe-7,5B-12,1Cr. The elemental distribution which is listed in Table 4.39 shows the composition of the reinforcement and matrix phases in this sample. The matrix (point 3) contains Fe(Cr) and iron (point 1). Comparing to the FE14 sample, the presence of Cr in this alloy inhibits the formation of Mo-Fe intermetallics. Two types of M_3B_2 complex borides with different Cr contents (points 2 and 4) presented in the reinforcement. The complex boride has a tetragonal crystal structure as described previously in the literature; therefore, it forms rectangularly shaped grains in the sample.

Table 4.39 : The energy dispersive spectroscopy analysis results of FE15 alloy synthesized by SHS method.

Point	Mo	Fe	B	Al	Cr
1	1.92	85.81	-	3.27	5.45
2	67.8	16.4	5.8	-	9.9
3	3.74	68.5	-	-	27.7
4	51.1	21.5	7.7	-	19.5

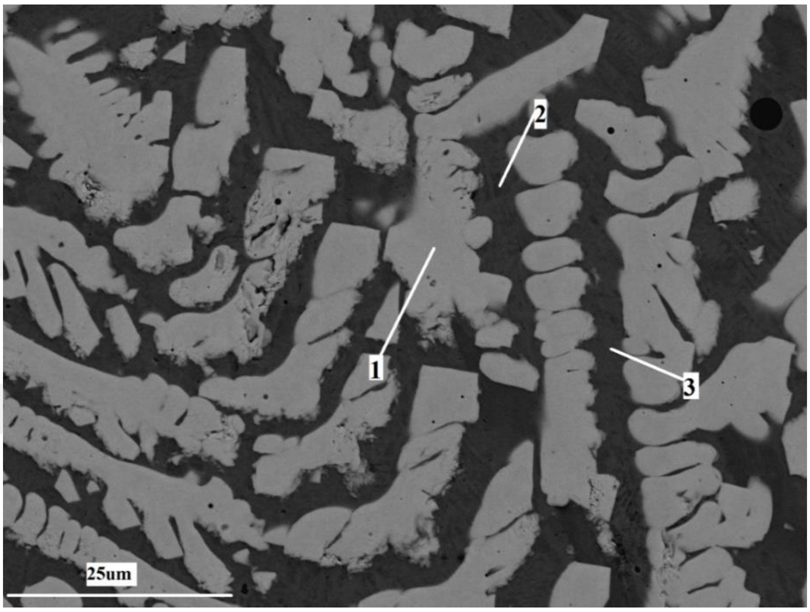

Figure 4.51 : SEM image of SHS synthesized FE16 alloy.

Figure 4.51 shows the SEM micrograph of the FE16 sample with the composition of 40,6Mo-47,1Fe-6,0B-4,2Mn. The elemental distribution was revealed by EDS analysis as listed in Table 4.40. Mn as a neighbor of Fe in the periodic table has the same crystal structure and atomic radius. Therefore, it is expected to observe a wide composition range of $(MoFeMn)_3B_2$ and (Fe, Mn) solid solutions. The Mo_2FeB_2 grains with rectangular shapes and rounded edges distribute uniformly in the matrix phase.

Table 4.40 : The energy dispersive spectroscopy analysis results of FE16 alloy synthesized by SHS method.

No	Mo	Fe	B	Al	Mn
1	70.5	19	8	-	2.5
2	35.9	46.6	11	-	6.3
3	76.5	21.2	-	-	2.3

Figure 4.52 shows the SEM micrograph of the FE17 alloy with the composition of 38Mo-43.6Fe-6.1B-11.9V. The V addition results in the different morphology compared to the FE14 sample.

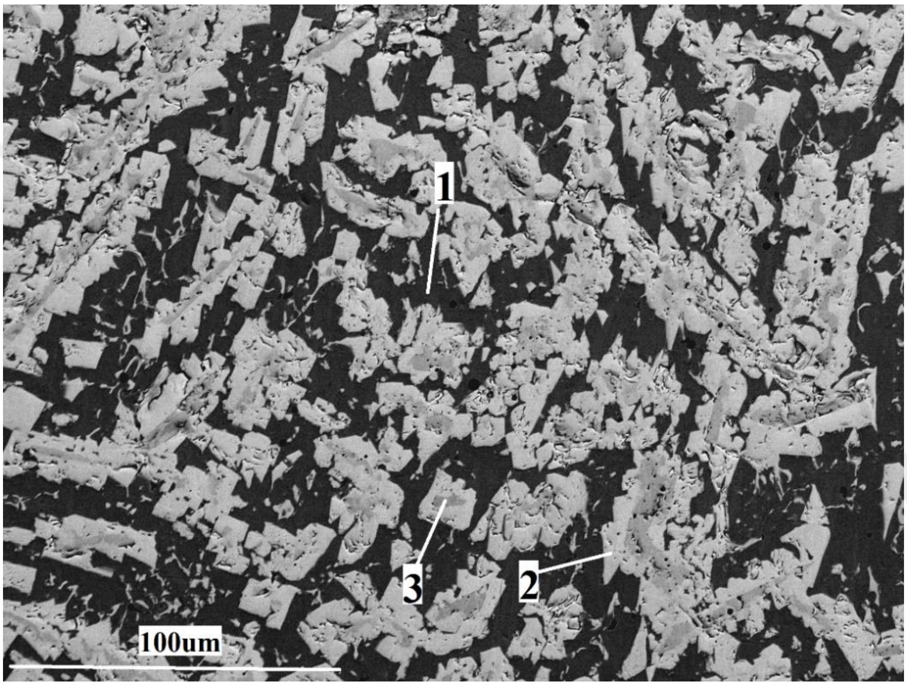

Figure 4.52 : SEM micrograph of SHS synthesized FE17 alloy (x1000 magnification).

Table 4.41 presents the EDX analysis results of the FE17 sample. M_3B_2 compound forms with the $(MoFeV)_3B_2$ complex boride composition (point 1, light gray). The Mo_2VB_2 ternary borides form at the middle of the grains (dark gray). The matrix region contains a Fe-rich phase with the dissolving of Mo, V, Al, and Cu.

Table 4.41 : The energy dispersive spectroscopy analysis results of FE17 alloy synthesized by SHS method.

Point	Mo	Fe	V	B	Al	Cu
1	10	80.4	3.2	-	4.3	2
2	61.9	14.7	12.7	10.5	-	-
3	64.5	1.8	19.7	14	-	-

The results of microstructural analysis of FE19 and FE14 alloys show that the reinforcement percentage increases significantly by reducing Al %wt in composition. The reinforcement area fraction of the FE19, FE14, FE15, and FE16 samples are 60, 56, 55.92 and 59.37, respectively. The increase in iron weight percentage reduces the percentage of boride based phases in reinforcement and accordingly results in a higher matrix percentage as shown in FE14 alloy's microstructure. The FE15, FE16 and FE17 samples with the additional alloying elements in compositions have higher reinforcement area fraction compared to the alloy FE14 microstructure. The differences in B and Al weight percentages dominate the microstructure and the reinforcement/matrix ratio. And also, the addition of alloying elements changes the matrix composition and consequently the microstructure.

4.2.3 Vickers microhardness testing results of the Mo_2FeB_2 containing composites

Table 4.42 presents the Vickers microhardness (HV) values of the FE10, FE12, and MFB8 samples. These results change between 875.3 and 903.53HV that the FE10 and MFB8 alloys have the lowest and the highest values, respectively. Both the FE10 and FE12 samples contain Mo_2FeB_2 ternary boride. But, in the MFB8 sample which doesn't contain Mo_2FeB_2 has higher hardness than FE12 because hard MoB binary boride is the main phase in the sample MFB8. According to the SEM/EDS analysis results, all the samples have Fe-rich matrix which strengthened by FeAl. The formation of FeMo sigma phase in the matrix of the sample FE12 causes a higher hardness value of this alloy.

Table 4.42 : Vickers microhardness values of SHS synthesized alloys.

Exp. No	HV (mean value)
FE10	875.30±134.34
FE12	945.95±176.06
MFB8	903.86±48.56

Table 4.43 presents the Vickers microhardness (HV) values of the FE21, FE19, and FE14 samples. These results change between 949 and 1301HV while the lowest and the highest values belong to FE19 and FE21 samples, respectively. The hardness results depend on the following parameters: grain size, reinforcement/matrix ratio, the formation of binary borides and the percentage of Mo_2FeB_2 in the obtained SHS alloys. Due to the presence of MoB and Fe_3B phases in FE21 sample and the high hardness

of Fe-B binary borides [76], this sample shows the highest hardness value. In sample FE14, there are two type grains of reinforcement particles containing Mo_2FeB_2 and the smaller particles of Mo_2FeB_2 boride dispersed in the matrix. The smaller grain size of sample FE14 causes a high hardness value although the reinforcement/matrix ratio in this sample is lower than the other samples.

Table 4.43 presents the Vickers microhardness (HV) testing of the FE15, FE16, and FE17 samples with the additional elements. The hardness values change between 675.99 and 996.7HV. These results depend on the matrix composition of the alloys whereas the lowest hardness value refers to the FE17 sample with higher Al content in the matrix phase. It was reported that the optimum V addition to the Mo_2FeB_2 based cermets is 2.5 %wt but further increase in V content causes aggregation and decreases the hardness [52]. The alloying of Fe matrix with 27 %wt Cr in the matrix causes relatively high hardness in the sample FE15. However in this composite, the reinforcement phase with the complex M_3B_2-type composition consists of relatively large grains. The Mn exists in both reinforcement and matrix phases in the FE16 sample causing the formation of MoFe(3 %wt Mn) in the matrix which increases the hardness of this sample. Therefore, Mn is effective in order to increase the hardness value to 996.7 which is the highest value in this group of Mo-Fe-B containing hard alloys. Also, according to the previous reported results, Mn is used for the hardenability of steels. Very large additions of manganese, about 12 to 15%, make the Hadfield's steel austenitic at room temperature. The M_3B_2-containing reinforcement percentage for all the three samples with additional elements were about 55-60%.

Table 4.43 : Vickers microhardness values of SHS alloys obtained from experimental study about the effect of additional alloying elements (Cr, V and Mn).

Exp. No	HV (mean value)
FE21	1301±162
FE19	1141±200
FE14	949±172
FE15	817.43±125
FE16	996.7±153.89
FE17	675.99±121.23

4.3 Production of Mo_2CoB_2 Ternary Boride Based Alloys

In this section, the combustion synthesis in Mo-Co-B ternary system was performed to produce the Mo_2CoB_2-based composites. The effect of the addition of Al_2O_3, excess Al and B_2O_3 on adiabatic temperature was discussed using FactSage simulations and experimental trials. Also, different Co_3O_4, B_2O_3, and Co_3O_4/MoO_3 ratios were examined to study the effect of raw materials on the product compositions. The composition, microstructural and mechanical properties of the obtained composites were analyzed by using AAS, XRD, SEM/EDS analyses and Vickers indentation. Finally, the Cr, Mn and V alloying elements were added to three ternary systems to observe their effect on the produced Mo_2CoB_2 ternary boride and the matrix phase.

4.3.1 Effect of diluent addition on the SHS products

In the first series of experiments, the excess Al and Al_2O_3 (as diluents) with different ratios of Co_3O_4 and B_2O_3 raw materials were used to study the effect of functional additive on the formation and microstructure of the final products. Before experiments, the simulation calculations were conducted to determine the effect of excess Al and Al_2O_3 diluents on the adiabatic temperature and produced species. The composition and microstructure of the obtained alloys change by the formation of Co-Al intermetallics in the matrix of alloys. In the second series of the experiments, the excess B_2O_3 and the different raw materials mixture (i.e. Co_3O_4/MoO_3 ratios) were used to observe the effect of B_2O_3 (as diluent) on the final products. The phase composition, microstructure, and hardness of obtained composites were investigated to observe how they are affected by the formation of Mo_2CoB_2 (in the reinforcement) and Co (in the matrix). In the third series of the experiments, the microstructure of ternary boride composites was investigated to determine how it is improved by the addition of alloying elements.

4.3.1.1 Thermodynamic investigations

Before the first series of SHS experiments, 1 mole MoO_3, 0.44 mole Co_3O_4, and 0.5 mole B_2O_3 were equilibrated with different amounts of Al to simulate the reaction. Figure 4.53 presents the simulation of the possible product contents formed with increasing Al ratios in the initial mixture. The released heat was assumed to increase the adiabatic temperature by initiation of the exothermic reaction resulting in the formation of liquid Mo, Ni, B, and Al in the products.

Among the oxides in the initial materials mixture, B_2O_3 starts to dissolve in the slag phase due to its lower melting temperature. MoO_3 transforms into MoO_2 sub-oxide and then reduces to release Mo. The primary molten nickel in the system reacts with obtained Mo to produce alloys by increasing Al ratio. Then, the reduction of B_2O_3 in the slag phase starts when Al reaches to 1 moles. The adiabatic temperature was raised by increasing Al ratio in the initial mixture when it reaches to 3 moles, the undesired Al in the system dissolves in the liquid alloys. The boron reduction continues even after the complete reduction of MoO_3 and Co_3O_4 oxides. By increasing the Al ratio, at the stoichiometric amount of Al (4.173 moles), the maximum contents of Mo, Co, B, and Al form but the gasification increases. In the figure, the GAS curve belongs to the total produced gaseous species.

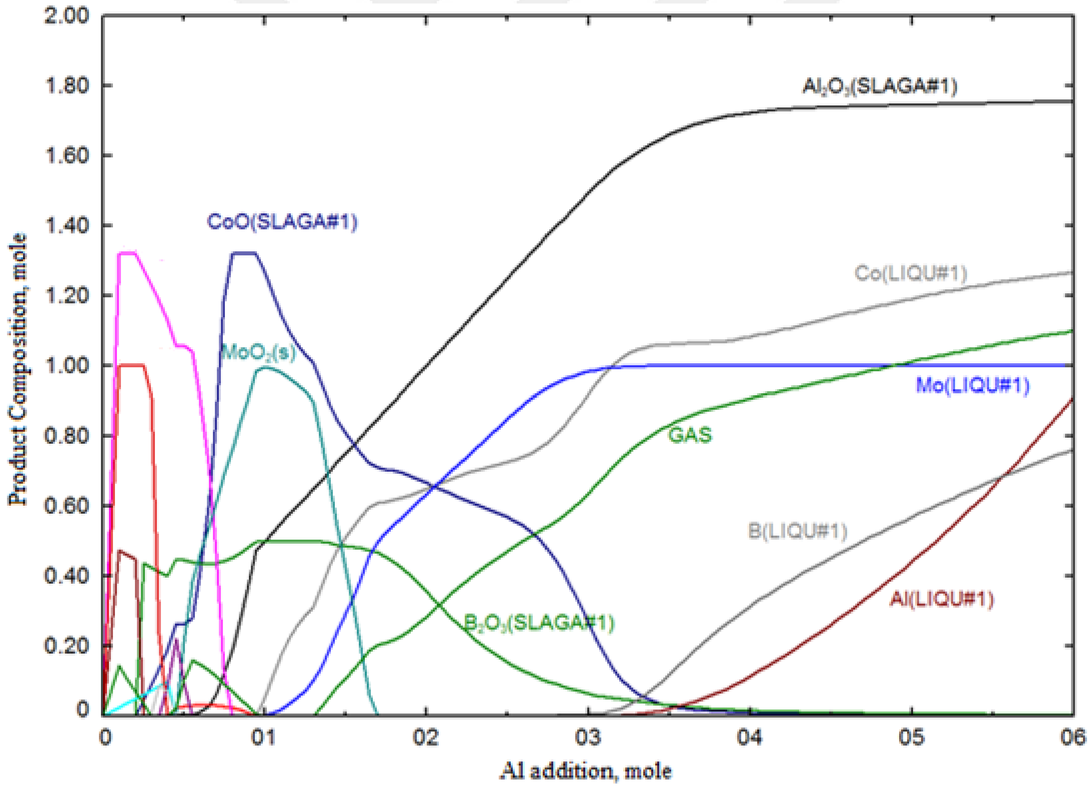

Figure 4.53 : Simulation of reaction products (molar ratio) using 2 mole MoO_3, 0.44 mole Co_3O_4 and 1 mole B_2O_3 raw materials mixture at 1 atm and room temperature (25 °C) with different amounts of Al additions.

Figure 4.54 presents the amounts of produced alloys and slags in the different reducing agent Al amounts. The SHS produced alloy weight is 182.04 gram that consists of 52.71% Mo, 40.82% Co, 3.75% B, and 2.72% Al (in wt%) at the stoichiometric ratio of Al (4.173 moles) in the system. Although thermodynamically, the complete reduction of metal oxides and boron trioxide occurs but the diffusion of Al in the final product composition could not be avoided due to the high percentage of gas formation during combustion. When the excess Al with the 5% additional amount was used, the weight of obtained alloy increases to 186.08 gram that consists of 51.57% Mo, 40.19% Co, 4.094% B, and 4.145% Al.

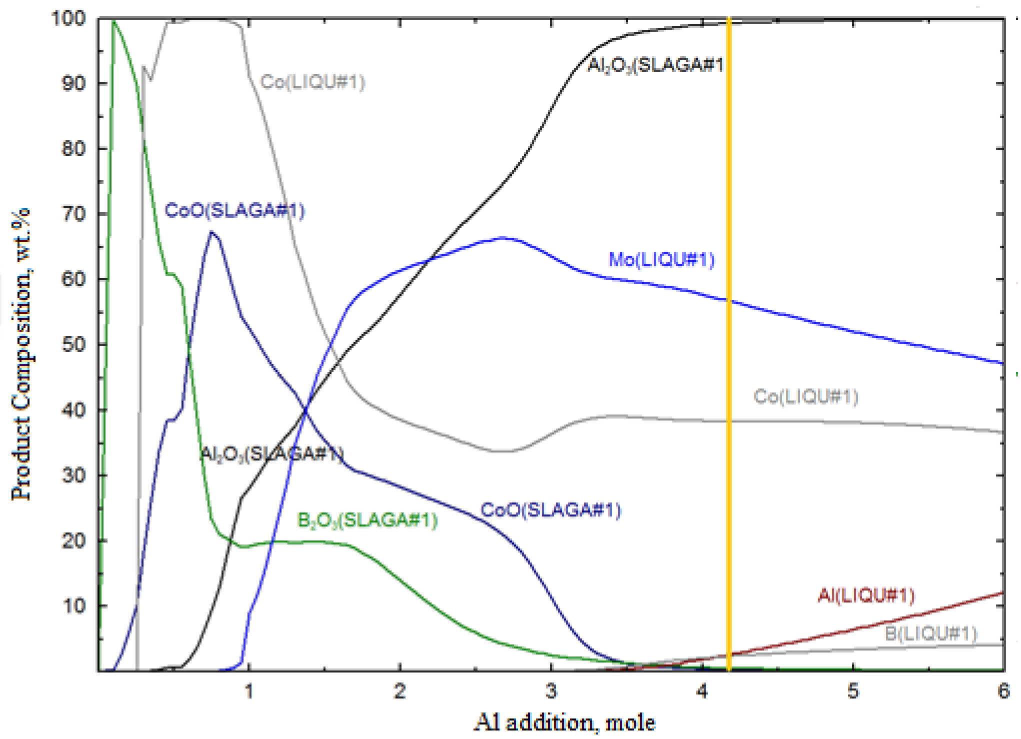

Figure 4.54 : Simulation of reaction products (wt%) using 2 mole MoO_3, 0.44 mole Co_3O_4 and 1 mole B_2O_3 raw materials mixture at 1 atm and room temperature (25 °C) with different amounts of Al addition.

The gaseous species weight equals to 0.36484 moles that comprise the 4.35 weight percent of total final products. The produced gases are 45.19% $AlBO_2$(g), 1.718% Co(g), 1.264% BO(g), 1.053% Al_2O(g) and other species. On the other hand, the total slag weight is calculated to be 255.1 gram that consists of 99.06% Al_2O_3, 0.76% B_2O_3 and 0.3456% CoO (in wt%).

The Al_2O_3 additions to the initial mixture decrease the adiabatic temperature as shown in Figure 4.55. This functional additive reduces the loss of the material and inhibits the gasification. The amounts of Al_2O_3 addition are 0, 0.05, 0.1 and 0.15 percentages of the total initial mixture which reduce the adiabatic temperatures to 2721.54, 2692.96, 2669.23, and 2641.54 °C, respectively.

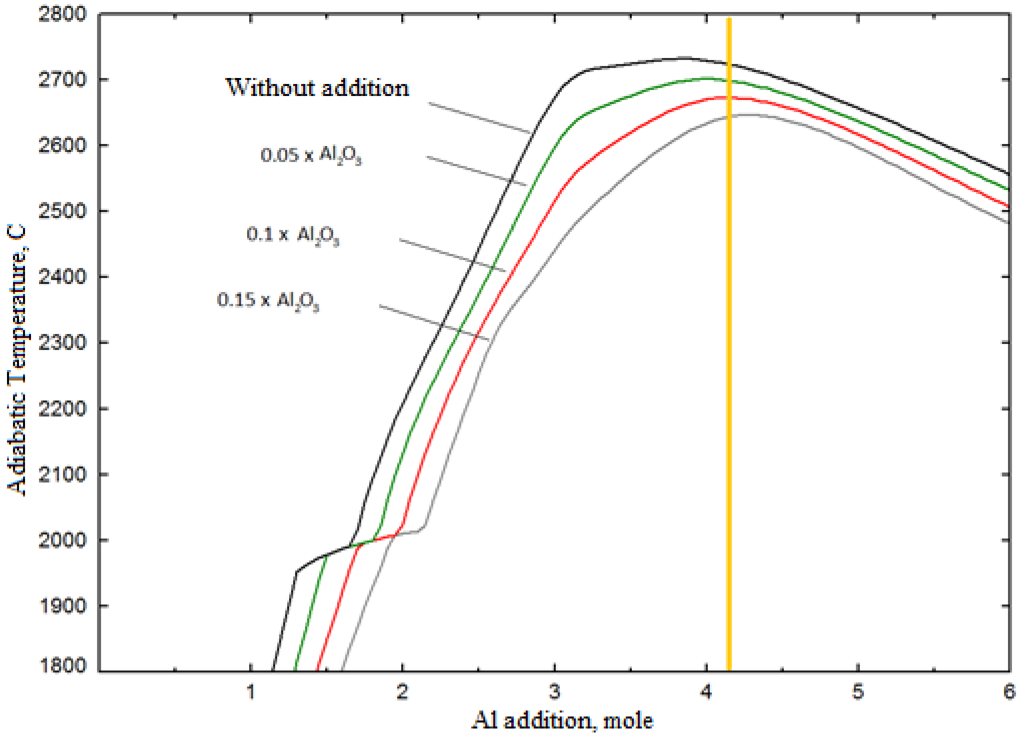

Figure 4.55 : Simulation of adiabatic temperature variation versus different amounts of Al and Al_2O_3 additions using 2 mol MoO_3, 0.44 mol Co_3O_4 and 1 mol B_2O_3 raw materials mixture at 1 atm and room temperature (25 °C).

4.3.1.2 Effect of excess Al and Al_2O_3 additions on SHS products

In the experiments, the amounts of MoO_3, Co_3O_4, and B_2O_3 and their ratios were fixed to observe the effect of Al and Al_2O_3 addition on the yield of target and materials loss. The amounts of Al and Al_2O_3 addition change between 0 and 10 (weight% of total raw materials weight).

Also, the target yield, materials loss, and burning velocity values were found to change by excess Al and Al_2O_3 diluents. Figure 4.56 presents that the target yield values range between 70% and 80% while the loss of materials values change between 20% and 30% using different Al_2O_3 additions.

Table 4.44 presents the effect of Al_2O_3 addition on the elemental compositions of obtained SHS alloys. The elemental analysis results present that impurities such as Al, Cu, and W contents in the compositions reach to the maximum of 11, 4, and 3.6wt%, respectively. The optimum Al and Al_2O_3 additions were 5 wt% and 10 wt% of total initial mixture.

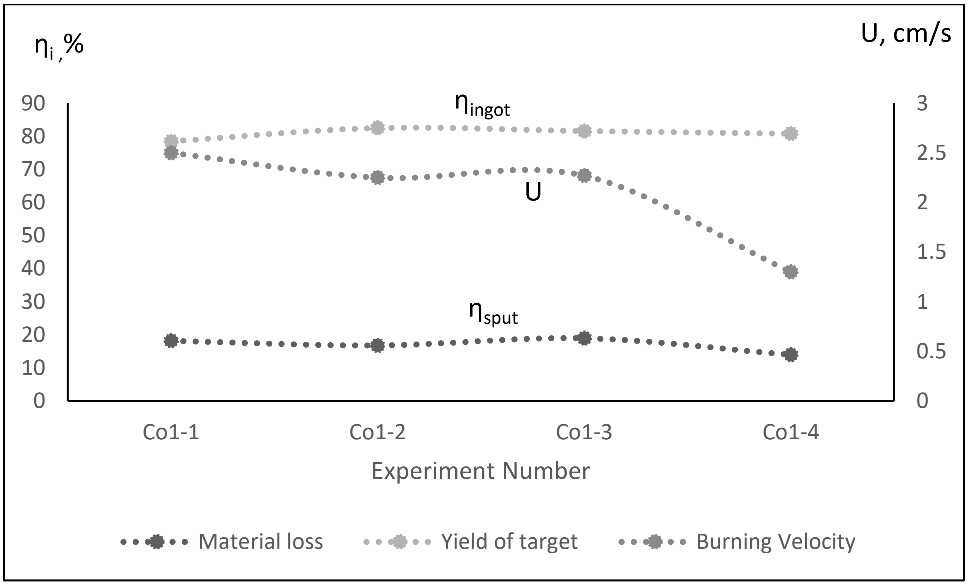

Figure 4.56 : The effect of Al_2O_3 addition on SHS parameters such as yield of target, material loss and burning velocity.

Table 4.44 : XRF analysis results of the SHS alloys obtained from the experimental study about the effect of Al_2O_3 addition.

No	Mo	Co	Al	Cu	W	Fe
CO1-2	41.23	45.8	7.45	0.23	1.04	2.99
CO1-3	36.87	44.07	10.84	2.42	1.5	3.03
CO1-5	35.9	40.14	14.76	7.32	1.26	0.31

Effect of initial Co_3O_4 additions on SHS products

In the following experiments, the combination of 5% Al and 10% Al_2O_3 was used to reduce the combustion temperature. Besides the 5% excess Al and 10% Al_2O_3, 23.8 and 31.65 gram of Co_3O_4 were used to observe the effect of oxide ratios on composition. Table 4.45 shows the initial mixture amounts with increasing Co_3O_4.

Table 4.45 : Raw materials amounts for combustion synthesis of alloys with increasing Co_3O_4.

No	Estimated target composition, wt%	MoO_3	Co_3O_4	B_2O_3	Al	Al_2O_3
Co1	52.15Mo-42Co-5.85B	46.89	34.32	11.31	36.49	6.50
Co2	50.04Mo-44.33Co-5.6B	46.89	37.75	11.31	37.53	6.70
Co3	47.9Mo-46.7Co-5.37B	46.89	41.18	11.31	38.5	7.00
Co4	45.78Mo-49.08Co-5.1B	46.89	44.61	11.31	40.7	7.20
Co5	43.6Mo-51.4Co-4.8B	46.89	50.26	11.31	41.26	7.50

Increasing percentage of Co_3O_4 in the initial mixture changes the produced phases in the alloy as in Figure 4.57.

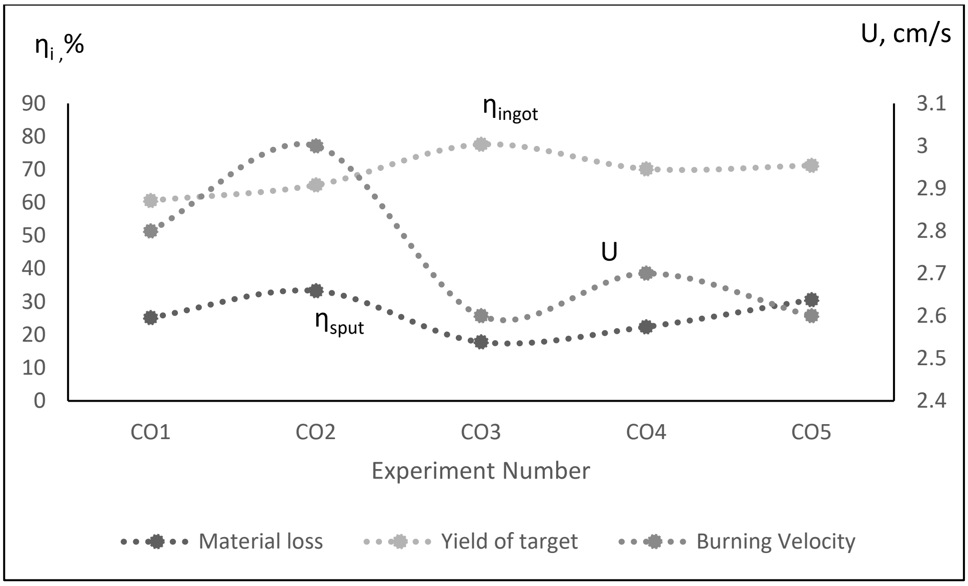

Figure 4.57 : The effect of Co_3O_4 addition on SHS parameters such as yield of target, material loss and burning velocity.

Target yield varies in the range of 60.6 to 77.6 % and the material loss changes between 20 and 33.3% due to the higher amount of gasifications. Cobalt weight percentage in the product composition changes between 42 and 51.4 wt%, according to XRF results which are presented in Table 4.46.

Table 4.46 : XRF analysis results of the SHS alloys obtained from the experimental study about the effect of Co_3O_4 and B_2O_3 additions.

No	Mo	Co	Cu	B	Al
CO1	37.45	40.79	5.73	2.62	13.42
CO3	35.89	43.58	5.76	2.15	12.62
CO5	36.36	43.25	5.7	2.23	12.48
MCB5	35.03	42.07	4.92	3.72	14.26

Figure 4.58 shows the XRD results of the CO1, CO3 and CO5 samples with increasing Co_3O_4 amount in the initial mixture. According to this figure, sample CO1 composes of MoB, Mo_2CoB_2, and $Co_{27}Al_{73}$/AlCo. By increasing the Co content to 46 wt% in the final composition of the CO3 sample, the Mo-rich phases are eliminated and ternary boride Mo_2CoB_2 becomes the dominant phase. The Mo_2CoB_2 phase has the structure of Mo_2NiB_2 and W_2CoB_2. Therefore, the peaks of Mo_2CoB_2 in the Figure 4.57 refers to the Mo_2NiB_2 pattern (Card Number: 01-089-2542). The CoAl intermetallic formed in all three samples due to the high content of remaining Al in the products.

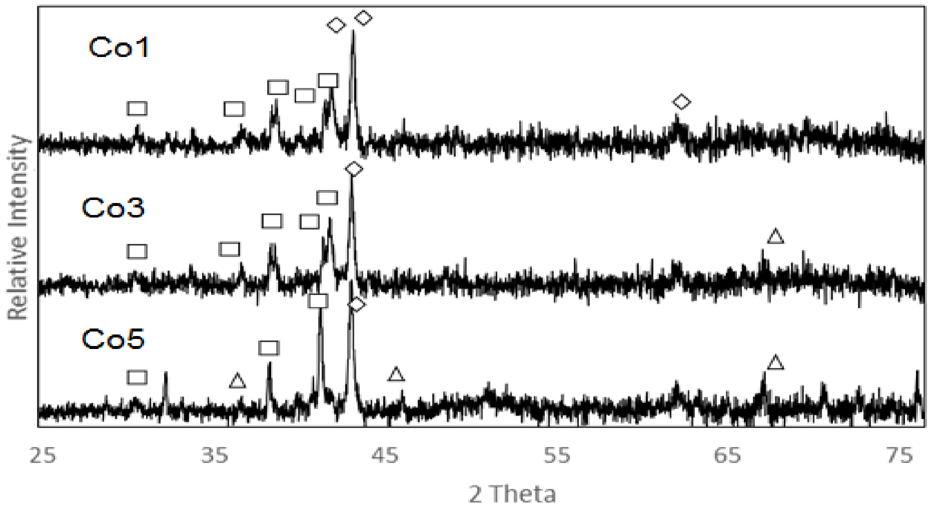

Figure 4.58 : XRD analysis results of CO1, CO3 and CO5 as-cast alloys obtained from combustion synthesis method (□ Mo_2CoB_2, Δ MoB, ◊ CoAl (03-065-4903)).

Figure 4.59 presents the SEM micrographs of Co1 sample at X500 magnification. Also, the elemental distributions of the phases in this sample were revealed by EDS. Co-Al intermetallic forms in the matrix phase (point1) due to the high Al content (13.42%) that also dissolves the elements such as Cu and Mo. According to the Co-Cu phase diagram, the dissolution of lower amounts of Cu (8 to 10 wt%) in Co-rich alloys cause the transformation of fcc cobalt into hcp. The elongated grains that cover all over the sample are composed of MoB. The light gray regions in interface near the grain boundaries are composed of Co-Al intermetallic with dissolved Mo. The dendritic structure formed in the matrix (points 2 and 3) is the same as γ/γ’ structure which is presented in Ni superalloys [2].

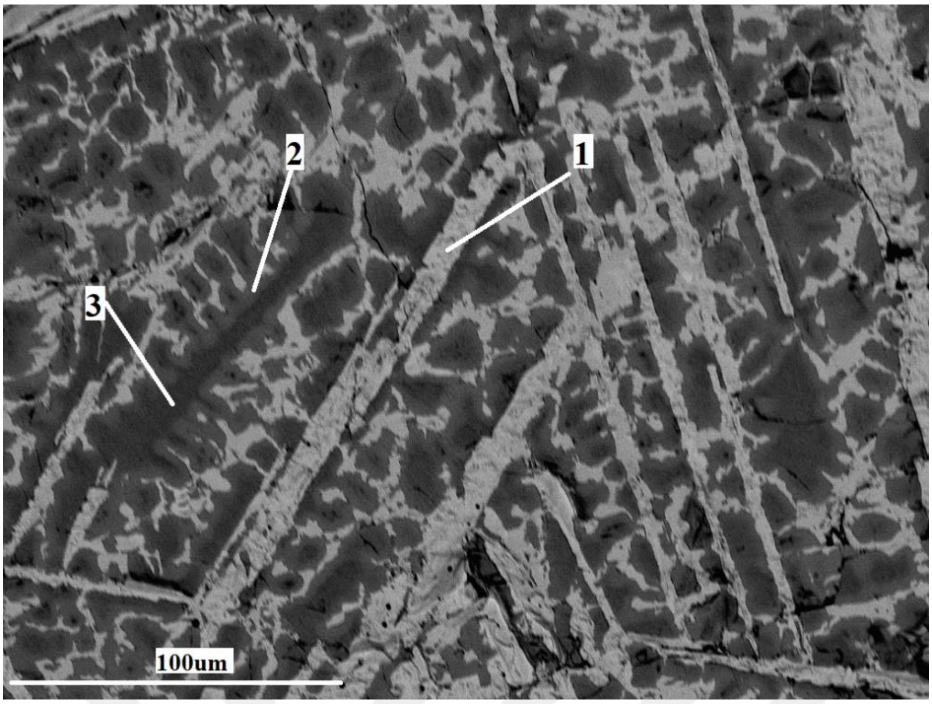

Figure 4.59 : SEM-BSE image of SHS synthesized as-cast CO1 sample at x500 magnification.

Figure 4.60 presents the SEM micrographs of Co3 sample at X500 magnification. Also, the elemental distributions of the phases in this sample which was revealed by EDS, presents the formation of the CoAl in the matrix (points 2 and 3) due to the high weight percentage of Al (12.62 wt%) that also have dissolved Cu. The microstructure of Co-Mo-Al alloy in the matrix phase is similar to Co1 sample. The dendritic coarse (point 1, light gray) phases in the reinforcement have compositions close to Mo_3Co_2 intermetallic (σ phase). The elongated grains in the reinforcement correspond to MoB phase. Due to the higher Co weight percentage in this sample, the percentage of dendritic phase increases while the MoB phase decreases.

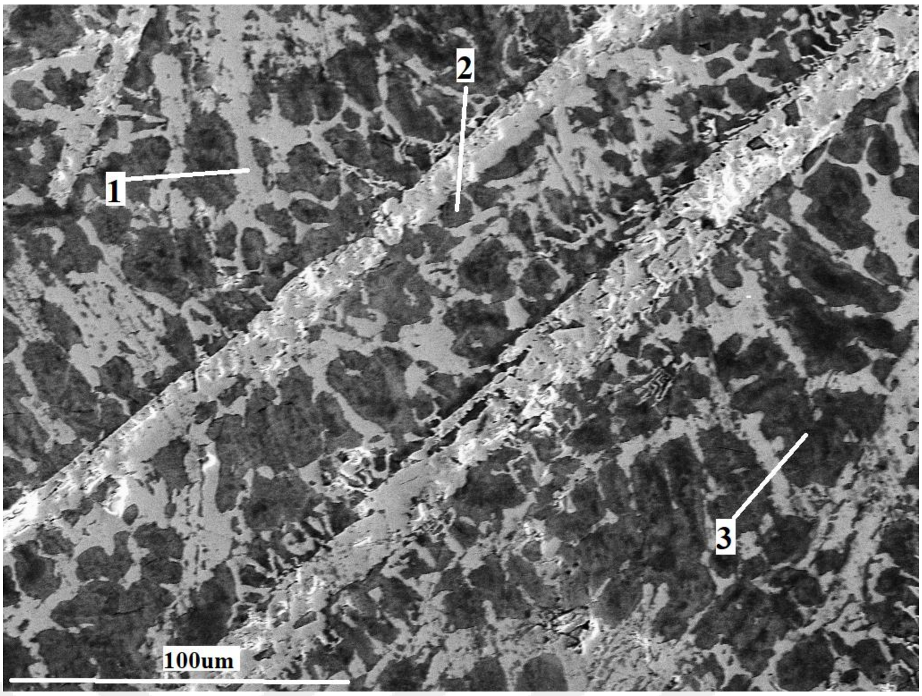

Figure 4.60 : SEM-BSE image of SHS synthesized as-cast CO3 sample at x500 magnification.

Figure 4.61 presents the SEM micrographs of the Co5 sample at X500 magnification. Also, the elemental distributions of the phases in the as-cast alloy was revealed by EDS analysis. CoAl forms in the matrix (point1) due to the high weight percentage of Al (12.62%) dissolving Mo and Cu. The β-phase (CoAl), a B2 ordered intermetallic, as a dark contrast phase was reported to be formed in Co-W-Al alloys with 1Si during cooling from solution heat treatment at 1300 °C. The formed B2 phase was found to be surrounded by a region of Co-rich (A1) phase free of γ' as observed in the present study [1]. In the reinforcement phase, MoB grains get smaller and Mo_3Co_2 phase changes to ternary boride of Mo_2CoB_2 with increasing Co content. The grains composed of Mo_2CoB_2 ternary boride (point 2, light gray) have higher content in this sample, and consequently, the ratio of reinforcement to the matrix is higher.

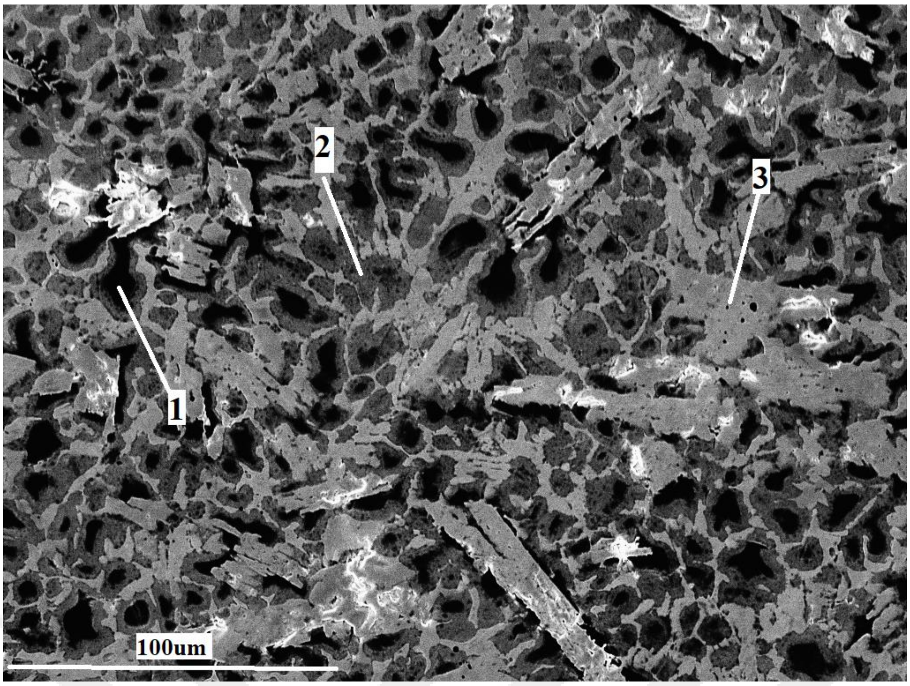

Figure 4.61 : SEM-BSE image of SHS synthesized as-cast CO5 sample at x500 magnification.

The size and morphology of produced borides in the obtained alloys are strongly dependent on the cooling rate and thermochemistry of the systems. These results are close to the shape of carbide particles (eutectic M_6C or M_7C_3-type) within the cobalt-rich Stellite alloys formed by different welding processes.

The reinforcement area fractions of CO1, CO3, CO5, and MCB5 samples were 37.21, 41.99, 46.55 and 35.07% as calculated by ImageJ analysis. All the samples are Mo-based except CO5 sample with the highest Co weight percentage. The microstructure of CO1, CO3, and CO5 samples changes considerably by increasing the cobalt weight percentage in composition. Although, the dissolution of Al changes the reinforcement/matrix ratio, the matrix percentage increases by increasing Co wt%. Incresing boron weight percentage changes the morphology of obtained alloys but the reinforcement/matrix ratio remains constant as it was observed in MCB5 alloy.

Effect of initial B_2O_3 additions on SHS products

In the initial mixture with excess Al and Al_2O_3, the amount of B_2O_3 was changed to observe its effect on the SHS parameters and phase composition of alloys. Table 4.47 presents the raw materials ratios with different amounts of B_2O_3 changing between 13.9 and 17.25 gram. These alloys are MCB1, MCB2, MCB3, MCB4, and MCB5 in order of the content of B_2O_3.

Table 4.47 : Raw materials amounts of the alloys with increasing B_2O_3.

No	Estimated target composition, % wt.	MoO_3	Co_3O_4	B_2O_3	Al	Al_2O_3
MCB2	52.15Mo-42Co-5.85B	46.89	34.32	12.43	37.34	6.5
MCB3	51.8Mo-41.7Co-6.4B	46.89	34.32	13.67	38.29	6.6
MCB4	51.5Mo-41.48Co-6.98B	46.89	34.32	15.02	39.34	6.7
MCB5	51.17Mo-41.2Co-7.62B	46.89	34.32	16.53	40.51	6.8

In this set-up, the boron weight percentage changes between 5.85 and 8.32 wt% as shown in Figure 4.62. The target yield was low in the range of 60.6 to 72.6%. The maximum material loss value and the average burning velocity value are 30.4% and 2.6 mm/s, respectively.

The MCB5 sample was analyzed by XRD to observe the phase composition. The alloy composes of MoB, Mo_2CoB_2 and AlCo phases. This sample has a relatively high percentage of Co that enables the formation of complex boride Mo_2CoB_2. However, the presence of Al makes the CoAl intermetallic a dominant phase with higher intensity in this alloy.

Figure 4.63 presents the SEM micrograph of MCB5 sample at X500 magnification. Also, the elemental distributions of the phases in this sample was revealed by EDS to determine the compositions. CoAl forms in the matrix (point 1) due to the high weight percentage of Al (14.62wt%) with dissolving Cu. The ration of reinforcement to the matrix is raised because of the formation of intermetallics in this sample. The coarse grains (point 2, light gray) composes of MoCoB, MoB, and Mo_2CoB_2 phases. The formation of phases in Mo-B system is high due to the increasing of boron in the final composition.

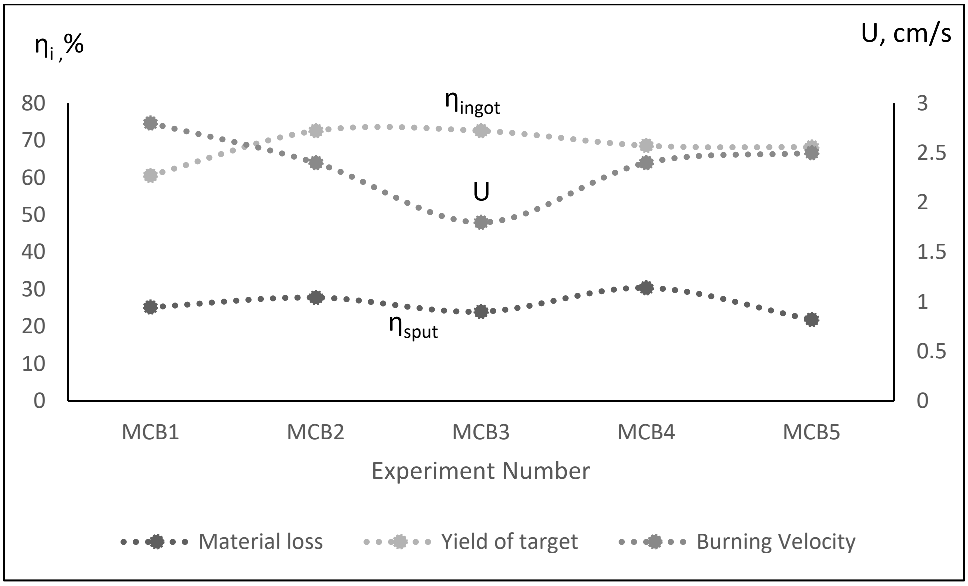

Figure 4.62: The effect of B_2O_3 addition on SHS parameters such as yield of target, material loss and burning velocity.

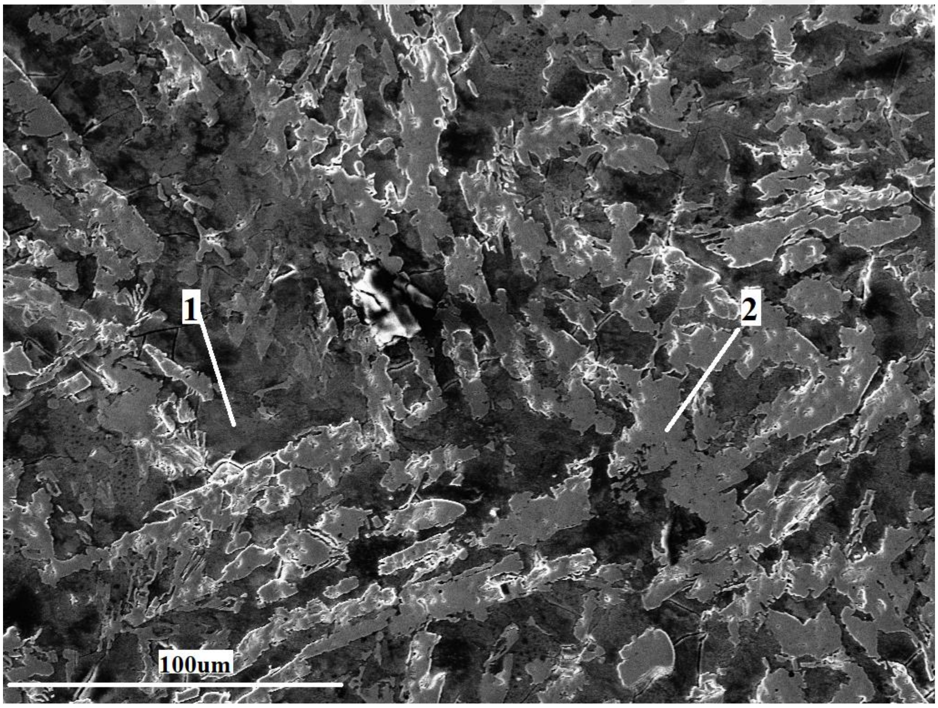

Figure 4.63: SEM-BSE image of SHS synthesized as-cast MCB5 sample at x500 magnification.

4.3.1.3 Effect of excess B_2O_3 on the SHS products

Effect of different Co_3O_4/MoO_3 ratio on SHS products

The amounts of raw materials mixture for production of Co6, Co10 and Co11 samples with decreasing Co weight percentage from 58 wt% to 39.15 wt% are presented in Table 4.48.

Table 4.48 : The amounts of raw materials for production of alloys with different Co_3O_4/MoO_3 ratio.

No	Target composition	MoO_3	Co_3O_4	B_2O_3	Al
Co6	35.6Mo-58Co-5.8B	40	60	40	47
Co10	47.01Mo-47.44Co-5.36B	28	25.9	18.5	24.69
Co11	54.3Mo-39.15Co-5.7B	31	20.93	18.6	25.58

Figure 4.64 presents the XRD analysis results of the CO11, CO10, and CO6 samples. Comparing with CO5, the higher amount of B_2O_3 in the sample CO11 causes the formatioon of Mo_2CoB_2 with higher intensity in the reinforcement and $Al_3Co_{20}B_6$ in the matrix due to the lower Al content. By further increasing the Co/Mo ratio in the sample CO10, the intensity of Mo_2CoB_2 and Co_2B phases increase while the matrix phase consists of Co and $Al_3Co_{20}B_6$. Therefore, the main phase formed in a sample with the highest Co/Mo ratio is Mo_2CoB_2. In this sample (CO6), the obtained phases are $Al_3B_6Co_{20}$ intermetallic and Co which substituted for Co-Al matrix phase. Furthermore, the MoB binary phase disappears as shown in the figure. This sample contains metallic Co and also Mo_2CoB_2 which is considered to be isomorphous to Mo_2NiB_2 and W_2CoB_2 crystal structures as it was reported in the literature [4].

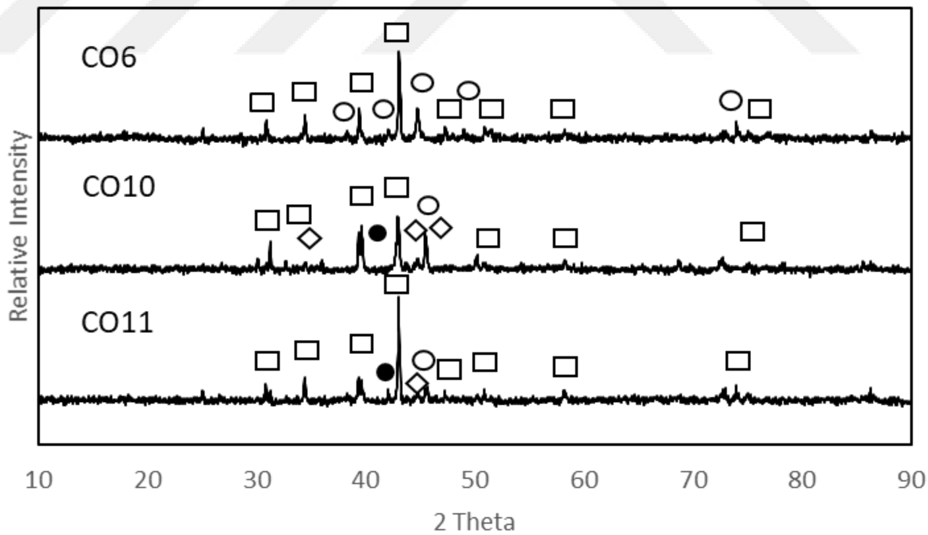

Figure 4.64 : XRD analysis of CO11, CO10 and CO6 samples (□ Mo_2CoB_2, ○ $Co_{20}Al_3B_6$ (01-089-3173), ◊ Co_2B (01-075-1063), ● MoB).

Figure 4.65 presents the SEM/BSE image of as-cast alloy (Co6) with 35.6Mo-58Co-5.8B composition. The elongated particles distribute in a dark gray matrix with an average area fraction of 42.9% (standard deviation of 3.1). The Mo_2CoB_2 ternary boride forms in the reinforcement (point 2, light gray). The matrix contains cobalt (Co (α)) with a maximum of 3wt% Al and 5wt% Mo (point1, dark gray). As B content in grain boundaries increases the percentage of $Co_{20}Al_3B_6$ ternary phase which was formed in these regions. The average width size of rectangle shape grains reaches 10.4um which is determined by ImageJ software considering 80 grains.

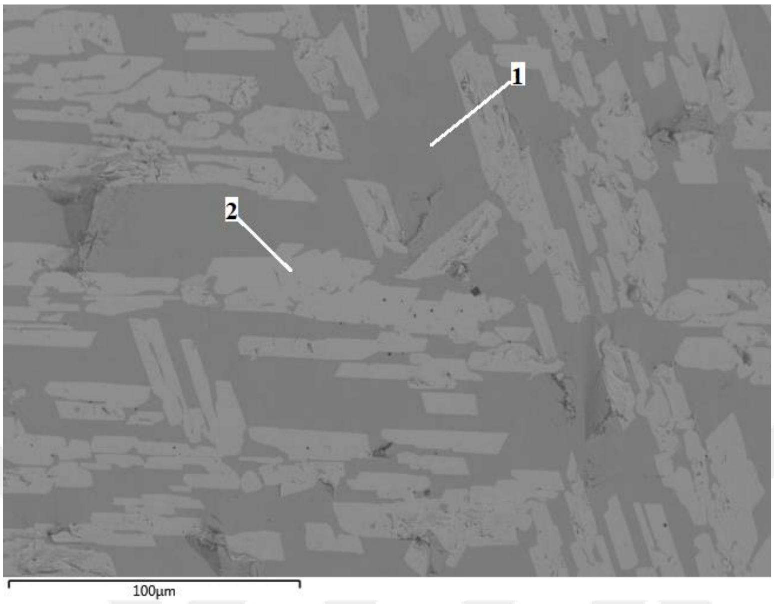

Figure 4.65 : The SEM micrograph of CO6 alloy (×1500 magnification).

Table 4.49 : Energy dispersive spectroscopy analysis results of CO6 alloy synthesized by SHS method.

Point	Mo	Co	B	Al
1	71	23.2	5.8	-
2	5.5	91.6	-	2.8
3	75.5	24.5	-	-

4.3.2 Effect of the addition of alloying elements on Mo_2CoB_2 containing composites

The additional amounts of alloying elements which used in the experiments were 5-12% of the total weight of the produced alloy. The 35.6Mo-58Co-5.8B composition was chosen to observe the effect of additives such as Cr, Mn, and V on the microstructure. Table 4.50 presents the estimated compositions and the amounts of the initial mixture which were used for combustion synthesis.

Table 4.50: The estimated composition and raw materials amount of the experimental study about the effect of different additional alloying elements.

No	Composition (%wt)	MoO_3 (g)	Co_3O_4 (g)	B_2O_3 (g)	Al (g)	MnO_2 (g)	Cr_2O_3 (g)	V_2O_5 (g)
Co7	38.7Mo-47.4Co-7B-6.1Mn	40	45	40	50	15	-	-
Co8	36.8Mo-45Co-6.1B-11.6V	40	45	40	50	-	-	15
Co9	35.6Mo-43.8Co-7.3B-12.6Cr	40	45	40	50	-	15	-

The alloys containing the alloying elements of Mn, Cr, and V are CO6, CO7, CO8, and CO9. Table 4.51 presents the AAS and XRF analysis results of the obtained alloys.

Table 4.51 : The atomic absorption spectroscopy analysis results of SHS alloys obtained from the experimental study about the effect of additional alloying elements (Cr, V and Mn).

No	Mo	Co	B	Al	Cr	Mn	V	Cu
CO6	33.09	65.4	5.1*	1.7*	-	-	-	0.17*
CO7	37.3	40.5	6.3*	2.10*	-	12.14	-	0.16*
CO8	20.6	60.3	-	-	-	-	6.4	-
CO9	32.7	48	4.9*	2.10*	11.1	-	-	0.55*

* AAS analysis

Figure 4.66 presents the XRD analysis results of the as-cast products obtained from the experiments using the initial mixture of MoO_3: Co_3O_4: B_2O_3: Al and other additional metal oxides (such as MnO, Cr_2O_3, and V_2O_5). Using Cr as an additional alloying element resultes in the formation of Mo_2CoB_2, MoCoB, and AlCo phases. The Mn addition in the Co7 alloy with the composition of 35.6Mo-58Co-5.8B results in the formation of Mo_2CoB_2, Mn_2AlB_2, AlCo, and Co. Also, the phases and intermetallics formed by the addition of V in the Co8 alloy are as follows: Mo_2CoB_2, MoCoB, $AlVCo_2$, and Co_2B. The Mo_2CoB_2/MoCoB mixture in the composition of Co9 is the same as reported in the literature [65]. Although the dissolution of Al in the alloys is very low (1-2 wt%) but there is some cobalt aluminides such as AlCo, and $AlVCo_2$.

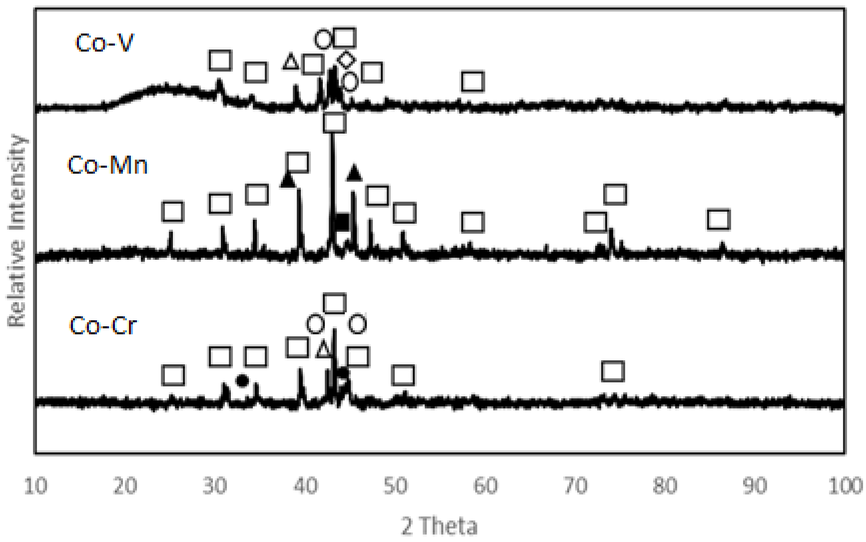

Figure 4.66 : XRD analysis results of Co-Cr, Co-Mn and Co-V samples (□ Mo_2CoB_2,○ MoCoB (01-072-2185), ◊ $Mo_{0.9}B_3$ (01-086-1098), Δ MoB, ● AlCo, ▪ Co (00-001-1254), ▲ Mn_2AlB_2 (01-080-2277)).

Figure 4.67 shows the SEM micrograph of CO7 with the composition of 38.6Mo-47.4Co-7B-6Mn-0.7Al. The addition of Mn to CO6 sample's composition resulted in the production of $(MoCoMn)_3B_2$ in the reinforcement. The dominant part of dissolved Mn in the alloy exists in the matrix phase. The matrix of this alloy consists of two regions as follows: 1) the dark spots in the gray Co-rich matrix are CoAl intermetallic containing the maximum 20wt.% Al, 2) the light gray areas close to the reinforcement in the matrix are CoBMn and MoCoMn. The middle part of the reinforcement contains M_3B_2 phase. The partitioning behavior of alloying elements in the Co-Al-W-X system is very similar to that of the Ni-Al-X system, where Ta, Nb, and Ti are strong γ' stabilizing elements, while Cr, Mn, and Fe are γ-forming elements [6].

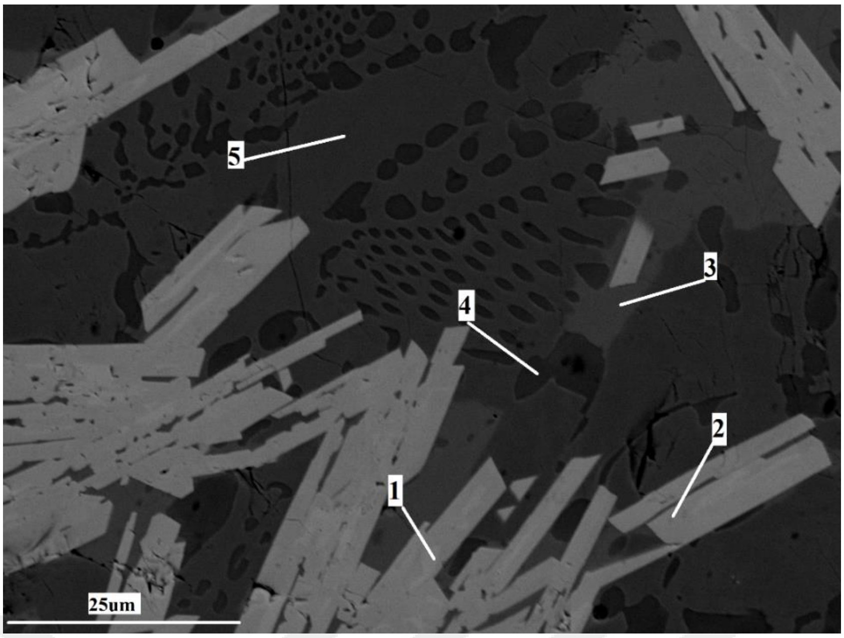

Figure 4.67 : The SEM micrograph of CO7 alloy (×1000 magnification).

Table 4.52 : Energy dispersive spectroscopy analysis results of CO7 alloy synthesized by SHS method.

No	Mo	Co	B	Mn	Al
1	70.5	22.4	4.9	2.1	-
2	-	80.5	-	19.6	-
3	72.7	24.7	-	2.5	-
4	-	79.5	-	12.5	8.2
5	-	84.7	-	15.3	-

According to Figure 4.66 corresponding CO7 sample's X-ray diffraction pattern; the main peaks in this sample belong to $(MoCoMn)_3B_2$ complex boride which is in agreement with EDS results. Due to the existence of 2.1 wt% Al, there are some $Al_3Co_{20}B_6$ ternary phase peaks presented in this sample.

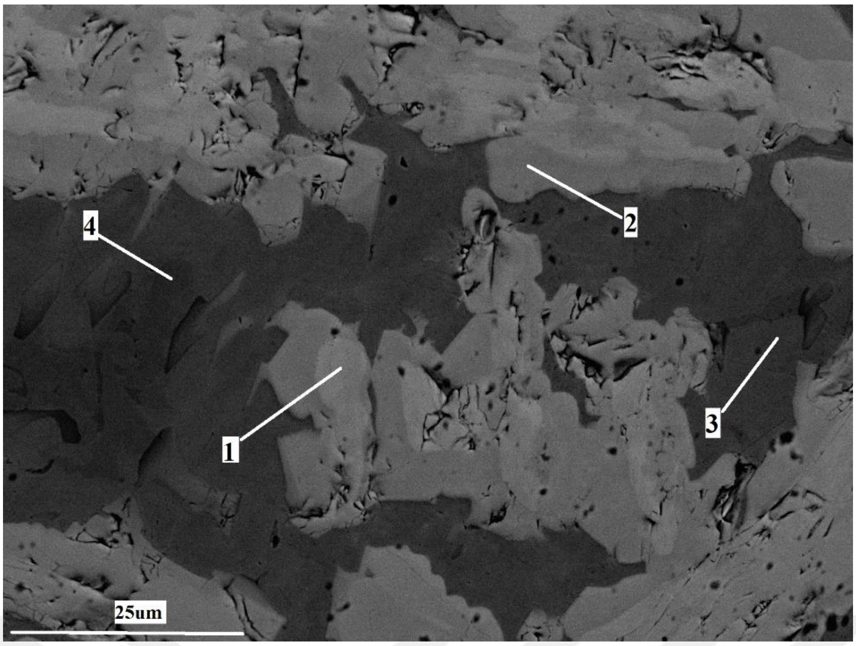

Figure 4.68 : The SEM micrograph of CO8 alloy (×1500 magnification).

Figure 4.68 shows the SEM image of CO8 alloy with the 36.8Mo-45Co-6B-11.6V-0.4Al composition. This alloy consists of different phases with elemental concentrations which are listed in Table 4.53. However, the ratio of the hard phase to the matrix is higher than that of the other samples. The light gray areas belong to $(MoVCo)_3B_2$ ternary borides at the middle of the grains which are rich in cobalt. The matrix contains Co-V solid solutions with maximum vanadium concentration of 9.34wt% (dark gray). There is not any detected Al but some contents of Cu has been found in some areas of the matrix phase.

Table 4.53 : Energy dispersive spectroscopy analysis results of CO8 alloy synthesized by SHS method.

Point	**Mo**	**Co**	**B**	**V**	Cu
1	60.4	17.3	10.6	11.7	-
2	44.6	38.9	6.7	9.7	-
3	-	90.6	-	9.4	-
4	-	90.7	-	7.03	2.2

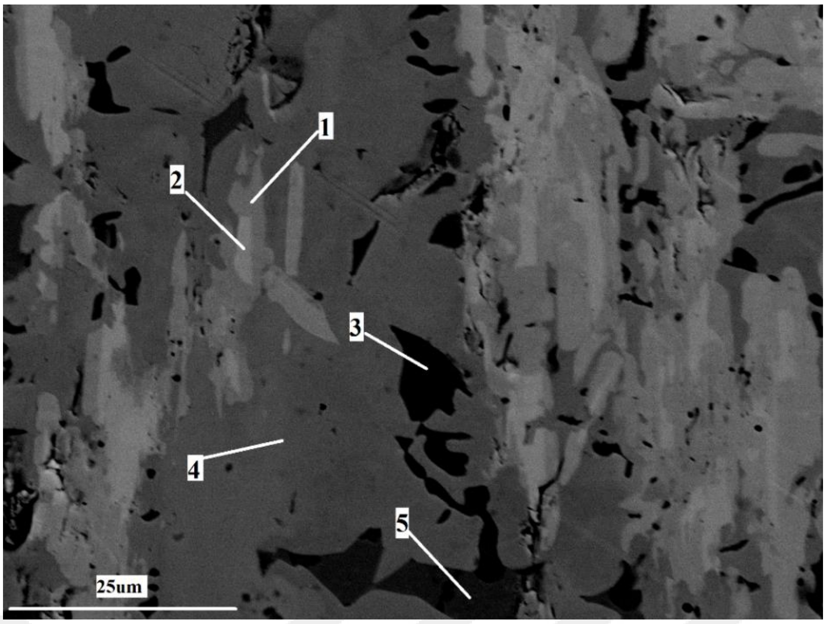

Figure 4.69 : The SEM micrograph of CO9 alloy (×1000 magnification).

Figure 4.69 shows the SEM micrograph of CO9 alloy with the 35.6Mo-43.8Co-7.3B-12.6Cr-0.5Al composition. In this sample, the reinforcement/matrix ratio is higher and the matrix contains Mo and Co. The distribution of elements in this sample determines the phases composition as shown in Table 4.54. The dark gray area belongs to $(MoCoCr)_3B_2$ complex borides. There is not any evidence of Al and Cu or other impurities in the composition of this alloy.

Table 4.54 : Energy dispersive spectroscopy analysis results of CO9 alloy synthesized by SHS method.

Point	Mo	Co	B	Cr
1	39	40.4	5.5	15
2	65.2	23.5	3.1	8.12
3	64.9	21.7	5	8.2
4	39.6	43.7	-	16.6

By reducing Al content in the final composition of Co6 sample, the reinforcement/matrix ratio does not change significantly compared to the CO5 sample. It was observed that the microstructure changes by phase composition. The microstructural analysis of Co7, Co8, and Co9 samples with additional alloying elements in compositions shows that the reinforcement area fractions are 73.33, 46.73 and 61.81%, respectively. There is a significant increase in reinforcement percentage of Co-Cr and Co-V samples due to the production of higher amounts of intermetallics. Like Ni-based and Fe-based composites, the addition of Mn does not change the morphology and grain size of obtained alloys compared to the base alloy. Accordingly, the reinforcement area fraction in Co-Mn sample has a small difference with the Co6 alloy.

4.3.3 Vickers microhardness testing results of the Mo_2CoB_2 containing compsoites

Table 4.55 presents the Vickers microhardness (HV) values of Co1, Co3, Co5, and MCB5 samples. The hardness values change between 721.2 and 1047.7 in which the lowest and highest values belong to Co3 and MCB5 samples, respectively. Both Mo_2CoB_2 and cobalt aluminide phases exist in all these samples. Among the combustion synthesized M_3B_2 based alloys, the Mo_2CoB_2 containing alloys have higher hardness values. In this series of samples, the high percentage of Al (12-15 %wt) in the final composition causes relatively low hardness values of the products. However among these alloys, MCB5 with the highest Al content has the highest hardness because the reinforcement to matrix ratio is high. Also, the reinforcement contains of Mo_2CoB_2 and MoCoB ternary phases.

Table 4.55 : Vickers hardness values of samples with increasing Co_3O_4.

Exp. No	HV (mean value)
Co1	855.5±111.43
Co3	721.2±159.38
Co5	853.6±59.79
MCB5	1152.75±188.94

Table 4.56 presents the Vickers microhardness (HV) values of Co11, Co10, and Co6 samples. These hardness values change between 804.5 and 1179.5HV in which the lowest and the highest values belong to CO11 and CO10 samples, respectively. Besides the Mo_2CoB_2 and Co percentages in the alloys, the presence of MoB or Co_2B borides influences the hardness values. The higher percentage of $Co_{20}Al_3B_6$ phase in the matrix of Co10 sample increases the hardness value significantly. Since all the samples have very low Al weight percentages, the hardness values exceed 800HV.

Table 4.56 presents the Vickers microhardness (HV) values of the Co7, Co8, and Co9 samples. The hardness values change between 735.7 and 1249.8 HV in which the lowest and the highest values belong to CO8 and CO7 samples, respectively. All the samples consist of Mo_2CoB_2 ternary boride with the substitution of additional alloying elements for Co position in the structures. The difference between hardness values of Co7 and Co8 samples attributes to the Mn and V dissolved in matrix phase as revealed by SEM. High percentages of Cr in the reinforcement phase increases the hardness value by producing Mo-Co-Cr composition. Therefore, it is observed that V addition results in a decrease in the hardness. It can be caused by the larger atom radius of V than by Co which leads to the weaker B-V bonds and Mo-V metallic bonds. The addition of the Mn to W_2CoB_2 hard alloy is the best choice which have high ductility, hardness and relatively high mechanical properties consistent with the modelling results about W-Co-B ternary boride hard alloys [77]. It is more likely that the formation of ternary Mn_2AlB_2 phase with the hardness ranged between 8-11GPa [78] in the matrix of the Co7 increased the hardness value. Moreover, the formation of dual phase MoCoB/Mo_2CoB_2 in the reinforcement of Cr containing compositions cause high hardness and wear resistance as it was reported in the literature [66].

Table 4.56 : Vickers microhardness values of the SHS alloys obtained from the experimental study about the effect of different additional alloying elements.

Exp. No	HV (mean value)
Co11	804.5±48
Co10	1179.5±200
Co6	958.3±158
Co7	1249.8±100
Co8	735.7±55
Co9	1033.1±83

4.4 Annealing of as-cast Alloys

In this section, the annealing, under the conditions of 1000 °C temperature and 2-6 hrs duration time, was examined to observe its effect on the structure, phase composition and hardness of as-cast alloys (NI7 and NI15).

After the annealing at 1000 °C for 2 hrs, the samples were ground by 180-1000 grit SiC papers and then polished by diamond 1, 3 and 9 μm. Figure 4.70 presents the SEM micrographs of NI7-A1 sample at X500 magnification. Also, the elemental distributions of the phases in as-cast alloys which are revealed by EDS scans, are listed in Table 4.57. The Ni_3Al intermetallic forms due to the remaining Al (8.9 wt%) in the matrix (points 2 and 3). The needle-like particles and the eutectic phases (points 1, 4 and 5) that dispersed in grain boundaries, compose of Mo_2NiB_2. The inner side of large grains composes higher percentages of MoB binary boride.

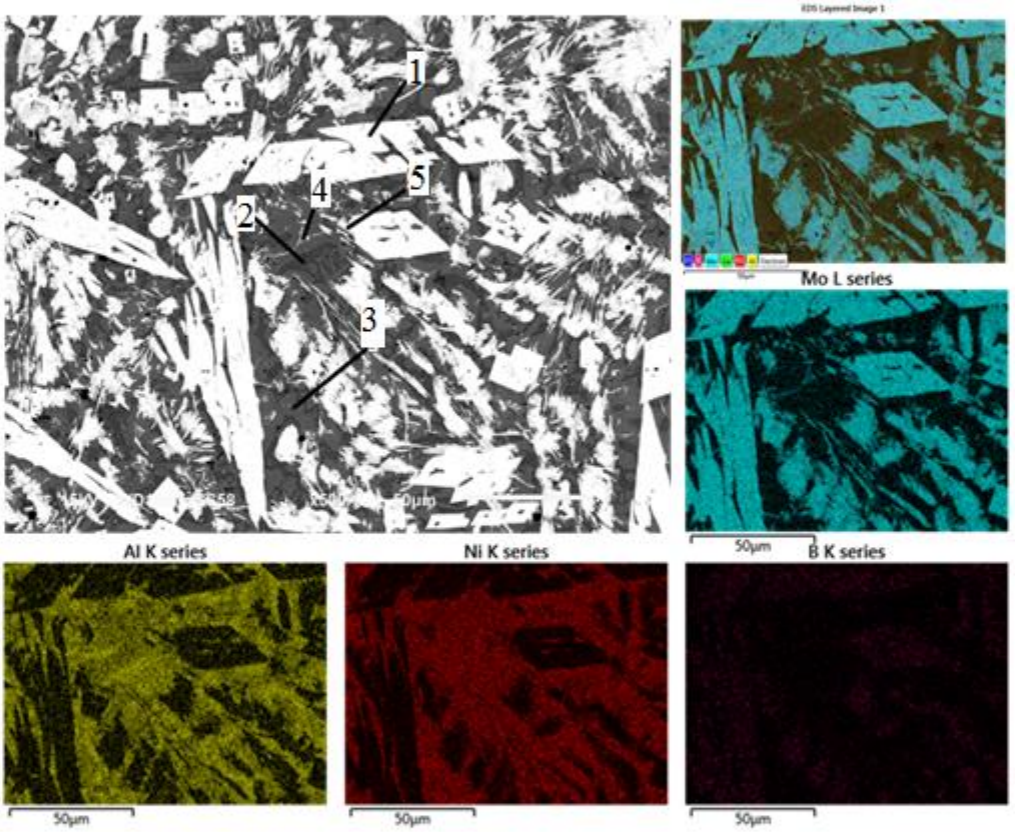

Figure 4.70 : SEM/BSE image of Ni7-A1 sample (x500 magnification).

Table 4.57 : Energy dispersive spectroscopy analysis results of Ni7-A1 alloy obtained from annealing at 1000 °C for 2hrs.

Point	1	2	3	4	5
B	18.86	10.73	20.17	-	-
Al	-	2.63	-	21.58	13.59
Ni	19.44	35.60	17.78	71.05	75.91
Cu	-	-	-	7.37	7.91
Mo	61.70	51.03	62.05	-	2.58

Also, the annealing was prolonged to about 6 hrs to study the effect of heat treatment on the microstructure and phase composition in the NI7-A2 sample. According to the SEM micrograph in Figure 4.71, the plate-like grains are Mo_2NiB_2 (points 2 and 4, light gray) and the inner part of grains consists of MoB (point 1). In this sample, the dendrites disappear, consequently, the Mo_2NiB_2 grains get enlarged. There are Mo-rich phases that spread all over the sample. The Ni_3Al intermetallic forms in the matrix because of the presence of Al (point 3).

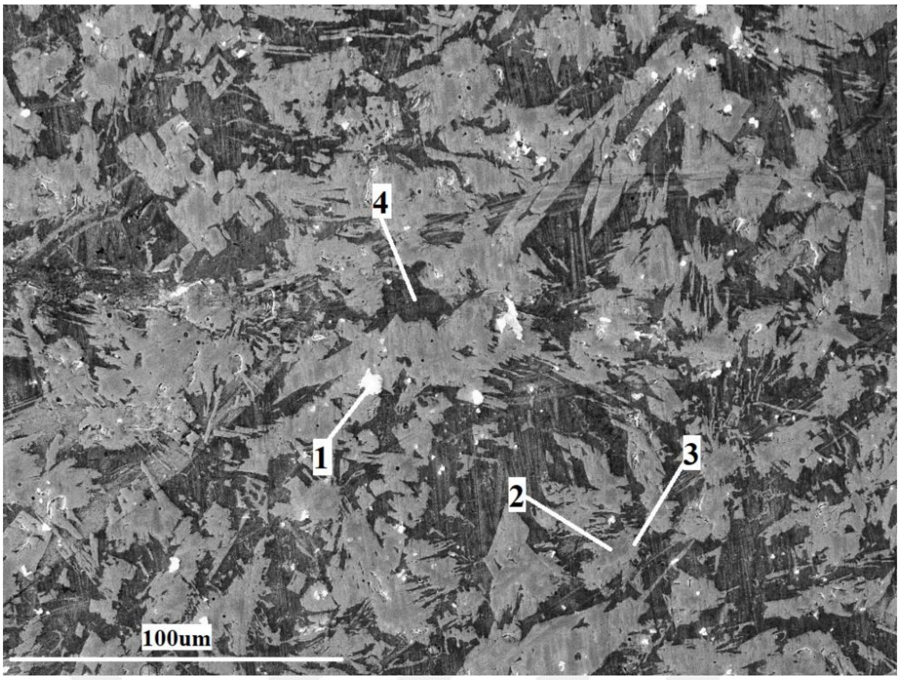

Figure 4.71 : SEM/BSE image of Ni7-A2 sample (x500 magnification).

Table 4.58 : Energy dispersive spectroscopy analysis results of Ni7-A2 alloy obtained from annealing at 1000 °C for 6hrs.

Point	**1**	**2**	**3**	**4**
B	6.91	5.54	3.83	3.83
Al	-	-	-	13.04
Ni	1.29	17.25	13.69	83.17
Cu	-	-	-	-
Mo	91.79	77.21	82.48	3.79

4.5 Arc Melting of SHS Alloys

In this section, the arc melting was performed to study its effect on the structure, phase composition and hardness of the combustion synthesized (as-cast) NI14 and NI15 alloys. The arc melted samples are NI14-M and NI15-M that were analyzed by SEM/EDS.

Figure 4-72 presents the SEM micrographs of NI14-M sample at X1000 magnification. Also, the elemental distributions of the phases in as-cast alloy were revealed by EDS scans.

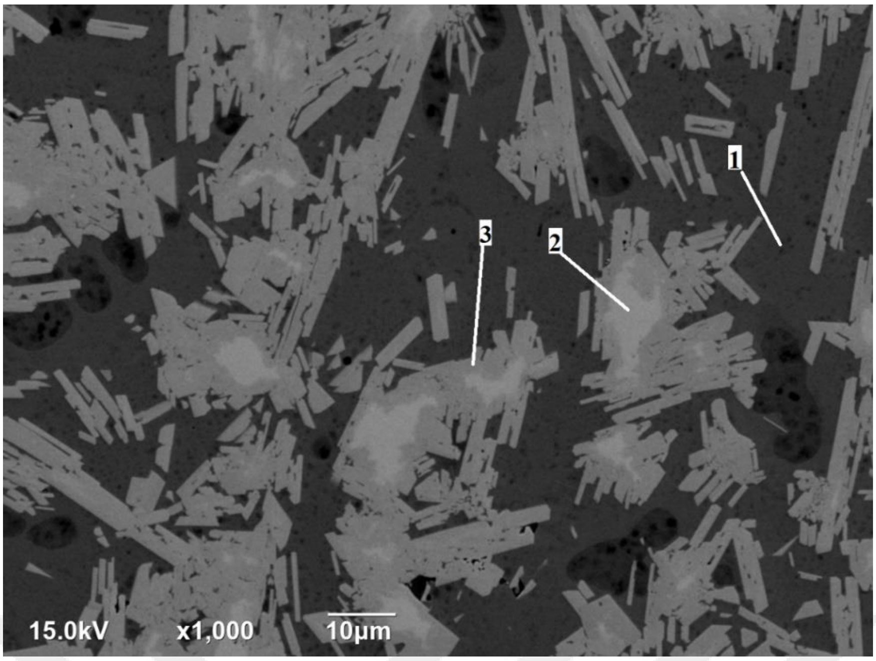

Figure 4-72: SEM/BSE image of SHS synthesized NI14M sample (x1000 magnification).

According to Table 4-59, the remaining Al (12 wt%) in NI14 was reduced and, Ni phase formed in the matrix (point 1). However, the weight percentage of boron with lower atomic weight decreased due to the high vapor pressures. Also in this alloy, matrix consists of Ni(Al) instead of Ni_3Al in Ni14 sample.

Table 4-59: Energy dispersive spectroscopy analysis results of NI14M alloy obtained from arc-melting after combustion synthesis.

Point	B	Al	Ni	Mo	W
1	7.36	-	1.76	88.6	2.28
2	3.28	-	23.5	73.2	--
3	-	4.53	95.4	-	-

Figure 4-73 presents the SEM micrographs of NI15-M sample at X1000 magnification. Also, the elemental distributions of the phases in as-cast alloy were revealed by EDS scans as listed in Table 4.60. The remaining Al (9 wt%) in the matrix phase in NI15 was reduced as intermetallic Ni_3Al matrix phase changes to Ni solid solution (points 3). However, like the NI14 alloy, the weight percentage of boron with lower atomic weight decreases due to the high vapor pressure. The NI15-M alloy consists of particles with similar morphology that disperse in the matrix. The inner part of large grains mainly composes of MoB binary borides.

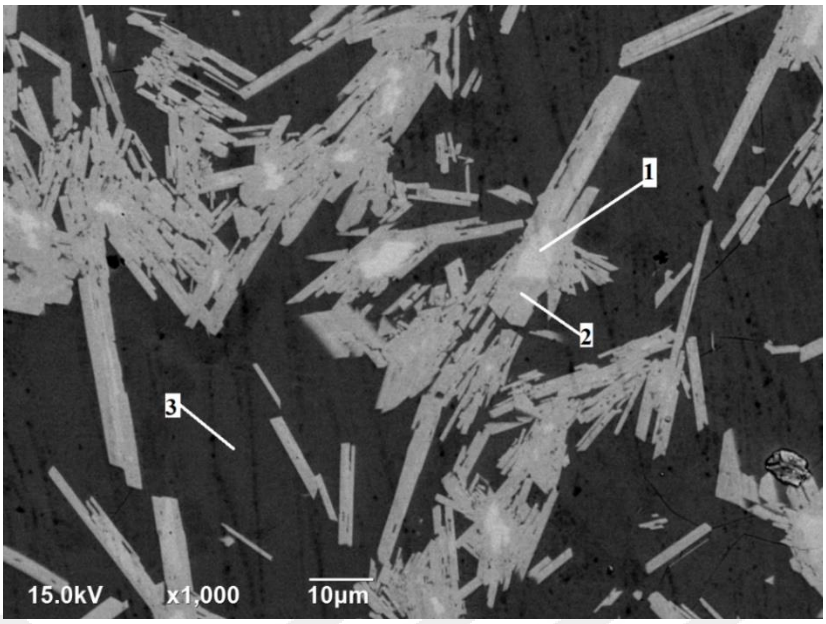

Figure 4-73 : SEM/BSE image of SHS synthesized NI15M alloy (x1000 magnification).

Table 4.60 : Energy dispersive spectroscopy analysis results of NI15M alloy obtained from arc-melting after combustion synthesis.

No	B	Al	Ni	Mo
1	7.75	-	2.29	89.96
2	2.62	-	24.33	73.05
3	-	4.4	95.6	-

Table 4.61 presents the hardness values of the arc-melted samples after combustion synthesis of Ni14 and Ni15 alloys. Arc melting slightly decreases the hardness values in both samples due to the evaporation of B and Al. According to the SEM images, the MoB phase content decreases after the arc melting in Ni14 and Ni15 samples.

Table 4.61 : Vickers microhardness results of NI14M and NI15M alloys obtained from arc-melting after combustion synthesis

No	Hardness (HV)
NI14M	1023.5
NI15M	902.28

4.6 Wear Resistance Test of Selected as-cast Alloys

Five as-cast alloys (NI11, NI14, NI15, FE14 and Co6) were subjected to reciprocating sliding wear tests at room temperature in a laboratory atmosphere by a Tribotech^{TM}

Oscillating Tribotester. The wear rate was calculated by the following equation: Wear rate = (Wear volume)/(Applied force*Sliding distance).

Where the applied force is 4 N and the sliding distance is 120 m. The studies on wear behaviors of the as-cast Mo_2NiB_2, Mo_2FeB_2 and Mo_2CoB_2 based alloys are limited in the literature. There are only few research works carried out on the wear properties of the Mo_2FeB_2 ternary boride dispersed metal matrix composites [7-9]. Sample NO8 has the highest average wear volume loss (0.001504 mm^3) and wear rate (3.1333e-9 mm^2/N) among the other alloys. On the other hand, the sample NI15 has the lowest average wear volume loss (0.000526 mm^3) and wear rate (.0958e-9 mm^2/N). The wear volume loss and wear rate of the other samples are presented in Table 4.62 which exhibits almost similar values to each other for Mo_2NiB_2 based samples (NI11 and NI14). It can be seen that these values are also comparable to the wear rate of the WC-Co which has 0.00058 mm^3 wear volume loss and 1.2083e-9 mm^2/N wear rate.

Table 4.62 : Wear volume loss, wear rate and relative wear resistance values of the as-cast ternary boride based alloys.

Sample Number	Wear volume loss (mm^3)	Wear rate(mm^2/N)	Relative wear resistance
NI11	8.7E-04	1.83E-09	1.711
NI14	6.22E-04	1.29E-09	2.418
NI15	5.26E-04	1.1E-09	2.859
FE14	1.5E-03	3.13E-09	1
CO6	7.26E-04	1.51E-09	2.072
WC-10Co	5.8E-04	1.21E-09	2.593

Figure 4-74 illustrates the images of wear tracks of M_3B_2 based SHS alloys as well as the WC-10Co cermet. Although it was attempted to have the wear tests on the pure parts of the samples which have no defects, but the presence of some porosities on the surface of the as-cast alloys were negligible as seen in Figure 4-74. The relatively lower width of the wear track of NI15 alloy in relation to the WC-10Co sample indicates the lower wear volume loss of this SHS alloy.

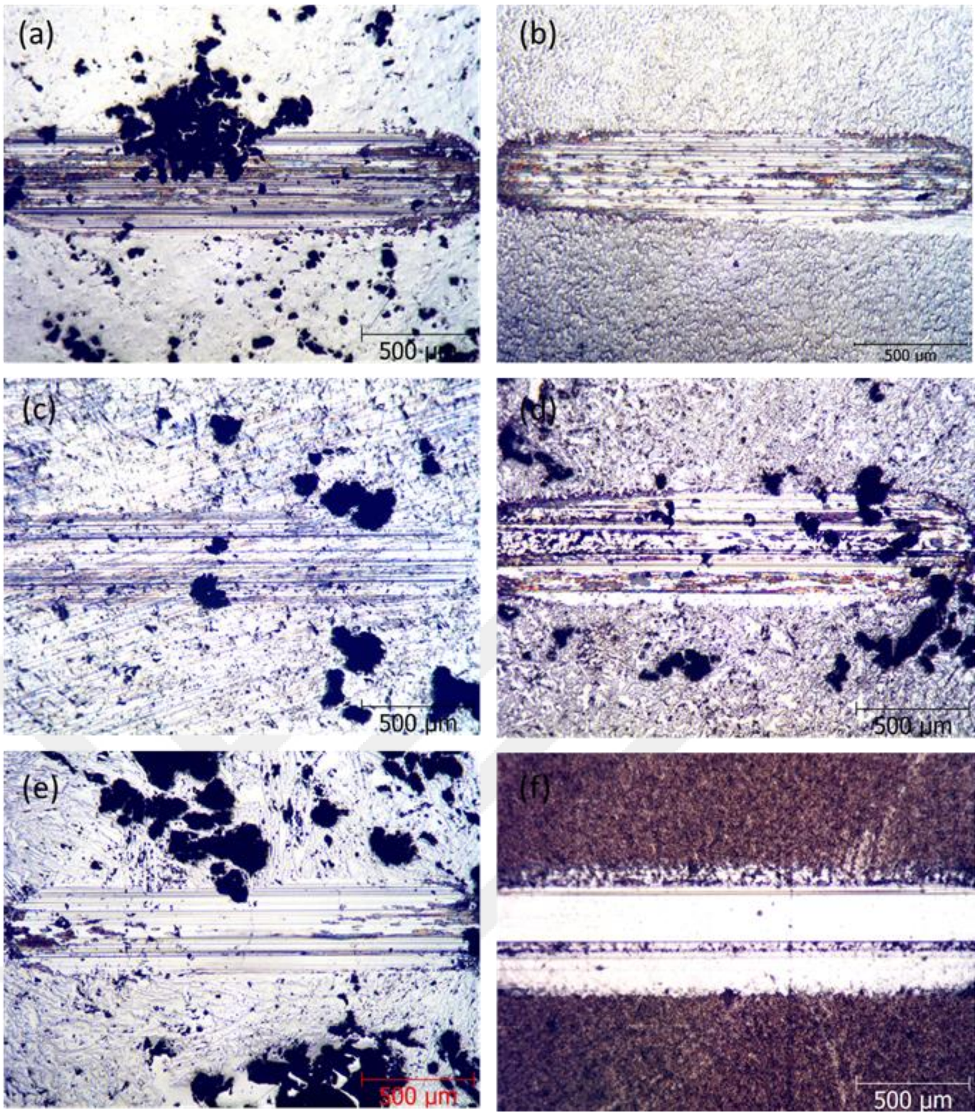

Figure 4-74 : Optical microscopy analysis of a) Sample NI11, b) Sample NI14, c) Sample NI15, d) Sample FE14, e) Sample Co6 and f) WC—10Co.

Figure 4-75 shows the SEM analysis micrograph of the wear tracks taken at the same magnifications (x5000) from the as-cast NI14 and NI15 samples and also the WC-10Co cermet for comparing the results. As seen from Figure 4-75 (a) and (b), the NI14 and NI15 samples exhibit some microgrooves along the sliding direction. The hard particles of abrasive ball has been stuck on the NI14 surface. The presence of these removed particles on the surface of the reinforcement phases confirms the higher hardness of this area in relation to the binder phase. The contact between abrasive ball and surface of alloy in sample NI15 is lower that can be attributed to the excellent wear resistance of this sample. The smooth appearance of the worn surface of the samples NI14 and NI15 can also be explained by the resistance against the material removal in the sliding surface due to their high hardness values. The cracks were observed on the surface of the as-cast alloy NI15 which was occurred near the grain boundaries due to the high hardness of reinforcing phases in comparison to the matrix. The SEM micrograph of worn surface of the WC-10Co cermet as a representative of wear resistant sample is shown in Figure 4-75(c). It depicts that the particles from some areas on the surface of the WC-10Co cermet have been removed during sliding. It can be concluded that the NI14 and NI15 samples containing Mo_2NiB_2 with high strength and high hardness, have better performance during abrasion in comparison to the tungsten carbide cermet.

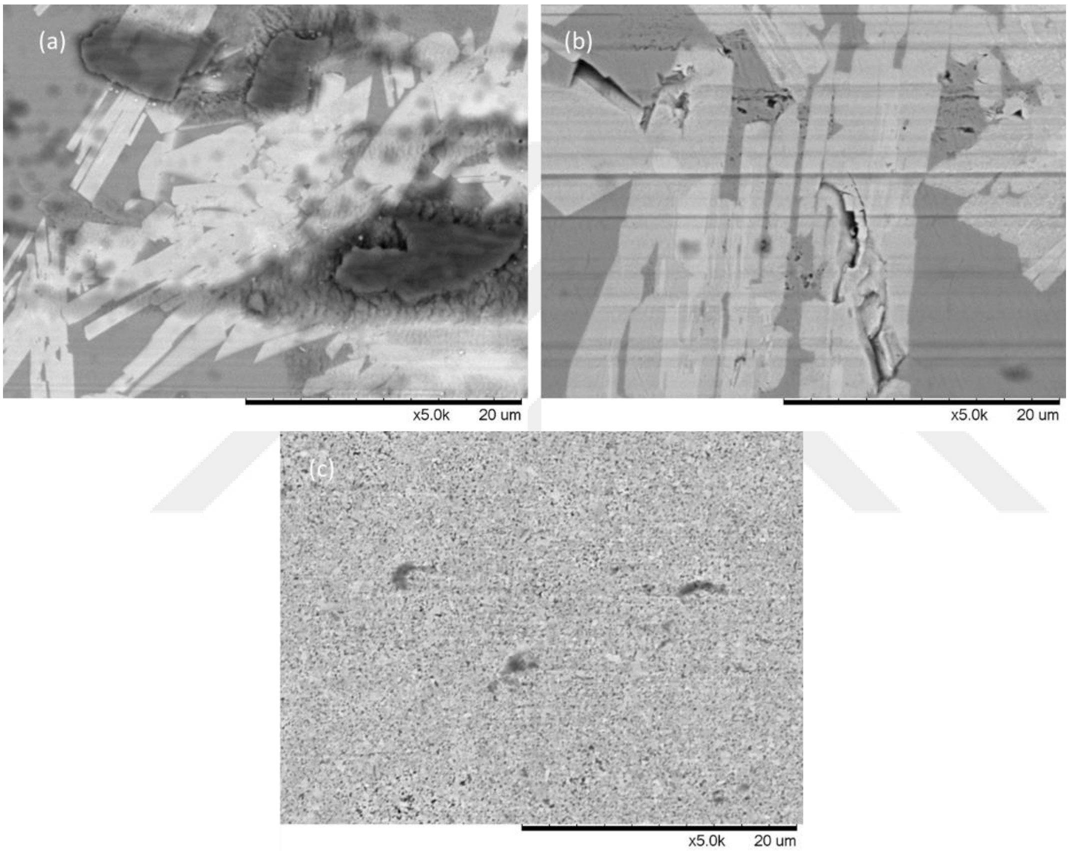

Figure 4-75 : SEM micrographs of worn surfaces of a) sample NI14, b) sample NI15 as-cast alloys and c) WC-10Co.

Figure 4-76 presents the mean friction coefficient of the NI11, NI14 and NI15 alloys with different compositions in Mo-Ni-B-Al system. Friction coefficients of the as-cast NI11 and NI14 samples sliding against abrasive ball are about 0.527 and 0.55 respectively that shows the similar friction characteristics ofthe WC-10Co cermet. But, the friction coefficient decreases to 0.345 with Ni addition in sample NI15. Among the alloys in Mo-Ni-B-Al system, it is observed that increasing the Mo/Ni ratio retains higher hardness values but higher wear rates. The results illustrate that friction results of sample NI15 is close to the Mo_2NiB_2 based coatings reported in the literature [8].

The mean friction coefficient values for samples FE14 and CO6 are 0.484 and 0.558, respectively. According to the literature, the Mo_2FeB_2 based cermets have been reported to exhibit better wear resistance than WC-10Co cemented carbides due to the formation of oxides on the worn surfaces during sliding [3]. In this study, the Mo_2FeB_2 based alloy exhibit relatively low friction coefficient but higher volume loss and wear rate in respect to the other samples.

All the five SHS alloys which were encountered sliding, appears to show a similar trend of increase with sliding time. However in the case of sample FE14, the friction coefficient was much lower than the steady value when sliding began. The overall results confirm that sample NI15 with the highest Ni weight percentage in composition and higher $Ni_{20}Al_3B_6$ ratio in the matrix phase exhibit excellent wear resistance behavior. The better wear performance, lower wear rate and lower friction coefficient of sample NI15 can also be attributed to the intermetallics presented in the Ni-rich matrix. The grain size and microstructure of M_3B_2 ternary borides dispersed in a brittle transition metal aluminide matrix phase of the obtained SHS composites, are responsible for the wear behavior of the obtained products.

Although the wear process is a very complex phenomenon that involves an interplay of several factors, it can be concluded that the wear rate in the five materials was predictable regarding to the hardness values of these samples.

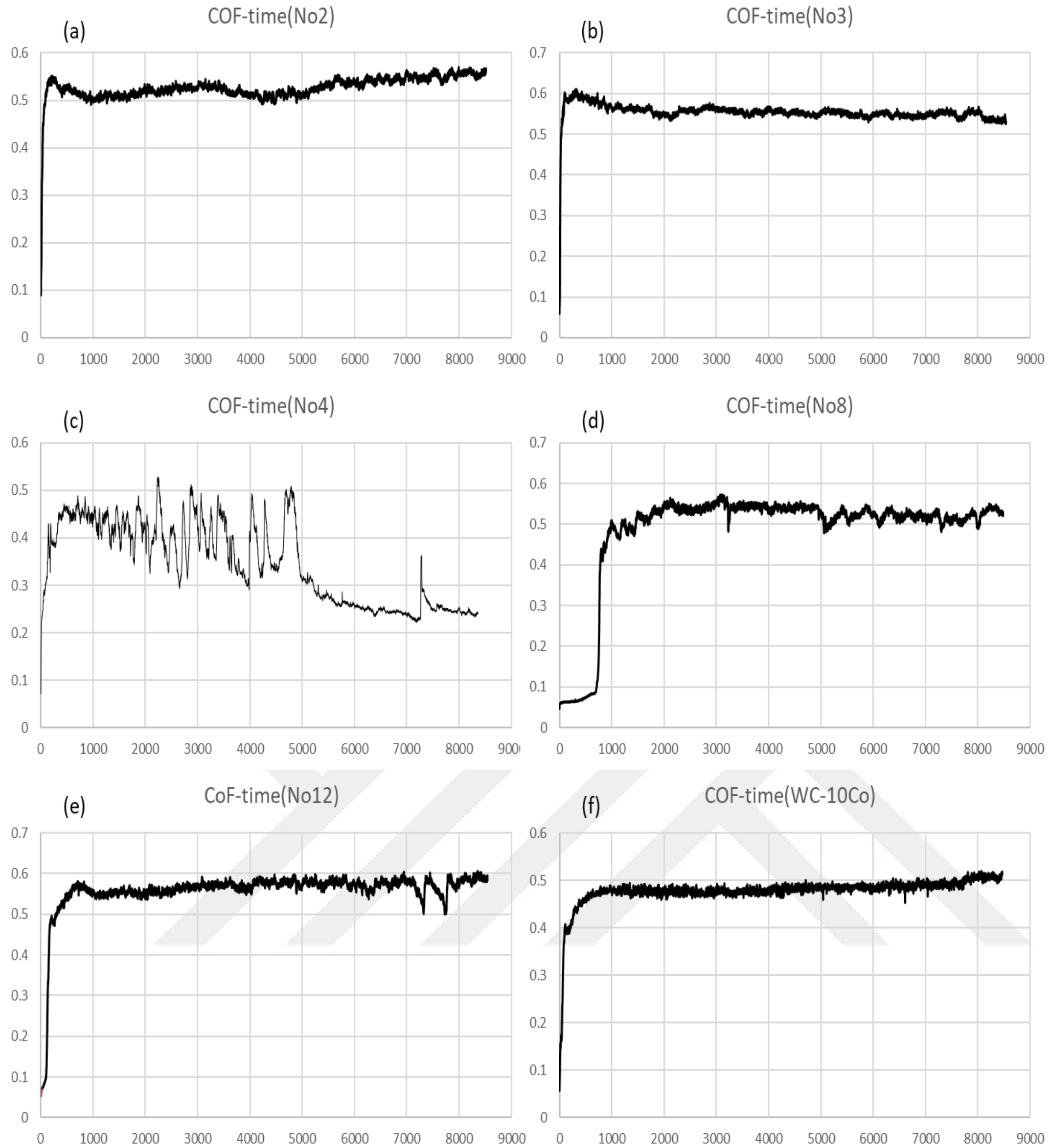

Figure 4-76 : Friction coefficient versus time curves of a) sample NI11, b) sample NI14, c) sample NI15, d) sample FE14, e) sample Co6 as-cast alloys and f) WC-10Co.

5. CONCLUSIONS AND RECOMMENDATIONS

The conclusions and results obtained from the experimental and simulation works in this study can be stated as follows:
The self-propagating high-temperature synthesis method under normal gravity has been used to fabricate ternary boride containing composites from metal oxides and boron trioxide as raw materials. The thermodynamical calculations, experimental studies, the characterization and the mechanical testing of the obtained materials cover the main chapters of this dissertation.

FactSage thermochemical software has been used to calculate the amounts of raw materials, the heat formed during combustion synthesis, the adiabatic temperature, and the product composition. In this case, the “Reaction” and “Equilib” modules were chosen for estimation of the results of the reactions.

Ternary boride based composites in Mo-Ni-B-(Al), Mo-Fe-B-(Al) or Mo-Co-B-(Al) ternary systems were produced by using raw materials mixture containing MoO_3, NiO, Fe_2O_3, Co_3O_4, B_2O_3, and Al. The combustion temperature decreases with Al_2O_3 as a functional additive. The Cr_2O_3, V_2O_5, MnO_2, Ta_2O_5, and Nb_2O_5 metal oxides have been used to observe the effect of addition of alloying elements Cr, Mn, V, Ta, and Nb on the SHS products.

The characterization methods such as AAS, XRD, SEM, SEM/EDS, and Vickers microhardness testing have been used to study the composition, microstructure, and hardness of the as-cast alloys. The products for chemical and XRD analyses were milled to obtain powder samples. Also, the bulk sections of the products were ground and polished to perform SEM/EDS analysis method.

According to the FactSage calculations, the adiabatic temperature for aluminothermic reduction of MoO_3 containing raw materials mixture reaches to 2700 °C. The excess Al (5-10 wt.%), Al_2O_3 (5-15 wt.%), and B_2O_3 have been examined to observe how they reduce the combustion temperature. Using functional additives suppresses the combustion temperature and reduces the residual Al in the final composition.

In Mo-Ni-B system, the addition of 5% Al and 5% Al_2O_3 in the initial mixtures reduces the adiabatic temperature to approximately 2600 °C. At these optimum amounts of Al and Al_2O_3, the yield of target and material loss were about 72% and 15%, respectively.

Furthermore, the amounts of 16-23 wt.% NiO, 18-30 wt.% Fe_2O_3, 26.5-33.5 wt.% Co_3O_4, and 9-12 wt.% B_2O_3 in the initial mixtures with excess Al (5 wt.%) and Al_2O_3 (5 wt.%) were used to achieve the Mo_2XB_2 containing composites. The increase in the metal oxide percentage increases the formation of Mo_2XB_2 but does not have any significant effect on the residual Al.

In Mo-Ni-B system, using excess B_2O_3 (twice more than the stoichiometric amount) in the initial mixture was found to decrease the adiabatic temperature from 2650 °C to 2300 °C. However, the yield of target and material loss values were similar to the values found when using Al and Al_2O_3 additives in the initial mixture.

According to the chemical analysis of the samples, the Al and Al_2O_3 addition to the initial mixture reduces the residual Al to 12 wt.%. But, the excess B_2O_3 reduces the residual Al to 3 wt.% in the same initial mixture.

In the Mo-Fe-B and Mo-Co-B systems, the addition of Al, Al_2O_3, and B_2O_3 to the initial mixtures was tried to achieve alloys with lower Al content. Also, in these systems, excess B_2O_3 and lower Al were more effective in reducing the residual Al content.

Furthermore, the different ratios of NiO/MoO_3, Fe_2O_3/MoO_3, and Co_3O_4/MoO_3 in the initial mixtures with lower Al and excess B_2O_3 were used to achieve the alloys with lower residual Al content. Increasing the ratio of the metal oxide to MoO_3 was found to reduce the residual Al and increase the formation of ternary borides (Mo_2XB_2) in the alloys.

The compositions which were calculated to carry out experiments using stoichiometric or non-stoichiometric initial mixtures for Mo-Ni-B system are as follows: 72Mo-21Ni-7B, 63.4Mo-29.4Ni-7.2B, 63.24Mo-29.3Ni-7.5B, 62.9Mo-29Ni-7.84B, 62.5Mo-28.9Ni-8.48B, 62Mo-28.8Ni-9B, 62.7Mo-30.2Ni-7.07B, 61.8Mo-31.2Ni-6.9B, 60Mo-33Ni-6.78B, 58.5Mo-34.9Ni-6.6B, 56.7Mo-36.8Ni-6.45B, 54.8Mo-38.8Ni-6.23B, 55Mo-39Ni-6B, 48Mo-46.5Ni-4.5B, and 34Mo-60Ni-5B.

According to the chemical analysis results, higher NiO/MoO_3 ratio in the initial mixture reduces the residual Al content; and the alloy with the composition of 34Mo-

61Ni-5B has the minimum Al content of 2-3 wt.% among the Mo-Ni-B ternary alloys tested.

In the reinforcement of alloys with 72Mo-21Ni-7B and 48Mo-46.5Ni-4.5B compositions, MoAlB ternary phase and the highest percentage of Mo_2NiB_2 ternary boride phase were detected, respectively. All the alloys obtained in Mo-Ni-B system, consist of binary Ni-Al intermetallics. Increasing the Ni/Mo ratio increases the Ni-Al-B phases in the matrix.

As a result of SEM/EDS analysis, all the SHS products exhibit two-phase structure containing the continuous matrix and the distributed particles of reinforcement. The alloy with the composition of 34Mo-60Ni-5B has the highest area fraction of matrix phase. As the weight percentage of Ni in the products decreases, the matrix phase area fraction changes by the content of Al which has dissolved in the obtained alloy composition.

The Vickers hardness values of samples depend on phase composition, residual Al, and the area fraction of reinforcements. Increasing the Ni/Mo ratio in the compositions results in the higher hardness values due to the decrement of the dissolved Al contents in matrices. The highest hardness was observed in the Ni11 composition due to the presence of binary boride MoB, Ni_3Al/NiAl and ternary $Ni_{20}Al_3B_6$ phases in addition to the Mo_2NiB_2. The homogeneous distribution of Mo_2NiB_2 in Ni-rich matrix for 34Mo-61Ni-5B composition presents the relatively high hardness of about 900 HV.

Using alloying elements of Cr and V in Mo-Ni-B system resulted in the production of complex M_3B_2-type (M : Mo, Ni, V or Cr) ternary boride containig composites. The addition of 12 wt.% Cr changes the structure of Mo_2NiB_2 from orthorhombic to tetragonal being in agreement with the literature results. The highest hardness value was observed in the Ni23 sample with fine elongated Mo_2NiB_2 particles distributed in 5 wt.% Mn containing Ni-rich matrix.

The compositions which were calculated to carry out experiments using stoichiometric or non-stoichiometric initial mixtures for Mo-Fe-B system are as follows: 64.13Mo-28.6Fe-7.22B, 63.6Mo-29.8Fe-7.16B, 63.2Mo-28.25Fe-8.5B, 62.76Mo-28.05Fe-9.18B, 61.04Mo-32.74Fe-6.87B, 59.43Mo-34.52Fe-6.69B, 57.57Mo-35.98Fe-6.47B, 56.18Mo-37.53Fe-6.3B, 55.6Mo-38Fe-5.89B, 52.8Mo-41.25Fe-5.8B, 48.7Mo-45.72Fe-5.5B, and 36.4Mo-56.2Fe-6.9B.

According to chemical analysis results, higher MoO_3/Fe_2O_3 ratio in the initial mixture increases the residual Al content; and the alloy with the composition of 36.4Mo-56.2Fe-6.9B has the minimum Al content of 2-3 wt.% in Mo-Fe-B ternary system.

In the reinforcement of alloys with 59.43Mo-34.52Fe-6.69B and 36.4Mo-56.2Fe-6.9B compositions, MoB binary phase and the highest percentage of Mo_2FeB_2 ternary boride phase were detected, respectively. All the alloys obtained in Mo-Fe-B system, consist of binary Fe-Al intermetallics. Increasing the Fe_2O_3 ratio increases the ferritic Fe in the matrix.

As a result of SEM/EDS analysis, all the SHS products exhibit a two-phase structure containing continuous matrix and rectangular particles of reinforcement. The alloy with the 36.4Mo-56.2Fe-6.9B composition has the highest area fraction of the matrix phase. By increasing Fe weight percentage in the produced alloys, the dissolution of Al in the matrix phase decreases.

The Vickers hardness values of samples depend on the phase composition, residual Al content, and the reinforcement area fraction. Increasing the Fe/Mo ratio in the compositions results in the higher hardness values due to the decreament of Al content in final compositions. The highest hardness value was observed in the Fe19 sample due to the presence of MoB and Fe_3B binary borides in addition to the Mo_2FeB_2 ternary phase. The homogeneous distribution of fine Mo_2FeB_2 particles in the Fe-rich matrix of the Fe14 sample with the 36.4Mo-56.2Fe-6.9B composition shows relatively high hardness of about 900 HV.

Using alloying elements of Cr, V and Mn in Mo-Fe-B system resulted in the production of complex M_3B_2 (M : Mo, Fe, Mn, V, or Cr) ternary boride containig composites with different grain morphologies. It was observed that Mn addition in Mo-Fe-B system increases the hardness value due to the formation of MoFe(Mn) in the matrix.

The compositions which were calculated to carry out experiments using stoichiometric or non-stoichiometric initial mixtures for Mo-Co-B system are as follows: 54.3Mo-39.15Co-5.7B, 52.15Mo-42Co-5.85B, 51.8Mo-41.7Co-6.4B, 51.17Mo-41.2Co-7.6B, 50.7Mo-40.8Co-8.32B, 50.4Mo-44.3Co-5.6B, 47.9Mo-46.7Co-5.37B, 45.78Mo-49.08Co-5.14B, 43.6Mo-51.4Co-4.8B, and 36.5Mo-58Co-5.8B.

According to chemical analysis results, higher MoO_3/Co_3O_4 ratio in the initial mixture increases the residual Al content; and the alloy with the composition of 36.5Mo-58Co-5.8B has the minimum Al content of 2-3 wt.% in Mo-Co-B ternary system.

Resulting from XRD anaalysis, in the reinforcement of alloys with 54.3Mo-39.15Co-5.7B and 36.5Mo-58Co-5.8B compositions, MoB binary phase and the highest percentage of Mo_2CoB_2 ternary boride phase were detected, respectively. All the alloys obtained in Mo-Co-B system, consist of binary Co-Al intermetallics. Increasing the Co_3O_4 ratio increases the Co in the matrix.

As a result of SEM/EDS analysis, all the SHS products exhibit two-phase structure containing continuous matrix and rectangular particles of reinforcement. The alloy with the 36.5Mo-58Co-5.8B composition has the highest area fraction of matrix phase. By increasing Fe weight percentage in the produced alloys, the dissolution of Al in the matrix phase decreases.

The Vickers hardness values of the samples depend on phase composition, residual Al content and the area fraction of reinforcement. Increasing the Co/Mo ratio in the compositions results in the higher hardness values due to the decrement of the dissolved Al in the matrices. The highest hardness value was observed in the Co10 sample due to the presence of Co_2B and MoB binary borides in addition to the Mo_2CoB_2 ternary phase. The homogeneous distribution of Mo_2CoB_2 elongated grains in the Co-rich matrix of the Co6 sample with the 36.5Mo-58Co-5.8B composition presents relatively high hardness of about 900 HV.

Using alloying elements of Cr, V and Mn in Mo-Co-B system resulted in the production of complex M_3B_2 (M : Mo, Co, Mn, V or Cr) ternary boride containig composites. The addition of Cr and V causes the formation of MoCoB ternary boride in addition to the Mo_2CoB_2 phase. The Mn addition in the base alloy composition with residual Al makes a Mn_2AlB_2 ternary phase in the matrix of the Co7 sample. The hardness values for Cr and Mn containing alloys are higher than that of the base alloy (Co6).

The annealing of the selscted sample in Mo-Ni-B system resulted in the increases in hardness values. The longer time duration has more effect on the hardness value of the sample. The microstructure analysis showed that the morphology and phase composition of reinforcement and matrix remain constant.

The arc-melting of the samples in Mo-Ni-B system resulted in the homogenous distribution of reinforcement phases. However, the weight percentage of boron decreases as well as the Al content in the matrix.

The wear resistance of the selected samples were compared with the WC-Co standard sample. The friction coefficient of the samples in Mo-Ni-B system changes by increasing Ni weight percentage. The optimum results for worn track image and friction coefficient belongs to sample NI15 with the highest Ni weight percentage. The lowest and highest wear rate values belong to the samples NI15 and FE14, respectively.

In order to improve the yield or mechanical properties of the products, the parameters like choosing different raw material resources, the shape and size of crucibles and the amount of initial mixture must be controlled. The effect of NaCl, MgO and different percentages of Al_2O_3, addition of Fe and etc as heat sinkers to the raw materials mixture can be studied in order to control the residual Al.

The corrosion resistance of Mo-Fe-B containing composites and fracture toughness of brittle Mo-Co-B systems can be improved by addition of alloying elements. Therefore, the effect of different additional elements such as Zr, Ti, W, Nb, Ta, Co, Ni, Fe and C can be examined to observe their effect on the matrix composition, microstructure and mechanical properties of ternary boride containing composites. Also, the double addition of Cr and V together with Mn can be studied to observe their effect on hardness and wear resistance of the as-cast alloys.

The mechanical and physical properties of the SHS composites must be controlled by using different compositions and additional elements. Therefore, further testing methods such as fracture toughness, corrosion resistance and wear resistance, micro indentation can be conducted on the as-cast composites.

REFERENCES

[1] **Kublii, V. Z. & Bondar A. A.** (2010). B-Mo-Ni Ternary Phase Diagram Evaluation, Ternary Alloy Systems: Phase Diagrams, *Refractory metal systems*, ***11***(E2)**.**

[2] **Rieger, W., Nowotny, H. & Benesovsky, F.** (1966). The crystal structure of W_2CoB_2 and isotypic phases, *Montash Chem*., ***97***(2), 378-382.

[3] **Asthana, R., Dahorte, N. B., Kumar, A.** (2006). *Materials Processing and Manufacturing Science.* United States, Butterworth-Heinemann.

[4] **Stephen W. T., Suong V. H. & Gay D.** (2002). *Composite Materials: Design and Applications*, United States, CRC Press.

[5] **Ibrahim I. A., Mohamed, F. A. & Lavernia, E. J.** (1991). Particulate reinforced metal matrix composites - a review, *journal of materials science*, ***26***, 1137-1156.

[6] **Ward-Close, C.M., Minor, R. & Doorbar, P.J.** (1996). Intermetallic-matrix composites-a review, *Intermetallics*, ***4***, 217-229.

[7] **Kainer, K. U.** (2006). *Metal Matrix Composites: Custom- made Materials for Automotive and Aerospace Engineering*, Germany, Wiley-VCH.

[8] **Suresh, S.** (1993). *Fundamentals of Metal-Matrix Composites*, United States, Butterworth-Heinemann.

[9] **Lloyd, D. J** (1989). The solidification microstructure of particulate reinforced aluminium/SiC composites, *Composites Science and Technology*, ***35***, 159-179.

[10] **Rangarajan, G., Vijaya & M.S.** (2014). *Materials Science*, (5th. Ed.). New Delhi : Tata McGraw-Hill.

[11] **Askeland, D. R., Fulay, P. P. & Wright, W. J.** (1996). *The Science and Engineering of Materials*, (6th.ed.). Michigan: CL Engineering.

[12] **Mitra, R.** (2015). *Structural Intermetallics and Intermetallic Matrix Composites*, (1st.ed.). IIT Kharagpur: CRC Press.

[13] **Angelo, P. C., Subramanian, R.** (2008). *Powder Metallurgy: Science, technology and applications*, New Delhi: PHI Learning Pvt. Ltd.

[14] **Sarin, V.K., Mari, D., Nebel, C. E. & Lianes, L.** (2014). *Comprehensive hard materials*, (1st. Ed.), Netherlands, Elsevier.

[15] **Matkovich, V. I., Samsonov, G. V., Hagenmuller, P. & Lundstorm, T.** (1977). *Boron and refractory borides*, New York: Springer-Verlag.

[16] **Habashi, F.** (2005). *Principles of extractive metallurgy*, (1st. Ed.) Routledge.

[17] **Pan, L. M.** (1992). Phase equilibria and elastic moduli of rapidly solidified Fe-Cr-Mo-B and Fe-Cr-Ni-B alloys, (Thesis submitted for the Ph.D.), University of Surrey.

[18] **Hu, X. B., Zhu, Y. L., Sheng, N. C. & Ma, X. L.** (2014). The Wyckoff positional order and polyhedral intergrowth in the M_3B_2- and M_5B_3-type boride precipitated in the Ni-based superalloys, *Scientific reports*, **4**, 7367.

[19] **He, T. W., Jiang, Y. H., Zhou, R. & Feng, J.** (2015). The electronic structure, mechanical and thermodynamic properties of Mo_2XB_2 and MoX_2B_4 (X = Fe, Co, Ni) ternary borides, *Journal of Applied Physics* , ***118***, 075902.

[20] **Doychak, J.** (1992). Metal- and Intermetallic- Matrix Composites for Aerospace Propulsion and Power Systems, *JOM*, ***44***, 46-51.

[21] **Davis, J. R.** (2000). Handbook: Nickel, Cobalt, and Their Alloys, ASM International Handbook Committee.

[22] **Yuan, K.** (2013). Thermal and Mechanical Behaviors of High Temperature Coatings, (Undergraduate thesis), Linköping.

[23] **Bhadeshia, H. K. D. H.** (1997). Recrystallisation of Practical Mechanically Alloyed Iron-base and Nickel-base Superalloys, *Materials Science and Engineering: A*, ***223***, 64-77.

[24] **Omori, S., Koyama, K., Hashimoto, Y. & Yamashita, M.** (1984). phase relationships in Ni-Mo-B and Ni-W-B systems at 1223K, *Journal of the Japan Institute of Metals and Materials*, ***48***, 682-687.

[25] **Kolomytsev, T. & Moskaleva, N. V.** (1966). phase composition and some properties of alloys of the system Molybdenum-Nickel-Boron, *Powder Metallurgy and Metal Ceramics*, ***5***, 665-670.

[26] **Kuzma, Y. B., Chepiga, M. V.** (1969). An X-ray diffraction investigation of the systems Ti-Ni-B, Mo-Ni-B and W-Ni-B, *Soviet Powder Metallurgy and Metal Ceramics*, ***8***, 832-835.

[27] **Morishita, M., Koyama, K., Yagi, S. & Zhang, G.** (2001). Calculated phase diagram of the Ni-Mo-B ternary system, *Journal of alloys and compounds*, ***314***, 212-218.

[28] **Kubliy, V. Z., Bondar, A. A., Utkin, S. V., Petyukh, V. M., Lysenko, S. I. & Velikanova, T. Y.** (2008). phase equilibria in the nickel corner of the Mo-Ni-B system at temperatures close to melting, Powder *Metallurgy and Metal Ceramics*, ***47***, 211.

[29] **Takagi, K. i.** (2006). Development and application of high strength ternary boride base cermets, *Journal of Solid State Chemistry*, ***179***, 2809-2818.

[30] **Corporation, A. E. M.** (1953). Patent No.790,917. London. Patent Office.

[31] **Yamasaki, Y., Nishi, M. & Takagi, K. i.** (2004). development of very high strength Mo_2NiB_2 complex boride base hard alloy, *Journal of Solid State Chemistry*, ***177***, 551-555.

[32] **Yuan, B., Zhang, G. J., Kan, Y. M. & Wang, P. L.** (2010). Reactive Synthesis and Mechanical Properties of Mo_2NiB_2 Based Hard Alloy, *Int. Journal of Refractory Metals and Hard Materials*, ***28***, 291-296.

[33] **Takagi, K. I., Koike, W., Momozawa, A. & Fujima, T.** (2012). Effects of Cr on the Properties of Mo_2NiB_2 Ternary Boride, *Solid State Sciences*, ***14***, 1643-1647.

[34] **Takagi, K. I.** (1998). development of high strength complex boride base hard materials produced by reaction borornizing sintering, *Journal of the Japan Society of Powder and Powder Metallurgy*, ***45***, 507-514.

[35] **Yamasaki, Y., Nakano, K., Okada, M. & Takagi, K. I.** (1995). Effects of CrB on the Sintering Mechanisms of Mo_2NiB_2 Hard Alloys, *Journal of the Japan Society of Powder and Powder Metallurgy*, ***42***, 1042-1046.

[36] **Takagi, K.I. & Yamasaki, Y.** (2000). Effects of Mo/B Atomic Ratio on the Mechanical Properties and Structure of Mo_2NiB_2 Boride Base Cermets with Cr and V Additions, *Journal of Solid State Chemistry*, ***154***, 263-268.

[37] **Hirata, K., Iwanaga, K., Yamasaki, Y. & Takagi, K. I.** (2007). Development of high corrosion resistant Mo_2NiB_2 boride base cermets for plastic injection molding machine parts, *Materials Science Forum*, ***534-536***, 1157-1160.

[38] **Matthew, J. & Donachie, S. J.** (2002). *Superalloys: A Technical Guide*, (2nd. Ed.). ASM International.

[39] **Kehler, W. F.** (1980). *Handbook of International Alloy Compositions and Designations*, United states, Defense Technical Information Center.

[40] **Moshka, O., Pinkas, M., Brosh, E., Ezersky, V. & Meshi, L.** (2015). Addressing the issue of precipitates in maraging steels-Unambiguous answer, *Materials Science and Engineering: A*, ***638***, 232-239.

[41] **Cikara, D., Rakin, M. & Todic, A.** (2009). Cast Steel-SiC Composites as Wear Resistant Materials, *FME Transactions*, ***37***, 151-155.

[42] **Pagounis, E. & Lindroos, V. K.** (1998). Processing and properties of particulate reinforced steel matrix composites, *Materials Science and Engineering: A*, ***246***, 221-234.

[43] **Zachariev, Z. T.** (2011). *New Superhard Ternary Borides in Composite Materials, Metal, Ceramic and Polymeric Composites for Various Uses*, Rietrieved July 7, 2018 from http://www.IntechOpen.com/.

[44] **Raghavan, V.** (2003). phase diagram evaluations, *Journal of phase equilibria*, ***24***, 449-450.

[45] **Korniyenko, K. & Bondar, A.** (2007). *B-Fe-Mo Ternary Phase Diagram Evaluation*, Rietrieved July 7, 2018 from http://www.msi-eureka.com/preview-html/10.11554.1.6/B-Fe-Mo_Ternary-Phase-Diagram-Evaluations/.

[46] **Sarasola, M., Gomez-Acebo, T. & Castro, F.** (2005). Microstructural development during liquid phase sintering of Fe and Fe–Mo alloys containing elemental boron additions, *Powder metallurgy*, ***48***, 59-67.

[47] **Wang, B., Liu, Y, Ye, J. W. & Wang, J.** (2013). Electronic, magnetic and elastic properties of Mo_2FeB_2: First-principles calculations, *Computational materials science*, ***70***, 133-139.

[48] **Wang, Q. F., Pan, Y. J., Hu, B. & Zhou, L.** (2011). Effects of alloys on Microstructure and Properties of Mo_2FeB_2-based, *Advanced Materials Research*, ***399-401***, 399-402.

[49] **Molinari, A., Gialanella, S., Straffelini, G., Pieczonka, T. & Kazior, J.** (2000). Dilatometry study of the sintering behavior of boron-alloyed Fe-1.5 pct Mo powder, *Metallurgical and Materials Transactions A*, ***31***, 1497–1506.

[50] **Upadhyaya, G. S., Bagdi, P. K.** (2000). Reactive Liquid Phase Sintering of Mo_2FeB_2-Fe Cermets, *International journal of materials and product technology*, ***15***, 275-291.

[51] **Karwan-Baczewska, J. & Rosso, M.** (2006). The Effect of Boron on the Properties of Fe-Mo PM Sintered Alloys, *Powder metallurgy progress*, ***6***, 11-19.

[52] **Tashiro, H., Hirata, K., Yamasaki, Y. & Takagi, K. I.** (2007). Metal Injection Molding Process of Mo_2FeB_2 Boride Base Cermets, *Materials science forum*, ***534-536***, 377-380.

[53] **Haizhou, Y. & Liu, W.** (2010). Effect of Mo/B Atomic Ratio on the Microstructure and Mechanical Properties of Mo_2FeB_2 Based Cermets, *International Journal of Refractory Metals and Hard Materials*, ***28***, 338-342.

[54] **Yongguo, W. & Zhaoqian, L.** (2002). Development of ternary-boride-based hard cladding material, *Materials Research Bulletin*, ***37***, 417-423.

[55] **Yu, H., Zheng, Y., Liu, W., Zheng, J. & Xiong, W.** (2010). Effect of Mn Content on the Microstructure and Mechanical Properties of Mo_2FeB_2 Based Cermets, *Int. Journal of Refractory Metals & Hard Materials*, ***28***, 286-290.

[56] **Yu, H., Zheng, Y., Liu, W., Zheng, J. & Xiong, W.** (2010). Effect of V Content on the Microstructure and Mechanical Properties of Mo_2FeB_2 Based Cermets, *Materials and Design*, ***31***, 2680–2683.

[57] **Yu, H., Liu, W. & Zheng, Y.** (2011). Effect of Carbon Content on the Microstructure and Mechanical Properties of Mo_2FeB_2 Based Cermets, *International Journal of Refractory Metals and Hard Materials*, ***29***, 724-728.

[58] **MA, Z., Wang, W., Zou, J. F., Dong, S. Z., Zhang, L. Y. & Li, Z. C.** (2011). Preparation and properties of flame-sprayed Mo-FeB-Fe cermet coatings, *Transactions of Nonferrous Metals Society of China*, ***2***, 1314-1321.

[59] **Ke, D., Pan, Y., Xu, Y., Yang, L., Wu, R. & Lu, Z.** (2017). Microstructure and mechanical properties of Mo_2FeB_2 ceramic-steels with Nb/V addition, *Advances in Applied Ceramics*, ***116***, 92–98.

[60] **SUN, C., Yu, H. & Liu, W.** (2017). Microstructure, mechanical properties and first-principles calculations of Mo_2FeB_2-based cermets with Mn addition, *Journal of the Ceramic Society of Japan*, ***125***, 677-680.

[61] **Jeitschko, W.** (1968). The crystal structure of MoCoB and related compounds, *Acta cryst.*, ***B24***, p. 930-934.

[62] **Davydov, A. & Kattner, U. R.** (1998). Thermodynamic Assessment of the Co-Mo System, *Journal of Phase Equilibria*, ***20***, 5-16.

[63] **Liu, Y. Q., Zhao, X. S., Yang, J. & Shen, J. Y.** (2011). Thermodynamic optimization of the boron-cobalt-iron system, *Journal of alloys and compounds*, ***509***, 4805-4810.

[64] **Mizuno, H. & Kitamura, J.** (2007). MoB/CoCr Cermet Coatings by HVOF Spraying against Erosion by Molten Al-Zn Alloy, *Journal of Thermal Spray Technology*, ***16***, 404-413.

[65] **Lv, H. P., Wang, J., Zhai, C. S., Li, F. & Sun, B. D.** (2007). Study of microstructure, vickers microindentation and microhardness distribution of HVOF sprayed composite MoB/CoCr coating, *Proceedings of the 2007 International Thermal Spray Conference*, Beijing, China, May 14-16.

[66] **Chen, X., Zhang, R.** (2012). Corrosion Behavior of Low Pressure Plasma Sprayed MoB/CoCr Coatings Exposed to Molten Al-12.07wt.%Si Alloy, *Procedia Engineering*, ***27***, 1766-1773.

[67] **Hamashima, K.** (2007). Application of New Boride Cermet Coating to forming of glass sheets, *Journal of Thermal Spray Technology*, ***16***, 32-33.

[68] **Indra, S.** (2016). A review on nano particulates reinforced metal matrix composites, *International Journal for Scientific Research & Development*, ***4***, 1292-1296.

[69] **Crider, J. F.** (1982). *Self-propagating High-temperature synthesis- A soviet method for producing ceramic materials*, Ceramic Engineering and Science Proceedings, Rietrieved June 8, 2018 from http://www.ism.ac.ru/handbook/84crid.htm.

[70] **Merzhanov, A. G., Sharivker, S. Y.** (1999). Self-Propagating High-Temperature Synthesis of Carbides, Nitrides, and Borides, *Materials Science of Carbides, Nitrides and Borides*, ***68***, 205-222.

[71] **Moore, J. J., Feng, H. J.** (1995). Combustion synthesis of advanced materials: PartI. Reaction parameters, *Progress in materials science*, ***39***, 243-273.

[72] **Munir, Z. A. & Anselmi-Tamburini, U.** (1989). Self-propagating exothermic reactions: The synthesis of high-temperature materials by combustion, *Materials Science Reports*, ***3***, 277-365.

[73] **Varma, A., Rogachev, A. S., Mukasyan, A. S. & Hwang, S.** (1989). Combustion synthesis of advanced materials: Principles and Applications, *Advances in chemical engineering*, ***24***, 79-226.

[74] **Borisov, A. A., Luca, L. D. & Merzhanov, A.** (2002). *Self-propagating High-temperature synthesis of materials*, Combustion Science and Tehnology Series, Volume 5, New York: Taylor & Francis.

[75] **Harold Sh, U.**, (2015), *Physical properties of various conductive metal diborides and their binaries*, (Ph.D. thesis), Iowa state university capstones

[76] **Kang, Sh., Xu, Zh., Choi, Y., Fujita, K., Matsugi, K. and Yu, J.**, (2016). Spark Sintering Behavior of Ubiquitously Fe-B and Fe Powders and Characterization of Their Hard Composites, *Materials Transactions*, ***75,*** 600-607.

[77] **Zhang, T., Yin, H., Zhang, C., Zhang, R., Jiang, X., Zheng, Q., and Qu, X.,** (2019). First-Principles Study on the Mechanical Properties and Electronic Structure of V Doped WCoB and W_2CoB_2 Ternary Borides, *Materials*, ***12,*** 967.

[78] **Kota, S., Chen, Y., Wang, J., May, S. J., Radovic, M., Barsoum, M. W.,** (2018). Synthesis and characterization of the atomic laminate Mn_2AlB_2, *Journal of the European Ceramic Society,* ***38,*** 5333-5340.

APPENDICES

APPENDIX A: Experimental conditions and results of the pre-compaction performed before the combustion synthesis of Mo-Ni-B containing alloys.

APPENDIX A: Experimental conditions and results of the pre-compaction performed before the combustion synthesis of Mo-Ni-B containing alloys.

Table A.1 : Effect of pre-compaction on the SHS parameters and XRF analysis results of the produced samples.

No	Expected composition			Raw materials					Crucible Type	Target yield	Material loss	Pre-compaction	XRF Analysis results				
	Mo	Ni	B	MoO_3	NiO	B_2O_3	Al	Al_2O_3					Mo	Ni	Al	Fe	Cu
8	63.4	29.4	7.2	41.18	16.02	9.95	28.17	4.69	Cu	49	20.73	None				_	
9	63.4	29.4	7.2	41.73	16.24	10.08	27.18	4.75	graphite			None				_	
10	63.4	29.4	7.2	41.73	16.24	10.08	27.18	4.75	Cu	60.7	15.21	None				_	
11	63.4	29.4	7.2	41.73	16.24	10.08	27.18	4.75	Cu	70.25	13.81	10	66.84	28.12	0.00	3.46	0.7
12	63.4	29.4	7.2	41.73	16.24	10.08	27.18	4.75	Cu	68.25	6.5	20	60.00	32.5	0.00	4.50	
13	63.4	29.4	7.2	41.73	16.24	10.08	27.18	4.75	Cu	45	9	40	56.75	37.54		_	0.35
14	63.4	29.4	7.2	41.73	16.24	10.08	27.18	4.75	Cu	72.12	11.50	60				_	
15	63.4	29.4	7.2	41.73	16.24	10.08	27.18	4.75	Cu			Vibration				_	
16	63.4	29.4	7.2	44.45	17.29	10.74	27.50	0.0	Cu	49.25	8.6	40	49.70	33.50	5.90	4.90	4.70
17	63.4	29.4	7.2	43.82	17.05	10.58	28.54	0.0	Cu	55.62	18.08	40	56.75	33.9	2.3	4.9	0.9

Table A.1 (continued) : Effect of pre-compaction on the SHS parameters and XRF analysis results of the produced samples.

No	Expected composition			Raw materials					Crucible Type	Target yield	Material loss	Pre-compaction	XRF Analysis results				
	Mo	Ni	B	MoO_3	NiO	B_2O_3	Al	Al_2O_3					Mo	Ni	Al	Fe	Cu
18	63.4	29.4	7.2	43.20	16.81	10.43	29.55	0.0	Cu	55.37	18.13	40	54.02	23.5	14.0	3.9	1.0
19	63.4	29.4	7.2	42.6	16.57	10.29	30.54	0.0	Cu	62.37	13.61	40	52.7	38.06		3.1	4.94
20	63.4	29.4	7.2	42.02	16.35	10.15	31.5	0.0	Cu			40	57.0	34.0	2.70	3.6	
21	63.4	29.4	7.2	43.20	16.81	10.43	29.55	0.0	Cu	71.12	11.5	Vibration	44.57	41.00	5.50	5.20	1.0
22	63.4	29.4	7.2	43.20	16.81	10.43	29.55	0.0	Cu	75.87	11.94	10	58.00	30.30	2.00	4.20	2.50
23	63.4	29.4	7.2	43.20	16.81	10.43	29.55	0.0	Cu	64.25	17.62	20				_	3.00
24	63.4	29.4	7.2	43.20	16.81	10.43	29.55	0.0	Cu	81.25	9.45	40	59.30	31.90	2.00	4.20	
25	63.4	29.4	7.2	43.20	16.81	10.43	29.55	0.0	Cu	40.06	19.26	60				_	0.5
26	63.4	29.4	7.2	41.18	16.02	9.95	28.17	4.69	Cu			40				_	
27	63.4	29.4	7.2	39.33	15.30	9.50	26.89	8.96	Cu			40	52.76	39.62	2.6	_	
28	63.4	29.4	7.2	43.20	16.81	10.43	29.55	0.0	Cu			Vibration	65.54	33.15		_	2.59
29	63.4	29.4	7.2	43.20	16.81	10.43	29.55	0.0	Cu			20	46.27	45.16		5.46	2.24
30	63.4	29.4	7.2	43.20	16.81	10.43	29.55	0.0	Cu			40	68.67	30.37		_	

CURRICULUM VITAE

Name Surname : Sevinch RAHIMI MOGHADDAM

Place and Date of Birth : Tabriz, 04/09/1986

E-Mail : Moghaddam@itu.edu.tr

EDUCATION :

- **B.Sc.** : 2009, Tabriz University, Faculty of Mechanical Enginnering, Ceramics Engineering
- **M.Sc.** : 2011, Sahand University of Technology, Faculty of Materials Engineering, Nano Materials

PROFESSIONAL EXPERIENCE AND REWARDS:

- 2014- ISTANBUL Technical University at the Laboratory of Pyrometallurgy.

PUBLICATIONS AND PRESENTATIONS ON THE THESIS:

- **Sevinch Rahimi Moghaddam**, Bora Derin, Onuralp Yucel, Seref Sonmez, Meltem Sezen, Feray Bakan, Vladimir N. Sanin, Dmitrii E. Andreev "PRODUCTION OF Mo_2NiB_2 BASED HARD ALLOYS BY SELF-PROPAGATING HIGH-TEMPERATURE SYNTHESIS", High Temperature Materials and Processes, 2019.
- **Sevinch Rahimi Moghaddam**, Faruk Kaya, Bora Derin, "Production of Mo2MB2-type (M = Ni, Fe, Co) Ternary Boride Containing Alloys by Self-propagating High Temperature Synthesis", Engineering Science and Technology, an International Journal., 2019.
- B. Derin, **S. R. Moghaddam**, O. Yucel, S. Sonmez, M. Bugdayci, M. Sezen, F. Bakan, V. Sanin, D. Andreev "INVESTIGATION OF Mo-Ni-B TERNARY ALLOYS FOR PRODUCTION OF BORIDE-BASED CERMETS BY SHS METHOD" International Symposium on self-propagating High-temperature Synthesis, Antalya, Turkey, 2015.

- **Sevinch Rahimi Moghaddam**, Bora Derin, Onuralp Yücel, M. Şeref Sönmez, Meltem Sezen, Feray Bakan, Vladimir Sanin, Dimitry Andreev "COMBUSTION SYNTHESIS OF MOLYBDENUM CONTAINING BORIDE BASED HARD ALLOYS" 18th International Metallurgy and Materials Congress, Istanbul, Turkey, 2016.
- Bora Derin, **Sevinch Rahimi Moghaddam**, Onuralp Yucel, Seref Sonmez, Mehmet Bugdayci, Meltem Sezen, Feray Bakan, Vladimir N. Sanin, Dmitrii E. Andreev "THERMOCHEMICAL CALCULATIONS AND EXPERIMENTAL INVESTIGATIONS ON Mo-Ni-B ALLOY SYSTEM PRODUCED BY COMBUSTION SYNTHESIS" Scientific Proceedings XIII International Congress "Machines. Technologies. Materials." 2016.
- **Sevinch Rahimi Moghaddam**, Bora Derin, "The Fabrication and Characterization of Ternary Boride Composites by Combustion Synthesis Method", 19th International Metallurgy and Materials Congress, Istanbul, Turkey, 2018.

OTHER PRESENTATIONS:

- Nadali Arefian, Narmin Montakhab, **Sevinch Rahimi**, Parisa Sowti Khiabani, Anahita Arefian, Mohammad Reza Vaezi "INVESTIGATION OF EFFECT OF INITIAL PH OF SOLUTION ON HYDROTHERMAL SYNTHESIS OF NANO TITANIUM OXIDE" 7th Iranian Conference of metallurgical engineering, Najafabad, Iran, 2007 (In persian).
- **Sevinch Rahimi Moghaddam**, Javad Moghaddam " NANO ZINC POWDER PREPARATION BY REDUCTION OF ZINC OXIDE WITH NATURAL GAS" First National Conference of nano materials, Shahroud, Iran, 2012 (In persian).
- **Sevinch Rahimi Moghaddam**, Javad Moghaddam " SYNTHESIS AND CHARACTERIZATION OF ZINC POWDER USING REDUCTION METHOD BY NATURAL GAS" International Congress of new and advanced materials, Isfahan, Iran, 2012.